UNIVERSITY OF CALIFORNIA, SAN DIEGO

Studies of Neutron Star X-ray Binaries

A dissertation submitted in partial satisfaction of the
requirements for the degree Doctor of Philosophy
in

Physics

by

Thomas W. J. Thompson

Committee in charge:

Richard E. Rothschild, Chair
William A. Coles
George M. Fuller
Brian G. Keating
Mark H. Thiemens

2008

The dissertation of Thomas W. J. Thompson is approved, and it is acceptable in quality and form for publication on microfilm:

Chair

University of California, San Diego

2008

To my mom

For pushing me to achieve my fullest potential

TABLE OF CONTENTS

LIST OF FIGURES

LIST OF TABLES

ACKNOWLEDGMENTS

Thanks to both of my parents for teaching me the value of hard work, and for raising me to know that I can accomplish absolutely anything that I set my mind to, to my mom for making me a perfectionist, to my dad for showing me how to be disciplined, to Christel Smith for helping me learn how to balance my parents' teachings with emotional sanity, to my little bro for being awesome, to the people of Minnesota for showing me how to be a good person, to Rick Rothschild for always asking the right questions that ultimately contributed to successful work, for being an all-around cool adviser, and for supporting me in my decision to save the world, to John Tomsick for his guidance, to Blair Savage and Chris Howk for getting me started in astronomy research, to Paul Yeatman and Pete James for their consistent help with computer or programming issues, to Regina Jorgenson, Simone Migliari, Alex Markowitz, Dave Collins, Mirko Krumpe, and Tom Gasaway for being my CASS buddies (PY also gets a nod here too), to Slawo Suchy for being a great officemate and friend, to George Fuller for providing the most stimulating class lectures I encountered at UCSD, to Katja Pottschmidt and Joern Wilms for the consistent willingness to help me with research questions and for providing feedback on many papers, to Tom Murphy and Kim Griest for talking to me about my future, and to all the members of my thesis committee for . . . agreeing to be on my committee.

I would also like to thank my research collaborators, particularly Duncan Galloway and Jean in 't Zand, as well as Herman Marshall, Roland Walter, and Lee Homer. Thanks to Biff Heindl, Tod Strohmayer, Lev Titarchuk, Rüdiger Staubert, Bruce Draine, Peter Predehl, Craig Markwardt, Keith Jahoda, Terry Gaetz, and Thomas Dame for help with technical questions, and the High Energy Astrophysics Science Archive Research Center Online Service, provided by the NASA/Goddard Space Flight Center. Finally, I gratefully acknowledge support from NASA contract NAS5-30720, and NASA grants GO2-3060X, NNG06GA85G, GO7-8046X.

Official Stuff: The text of Chapter 3 is a reprint of much of the material that appears in The Astrophysical Journal, Vol. 634, p. 1261, and Vol. 681, p. 506. Chapter 4 is largely material in The Astrophysical Journal, Vol. 650, p. 1063, and also includes work submitted to the journal that is not yet published (see astro-ph/0806.2859). Chapter 5 is material from The Astrophysical Journal, Vol. 649, p. 373, and Vol. 661, p. 447. The dissertation author is the primary investigator and first author on all papers. Richard E. Rothschild supervised the work, and John Tomsick, Herman Marshall, Jean in 't Zand, Roland Walter, Duncan Galloway, and Lee Homer were research contributors.

VITA

EDUCATION

2008	Ph.D., Physics, University of California, San Diego
2007	C.Phil., Physics, University of California, San Diego
2005	M.S., Physics, University of California, San Diego
2002	B.A., *magna cum laude*, Physics, Colorado College

PUBLICATIONS

The X-ray Halo of Cen X-3

Thompson, T.W.J., & Rothschild, R.E. 2008, ApJ, submitted, preprint: astro-ph/0806.2859

Deviations from the Flux-Recurrence Time Relationship in GS 1826-238: Potential Transient Spectral Changes

Thompson, T.W.J., Galloway, D.K., Rothschild, R.E., & Homer, L. 2008, ApJ, 681, 506

The Orbit of the Eclipsing X-ray Pulsar EXO 1722-363

Thompson, T.W.J., Tomsick, J.A., in 't Zand, J.J.M., Rothschild, R.E., & Walter, R. 2007, ApJ, 661, 447

Geometric Distance Determination using Type I X-ray Bursts

Thompson, T.W.J., Rothschild, R.E., & Tomsick, J.A. 2006, ApJ, 650, 1063

Orbital Parameters for the X-ray Pulsar IGR J16393-4643

Thompson, T.W.J., Tomsick, J.A., Rothschild, R.E., in 't Zand, J.J.M., & Walter, R. 2006, ApJ, 649, 373

Chandra and RXTE Spectra of the Burster GS 1826-238

Thompson, T.W.J., Rothschild, R.E., Tomsick, J.A., & Marshall, H.L. 2005, ApJ, 634, 1261

Hubble Space Telescope Imaging of Extraplanar Dust Structures in the Edge-On Spiral NGC 4217

Thompson, T.W.J., Howk, J.C., & Savage, B.D. 2004, AJ, 128, 662

Coupled Radio and X-Ray Emission and Evidence for Discrete Ejecta in the Jets of SS 433

Miller-Jones, J.C.A., Migliari, S., Fender, R.P., **Thompson, T.W.J.**, van der Klis, M., & Mendez, M. 2008, ApJ, accepted

PROCEEDINGS, PROPOSALS, ETC.

"Deviations from the Flux-Recurrence Time Relationship in GS 1826-238" Thompson, T.W.J., Galloway, D.K., Rothschild, R.E. 2007, *The Suzaku X-ray Universe*, San Diego, CA

"A Search for Spectral Features in the Clocked Burster GS 1826-238" Thompson, T.W.J., Rothschild, R.E., & Marshall, H.L. 2007, *Chandra X-ray Observatory* Cycle 9 Proposal

"Return to the Clocked Burster GS 1826-238" Thompson, T.W.J., Galloway, D.K., & Rothschild, R.E., & Kretschmar, P. 2007, *INTEGRAL* Cycle 5 Proposal

"Investigating Anomalous Bursting Episodes in GS 1826-238" Thompson, T.W.J., Galloway, D.K., & Rothschild, R.E. 2007, *XMM-Newton* Cycle 7 Proposal

"Revealing the Nature of Anomalous Bursting Episodes in GS 1826-238" Thompson, T.W.J., & Rothschild, R.E. 2007, *Suzaku* Cycle 3 Proposal

"Return to the Clocked Burster GS 1826-238" Thompson, T.W.J., Galloway, D.K., & Rothschild, R.E. 2007, *Rossi X-ray Timing Explorer* Cycle 12 Proposal

"Determining the Orbital Parameters for the *INTEGRAL* X-ray Pulsars" Thompson, T.W.J., Tomsick, J.A., Rothschild, R.E., in 't Zand, J.J.M., Walter, R., & Pottschmidt, K. 2007, *Rossi X-ray Timing Explorer* Cycle 12 Proposal

"Orbital Parameters for the X-Ray Pulsar IGR J16393-4643", Thompson, T.W.J., Tomsick, J.A., Rothschild, R.E., in 't Zand, J.J.M., Walter, R. 2006, *The Astronomer's Telegram*, No. 786

"The Orbits of the X-ray Pulsars IGR J17252-3616 and IGR 16393-4643" Thompson, T.W.J., Tomsick, J.A., Rothschild, R.E., in 't Zand, J.J.M., Walter, R. 2006, *American Astronomical Society/High Energy Astrophysics Division*, 38, 1.56

"GRB 060814: P200 NIR Observations" Cenko, S.B., Ofek, E. O., Gelino, D., Thompson, T.W.J., Price, P.A., & Berge, E. 2006, *GCN Circular*, No. 5457

"Measuring the Distance and Dust Distribution to Cen X-3 with X-Ray Halo Variability" Thompson, T.W.J., Rothschild, R.E., & Tomsick, J.A. 2006, *Chandra X-ray Observatory* Cycle 8 Proposal

"Distance Determination using Delayed Type I Bursts in the X-ray Halo" Thompson, T.W.J., Rothschild, R.E., Tomsick, J.A., 2005, *Six Years of Science with Chandra*, Boston, MA

"Chandra and RXTE Studies of the Burster GS 1826-238", Thompson, T.W.J., Rothschild, R.E., Tomsick, J.A., & Marshall, H.L. 2004, *American Astronomical Society Meeting*, 205, 102.02

FIELDS OF STUDY

Major Field: Physics and Astrophysics

Studies in Mathematical Physics:
Professor Donald R. Fredkin

Studies in Theoretical Mechanics:
Professor Patrick H. Diamond

Studies in Quantum Mechanics:
Professor Aneesh V. Manohar

Studies in Advanced Classical Electrodynamics:
Professor Thomas M. O'Neil

Studies in Equilibrium and Statistical Mechanics:
Professor Terrence Hwa

Studies in Plasma Physics:
Professor Valentin Shevchenko

Studies in Stellar Structure and Evolution:
Professor George M. Fuller

Studies in High Energy Astrophysics:
Professor George M. Fuller

Studies in General Relativity:
Professors Kenneth Intriligator

Studies in Cosmology:
Professor David R. Tytler

Studies in Physics of the Interstellar Medium:
Professor Arthur M. Wolfe

Studies in Galaxies and Galactic Dynamics:
Professor Arthur M. Wolfe

ABSTRACT OF THE DISSERTATION

Studies of Neutron Star X-ray Binaries

by

Thomas W. J. Thompson

Doctor of Philosophy in Physics

University of California, San Diego, 2008

Richard E. Rothschild, Chair

Neutron stars represent the endpoint in stellar evolution for stars with initial masses between ∼3 and 8 solar masses. They are the densest non-singularities in the universe, cramming more than a solar mass of matter into a sphere with a radius of about 10 km. Such a large mass-to-radius ratio implies deep potential wells, so that when mass transfer is taking place ∼10% of the rest-mass is liberated as gravitational binding energy, resulting in prodigious amounts of X-ray emission that contains valuable information on the physical characteristics in accreting binary systems.

Much of my research in this dissertation focuses on the spectroscopic and timing properties of the canonical thermonuclear bursting source GS 1826–238. By measuring the relationship between the X-ray flux (which is assumed to trace the accretion rate onto the stellar surface) and the time intervals between subsequent bursts, I find that although the intervals usually decreased proportionately as the persistent flux increased, a few measurements of the flux-recurrence time relationship were significant outliers. Accompanying spectral and timing changes strongly suggest that the accretion disk extends down to smaller radial distances from the source during these atypical episodes. This result is important for understanding the nature of accretion flows around neutron stars because it indicates that accretion disks probably evaporate at some distance from the neutron star surface at lower accretion rates.

I also contribute to our understanding of two newly discovered and heavily-absorbed pulsars (neutron stars with strong magnetic fields) by determining the orbital parameters of the systems through pulse timing analysis. Orbital phase-resolved

spectroscopy of one source revealed evidence for an "accretion wake" trailing the pulsar through its orbit, showing that X-rays emanating from the surface can ionize the stellar wind in its vicinity.

Finally, I develop an innovative application of dust scattering halos (diffuse emission surrounding X-ray sources, resulting from photons scattering from dust grains) to geometrically determine the distance and the distribution of dust along the line of sight to X-ray sources. The distance is clearly important for inferring the absolute luminosities of systems from measured fluxes, and knowledge of the distribution of dust can further understanding of the interstellar medium.

1

Introduction

This dissertation is a study of accreting neutron stars and their environments. Neutron stars are collapsed remnants of massive stars and are created during supernova explosions. They represent the final stage in the evolution of a star with an initial mass between roughly 3 $M_\odot$ and 8 $M_\odot$, and are the densest non-singularities in the known universe, with $\rho \sim 10^{14}$ g cm^{-3}. This density is so large that it is equivalent to taking a cube of water 460 m on a side and squeezing it down to the size of a sugar cube. Their final structure and composition represents the intermediate state of stellar remnants: Stars with smaller initial masses become white dwarfs (supported by electron degeneracy pressure), while stars with larger initial masses collapse into a singularity and become black holes. The extreme densities of neutron stars are coupled with extreme gravitational fields, extreme spin frequencies, extreme magnetic fields, and extreme accretion rates onto the surface of the star. As such, neutron stars provide the only probe of physical conditions that are well beyond the realm of conditions that are accessible in Earth-based laboratories.

By studying the timing and spectral characteristics of neutron star X-ray binaries—neutron stars that are accreting material from a nearby companion star, resulting in X-ray emission—one can learn about the conditions in the accretion disk and on the stellar surface. These conditions can further our understanding of the physics of accretion flows, the structure and formation of accretion disks, the physics of nuclear burning on the surfaces of neutron stars, and, the holy grail of X-ray astronomy: the equation of state for matter

at the highest densities.

I begin this introduction by discussing how compact objects form in the context of stellar evolution, and how one of three compact objects can form depending on the mass of the progenitor (§ 1.1). I then discuss how neutron stars are classified depending on the nature of the companion and the properties of the neutron star itself (§ 1.2). I continue by identifying X-ray binaries (compared to lone neutron stars; § 1.3). I finish the introduction by discussing the various types of accretion processes in X-ray binaries (§ 1.4), and the resulting emission from such systems (§ 1.5).

1.1 Compact Object Formation

Throughout the vast majority of a star's life, it remains in a quasi-static configuration where gravitational collapse is counterbalanced by thermal pressure created through the nuclear fusion of hydrogen to helium in its core. When the hydrogen fraction decreases to the point where the star falls out of hydrostatic equilibrium, the star contracts and the temperature of the core increases. The star reaches the endpoint in its lifetime as a main-sequence star.

As the temperature and pressure in the core of the star increase due to gravitational collapse, helium will fuse to carbon and oxygen by the triple-α process. The star will expand to a red giant, and if the red giant has insufficient mass to generate the core temperatures required to fuse carbon, an inert mass of carbon and oxygen will build up at its center. After shedding its outer layers to form a planetary nebula, it will leave behind a core composed largely of carbon and oxygen. The resulting remnant star is called a "white dwarf," which is thought to be the final evolutionary stage of all stars with a progenitor mass of $<$3–6 $M_{\odot}$, representing over 95% of the stars in our Galaxy (e.g., Fontaine et al. 2001). For white dwarfs, degeneracy pressure—a consequence of the Pauli exclusion principle, whereby two fermions cannot occupy the same quantum state simultaneously—ultimately halts the gravitational collapse. The resulting object radius is roughly that of the Earth, and the density is about 10^7 g cm^{-3}.

More massive stars are currently thought to evolve for about 10^7 yr through

nuclear burning of successively heavier elements. Similar to white dwarf progenitors, hydrogen and helium burning occurs over most of the star's lifetime. But unlike white dwarfs, further gravitational collapse in these massive systems creates high enough temperature and pressure in the core of the star to allow new nuclear burning regimes to become accessible. Burning then continues through ^{12}C, ^{20}Ne, ^{16}O, and ^{28}Si, and finally terminates with ^{56}Fe, which is the element with the maximum binding energy per nucleon. For each burning regime, the process repeats: The core collapses, the central temperature rises, and the collapse is halted by the nuclear burning of successively larger nuclei at higher temperatures and pressures. An onion-like structure forms, and each layer is prevented from collapse by the heat and outward pressure of the fusion process in the next layer inward (e.g., Iben 1991). The evolutionary progress accelerates, as each layer burns hotter and quicker than the previous one. The final burn of silicon to nickel, which then decays to iron, takes place in around one day.

With a sufficiently large star, the iron-nickel core will eventually exceed the Chandrasekhar limit (1.4 $M_{\odot}$)—the maximum non-rotating mass which can be supported against gravitational collapse by electron degeneracy pressure—at which point the pressure support mechanism catastrophically fails. The forces holding atomic nuclei apart in the innermost layer of the core suddenly give way, the core implodes due to its own mass, and no further fusion process can ignite or prevent collapse. Ultimately, in the case of a neutron star or black hole, a (type II) supernova explosion takes place. The precise mechanisms that lead to supernova explosions are not well understood, and I refer the reader to Janka et al. (2008) for recent work on the problem.

Neutron stars have progenitor star masses between roughly 3 $M_{\odot}$ and 8 $M_{\odot}$ and are one of the two remnants of supernova explosions. During the explosion, the outer layers are blown away, and the inner core collapses until it is halted by pressure of degenerate neutrons. The remnant object radius is between about 10 and 20 km, and the mean density is about 10^{14} g cm^{-3}. At this point, the star nearly behaves like one giant nuclei held together by self-gravity. Black holes, resulting from progenitors of mass greater than about 8 $M_{\odot}$, are the other remnants of supernova explosions. These objects differ from neutron stars in that there is no physical process that can hold back the inward

pull of gravity, so they collapse to within their event horizon to singularities. Note that another channel for the creation of neutron stars is through the accretion-induced collapse of a white dwarf (type I supernova), and black holes may form through the merging of two neutrons stars.

As a class, the three different objects—white dwarfs, neutron stars, and black holes—are called "compact" simply because they are exceedingly small in size. Because the gravitational potential is proportional to M/R, the small size of the compact objects leads to enormously strong surface gravitational fields. The values of the surface potential (GM/Rc^2) for the Sun, white dwarfs, neutron stars, and black holes are 10^{-6}, 10^{-4}, 10^{-2}, and 1, respectively. Thus, matter accreting onto a black hole will release about a million times as much energy as matter falling onto the surface of the Sun.

1.2 Neutron Stars Characteristics

Neutron stars can be classified by their mass, radius, surface magnetic field strength, spin frequency, age, surface temperature, and central density, among other characteristics. Their structure depends on the physics of the interactions between fundamental particles: protons, neutrons and their constituent quarks. The theory of such interactions, described by Quantum Chromodynamics (QCD), is not yet sufficiently constrained to accurately predict the state of matter at such extremes. Thus, the key uncertainty in models of neutron stars is the equation of state of nuclear matter, particularly above nuclear densities. The equation of state can be written in the polytropic form

$$P = K\rho_0^{\Gamma}, \tag{1.1}$$

where K and Γ are two constants. Various neutron star equations of state are described by Γ between 2 and 5. Polytropes with larger indexes correspond to "harder" equations of state. For comparison, a white dwarf can be described by $\Gamma = 5/3$, and main sequence stars like the Sun are usually modeled by a polytrope with $\Gamma = 4/3$ (Hansen et al. 2004). Questions regarding the equation of state of neutron stars are largely interested with the nature of matter in the interior of the stars. Does a superfluid of neutrons and protons form? Is the core made of a pion condensate of perhaps quark matter? To answer

these questions using QCD requires precise measurements of both the masses and radii of neutron stars.

Neutron stars appear to exist in nature with a limited range of masses, as shown in Figure 1.1. The neutron stars at the top of the figure are members of X-ray binary systems, and those at the bottom are radio pulsars. To determine the masses of neutron stars requires knowledge of the X-ray and optical mass functions, and the inclination of the binary system. The X-ray mass function is

$$f(M_\star, M_X, i) = \frac{(M_X \sin i)^3}{(M_X + M_\star)^2} = \frac{P v_1^3}{2\pi G}, \tag{1.2}$$

where $M_\star$ and v_1 are the mass and radial velocity of the optical companion, respectively, M_X is the mass of the compact object, and i is the inclination of the binary system. By itself, the X-ray mass function represents the lower limit to M_X. To constrain the mass further requires the binary inclination and the mass of the optical companion star, which can be determined by using advanced spectral analysis techniques and optical polarimetry (see e.g., Barziv et al. 2001).

The maximum mass for a neutron star is a sensitive function of the unknown equation of state for nuclear matter. Numerical models and several analytical models have been employed, and in the most realistic and sophisticated models the maximum mass is less than 2 $M_\odot$ (e.g., Schulze et al. 2006). The discovery of a neutron star with a significantly larger mass than the this mass would force theoreticians to reconsider their models. Although accurate masses for some neutron stars have been obtained from observations of young neutron star pulsars in binary systems, and in some cases binary pulsars (Fig. 1.1), unfortunately very little is known about the radii.

1.3 X-ray Binaries

Although the study of the equation of state of neutron stars is extremely interesting, in this thesis I focus my research on accreting neutron stars in binary systems, where a neutron star and a non-compact star (though sometimes a white dwarf) orbit about a common center of mass, and mass transfer is taking place. These systems are referred to as "X-ray binaries," because the high gravitational potential provides for accelerating

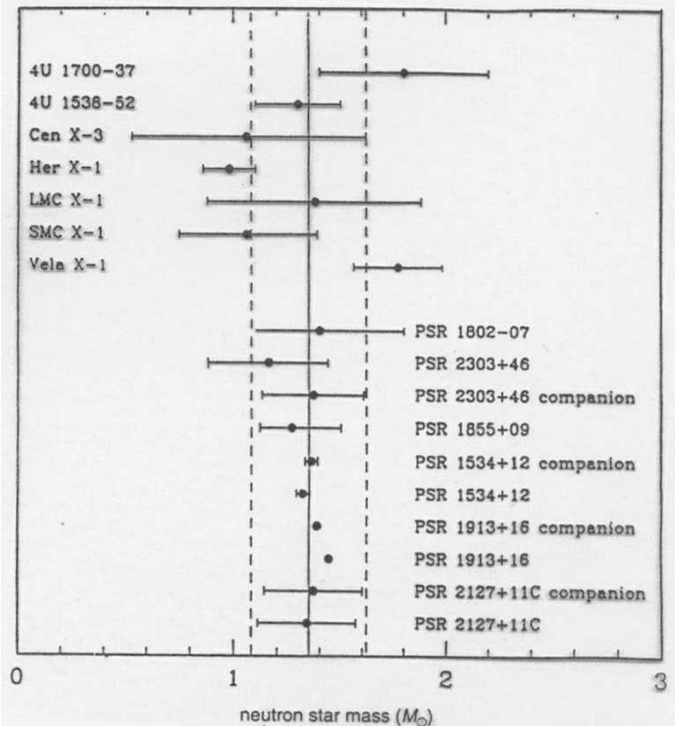

Figure 1.1: Masses of a selected set of neutron stars.

accreted material from the companion star to X-ray temperatures. They are the most luminous class of X-ray source in the sky and have been one of the primary subjects of X-ray astronomy since its inception. In these systems, accretion can occur via Roche-lobe overflow or the capture of stellar wind. Due to the enormous gravitational fields, accreted matter releases about 200 MeV per nucleon (in the case of neutron stars) of gravitational binding energy, resulting in the observed X-ray luminosity. The mass-donating companion stars can range from low-mass dwarfs to high-mass supergiants, providing for the separation of X-ray binaries into two main classes depending on the nature of the companion star: low-mass X-ray binaries (LMXBs) or high-mass X-ray binaries (HMXBs). However, the class division involves much more than mass. For example, there are distinct differences in the type of accretion, the age of the system, and the magnetic field strength. These differences are discussed in further detail below.

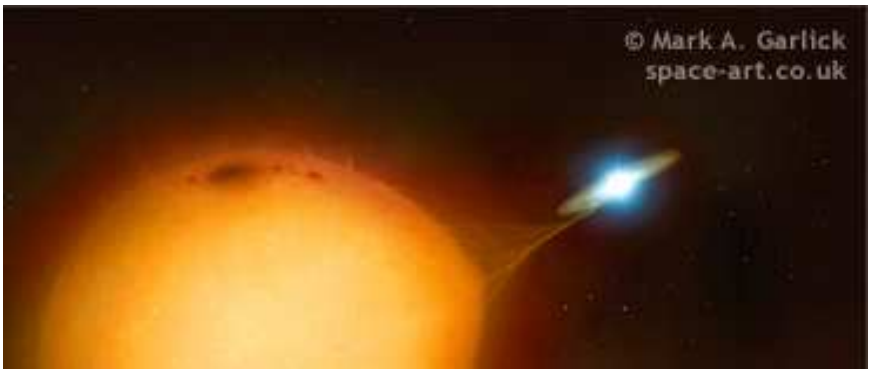

Figure 1.2: Artist's impression of a LMXB as seen from a hypothetical planet in the system. Used with permission from Dr. Mark A. Garlick (space-art.co.uk).

1.3.1 Low-mass X-ray Binaries

Figure 1.2 shows an artist's impression of the view of a LMXB from the surface of a hypothetical planet in the system. These systems consist of either a neutron star or a black hole with a low-mass companion star ($< 2.5\ M_{\odot}$). (White dwarfs are not on this list, despite the fact that they are compact objects, simply because they emit a significantly lower X-ray flux.) Because smaller stars evolve on much longer timescales, LMXBs tend to belong to an older population of stars. Their magnetic fields are typically relatively weak ($< 10^9$ G), so the vast majority of LMXBs do not show coherent pulsations. It is thought that the accretion is responsible for reducing the magnetic field strength, however, the precise physical processes leading to this currently remain uncertain (Bhattacharya & van den Heuvel 1991).

Accretion occurs through Roche-lobe overflow, resulting in the formation of an accretion disk. The accretion disk extends close to the surface of the star, though it may be truncated hundreds to thousands of kilometers from the surface at sufficiently low accretion rates via evaporation of the inner disk (e.g., Mayer & Pringle 2007), and matter is accreted equatorially due to the relatively weak magnetic field strength in these systems. Stellar wind accretion does not significantly contribute to the overall flux simply because the wind of low-mass stars is relatively tiny compared to that of a high-mass star.

Hasinger & van der Klis (1989) developed a description of the neutron star LMXBs using the correlated variations of the X-ray spectral and rapid X-ray variability

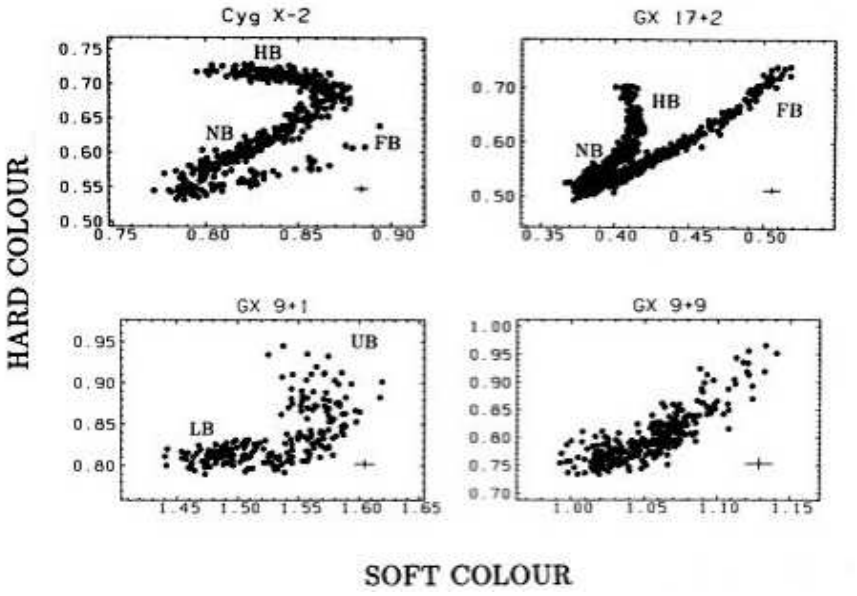

Figure 1.3: Examples of color-color plots for "atoll" and "Z" LMXBs (from Hasinger & van der Klis 1989). The top two sources are examples of "Z" sources, and the bottom two are examples of "atoll" sources.

properties. They distinguished two sub-types of LMXBs called the "Z" sources and the "atoll" sources, whose names were inspired by the shapes of the tracks that they trace out in an X-ray color-color diagram on timescales of hours to days (Fig. 1.3). Note that X-ray colors are counting rate ratios in two bands, and are discussed in § 2.4.2. For each type of source, several spectral and timing states are used to characterize it, which are thought to arise from qualitatively different inner flow configurations (e.g., presence or absence of a corona, structure of accretion disk, jets). One of the primary reasons for the different tracks in the color-color diagrams is that the "Z" sources generally have much higher accretion rates. The physical processes behind the different states are discussed in § 1.5.

X-ray Bursters

A subset of weakly-magnetized neutron stars show type I bursts, which are brief episodes where the X-ray flux increases rapidly and decays more slowly. There are close to 100 type I bursters that are known in the Galaxy[1], and the vast majority

[1]For an updated list of Galactic type I X-ray bursters, see http://www.sron.nl/∼jeanz/bursterlist.html.

are "atoll" LMXBs. Investigations of burst recurrence rates and energetics have lead to convincing arguments that type I bursts stem from unstable thermonuclear burning of accreted hydrogen and helium (e.g., Strohmayer & Bildsten 2003). As freshly accreted material falls onto the NS surface, it is hydrostatically compressed by new material at a rate per unit area $\dot{m} \sim 10^4$ g cm^{-2} s^{-1}, assuming isotropic accretion and a NS radius of 10 km. The thermal energy deposited by the infalling matter causes temperatures in most of the thin NS "atmosphere" to exceed 10^7 K, so that during the accumulation phase hydrogen burns via the hot CNO cycle at a rate that is limited only by the mass fraction $Z_{\rm CNO}$ and not the temperature (Bildsten 2000). Within hours to days, the extreme gravity on the NS surface ($\sim 10^{14}$ cm s^{-2}) compresses the accumulated matter to the point where the nuclear energy generation rate of the 3α-reaction becomes more sensitive to temperature perturbations than the radiative cooling. At this point the resulting thermonuclear instability leads to runaway burning of some or all of the matter that has been deposited since the previous burst.

Although the basic physics of type I X-ray bursts is understood, detailed comparisons between observations and theoretical models have had mixed success (e.g., Woosley et al. 2004). The most successful comparison has been with the "clocked burster" GS 1826–238 (also known as Ginga 1826–238), whose bursts are consistently quasi-periodic (Ubertini et al. 1989; Cocchi et al. 2001; Cornelisse et al. 2003). GS 1826–238 has nearly limit-cycle behavior with stable hydrogen burning during the accumulation phase followed by mixed hydrogen and helium burning triggered by thermally unstable helium ignition (Bildsten 2000). The α-parameter – the ratio of the integrated persistent fluence between bursts to the burst fluence – and the long burst duration ($\sim$ 150 s), imply that after thermonuclear ignition the hydrogen burns via the rapid-proton (rp) process where energy is released through successive proton captures and β decays (Wallace & Woosley 1981). The periodicity of the type I bursts from GS 1826–238 has been remarkably stable over the span of years (Ubertini et al. 1999). Although quasi-periodic bursting is not unique among LMXBs, such consistency over long durations is indeed unusual. The regular intervals between bursts suggest that the accretion rate is stable, that the accreted matter is completely consumed during the bursts, and that the fraction of the stellar sur-

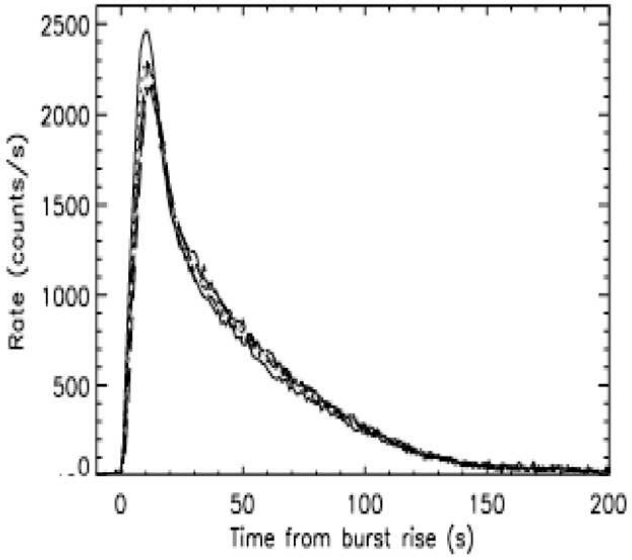

Figure 1.4: Burst light curves from GS 1826–238 made with the PCA instrument onboard *RXTE* between 1998 June and 2006 August.

face covered prior to each burst is approximately constant. The evolution of the spectrum throughout bursts, and the relationship between the accretion rate and burst recurrence time in GS 1826–238 is presented in Chapter 3.

Because black holes have no solid surface, type I bursts are a distinctive sign for the presence of a neutron star. In addition, bursts only occur up to some critical mass accretion rate: If the local mass accretion rate is high enough, hydrogen and helium will burn continuously and stably as the matter is accreted. It is only at lower mass accretion rates that the burning thermally unstable (Bildsten 2000), which explains why bursts are rarely seen in the higher accretion rate "Z" sources.

The light curves of X-ray bursts show a wide variety of characteristics (Cornelisse et al. 2003), but usually they can be described by a fast rise followed by a quasi-exponential decay. Figure 1.4 shows the aligned burst light curves from GS 1826–238 for all observations made with the Proportional Counter Array onboard *RXTE* (§ 2.3) between 1998 June and 2006 August. Burst rise times can vary from less than a second to about 10 s, and are interpreted as the photon diffusion time from the base of the accreted layer, or to the time it takes for the explosion to propagate around the surface of the star

(Spitkovsky et al. 2002; Woosley et al. 2004). The decay of the burst light curve lasts for about 10 s to a couple minutes. Depending on the source, the decay time can be the time to exhaust all of the helium in the accreted layer, or can be the signature of the *rp*-process. Time-resolved spectral analysis of type I bursts indicate that the rise and the exponential decay can be interpreted as heating resulting from the initial fuel ignition, followed by cooling of the ashes upon exhaustion of the fuel (Galloway et al. 2006).

A small fraction of bursts, called radius expansion bursts, are thought to provide a standard candle since their peak luminosities are close to the Eddington luminosity. The Eddington luminosity is the luminosity at which the radiation pressure from photons emitted from the stellar surface equals the pressure of the infalling material (assuming spherically-symmetric accretion), so that the accretion is halted. It is equal to

$$L_{\rm Edd} = 4\pi M m_{\rm p} c/\sigma_{\rm T} \approx 1.3 \times 10^{38}\ (M/M_{\odot})\ {\rm erg\ s^{-1}}. \tag{1.3}$$

Radius expansion bursts are given this name because material is actually raised off the surface by radiation pressure during bursts. The distance to the source can be estimated using radius expansion bursts by measuring the flux and finding the distance corresponding to the Eddington luminosity.

Although X-ray bursts were known since the 1970s, it was not until after the launch of *RXTE* (§ 2.3) that coherent oscillations (so-called "burst oscillations") were observed during type I bursts. The location of the burning during bursts is not assumed to be spherically symmetrical. It is likely that ignition begins near the stellar equator since matter is preferentially deposited there during accretion (Spitkovsky et al. 2002). It is thought that the anisotropic burning caused by the hot spot at the point of ignition results in the burst oscillations. A cartoon of this geometry is shown in Figure 1.5. The oscillation frequency is an excellent estimate of the spin frequency (within 1 Hz) for a given source as has been confirmed by the detection of burst oscillations at the observed spin frequency in the accreting millisecond pulsars SAX J1808366 and XTE J1814338 (Chakrabarty et al. 2003; Strohmayer & Bildsten 2006).

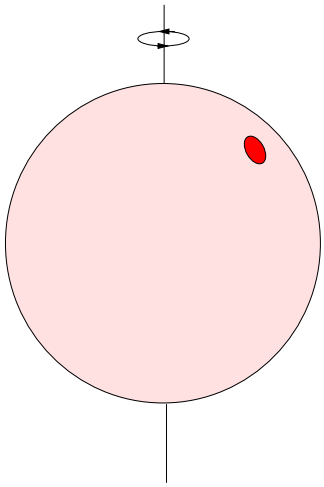

Figure 1.5: Cartoon of an isolated hot spot on a neutron star, which acts as the source of burst oscillations.

1.3.2 High-mass X-ray Binaries

HMXBs are composed of a compact object and a massive early-type companion star. Due to the relatively short lifespan of the supergiant companions, they necessarily belong to a younger stellar population. These younger neutron stars have magnetic fields approaching 10^{13} to 10^{14} G, and so X-ray pulsars are almost always members of HMXB systems.

Accretion occurs through capture of the dense stellar winds, which can reach terminal velocities of up to a few thousand km s^{-1}. When the companion is a giant or supergiant OB star, the accretion and thus X-ray flux is quasi-persistent. The orbital periods for persistent HMXBs typically range from a few hours to days, and the orbital separation can be as small as a couple stellar radii. The orbital eccentricity is usually quite low, and many exhibit periodic eclipses (e.g., Liu et al. 2006).

Most known HMXBs, however, are Be-transient systems (e: strong emission lines). These companion stars are spinning rapidly and have a excretion disk in their rotational equatorial planes. The transient systems have wide orbits with moderate eccentricities, and accretion occurs in short outbursts at the orbital period of the system when matter is captured at periastron. It is thought that the differences between quasi-persistent and transient HMXBs are due to the former type of binary system losing a large

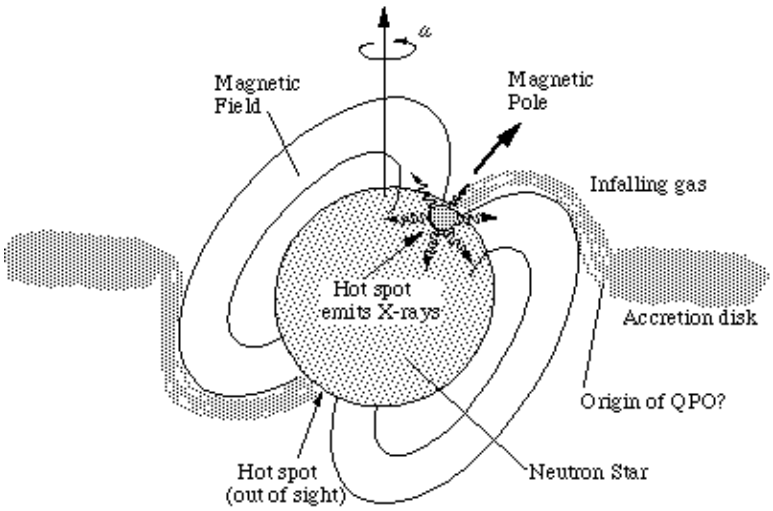

Figure 1.6: Image of accretion onto the poles of a pulsar.

amount of mass and angular momentum in the course of their evolution. The mechanism that provides these loses is the spiral-in mechanism (Paczyński 1976), which occurs when the envelope of the companion star engulfs the neutron star.

Lower luminosity HMXBs exhibit variations in the source flux of up to a factor of 100 on the timescale of minutes. Because the X-ray source is powered by material captured by the wind, the flaring behavior can be explained as being due to inhomogeneities in the wind. Higher luminosity systems, on the other hand, show much less variability. Yet the luminosities in these systems appear to be higher than can be attributed to stellar wind capture (Conti 1978), which suggests that the mass flow to the neutron star is somehow enhanced, possibly involving an accretion disk.

Pulsars

In the early 1970s, the discovery of periodic pulsations from Cen X-3 and Her X-1 that were modulated at the orbital period of the system quickly uncovered the nature of X-ray pulsars as rotating neutron stars with very strong magnetic fields ($B > 12$ G) in binary systems (Schreier et al. 1972; Tananbaum et al. 1972). With a sufficiently strong magnetic field, for typical mass transfer rates the energy density in the field will be

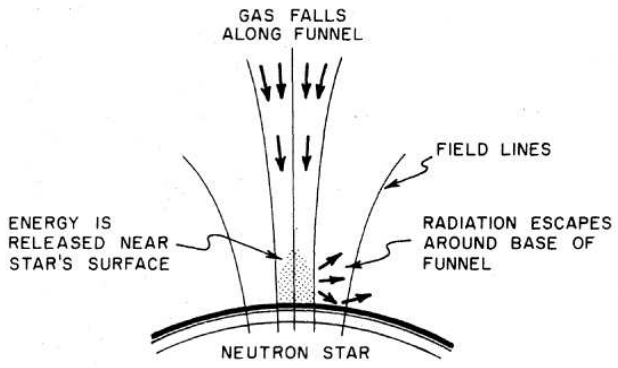

Figure 1.7: Cartoon of the accretion flow near the poles of the pulsar, from Davidson & Ostriker (1973).

greater than the kinetic energy density of the accreting plasma at some radius. Assuming a dipole-like magnetic field ($B \sim \mu/R^3$), the magnetic pressure is proportional to R^{-6} so there comes a point called the Alfvén radius where the accreting matter becomes entrained in the B-field lines and is channeled to the polar caps of the magnetic field (Figs. 1.6 & Fig. 1.7). About 200 MeV per nucleon of gravitational binding energy is therefore released onto two "hot spots" at the magnetic poles. If the magnetic and spin axes are misaligned, the X-ray emission will exhibit pulsations that are modulated at the rotation period of the star through a light house effect. Pulsars emitting X-rays are called "accretion-powered" pulsars (for a review of their properties, see Bildsten et al. 1997). Pulsations from an accretion-powered X-ray pulsar are shown in Figure 1.8.

The other broad category of pulsar are those that are powered by the rotational energy of the neutron star. Charged particles become accelerated when they are entrained in the B-field, emitting non-thermal magnetic dipole radiation (e.g., Faucher-Giguére & Kaspi 2006). These "rotation-powered" pulsars, of which there are more than 700 members, are also referred to as "radio pulsars." Because the energy carried away originates from the rotational kinetic energy of the neutron star, the pulsar spin rate slows down over time. Unlike the pulsars that are commonly studied in X-ray wavelengths, most radio pulsars are isolated rather than members of binary systems. Their spatial distribution follows the overall distribution of matter in the Galaxy, i.e., primarily in the Galactic bulge and along the Galactic plane.

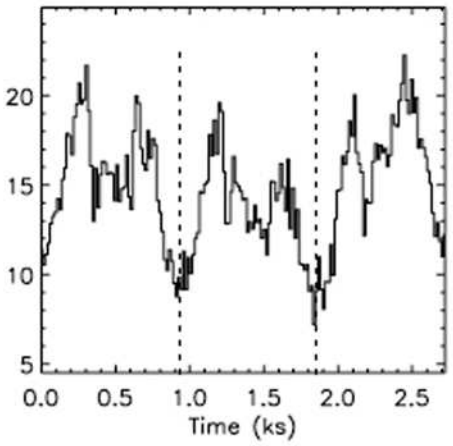

Figure 1.8: Pulsations from an accretion-powered X-ray pulsar for three cycles.

Many of the radio pulsars are millisecond pulsars. They are generally quite old, as suggested by their location, and from their very low spin-down rates, which indicates a weak magnetic field strength. It is thought that the neutron stars in these systems underwent an extended period of mass accretion, which acted to spin-up the star to very high frequencies over $\sim 10^7$ yr. Mass transfer eventually halts and along with it X-ray emission, at which point the neutron star begins emitting millisecond pulsations in radio wavelengths.

When the pulsar is a member of a binary system, the timing of the pulsations will reveal the binary motion of the system, as was first discovered by Hulse & Taylor (1975) in the binary pulsar PSR 1913+16. Subsequent research found that the orbital period of the system was decaying very slowly. This change was presumed to occur because the system is emitting energy in the form of gravitational waves in accordance with Einstein's general theory of relativity. The theoretically calculated value from the relativity theory agrees to within about one half of a percent with the observed value. I use pulsar timing to determine the orbital solutions to two X-ray pulsars in Chapter 5.

A new class of X-ray pulsars with unusual properties are called "anomalous X-ray pulsars." They are so named because the rotational energy loss is not enough to power the observed luminosities, and they apparently do not have a companion. Furthermore, these pulsars are continuously spinning down, which indicates that no accretion is occur-

ring. It has been proposed that anomalous X-ray pulsars are extremely highly magnetized ($B \sim 10^{14}$–10^{16} G) neutron stars, or "magnetars," that are powered purely through the decay of the strong magnetic fields. This was discovered by measuring the spin-down rate and comparing it to the magnetic dipole formula, which shows the relationship between the pulse period and its derivative:

$$-\dot{P} \propto \mu^{2/7} M^{-3/7} R^{6/7} I^{-1} P^2 L^{6/7} \text{ s s}^{-1}, \tag{1.4}$$

where μ is the magnetic dipole moment, M is the mass of the neutron star, R is its radius, the moment of inertia is I, and the luminosity is L (Ghosh & Lamb 1979). The rapid spin-down rates that are observed can only be explained in the presence of extreme (even for neutron star standards) magnetic fields. This class of pulsars has also been associated with Soft γ-ray Repeaters (SGRs), which show recurrent soft γ-ray bursts, and softer quiescent spectra compared to anomalous X-ray pulsars. A discussion of the origin of these unusual sources is given by Marsden et al. (2001).

1.4 Accretion Mechanisms

1.4.1 Roche Lobe Overflow

Neutron stars with low-mass companion stars accrete through Roche-lobe overflow. The Roche-lobe is the region around a star in a binary system within which orbiting matter is gravitationally bound to the star (Figure 1.9). The shape of the equipotential surfaces is approximately tear-shaped, with the two lobes forming an equipotential surface that joins at the inner Lagrangian point L_1. For mass transfer to occur, either the envelope of the companion star shrinks, or the separation of the two stars decreases to the point where the companions star fills its Roche lobe. Matter reaching L_1 can flow into the lobe of the compact object, forming an accretion stream that feeds an accretion disk.

The distance to L_1, also called the radius of the Roche lobe, is determined by the binary separation a and the ratio of the masses of the two stars q through the simple

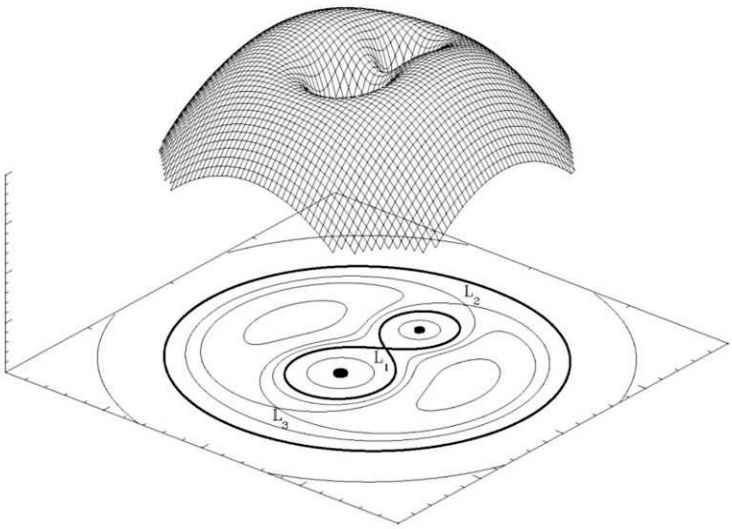

Figure 1.9: Three-dimensional representation of the Roche lobe geometry for binary system with a mass ratio of 2. The solid lines at the bottom of the figure represent equipotential surfaces. The Lagrangian points L_1, L_2, and L_3 are where the gravitational forces cancel out.

analytic approximation of Eggleton (1983):

$$R_{\rm RL} \approx a \frac{0.49 q^{2/3}}{0.6 q^{2/3} + \ln\left(1 + q^{1/3}\right)}. \tag{1.5}$$

Therefore, if the radius of the companion star is larger than $R_{\rm RL}$, matter will flow through L_1 and into the gravitational potential well of the compact object. As matter continuously flows through the Roche lobe, the stream of material will eventually intersect itself. Energy dissipation causes the material to settle into a circular orbit at a radius determined by the angular momentum of the material exiting L_1.

1.4.2 Accretion Disks

Matter in the disk must lose angular momentum in order to move inwards towards the compact object. When enough material has collected at one particular distance from the compact object, viscous torques between neighboring layers of matter leads to shearing and a transfer of angular momentum, subsequently forming an accretion disk (Pringle 1981). The common model of accretion disks is the standard α-disk of Shakura & Sunyaev (1973), which assumes a geometrically thin disk that radiates the released

gravitational binding energy locally, and each parcel of gas rotates at the Keplerian frequency. Emission from this model disk is described by a multi-color blackbody that gets cooler farther from the central source as $T(r) \propto R^{-3/4}$.

If the magnitude of the viscosity is ν, and the surface density of matter in the disk is Σ, the nonlinear diffusion equation that governs the time evolution of the spreading of material in a disk is given by

$$\frac{\partial \Sigma}{\partial t} = \frac{3}{R}\frac{\partial}{\partial R}\left[R^{1/2}\frac{\partial}{\partial R}\left(\nu \Sigma R^{1/2}\right)\right], \tag{1.6}$$

as presented in Frank et al. (1992). For a steady-state accretion disk, and assuming all gravitational binding energy is released locally, it turns out that the viscous dissipation of energy per unit disk face area ($D(R)$) is independent of the viscosity,

$$D(R) = \frac{3GM\dot{M}}{8\pi R^3}\left[1 - \left(\frac{R_\star}{R}\right)^{1/2}\right]. \tag{1.7}$$

This result if important because it is a measurable quantity.

Magneto-Rotational Instability

For many years, there was no clear mechanism for the transfer of angular momentum in accretion disks because normal atomic/molecular viscosity is many orders of magnitude too small. This absence of understanding greatly hindered theoretical studies of accretion disks. However, Balbus & Hawley (1991) identified the magneto-rotational instability (MRI) as a channel for angular momentum transfer. They showed that the presence of a weak magnetic field will make material in the accretion disk susceptible to a powerful local magneto-hydrodymanic (MHD) shear instability. Assuming MHD equations apply, they showed that the MRI would occur when that the angular velocity of the disk decreases outwards, $d\Omega^2/dr < 0$. Such a condition is satisfied for any accretion disk around a compact object.

Inverse Compton Scattering

The MRI theory also provides a source of heating for a hot coronal plasma above the disk, which is important because hard X-ray spectra are observed in compact objects,

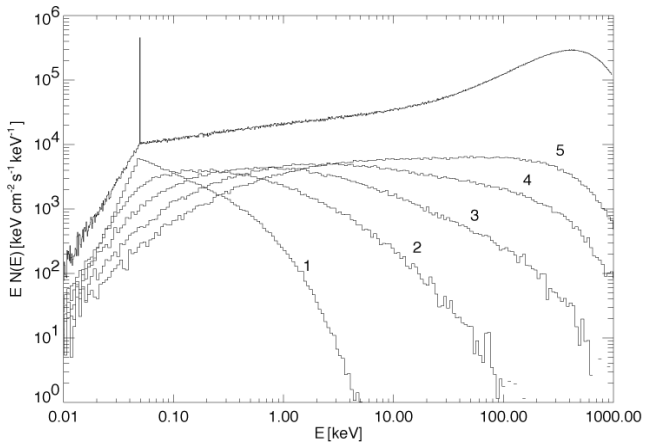

Figure 1.10: Comptonization spectrum for a sphere with optical depth of 5 and electron temperature of 204.4 keV. The labeled spectra are the emerging spectra for given number of scatterings (from Wilms 1998).

and one explanation is the heating of such a plasma. Soft photons from the accretion disk, or from the surface (in the case of a neutron star), become inverse Compton scattered by the hot plasma, forming the non-thermal spectra that are commonly seen. Compton scattering is where photons collide with electrons and exchange energy and momentum. In the reference frame of the electron, the initial E and final energy E' of the electron after a scattering event are given by

$$E' = \frac{E}{1 + \frac{E}{m_\mathrm{e}c^2}\left(1 - \cos\theta\right)}. \tag{1.8}$$

The difference in energy is given to the photon. In the limit of coherent scattering, equation (1.8) becomes the classical formula for Thomson scattering. The electrons are not stationary, however, so for electrons with $kT_\mathrm{e} < m_\mathrm{e}c^2$, the average change in the photon energy is

$$\frac{\Delta E}{E} \approx \frac{4kT_\mathrm{e} - E}{m_\mathrm{e}c^2}. \tag{1.9}$$

This equation clearly shows that the photons gain energy on average so long as $E < 4kT_\mathrm{e}$ (Rybicki & Lightman 1979).

The resultant Comptonization spectrum can be understood by describing the process as a diffusion problem. The soft "seed" photons from the accretion disk or boundary layer of the neutron star begin with a thermal distribution, but gain energy as they

"random walk" through the plasma, with the average number of scattering events being $\max(\tau, \tau^2)$, where τ is the optical depth of the plasma. When the optical depth is greater than unity, and the plasma temperature is well below $m_e c^2$, the diffusion problem can be solved using the Kompaneets equation (Titarchuk 1994). Figure 1.10 shows the emerging spectra for a given number of scatterings. In Chapter 3, I employ a Comptonization model extensively to describe the broadband emission from GS 1826−238.

1.4.3 Advection-Dominated Accretion Flows

Recent advances in modeling accretion flows suggest that at low accretion rates the optically thick, thermal, inner accretion disk can evaporate into an optically thin, non-thermal, hotter flow, i.e., a so-called advection-dominated accretion flow (ADAF; Meyer & Meyer-Hoffmeister 1994, Różańska & Czerny 2000, Mayer & Pringle 2007). Theoretically, the structure of the hot flow is not well understood. Narayan & Yi (1995) considered the case where the density of the accretion disk was so low that the flow becomes optically thin to electron-proton collisions. Because the protons are unable to pass their energy to the electrons on the time scale of accretion, the energy is advected into a black hole, or redeposited in the boundary layer (see below), in the case of a neutron star. This advected energy could also act to power the base of a jet (Blandford & Begelman 1999).

A major component of ADAFs is the existence of some radius $r_{\rm tr}$ where the standard α-accretion disk transitions to a hot, optically thin flow. Esin et al. (1997) considered the relationship between the mass accretion rate and the disk truncation radius ($r_{\rm tr}$), and developed a consistent qualitative picture of how the varying geometries explain the different spectral states in Galactic black holes. As the accretion rate increases, the disk moves closer to the central source (Fig. 1.11), and a greater fraction of the accretion energy is liberated as thermal emission, as I find for GS 1826–238 in § 3.2.

1.4.4 Stellar Wind Accretion

In persistent HMXB systems with OB companion stars, the binary separation is small enough that the compact object is embedded in a dense stellar wind, with mass

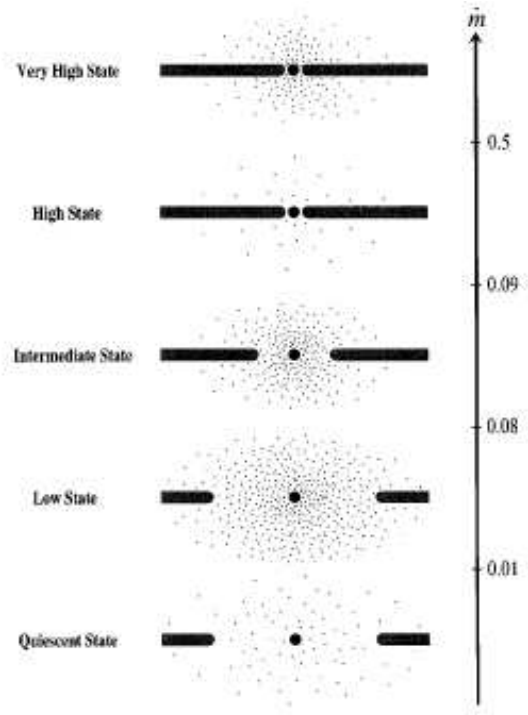

Figure 1.11: Cartoon of the change in the geometry as a function of the advection-dominated accretion rate, from Esin et al. (1997).

loss rates of 10^{-5} $M_\odot$ yr^{-1} to 10^{-6} $M_\odot$ yr^{-1} in the case of evolved stars (Fig. 1.12). The velocity of the stellar wind is approximately the escape velocity from the stellar surface, which is given by

$$v_{\rm wind} \approx \sqrt{\frac{2GM_\star}{R_\star}}, \tag{1.10}$$

where $M_\star$ and $R_\star$ are the mass and radius of the star. While for low-mass main sequence stars like the Sun stellar wind velocities are around 600 km s^{-1}, for main sequence OB stars the stellar wind has a much higher velocity of a few thousand km s^{-1}. As the compact object orbits through the dense wind flow, material in its vicinity can be accreted, thereby powering the X-ray source.

The accretion rate from a stellar wind can be approximated by assuming the compact object accretes material from a cylindrical region whose border is determined by where the gravitational pull of the compact object can overcome the momentum of the wind. Davidson & Ostriker (1973) showed that this radius is given by

$$r_{\rm acc} \approx \frac{2GM_{\rm NS}}{v_{\rm wind}^2 + v_{\rm NS}^2}, \tag{1.11}$$

where $M_{\rm NS}$ and $R_{\rm NS}$ are the mass and radius of the neutron star. Typically, the velocity of the neutron star is neglected because it is so much smaller than the velocity of the stellar wind. The fraction of the stellar wind that is accreted is

$$f \approx \frac{1}{4}\left(\frac{M_{\rm NS}}{M_\star}\right)\left(\frac{R_\star}{a}\right)^2, \tag{1.12}$$

where a is the binary separation. By using typical system parameters, f is $\sim$0.01%; the tiny fraction of captured matter is primarily the result of the small solid angle subtended by the neutron star from the viewpoint of the surface of the companion star. Although the vast majority of material escapes to the interstellar medium, with only about 10^{-8} $M_\odot$ yr^{-1} accreting onto the compact object, the accretion rate is still a significant fraction of the Eddington luminosity. Conti (1978) also revealed that in some sources the stellar wind can act to feed an accretion disk that forms around the compact object. In other cases, a compact object may be accreting via Roche-lobe overflow and via stellar wind simultaneously.

The presence of X-ray flux from the compact object can ionize the wind in its vicinity. Since stellar winds propagate through resonant line scattering, an ionized region

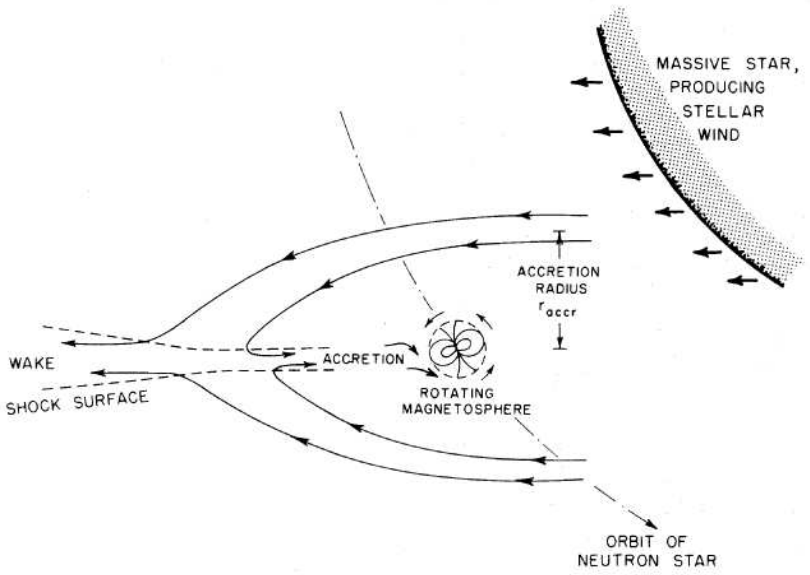

Figure 1.12: Cartoon of stellar wind accretion in a HMXB system, from Davidson & Ostriker (1973).

of space acts to stall the wind in its place, leading to an "accretion wake" trailing the compact object (e.g., Blondin et al. 1990). At later orbital phases, the line of sight to the compact object can pass through the accretion, leading to enhanced absorption. This effect has only been observed in a handful of cases, although I find convincing evidence this is occurring in the X-ray pulsar EXO 1722−363 in Chapter 5.

1.5 Spectral States

The energy spectra of X-ray binaries will show a range of characteristics reflecting different accretion flow geometries depending on the accretion rate onto the compact object, the nature of the compact object, and the presence and strength of a magnetic field. These characteristics are typically described by referring to the "spectral state" of the X-ray binary. When a hard, non-thermal, power-law component with photon index in the range 1.5–2 dominates the energy spectrum, it is said that the source is in its "low/hard" state. When a soft, thermal, blackbody component with temperature $kT \sim 1$ keV dominates, then the source is in its "high/soft" state.

The determination of the state depends on the type of accretion flow that dominates. The high/soft state occurs when most of the gravitational binding energy is dissipated in an accretion disk. In this state, a multi-color disk blackbody from the inner parts of an optically thick accretion disk contributes to the LMXB spectrum. In addition, a hot corona, possibly powered by the MRI, creates a hard, non-thermal power-law component. This component could arise from inverse Compton scattering of soft seed photons by relativistic electrons (Sunyaev & Titarchuk 1980). On the other hand, the low/hard state occurs when there is a hot, optically thin flow (perhaps an ADAF). In this case, the accretion disk is probably truncated far from the surface of the neutron star, or far from the event horizon in the case of black holes. The multi-color blackbody component will still be present in the spectrum, but the temperature of the inner disk will be cooler and the fraction of the bolometric flux dissipated in the disk will be lower. If interstellar photoelectric absorption, whose effects are most pronounced at lower energies, is large enough, the multi-color thermal spectrum of the accretion disk may seem to be entirely absent. Nevertheless, the low/hard state shows a dominant hard ($\sim$20 keV) power-law component, and is detected in the spectra preferentially (but not exclusively) during phases of relatively low 2–10 keV fluxes. This power-law component does not always extend to extremely high energies ($>$ 100 keV), but shows a characteristic roll-over near the hottest temperature reached by the Compton upscattering plasma. Figure 1.13 shows the accretion geometries and corresponding spectra for three variations of a source in a low/hard state. Note how as the inner edge of the accretion disk approaches the compact object, more of the gravitational binding energy is released as thermal, lower energy photons.

The plasma temperature in neutron star X-ray binaries is generally lower than in black holes due to the presence of a solid surface (Done et al. 2007). As photons are accreted onto the neutron star surface, the resulting thermal photons from the surface are upscattered by the surrounding plasma. Not only do the thermal photons gain energy, but due to energy conservation, the energy in the plasma must necessarily decrease, lowering the plasma temperature. Therefore, one of the main differences between the low/hard state in black holes and neutron stars is that the photon index of neutron stars have a

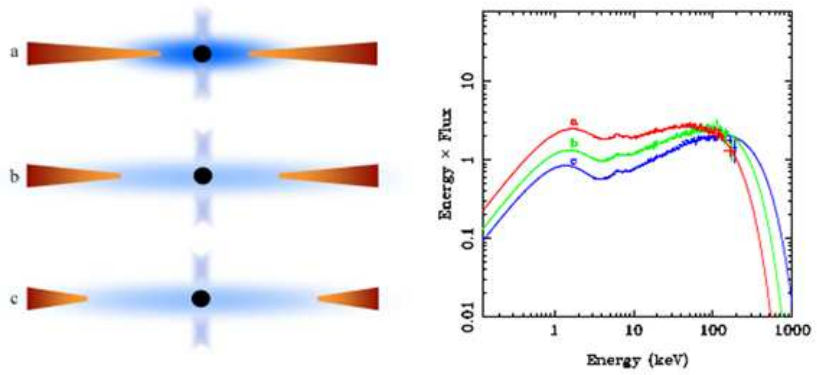

Figure 1.13: Examples of various accretion geometries and corresponding spectra for a source in the low/hard state. The left figure is from Done et al. (2007), and the right figure is from Ibragimov et al. (2005).

comparatively low cut-off energy indicative of the typically cooler neutron star plasma (Strickman et al. 1996). This effect can also be seen in Fig. 1.13: When the disk moves inwards, more of the thermal photons intercept the optically thin, hot plasma, thereby cooling it, and causing the spectrum to roll-over at a lower energy.

The physical processes governing the transition from one state to the other are not completely understood, but most observational evidence suggests that at lower accretion rates the disk evaporates in the inner regions (Meyer & Meyer-Hoffmeister 1994). The flow becomes optically thin and non-thermal, or the accretion energy may be advected. In the case of black holes, advected energy is simply lost to the event horizon, and for this reason, black hole binaries are often conspicuously underluminous. Advection of energy can also occur in neutron star X-ray binaries, but any energy carried inward is eventually thermalized in the "boundary layer"—a region of significant angular momentum transfer, where up to half the accretion luminosity may be liberated—or on the surface. The absence of a clear description of the flow and thermal structure of this layer has been problematic for spectral modeling of boundary layers. Narayan & Popham (1993) performed numerical solutions of a model of thin accretion disks including a self-consistent description of the boundary layer. Two distinct types of solution exist, depending on the mass accretion rate. At high rates, optically thick boundary layers are present whose radial width and peak temperature decrease with decreasing accretion rate.

When the accretion rate falls below a critical value, however, the boundary layer becomes optically thin, and the width and temperature increase dramatically. Black holes do not have boundary layer emission because the emission mechanism requires torques between material in the disk and the stellar surface, which black holes obviously lack.

The presence of a magnetic field is the other major factor determining the nature of the X-ray emission. The X-ray spectra of accretion powered pulsars are typically non-thermal, show pulse-phase dependence, and have a characteristic cut-off energy that may be related to the strength of the magnetic field. Currently, most spectral models are empirical and a preeminent theoretical model has yet to be established. A unique quality of X-ray pulsars is what appears to be an absorption feature at some energy ∼10–30 keV. These have been interpreted as cyclotron resonance scattering features (CRSF), also known as a cyclotron line, that traces the magnetic field strength. CRSFs are created due to the interplay of photons with a population of electrons at quantized Landau levels. These levels are the discrete energy states of electrons in strong magnetic fields. Photons corresponding to the energy difference between the Landau levels are absorbed and re-emitted by the electrons, and scattered out of the line of sight or redistributed to a different energy, thus appearing as an absorption-like feature in the spectrum. Observations of these features provide the only avenue for direct detection of the magnetic field strength through the relation:

$$E_{\rm cyc} = \frac{1}{1+z}\frac{\hbar e B}{m_{\rm e}} \approx \frac{11.6\ {\rm keV}}{1+z} B_{12}, \tag{1.13}$$

where B_{12} is the magnetic field strength of the neutron star at its surface in units of 10^{12} G and z is the gravitational redshift (Canuto & Ventura 1977).

1.6 Where I contribute

From the discussion above, it is clear that the study of accreting neutron stars encompasses a wide range of characteristics. Figure 1.14 shows the general areas where I specifically make a contribution to current research through a flow chart. Specifically, I study the geometry of the accretion flow in LMXBs through spectral and timing analysis, I study the dependence of the recurrence time of type I X-ray bursts on the accretion rate,

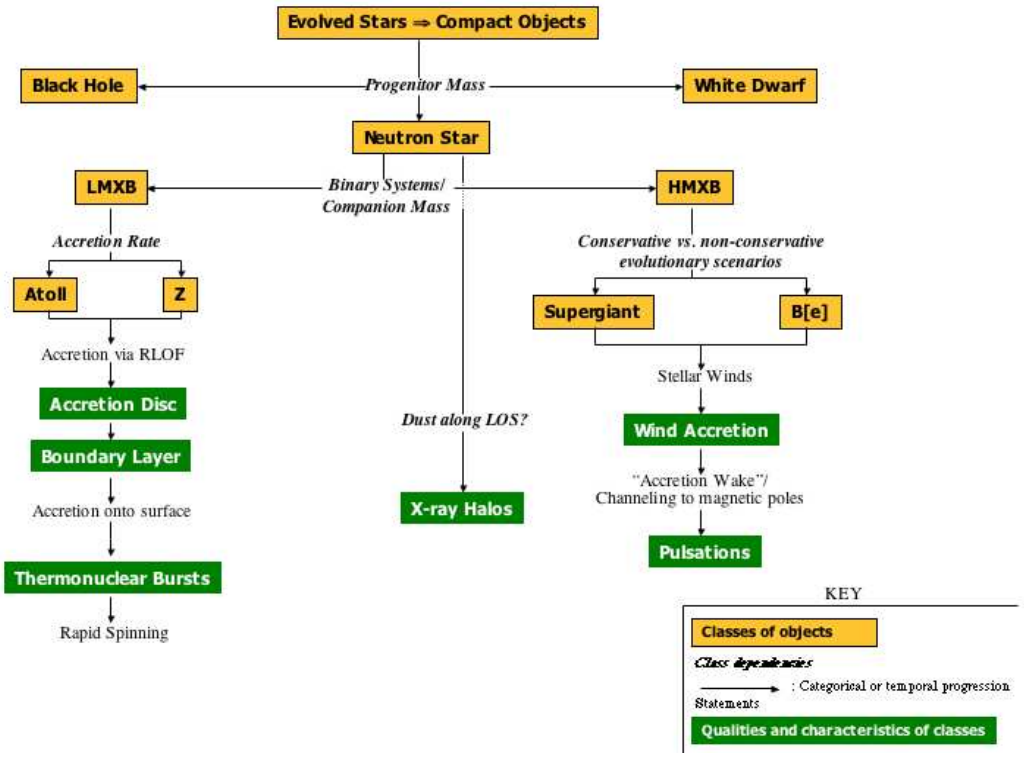

Figure 1.14: Flow chart indicating the general areas of study of neutron star X-ray binaries where I make a contribution to current research. Note that "RLOF" stands for Roche-lobe overflow, and "LOS" stands for line of sight.

I use indications of rapid spinning to measure the spin frequency of one particular neutron star, I study X-ray halos to determine the feasibility of using type I bursts as distance indicators, and to determine the dust distribution and distance to the well-studied pulsar Cen X-3, and I determine the nature of two recently-discovered HMXB systems through pulse timing analysis.

After a brief outline of the instrumentation and analysis techniques (Chapters 2), the remainder of this dissertation can be divided into three parts. In Chapter 3 I study the "clocked burster" GS 1826−238 in detail, where I discover "burst oscillations" in this source for the first time, find evidence for Compton cooling of the boundary layer during bursts, and develop a self-consistent explanation for deviations in the flux-recurrence time relationship that suggest a wholesale shift in the location of the inner edge of the accretion disk. In Chapter 4 I study dust-scattered X-ray halos (diffuse emission surrounding X-ray

sources due to scattering along the line of sight), and in particular, the variability in the halo which allows for geometric distance determination. Such methods have only been applied successfully in a few other cases. Finally, in Chapter 5 I use pulse timing analysis to find the orbital parameters for two newly-discovered pulsars in high-mass X-ray binary systems. For one source, I study the orbital phase-resolved spectroscopy to find evidence for the creation of an "accretion wake" trailing the source through its orbit.

2

X-ray Observatories, Instrumentation, & Analysis Techniques

In this work, I have used data from many space-based observatories, although primarily the *Chandra X-ray Observatory* and the *Rossi X-ray Timing Explorer*, to study accretion processes onto neutron stars, to probe the physics of unstable thermonuclear explosions on their surfaces, and to discover the orbital parameters of a newly-discovered class of heavily-absorbed pulsars. I have also developed a method to geometrically measure the dust distribution and distance to neutron stars using X-ray halos, which are created through small-angle scattering of X-ray photons off of dust grains in the interstellar medium. My investigation of X-ray halos exploits the superb angular resolution of the *Chandra X-ray Observatory*.

2.1 Introduction

Since the Earth's atmosphere is opaque to radiation in the X-ray band, one must study X-ray sources from above the atmosphere. Early observations of X-ray sources, lasting minutes to hours, were made with instruments borne aloft by rockets or balloons, providing initial insights into the distribution and characteristics of these objects.

Subsequent substantial advances were made with orbiting observatories. The first X-ray satellite, *UHURU*, was launched in 1970, detecting over 400 X-ray sources, including X-ray binaries and clusters of galaxies. The next major advance came with the launch of the *Einstein* observatory due to its high resolution imaging capabilities. Further improvements were made to the resolution of the images in 1990, when the *ROSAT* satellite was launched. Today, there is a veritable fleet of observatories investigating high-energy phenomena in a wide range of energy pass bands, including the *Rossi X-ray Timing Explorer*, the *Chandra X-ray Observatory*, *Swift*, *INTEGRAL*, *XMM-Newton*, and most recently *Suzaku*. The primary scientific objectives of each observatory are different, so each is built with particular emphasis placed on, for example, excellent energy and/or timing resolution, a large collecting area, or rapid response to transient events. Table 2.1 shows some of the features of the current set of observatories, in operation as of mid-2008. The majority of the investigations in this thesis used data from the *Chandra X-ray Observatory* and the *Rossi X-ray Timing Explorer*. More detail on these observatories is provided below.

2.2 The Chandra X-ray Observatory

The *Chandra X-ray Observatory* is a high-resolution telescope with a set of sophisticated imaging and spectroscopic capabilities (Fig. 2.1). The greatest achievement in the engineering of the telescope is the construction of the High Resolution Mirror Assembly (HRMA), delivering the highest angular resolution of any X-ray observatory ever built. The assembly consists of a set of four nested circular grazing-incidence mirrors of unprecedented smoothness. Along the optical path, the shape of the mirrors is a paraboloid turning into a hyperboloid (Wolter Type-I). X-ray photons enter the telescope aperture and scatter twice before reaching the focal plane.

Because of the short wavelength of X-ray photons, even tiny imperfections in the surface of the mirror appear relatively large to the incoming photons, and therefore do not scatter in a precisely specular manner (with an equal angle of incidence and reflection). As a result, a point source appears in an X-ray image as a small fuzzy dot. The size and

Table 2.1. Current Space-Based X-ray Observatories

Observatory	Energy Range (keV)	Energy Res. ($\Delta E/E$)	Timing Res. (s)	Angular Res.
Chandra[a]	0.5–10	5%/0.5%[b]	1.7	$0.5''$
RXTE[c]	2–250	15%	10^{-5}	1°
XMM-Newton[d]	0.3–10	10%	10^{-5}	$5''$
Suzaku[e]	0.4–500	2%	8	$2'$
INTEGRAL[f]	15–1000	5%	10^{-5}	$12'$
Swift/BAT	0.2–10	3%	0.1	$15''$
Swift/XRT	15–150	10%	10^{-3}	$15''$

Note. — Most of the observatories are comprised of a set of instruments. The observatories listed here are in operation as of early 2008.

[a]For further details, see http://cxc.harvard.edu/proposer/POG/html/index.html

[b]ACIS CCD/High-Energy Transmission Grating

[c]For further details, see the *RXTE* technical appendix at http://rxte.gsfc.nasa.gov/docs/xte/appendix_f.html

[d]Timing resolution in "timing" mode, energy resolution of the pn detector. See http://xmm.esac.esa.int/external/xmm_user_support/documentation/index.shtml

[e]Timing resolution in "normal" mode, energy resolution for the XIS. See http://www.astro.isas.ac.jp/suzaku/doc/

[f]Characteristics of the ISGRI detector. See http://isdc.unige.ch/Outreach/Integral/integral.html

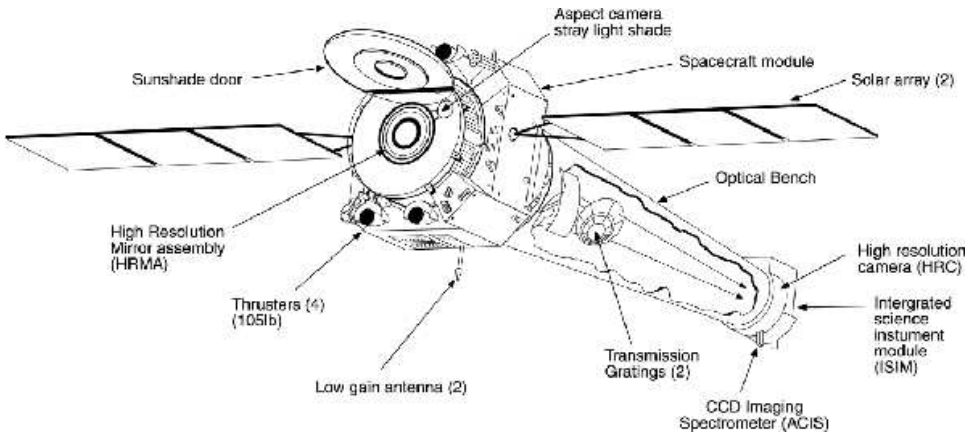

Figure 2.1: Schematic diagram of the *Chandra X-ray Observatory*, from Brissenden (2001).

shape of the projection of a point source onto the focal plane is referred to as the point spread function (PSF). In general, the PSF is a function of energy and position of the source in the focal plane.

Although the HRMA represents the greatest achievement in the engineering of *Chandra*, the observatory also offers moderate resolution CCDs, sensitive to X-rays between 0.5 and 10 keV, that can be used in conjunction with the High Energy Transmission Grating (HETG; Canizares et al. 2005) or Low Energy Transmission Grating (LETG) to obtain higher resolution spectra. The set of CCDs are referred to as the Advanced CCD Imaging Spectrometer (ACIS), which is composed of 10 planar, 1024×1024 pixel CCDs; four arranged in a 2×2 array (ACIS-I) used for imaging, and six arranged in a 1×6 array (ACIS-S) used either for imaging or as a grating readout. Two of the CCDs are back-illuminated (BI) and eight are front-illuminated (FI). The nominal frame time of the CCDs is 3.2 s. Much further detail about this instrument is provided by Garmire et al. (2003). The HETG consists of two gratings with different periods. The Medium Energy Grating (MEG) intercepts rays from the outer HRMA shells and is optimized for detection of medium energy photons. The High Energy Gratings (HEG) intercepts rays from the two inner shells and is optimized for high energy photons. Both gratings are mounted on a single support structure that can optionally be inserted into the optical path. The two sets of gratings are used concurrently with their rulings at different angles

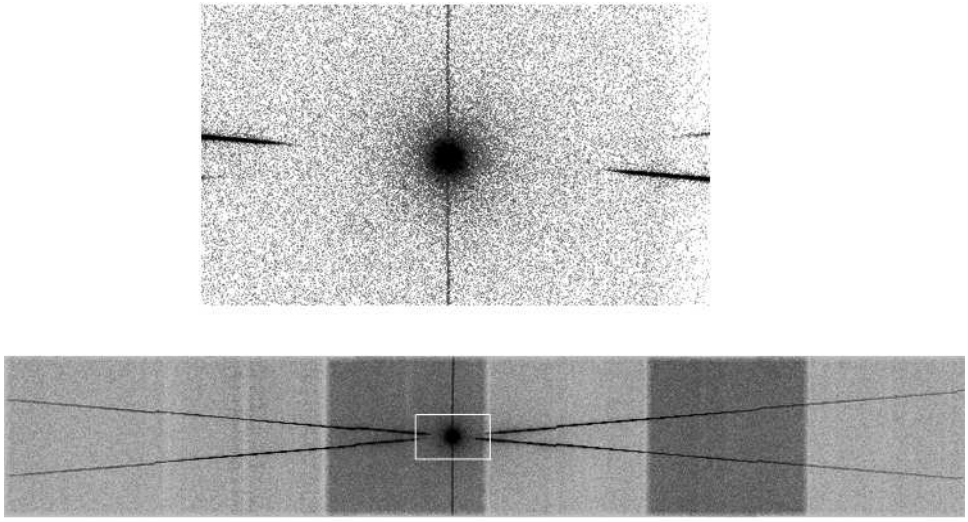

Figure 2.2: An example of an image from a *Chandra*/HETG observation using the six ACIS-S chips. The white border in the bottom panel indicates the zoomed-in portion of the image in the top panel. Note the "whiskers" from the transmission grating, and the different grayscales for the two back-illuminated and four front-illuminated CCDs. The vertical line is an image artifact called the "readout" strip, and results from X-rays hitting the CCDs during frame readout. The diffuse emission surrounding the source is the convolution of the point spread function and the X-ray halo (§ 4.1).

so that the dispersed images form a shallow X or cat whiskers centered at the undispersed (zeroth-order) position. Figure 2.2 shows an example an image from a *Chandra*/HETG observation using the six ACIS-S chips. The LETG has a similar design as the HETG, but is optimized for much lower energy photons between 0.07 and 0.2 keV. I do not use the LETG in any of the following work.

2.3 The Rossi X-ray Timing Explorer

The *Rossi X-ray Timing Explorer* orbits the Earth at an altitude of 580 km with an inclination of 23°. A schematic diagram of the observatory is shown in Fig. 2.3. Although this observatory does not have imaging capabilities like *Chandra*, two of the primary instruments, the Proportional Counter Array (PCA; Jahoda et al. 2006) and the High Energy X-ray Timing Experiment (HEXTE; Rothschild et al. 1998), were designed to perform sub-millisecond timing studies of Galactic X-ray sources, with timing resolution of 1 μs and 10 μs, respectively. The third main instrument onboard the satellite

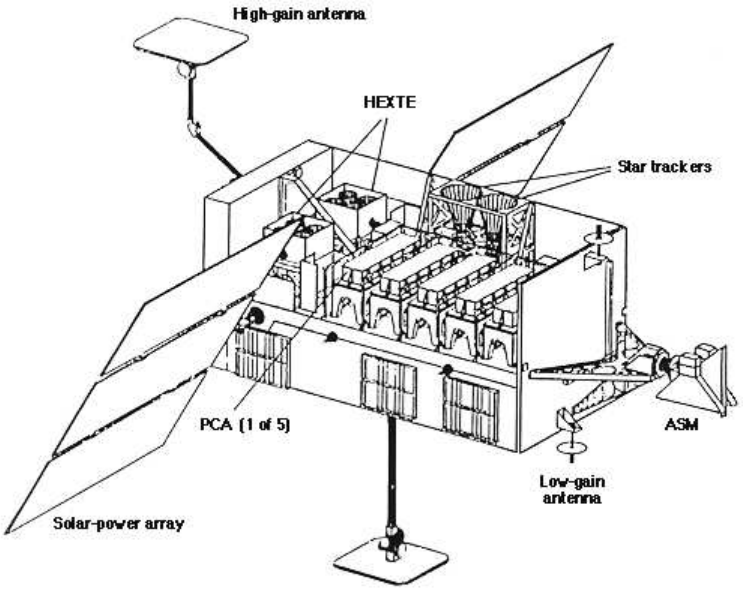

Figure 2.3: Schematic diagram of the *Rossi X-ray Timing Explorer*.

is the All Sky Monitor (ASM), which was designed to be able to simultaneously monitor the fluxes of many discrete sources from 2 to 12 keV (Levine et al. 1996). The three cameras that comprise the ASM are mounted on a platform at one end of the satellite and operate independently of the PCA and HEXTE during pointed observations. The platform rotates once about its axis during each orbit, resulting in ∼80% sky coverage.

The configuration of the orbit is such that the satellite passes through the South Atlantic Anomaly (SAA)—the region where Earth's inner van Allen radiation belt makes its closest approach to the planet's surface—in 6 of the 14-15 daily orbits. These passages last 10–20 minutes, during which time the instruments are put in a safe mode to protect them against the high particle flux. Even if the satellite does not pass through the SAA, X-ray sources will be occulted by the Earth for about 30 minutes out of each 100 minute orbit depending upon location. The only sources to avoid being occulted are located near one of the poles of the orbit.

2.3.1 The Proportional Counter Array

The PCA consists of five coaligned (1° FWHM), xenon/methane multi-wire, multi-layer proportional counters (PCUs) sensitive to X-rays from 2–60 keV. Proportional counters operate by applying an electric field to the gas, and measuring the amount of charge that collects on the electrodes after a photon interacts with the gas. A photon from an X-ray source passes through the collimator and interacts with the gas through photoelectric absorption, creating a region of electron-ion pairs. The voltage applied to the gas causes the electrons to be accelerated to the cathode (the ions mostly stay at their initial location because of their much larger mass), and as the electrons migrate to the electrode, collisions take place with other neutral gas molecules, leading to the creation of more electron-ion pairs. These secondary pairs release more electrons into the gas that are accelerated, undergo collisions, and create a cascade of further ionizations. The size of the cascade, measured by the size of the charge collected at the cathode, is nearly linearly proportional to the energy of the incident photon for appropriate values of applied voltage.

Each of the individual proportional counter units (PCUs), numbered 0 to 4, operates independently, has an effective area of about 1,400 cm^2, and a timing accuracy of about 1 μs. The PCA adopts the cell to cell, layer to layer connection scheme similar to the HEAO-1 A2 HED detectors, with an active propane anti-coincidence layer in the front and an anti-coincidence xenon/methane outer cell on the three other sides of the detector. This setup allows rejection of background events caused by charged particles, which outnumber X-rays 100 to 1, with high efficiency that significantly reduces the residual background event rate at lower energies. Although the PCUs are identical, they differ in the details of their energy calibration and background.

2.3.2 The High Energy X-ray Timing Experiment

The HEXTE, co-aligned with the PCA, is composed of two clusters of four NaI/CsI phoswich scintillation detectors that are sensitive to X-rays from 15 to 250 keV. The phoswich detector architecture substantially reduces the charged particle background through pulse shape discrimination (Peterson 1975). The main NaI crystal ex-

hibits shorter response to ionization when compared to the CsI crystal directly behind the NaI crystal. In addition, measurements of the cosmic X-ray background are made by "rocking" the two clusters orthogonally to each other to an offset of 1.5°. In a 16 s cycle, four background positions are sampled. When one cluster moves on-source, the other cluster is off-source. Then, the two clusters move again so that the former is off-source and the latter is on-source.

Similar to the PCA instrument, the HEXTE provides unprecedented timing information on the nature of compact objects. The use of HEXTE has allowed the study of the high-energy spectra of many Active Galactic Nuclei (AGN) for the first time, and also allowed tests of theories for the origin of the X-ray background. Together the PCA and HEXTE experiments provide simultaneous spectroscopic coverage from 2–200 keV with an overlap from about 20 to 60 keV.

2.4 Data Modeling & Analysis

Time tagged spectral data allows for studies of temporal variability, spectral shape, and combined spectral/temporal variability. Each provides unique insight into the physical processes in X-ray sources.

2.4.1 Spectral Analysis

A wide variety of instrumentation is used to measure astrophysical X-rays. Each type of detector, whether it be a CCD, a scintillator, or a proportional counter, among many others, has a unique set of characteristics that affects the efficiency of the detection of photons at different energies. Spectral data is measured as the number of observed counts C in each instrumental channel I. This data contains the signature of the particular instrument's response to X-rays as a function of energy. In order to extract the true spectrum from an X-ray source, one must parametrize the detection efficiencies through an instrumental response matrix $R(I, E)$, which represents the probability that the incoming photon of energy E will be detected in detector channel I. Prior to launch, the response matrix behavior is determined through detailed simulations of photon inter-

actions in the detector media. In orbit measurements allow for small corrections that include affects of cosmic rays. The calibration sources have a known spectrum, and the most common source used in X-ray astronomy is the Crab nebula.

The measured spectrum is related to the actual source spectrum $S(E)$ through

$$C(I) = \int_0^\infty S(E)R(I,E)dE. \tag{2.1}$$

The integral equation must be inverted in order to infer the spectrum $S(E)$, but this is usually not feasible because inversion can result in non-unique solutions that are unstable to small changes in $C(I)$. Determination of the spectrum of an X-ray source therefore involves choosing an analytical model spectrum that is described by a set of parameters, convolving the model spectrum with the instrumental response matrix, and comparing the predicted counts spectrum $C_{\rm p}(I)$ to the measured counts spectrum $C(I)$. The best estimate of the model parameters is inferred through χ^2-minimization (Bevington & Robinson 2002).

Common spectral models $S(E)$ that I employ in this thesis are (1) a blackbody to describe thermal emission during type I X-ray bursts, (2) a multi-color disk blackbody to describe the integrated spectrum of an accretion disk, (3) a power-law to describe non-thermal emission, and (4) an analytically-derived Comptonization model to describe the emission resulting from inverse Comptonization, among others. Each model has its own set of parameters. A blackbody, for example, is characterized by a temperature and a normalization, while the Comptonization model is characterized by an electron temperature, a "seed" photon temperature, an optical depth, and a normalization.

Chi-squared Fit Statistic

To quantify the degree to which the predicated and measured counts spectra agree, one typically uses the fit statistic "chi-squared":

$$\chi^2 = \sum \frac{[C(I) - C_{\rm p}(I)]^2}{\sigma(I)^2}, \tag{2.2}$$

where $\sigma(I)$ is the Poisson uncertainty in the number of counts in channel I predicted by the model, i.e. $\sigma(I) = \sqrt{C_{\rm p}(I)}$. The spectral model parameters are then adjusted until

the minimum of χ^2 is reached. The resulting parameter values are referred to as "best-fit" parameters. Note that there are many other fit statistics that are used in probability theory, although the chi-squared distribution is one of the most widely used distributions in statistical significance tests.

To determine if the fit is acceptable, one must compare the value of χ^2 to the number of degrees of freedom ν in the fit, which is the number of channels minus the number of parameters in the model. If the model describing the data is a good one, then the "reduced chi-squared," which equals χ^2/ν should be approximately equal to unity, or equivalently, $\chi^2 \sim \nu$. A reduced-χ^2 that is much larger than one indicates a poor fit, while a reduced χ^2 that is much less than one indicates either the uncertainties in the channels are too large, or the model has more parameters than are necessary to describe the data. If a quality fit is achieved, it is still impossible to claim that the model fitting the data is unique. The discrimination of competing models is a matter of scientific judgement.

A more quantitative approach to testing whether or not a model accurately describes a dataset is to consider the probability of obtaining a value of χ^2 as large as (or larger than) what is observed $\chi^2_{\rm obs}$ if the measurements actually followed the assumed model. In other words, one is testing whether or not the *null hypothesis* that the measurements came from a particular distribution is true. If $\mathrm{Prob}(\chi^2 > \chi^2_{\rm obs})$ is large, the observed and expected distribution are *consistent* (recall that one cannot specify if the chosen model is unique); if the probability is small, then they disagree. The probabilities, which depend on the number of degrees of freedom ν, are determined by integrating over the χ^2-distribution, *viz.*

$$\mathrm{Prob}_\nu(\chi^2 > \chi^2_{\rm obs}) = \frac{2}{2^{\nu/2}\Gamma(\nu/2)} \int_{\chi^2_{\rm obs}}^{\infty} x^{\nu-1} e^{-x^2/2} dx \tag{2.3}$$

When the probability is less than about 5%, the disagreement is significant and one states that "the assumed distribution is rejected at the 5% level." When the probability is less than 1%, the disagreement is highly significant.

Parameter Uncertainties

An estimate for the best-fit value of a parameter is worthless unless some quantitative statement can be supplied regarding its accuracy. For a given best-fit parameter

Table 2.2. Confidence Intervals

Confidence Level	Parameters		
	1	2	3
68%	1.00	2.30	3.50
90%	2.71	4.61	6.25
99%	6.63	9.21	11.30

Note. — The lower-right 3×3 matrix represent the value of $\Delta\chi^2$ leading to the confidence interval (at left) for a given number of interesting parameters.

value, the dependence of the value of χ^2 on small changes in the parameter provides a way to measure the parameter's uncertainty. An extremely important note is that the uncertainty in a parameter value is *always* accompanied by a "confidence interval." For example, one could say the temperature of some neutron star is 500 ± 100 eV with 68% confidence. This means that if the measurement were repeated 100 times one would expect to see 68 of these repeated measurements fall between 400 eV and 600 eV. Larger confidence intervals always have larger uncertainties (e.g., 500 ± 150 eV with 90% confidence) because a greater amount of certainty necessarily requires one to include a wider range of possible values. It is never impossible to obtain 100% confidence in the actual value of a parameter, unless one invokes utterly useless parameter limits, such as saying the temperature of some neutron star is between 0 and infinity with 100% confidence.

The amount that the value of χ^2 increases when changing a certain parameter value determines the parameter uncertainty (Lampton et al. 1976). For example, if a decrease in a parameter p of δp leads to $\Delta\chi^2 = 1$, one says the parameter value is $p \pm \delta p$ with 68% confidence. The cut-off values of χ^2 that determine the confidence interval is determined from the form of the χ^2 distribution. Furthermore, two (or more) parameters of a model may be correlated with one another, where perturbations in one parameter can be to some extent compensated by readjustments in other parameters. Thus, for two

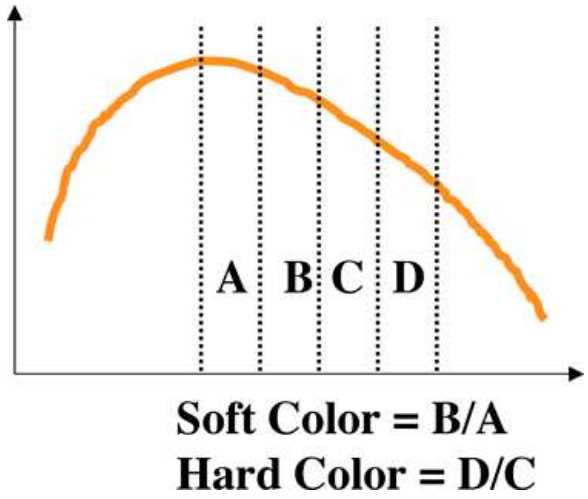

Figure 2.4: Example of X-ray colors from a hypothetical source spectrum (with the y-axis corresponding to the flux, and the x-axis corresponding to the photon energy).

or more parameters of interest it is appropriate to specify a two- or higher-dimensional "confidence region." Table 2.2 shows the necessary changes in the χ^2 statistic leading to various confidence ranges based on simultaneously varying 1, 2, or 3 parameters.

2.4.2 X-ray Colors

Spectral models, such as the inverse Comptonization model, often have a number of parameters that affect the overall spectral shape. The large number of potential parameters makes comparison problematic. Furthermore, the physical reality of these models is uncertain and in many cases the data can be satisfactorily described by different models, making the results of such spectral analysis inconclusive. Sometimes it is more convenient to compare spectra in a model-independent manner, which is accomplished using X-ray color-color diagrams. To calculate the colors, the X-ray spectrum is divided into energy bands. A color is defined as the ratio of count rates in two different energy bands. Different bands are typically chosen for neutron stars and black holes, which have different spectral variability characteristics. Figure 2.4 shows a hypothetical spectrum divided into four energy ranges, from which two colors are created. The colors are obtained without adjusting for the effects of the instrumental response, so comparisons of colors are most useful when using the same measuring apparatus.

By noting the definitions of colors in Fig. 2.4, it is clear that smaller colors indicate a steeper spectrum. Examples of color-color plots for "atoll" and "Z" sources were shown in Fig. 1.3. By using X-ray colors to compare the spectral shape in GS 1826–238 in § 3.2.4, I find a 3–4% color change that reveals a significant change in the configuration of the accretion disk in the source.

2.4.3 Timing Analysis

In addition to X-ray spectroscopy, investigations of rapid variability in the source flux can be used to learn about the physical environment in the vicinity of compact objects, in particular the nature of the gravitational potential. The detailed study of these features provide one of only a few probes of general relativistic effects near compact objects. Rapid timing signatures are created by matter orbiting the compact object, with successively higher frequencies probing the accretion flow successively closer to the source. These features can indicate that presence of time-variable inhomogeneities ("blobs") orbiting in the disk, or can represent filtration of a noise spectrum originating farther out in the disk (Psaltis & Norman 2000). The former generally lead to coherent features that are referred to as quasi-periodic oscillations (QPOs), while the latter noise components can be spread out over a wide range of frequencies.

Power Spectra

Light curves in X-ray sources are typically expressed as a time series of counts over some chosen energy range. If each time bin of length Δt is expressed as x_h, its discrete Fourier transform X_j is given by

$$X_j = \sum_{h=0}^{n-1} x_h e^{2\pi i j h/m}, \tag{2.4}$$

where m is the number of time bins (for a total dataset of length $T = m\Delta t$) and $i = \sqrt{-1}$. By adjusting j one obtains the set of independent Fourier frequencies

$$f_j = \frac{j}{T}. \tag{2.5}$$

Clearly, the minimum accessible frequency is $1/T$; the maximum accessible frequency, called the Nyquist frequency, is given by $1/(2\Delta t)$. Note that the Fourier transforms are complex quantities.

To measure the variability, one uses the power spectral density (PSD), which is a non-complex quantity that gives the distribution of power over frequency. In an *unnormalized* form, it can be estimated from the discrete Fourier transform and its complex conjugate.

$$P_j = X_j^* X_j = |X_j|^2 \tag{2.6}$$

If x_h is assumed to be roughly normally distributed, then the PSD values are χ^2 distributed with two degrees of freedom. The statistical uncertainty of the individual PSD value is about as large as the PSD itself (van der Klis 1989), therefore prior to rebinning the PSDs, the power spectrum is not useful. Improvements to the accuracy can be achieved by averaging over a set of PSDs, with the uncertainty being reduced by the square root of the number of averaged independent measurements M:

$$\sigma\langle P\rangle = \frac{\langle P\rangle}{\sqrt{M}} \tag{2.7}$$

Generally, two different types of averaging are applied. The first method is to rebin the original Fourier frequencies to a new grid with larger frequency bins, reducing the frequency resolution, and second is to average the PSDs over different time intervals. If one does not expect significant changes to the PSD shape, the second method can be applied.

After rebinning and/or averaging the PSDs, power spectra are usually normalized using one of a few schemes that are useful for describing X-ray sources. Different normalizations are achieved by multiplying the averaged PSD by a normalization factor A. One normalization, called the "Leahy" normalization, scales the PSD by $2/TR$, where R is the total time-averaged count rate $R = \langle x_h\rangle$. In this manner, the PSD delivers the variance of the light curve (also called the squared root mean square variability, rms^2, per frequency range), and the Poisson noise level is 2 independent of the source brightness (Leahy et al. 1983). The second common normalization is the "Miyamoto" normalization, which scales the PSD by $2/TR_{\mathrm{src}}^2$, where R_{src} is the total *source* or signal count rate

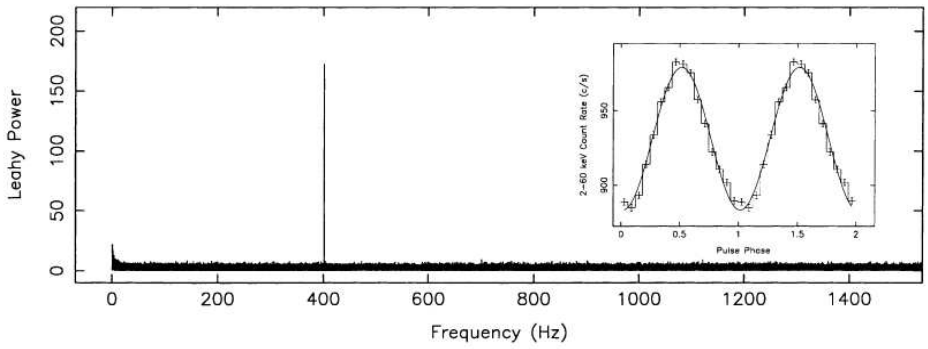

Figure 2.5: Leahy power spectrum of accreting millisecond pulsar SAX J1808.4−3658, from Wijnands & van der Klis (1998).

and requires a model or a measurement of the background count rate, $R_{\rm src} = R - R_{\rm bkg}$ (Miyamoto & Kitamoto 1989). This normalization gives the power spectrum in units of squared *fractional* rms variability per frequency interval, in units of $(\text{rms/mean})^2/\text{Hz}$. The Miyamoto normalization is the most-widely used method because it allows for a comparison of the shapes of PSDs in a way that is independent of the source brightness. Note that the same normalization factor must be applied to the PSD uncertainty.

Flux measurements are always accompanied by noise, primarily Poisson noise. In principle, the light curve can be divided into its independent components: the signal S_j and the noise N_j. Similarly, for an individual time bin, the total number of counts is composed of the sum of the signal and the noise, i.e., $x_h = s_h + n_h$. Under the Leahy normalization, the Poisson noise level is 2. By subtracting this noise component, one is left with the source variability. If the PSD is unnormalized ($A = 1$) the noise level is TR, and under the Miyamoto normalization the noise level is $2/R_{\rm src}$. Strictly speaking, however, these components will be modified by the instrumental deadtime, which is the time between the triggering of an X-ray event and when the detector can register a new event. For example, in a proportional counter the deadtime is the time elapsed until the electrons generated by the incoming X-ray photon in the detector are neutral again, plus the time for the electronics to complete event processing. The deadtime has the effect of reducing the noise level in a frequency-dependent manner.

Individual, coherent or quasi-coherent features in the power spectra of X-ray

sources are commonly fit with a Lorentzian model. An individual Lorentzian is given by

$$P(\nu) = \frac{r^2\Delta}{\pi}\frac{1}{\Delta^2 + (\nu - \nu_0)^2} \tag{2.8}$$

where ν_0 is the centroid frequency of the Lorentzian, r is the integrated fractional rms, and Δ is the half-width of the function at half-maximum (HWHM). A Lorentzian function is the Fourier power spectrum of an exponentially-damped sinusoid, and has been consistently shown to provide the best description of the power spectra of X-ray sources, despite the fact that the description is *empirical* in nature and does not truly represent the physics of the accretion flow. For a time series containing a single sinusoidal component, the PSD will show a sharp peak at the signal frequency (Fig. 2.5). When these variations are very centrally peaked ($Q \equiv \nu_0/2\Delta > 2$) but not completely coherent, they are referred to as quasi-periodic oscillations (QPOs). Aperiodic variability ("noise") shows power over many decades in frequency.

For years, the study of aperiodic variability considered "shot noise" models where the light curves of X-ray sources appear to be a series of discrete, short bursts. The power spectra were usually well fit with a power-law spectrum. With the launch of the *Rossi X-ray Timing Explorer*, high time resolution data revealed that describing the shape of the broadband power spectrum as a smooth $f^{-\alpha}$ function was a rather approximate treatment because the PSDs of black holes and neutron stars revealed many small structures. Therefore, recent work has shifted its focus to describing the power spectra as the sum of 3–4 broad Lorentzians, plus peaked Lorentzians if QPOs are present (Belloni et al. 2002). This approach is advantageous because coherent components and noise components are described using the same type of model. It may also be a more appropriate physical model if the noise and coherent features are simply different manifestations of the same physical phenomena, as suggested by Psaltis & Norman (2000).

Timing Analysis of Unevenly Sampled Data

The Fourier analysis techniques described above can be applied to the study of the temporal behavior of an X-ray source provided the data do not contain gaps and are not unevenly sampled. With realistic observing programs, however, both effects will

usually be present. The Fourier techniques can therefore only be used to characterize the short term behavior (during one satellite orbit, for example) and other methods must be applied to the study of long-term behavior. Scargle (1982) performed a comprehensive analysis of the periodogram to astronomical time series, and found that a modified periodogram should be used instead of equation (2.6) when searching for periodicities in the frequency domain. The periodogram was subsequently named the Lomb-Scargle periodogram.

$$P(\omega) = \frac{1}{2}\left\{ \frac{\left[\sum_{h=0}^{n-1} \tilde{x}_h \cos\omega(t_h - \tau)\right]^2}{\sum_{h=0}^{n-1} \cos^2\omega(t_h - \tau)} + \frac{\left[\sum_{h=0}^{n-1} \tilde{x}_h \sin\omega(t_h - \tau)\right]^2}{\sum_{h=0}^{n-1} \sin^2\omega(t_h - \tau)} \right\}, \tag{2.9}$$

where τ is defined through

$$\tan(2\omega\tau) = \frac{\sum_{h=0}^{n-1} \sin 2\omega t_h}{\sum_{h=0}^{n-1} \cos 2\omega t_h}, \tag{2.10}$$

and where ω is the frequency at which the power is calculated. The t_k are the time stamps of the data, and $\tilde{x}_h$ is the time series normalized to mean zero and variance unity. Thus $\tilde{x}_h = (x_k - \langle x \rangle)/\sigma$, where the average count rate is $\langle x \rangle$ and σ is the standard deviation. Unfortunately, the Lomb-Scargle periodogram is still subject to aliasing.

2.4.4 Monte Carlo Simulations

A Monte Carlo simulation is an extremely versatile computational algorithm that relies on random sampling of variables from a given distribution. The term "Monte Carlo simulation" includes a wide range of different approaches, but in general a simulation calculates multiple hypothetical scenarios of a model by repeatedly sampling values from the probability distributions of uncertain variables.

As a simple example, consider trying to numerically determine the value of $\pi \approx 3.1415\ldots$. A straightforward method to imagine a circle inscribed within a square, so that twice the radius of the circle equals the side of the square. The ratio of the area within the circle to the area of the square is

$$\frac{A_{\text{circle}}}{A_{\text{square}}} = \frac{\pi r^2}{(2r)^2} = \frac{\pi}{4} \approx 0.785, \tag{2.11}$$

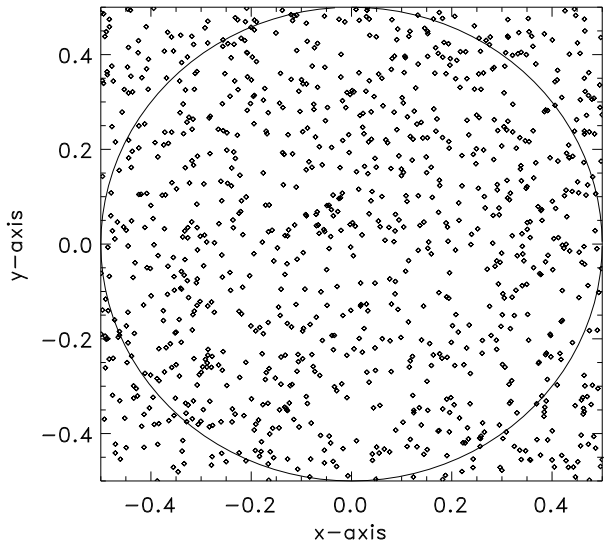

Figure 2.6: Example of using a Monte Carlo simulation to measure the value of π. There are 1000 points in the figure.

where the length of the side of the square is $2r$. If you were to randomly throw darts at the square, you would expect approximately 79% of the darts to be inside the circle. A Monte Carlo simulation uses a random number generator as the dart thrower. One way to calculate π is therefore to produce random x values between -0.5 and 0.5, and likewise random y values between -0.5 and 0.5. One trial value $[x_i, y_i]$ determines where the dart is thrown. Remember that each x_i and y_i are both independently *random*; there is equal probability to obtain any value between -0.5 and 0.5. Figure 2.6 shows an example of 1000 trial points inside a square. The distance from the center $(0, 0)$ is just $d_i = (x_i^2 + y_i^2)^{1/2}$. Therefore,

$$\frac{\pi}{4} \approx \frac{|\{d_i | d_i \leq 0.5\}|}{|\{d_i\}|}, \tag{2.12}$$

where $|\{d_i | d_i \leq 0.5\}|$ indicates the number of the subset of trials (cardinality) where the "darts" are inside the circle, and $|\{d_i\}|$ is the total number of trials. Therefore, by using a random number generator as the dart thrower, the value of π can be obtained to an arbitrary accuracy level depending on the number of trials.

In the example above, the probability distributions for x and y were flat over the range $[-0.5, 0.5]$. Yet any type of probability distribution can be used. In this

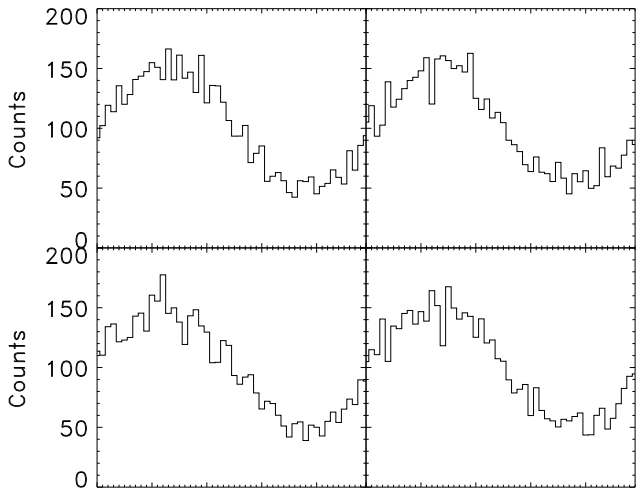

Figure 2.7: Four simulated light curves for an expected distribution $\lambda(\theta) = 100\sin(\theta) + 100$.

dissertation, I used Monte Carlo methods to create hypothetical data sets that were used to quantify the uncertainty in some inferred parameter, based on the uncertainty in the data points. Consider a hypothetical source that has an X-ray light curve (time series) exhibiting perfectly sinusoidal variability. Because the measured X-ray photons are individual events, the uncertainty in the number of counts in a time bin is equal to the square root of the total number of counts (Poisson process). According to the Poisson distribution Y, if the expected number of counts in some interval (time bin) is λ, then the probability of obtaining exactly k counts is equal to

$$P(Y = k) = \frac{e^{-\lambda}\lambda^k}{k!},\ k = 0, 1, 2, \ldots \tag{2.13}$$

Therefore, although the true or expected time series may be a perfectly sinusoidal function, the *measured* time series will show scatter about the sine wave due to photon counting statistics. Figure 2.7 shows four simulated light curves using an underlying distribution of $\lambda(\theta) = 100\sin(\theta) + 100$ over the range $\theta = [0, 2\pi]$. The construction of these trial light curves is straightforward. For each point θ, the Poisson process dictates that the probability distribution for each point is $Y \sim \text{Poisson}(\lambda(\theta))$. Thus, at each point a number is drawn randomly for the Poisson distribution for an expected number of counts

of $\lambda(\theta)$.

In reality, however, one does not know the expected distribution, but one can still use the measurements and their associated uncertainties to simulate datasets. The power of the Monte Carlo method is that is allows one to create an infinite number of datasets that *could have been physically realizable*. The measurements invariably have some uncertainty, so the simulated datasets are really no less "real" than what is actually measured. The additional datasets then allow one to quantify the uncertainty in some inferred parameter. For example, in the case above of a sinusoidal light curve, one knows the *expected* minimum is at $\theta = 3\pi/2$, but one will almost never obtain this exact value. From the actual dataset, only one value of the light curve minimum is obtained. Yet by simulating new light curves, an entire set of minima is acquired. The 1σ uncertainty in the light curve minimum, for example, can then be inferred by finding the range of minima that encloses 68% of all trials.

2.4.5 Cross Correlation

Oftentimes it is desirable to measure how "shifted" two periodic signals are with respect to one another. If one has two light curves normalized to zero mean, i.e., $\tilde{x}(t_i) = x(t_i) - \langle x \rangle$ and $\tilde{y}(t_j) = y(t_j) - \langle y \rangle$, it is possible to measure the shift (in time or phase) between them using the cross correlation function.

$$C_{xy}(t_{\rm lag}) = \frac{\sum_{i=0}^{N-1} \tilde{x}(t_{\rm lag})\tilde{y}(t_j)}{\sqrt{\left(\sum_{i=0}^{N-1} \tilde{x}(t_i)\right)^2 \left(\sum_{j=0}^{N-1} \tilde{y}(t_j)\right)^2}}, \tag{2.14}$$

where $t_{\rm lag} = t_i - t_j$. Given the normalization, the cross correlation function can take values between -1 and 1, where the former means they are perfectly anti-correlated, and the latter that they are perfectly correlated. Usually, the two periodic signals are not identical to each other, so the maximum value of C_{xy} will be less than 1. The time shift to apply to the light curves in order to achieve the greatest level of agreement is the value of $t_{\rm lag}$ corresponding to the maximum value of C_{xy}. I apply this method in Chapter 5 to measure the times of the pulse minima in order to perform pulse timing analysis for the determination of the orbital parameters of two newly-discovered and heavily-absorbed HMXBs.

3

Accretion & Thermonuclear Explosions in GS 1826–238

3.1 X-ray Emission & Timing Characteristics

3.1.1 Introduction

The low-mass X-ray binary (LMXB) GS 1826–238 was discovered with *Ginga* in 1988 (Makino et al. 1988). Due to its temporal and spectral similarities to Cyg X–1 and GX 339–4, the source was originally tentatively classified as a black hole candidate (BHC; Tanaka 1989). Later optical studies lead to the identification of a $V = 19.3$ mag optical counterpart (Barret et al. 1995). The companion was subsequently found to have a 2.1 hr modulation (and implied orbital period) and a refined position of $\alpha = 18^{\rm h}29^{\rm m}28.2^{\circ}$ and $\delta = -23'47''49.12^{\circ}$ (J2000) (Homer et al. 1998).

The spectral and temporal characteristics that Tanaka (1989) initially used to associate GS 1826–238 with a black hole system were later found to be present in other X-ray bursters (e.g., 4U 1608–522, Yoshida et al. 1993). Moreover, the photon index of its energy spectrum was measured to have a relatively low cut-off energy ($\sim$ 58 keV) for a BHC, and was perhaps more indicative of the typically cooler neutron star (NS) hard X-ray spectra (Strickman et al. 1996). X-ray bursts from this source were first conclusively observed with *BeppoSAX* by Ubertini et al. (1997), firmly establishing the

source as a NS and strongly suggesting it to be weakly magnetized ($B < 10^{10}$ G).

The periodicity of the type I bursts from GS 1826–238 has been remarkably stable over the span of years (Ubertini et al. 1999). Although quasi-periodic bursting is not unique among LMXBs, such consistency over long durations is indeed unusual. The regular intervals between bursts suggest that the accretion rate is stable, that the accreted matter is completely consumed during the bursts, and that the fraction of the stellar surface covered prior to each burst is approximately constant. Investigations of burst recurrence rates and energetics have lead to convincing arguments that type I bursts stem from unstable thermonuclear burning of accreted hydrogen and helium (e.g., Strohmayer & Bildsten 2003). As freshly accreted material falls onto the NS surface, it is hydrostatically compressed by new material at a rate per unit area $\dot{m} \sim 10^4$ g cm^{-2} s^{-1}, assuming isotropic accretion and a NS radius of 10 km. The thermal energy deposited by the infalling matter causes temperatures in most of the thin NS "atmosphere" to exceed 10^7 K, so that during the accumulation phase hydrogen burns via the hot CNO cycle at a rate that is limited only by the mass fraction $Z_{\rm CNO}$ and not the temperature (Bildsten 2000). Within hours to days, the extreme gravity on the NS surface ($\sim 10^{14}$ cm s^{-2}) compresses the accumulated matter to densities high enough to trigger unstable thermonuclear ignition. GS 1826–238, in particular, has near limit-cycle behavior with stable hydrogen burning during the accumulation phase followed by mixed hydrogen and helium burning triggered by thermally unstable helium ignition (Bildsten 2000). The α-parameter – the ratio of the integrated persistent fluence between bursts to the burst fluence – and the long burst duration ($\sim$ 150 s), imply that after thermonuclear ignition the hydrogen burns via the rapid-proton (rp) process where energy is released through successive proton captures and β decays (Wallace & Woosley 1981). The measured α-value for GS 1826–238 of $\sim$ 42 (Galloway et al. 2004; hereafter G04) is remarkably consistent with theoretical predictions: The gravitational energy released during accretion onto a 1.4 $M_\odot$ NS is about 200 MeV per nucleon, while the energy released through thermonuclear fusion is about 5 MeV per nucleon for a solar mix going to iron group elements, giving an expected value of 40. Moreover, the variation in α with the global accretion rate $\dot{M}$ implies solar metallicity in the accreted layer (G04), although recent

work using an adaptive nuclear reaction network shows that the critical mass required for a burst is independent of the composition of the accreted material (Woosley et al. 2004), and so attempts to infer the metallicity of the fuel from burst properties is complicated. During accretion the gravitational potential energy released per nucleon is deposited partly in the disk, and partly in the boundary layer or on the NS surface.

In low accretion rate (atoll) LMXBs, the dominant persistent emission spectral component is clearly inverse Comptonization, where soft "seed" photons emitted from a cold layer in the accretion disk gain energy in successive scatterings with hot electrons in the disk or surrounding accretion disk corona (ADC; Church 2001). Stable hydrogen burning between bursts and the thermal energy released on impact are observable as blackbody emission, assuming there is an optical path through which the radiation can escape. The addition of a blackbody component in spectral models is not always necessary (as I find in § 3.1.4), which suggests this form of radiation is (up)scattered or absorbed by the obscuring disk or ADC. Another possibility is that the blackbody component is simply too weak to be observed relative to the Comptonized emission. Mitsuda et al. (1989) proposed that most LMXB spectra can be described by a multi-temperature disk blackbody from the inner accretion disk plus blackbody emission from the NS which is Comptonized in the local region of the star. More recently, the dipping class of LMXBs—sources that show dips in their light curves, which are thought to be caused by partial obscuration of the nearly edge-on X-ray source by a bulge of material at the point where the incoming gas stream impacts the accretion disk (White & Holt 1982)—has constrained the types of emission models that are most likely. The constraints are provided by the fact that the models must fit the persistent emission at various levels of decreased flux resulting from partial occultation and absorption of the NS, accretion disk, and corona by the bulge in the outer disk where accretion flow from the companion star impacts. The evolution of these spectra at various levels of flux are well-described by a model consisting of point-like blackbody emission plus Comptonized emission from an extended accretion disk corona (e.g., Church et al. 1997, 1998; Bałucińska-Church et al. 2001; Smale et al. 2001). During the dips in the light curves, the blackbody component is observed to disappear rapidly, indicating that the emission comes from a point and not from an

extended region. As expected, the Comptonized component is observed to gradually decrease. By measuring the ingress times of the dip, Church (2001) was able to estimate the size of the Comptonizing region for several sources and found the radius of the region to be typically $\sim$ 50,000 km. This measurement is consistent with the value obtained much earlier by Canizares (1976) for 3U 1820–30. The large extent of the emission region is evidence for a Comptonized component that is emitted from an ADC and not the disk itself. Moreover, Smale et al. (2001) observed complete covering of this region in many sources, suggesting that the corona must be geometrically thin, as it would be unlikely that a corona with spherical geometry would be completely occulted. On the contrary, studies of emission and absorption features in dipping sources by Boirin et al. (2005) show that the spectra are also consistent with a less strongly ionized absorber along the line of sight rather than a simple increase in absorption. Progressive covering of the Comptonized component in their models is not required.

The persistent emission spectrum of GS 1826–238 has been discussed by previous authors (e.g., Barret et al. 1995, Ubertini et al. 1999, Del Sordo et al. 1999, in 't Zand et al. 1999a, Barret et al. 2000, Kong et al. 2000). The spectral model that has consistently produced an acceptable fit is a blackbody plus Comptonized emission, the latter being modeled in XSPEC with either a cut-off power law (`cutoffpl`) or the more explicit `comptt`. Broadband *BeppoSAX* spectra in the 0.1–200 keV range found the spectrum to be consistent with the Comptonization of a 0.6 keV Wien spectrum by a plasma with $kT_{\rm e} \sim 20.7$ keV, plus a 3.8 keV blackbody (in 't Zand et al. 1999a). Del Sordo et al. (1999) found the spectrum to be well-fitted with a blackbody plus cut-off power law, with $kT_{\rm bb} \sim 0.9$ keV, $\Gamma \sim 1.3$, and cut-off energy ~ 50 keV. Strickman et al. (1996) and in 't Zand et al. (1999a) also obtained a fit with this model and the results of each group are fairly consistent. Kong et al. (2000) fit the persistent emission spectrum from 0.5–10 keV with a blackbody (~ 0.7 keV) plus power law ($\Gamma \sim 1.1$).

The burst emission spectrum has been studied a few times previously. in 't Zand et al. (1999a) studied burst spectra and found significant flux up to 60 keV, indicating that the burst emission may be Comptonized in a similar manner as the persistent emission. The peak blackbody temperature was measured to be ~ 2 keV, which cooled to about 1.3

keV over 100 s. Ubertini et al. (1999) studied the spectrum for two bursts, though with only two separate integration bins of 13 s at burst peak and 43 s through the decay. The peak spectrum was fit with a blackbody temperature of $\sim$ 2.1–2.3 keV and the decay with temperature $\sim$ 1.6–1.9 keV. Kong et al. (2000) fit the burst spectrum by fixing the power law component to its persistent value and adding a blackbody; the peak temperature was $\sim$ 2.6 keV.

3.1.2 Observations & Analysis

In this section I utilize two simultaneous observations from 2002 July 29, taken with *Chandra* and *Rossi X-Ray Timing Explorer* (*RXTE*). The 68.2 ks *Chandra* observation was made using the Advanced CCD Imaging Spectrometer (ACIS; Garmire et al. 2003) and is sensitive to photons from 0.3–10 keV. The source was focused onto one of the back-illuminated ACIS chips (S3). To minimize the adverse effects due to pile-up, and to gain better time resolution on the rise of the bursts, I used half-frame readout with 1.74 s frame-time. I use the "level 2" event lists from the standard data processing, and apply a standard correction to destreak the ACIS-S4 chip caused by a flaw in the chip readout. To obtain high resolution spectra, I had the High Energy Transmission Grating (HETG; Canizares et al. 1992) inserted into the optical path.

The 36 ks *RXTE* observation uses the Proportional Counter Array (PCA; Jahoda et al. 1996), and the High Energy X-Ray Timing Experiment (HEXTE; Rothschild et al. 1998). The PCA is made up of five proportional counter units (PCUs) and is sensitive to photons from 2–60 keV. The HEXTE instrument comprises two clusters, each of which contains four NaI/CsI scintillation detectors, and is sensitive to photons from 15–250 keV. Both instruments have large effective areas ($\sim$ 6000 cm^2 and 1400 cm^2, respectively) and microsecond timing. Table 3.1 provides a summary of the GS 1826–238 observations used in the spectral analysis.

Data Preparation for Spectral Analysis

The *Chandra* HETG Spectrometer is composed of the Medium Energy Grating (MEG) and the High Energy Grating (HEG). The two gratings are slightly offset and

Table 3.1. Chandra/RXTE Observations of GS 1826–238 in 2002 July

ObsID	Telescope/ Instrument	Energy Band (keV)	Exposure (ks)
2739	*Chandra*/ACIS-S	0.5–8.3	68.2
01,02,000[a]	*RXTE*/PCA	3–23	24.6[b]
01,02,000[a]	*RXTE*/HEXTE	17–200	19.4[b]

Note. — All observations are from 2002 July 29.

[a]The *RXTE* observation IDs are each preceded by 70044-01-01-

[b]Due to earth occultation and the satellite's passage through the South Atlantic Anomaly, there are time gaps of 15–30 min in coverage; the times listed represents the sum of 9 separate observation intervals.

appear as "whiskers" traversing all ACIS chips. The MEG is calibrated from 0.3–5.0 keV and the HEG is calibrated from 1.0–8.3 keV. In this analysis, I only made use of the 1st order MEG/HEG data. All of the *Chandra* analysis made extensive use of the Chandra Interactive Analysis of Observations (CIAO) version 3.01 software with calibration version (CALDB) 2.26. I used the CIAO routine *tgextract* for the extraction of grating spectra, *mkgrmf* to produce response matrices, and *fullgarf* to create the auxiliary response matrices. I added the positive and negative diffraction orders and their corresponding auxiliary response files using the script *add_grating_orders*. Systematic errors of 10% were derived from calibration observations of the Crab pulsar and Mrk 421, and were added to both the persistent and burst emission fits.[1] We binned the persistent and burst emission data in the largest possible bins to obtain maximum statistical quality, while maintaining sufficient resolution to observe prominent absorption or emission lines. For the persistent emission analysis I binned the data in 1000 count PHA bins, and in the burst analysis I used 500 count bins. This generally led to bins with width $\sim$ 50–100 eV. We excluded the MEG 1st order data from 0.8–0.9 keV because these data fall on a gap

[1]see http://space.mit.edu/ASC/calib/hetgcal.html

between the ACIS chips. After preliminary analysis, I concluded that the data near 2.1 keV are affected by a residual calibration uncertainty in the response due to an iridium M-edge. To correct for this, I included an inverse edge (e.g., Miller et al. 2002), frozen at 2.065 keV though allowing the optical depth to vary. The best-fit optical depth was consistently ~ -0.16. In addition, the data from 2.0–2.5 keV are possibly affected by pile-up, which I estimate to be about 10% at the maximum. Spectral distortion due to pile-up is accounted for by the HETG systematics.

The extraction of PCA and HEXTE energy spectra used scripts developed at the University of California, San Diego and the University of Tübingen that incorporate the standard software for *RXTE* data reduction (FTOOLS). The large effective area of the PCA provides excellent statistics without rebinning the data, however the first three channels and the data above 23 keV were not used. I placed systematic uncertainties of 0.5% on the PCA data to account for the likely uncertainty in the response (Kreykenbohm et al. 2004). The HEXTE data below 17 keV and above 200 keV are not included in the analysis. I used successively larger energy bins at higher energies to account for the decreasing flux density. During the burst intervals HEXTE did not yield a significant number of counts above 40 keV. We included no systematics to the HEXTE data. For analysis during the burst time intervals I added the data for the 3 bursts (corresponding to the $2^{\rm nd}$, $3^{\rm rd}$, and $6^{\rm th}$ *Chandra* bursts) viewed when PCUs 0 and 2 were taking data; PCUs 0 and 2 had the greatest coverage in this observation. The PHA bins were added together using the FTOOLS task *mathpha*.

3.1.3 Burst Periodicity & Timing

As discussed in § 3.1.1, GS 1826–238 has exhibited a nearly periodic bursting behavior since type I bursts from this source were first discovered in 1997. The remarkable consistency of the burst cycle can easily be seen in Fig. 3.1. The *Chandra* light curve uses all HETG data from 0.3–8 keV, but does not include any counts from the zeroth order source region as these data are affected by severe pile-up. Not only is the burst recurrence time approximately constant, but the light curve of any particular burst is virtually indistinguishable from any other (see Fig. 3.1*c*). Although the time between

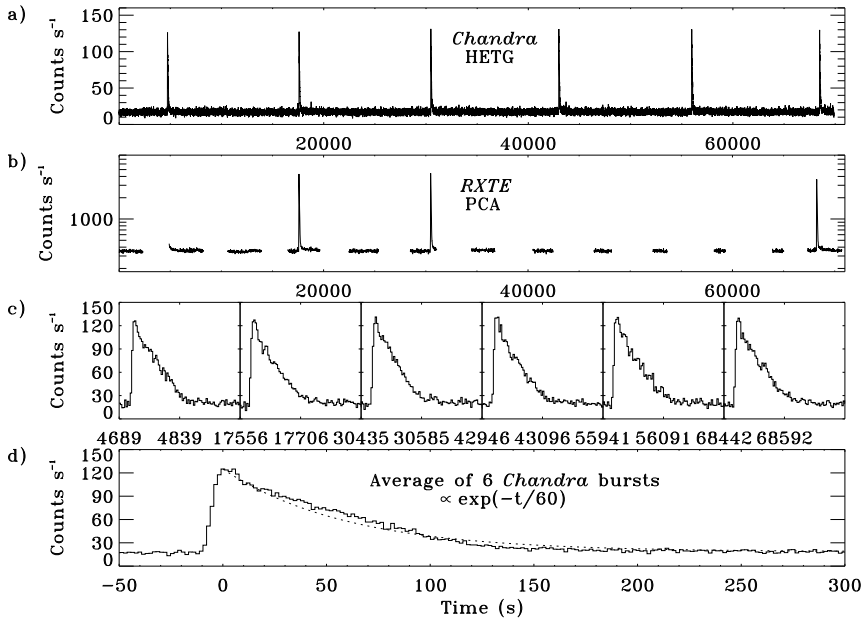

Figure 3.1: Light curves for the *Chandra* HETG and *RXTE* PCA instruments. The top two light curves (*a* and *b*) show the intervals when each telescope was taking data. The *Chandra* light curve includes the HETG data from 0.3–8 keV and has time resolution of 3.48 s, as does the data in plot (*c*). The PCA light curve includes data from 3–8 keV and uses 16 s time bins. The time axis of the top three plots begins at MJD 52484.2039. The lower plots show the individual (*c*) and average (*d*) of the 6 *Chandra* bursts. I used the smallest possible binning of 1.74 s, and the curves were aligned using the rises of the bursts. The zero point reference time for plot (*d*) also corresponds to the peak of the burst. The curve can be approximated by a decaying exponential with scale time 60 s, however this value cannot be interpreted physically since it includes all instrumental effects resulting from differences in the detector response with energy.

sequential bursts has been rather constant, the average burst recurrence time has been observed to be steadily decreasing over long time scales (Cocchi et al. 2000, G04). Using a total of 44 *RXTE* observations from 1997 November to 2002 July, G04 measured the burst interval to be 5.74 ± 0.13 hr initially, 4.10 ± 0.08 hr in 2000, and 3.56 ± 0.03 hr in 2002. I measured the average burst recurrence time of the five complete *Chandra* intervals to be 3.54 ± 0.03 hr (12750 ± 102 s; also in 2002). The individual intervals were measured from burst peak to peak and are listed in Table 3.2. The 2002 recurrence time measurement by G04 was measured using the same PCA data that I use in this paper, while our measurement is based on the *Chandra* data.

The 40% decrease in the burst recurrence time from 1997 to 2002 has been

Table 3.2. Burst Intervals

Burst Interval	Δt (s)
1⟶2	12861
2⟶3	12884
3⟶4	12510
4⟶5	12994
5⟶6	12502

Note. — The individual burst intervals were measured from the peak of one burst to the next. There is a small uncertainty in these measurements since the *Chandra* data have a frame time of 1.74 s.

coupled with a 66% increase in the mean persistent flux (G04). Such behavior is expected since the increase in persistent luminosity is assumed to be due to an increase in the global accretion rate, and therefore less time is required to reach the critical amount of fuel. While the observations of G04 are consistent with this trend, Bildsten (2000) found exactly the opposite behavior in many low accretion rate LMXBs. For example, bursts from 4U 1705–44 became less frequent as $\dot{M}$ increased. To explain the conundrum, Bildsten (2000) suggested that a greater fraction of the stellar surface of 4U 1705–44 may be covered prior to ignition, so that the accretion rate per unit area actually decreased. This may also be the case for GS 1826–238: If the relation between the rise in the persistent flux and the decrease in the burst recurrence time were linear, one would expect an even greater decrease in burst recurrence time than has been observed by G04. Another possible explanation for the longer-than-expected recurrence time regards the fact that at smaller recurrence times, less helium will be made prior to ignition, and so the column depth required to produce the instability will increase (Cumming & Bildsten 2000).

As mentioned in the introductory chapter, the location of the burning during bursts is not assumed to be spherically symmetrical. It is likely that ignition begins near the stellar equator since matter is preferentially deposited there during accretion (Spitkovsky et al. 2002). The anisotropic burning caused by the hot spot at the point of ignition may be revealed through the observation of burst oscillations, the frequencies of which correspond to the NS rotation frequencies (e.g., Muno 2004).

I searched for burst oscillations by computing and averaging the power spectra for the 3 bursts observed with 125 μs resolution event mode PCA data using a sampling rate of 2048 Hz (Nyquist frequency: 1024 Hz). To improve statistics, I averaged power spectra for sequential 0.25, 0.5 and 1 s sections of the light curve (4, 2, and 1 Hz resolution), with total segment lengths varying from 3 to 30 s. I searched in the $\sim$ 10 s rise, around the burst peak, and at different times during the burst decay until 65 s from the burst peak. PCA deadtime effects cause a $\sim$ 1% decrease in the mean value of the Poisson noise to 1.98 (from 2.0) in the Leahy normalization (see Leahy et al. 1983). I initially included the entire 2–60 keV energy band and made no significant detections at any point during the burst. I then tried varying the energy ranges included in the PCA light curves. With the 10–30 keV data, I made a detection 15–30 s from the burst peak around 612 Hz (Figure 3.2). The significance of the signal was maximized with 0.25 s segment light curves; therefore, 180 separate power spectra were averaged. The signal could be observed in each burst separately though with less significance. I then tried expanding the energy range that was included in the PCA light curves; the signal weakened with the inclusion of either higher and lower energy photons. The 10–1024 Hz Leahy-normalized power spectrum is presented in Figure 3.2, along with a power spectrum centered on the signal and a histogram of the difference in power from the mean. The power at 612 Hz deviates from the Poisson level by 4.7σ, which with 256 bins means that there is a 0.033% chance that the detection is spurious. Using a power spectrum with 1 Hz resolution, I fit a Lorentzian function to the peak, giving a frequency $\nu_{\rm o} \approx 611.2$ Hz with $\Delta\nu_{\rm FWHM} \approx 3.1$ Hz. The average rms amplitude of the peak is 4.8%, which is consistent with the 5% rms amplitude of typical burst oscillations observed in LMXBs (Muno 2004).

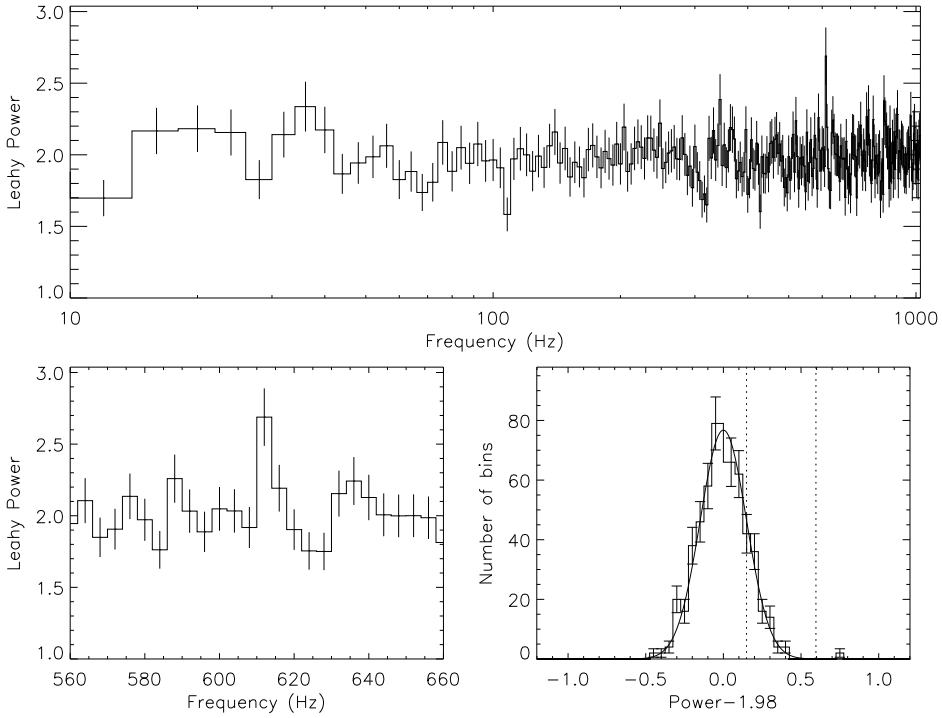

Figure 3.2: Averaged Leahy-normalized power spectrum for the 3 bursts (15–30 s from burst peak) observed with the PCA (top and bottom left), and a histogram of the distribution of the powers scaled to zero mean (bottom right). The frequency bins are 4 Hz. The vertical dashed lines in the bottom right sub-figure represent 1σ and 4σ standard deviations from the mean. The power at 611.2 Hz deviates from the Poisson level by 4.7σ.

3.1.4 Persistent Emission Spectrum

Evolution between Bursts

Along with burst energetics and timing, one can learn much from GS 1826–238 through its energy spectra. I began the investigation by creating spectra for 1 ks intervals following the onset of a burst in order to see if there were significant changes in the best-fit parameters between bursts. Since the average burst recurrence time for the five complete burst intervals in the 68 ks *Chandra* observation was measured to be 12750 ± 102 s, I was able to create 1 ks intervals up to 11–12 ks after the burst. To improve statistics we stacked the datasets from all five *Chandra* burst intervals. I also constructed nearly two complete burst intervals using the simultaneously acquired *RXTE* data. Although these

data have time gaps, I determined the time since the previous burst for any individual *RXTE* dataset by comparing it to the *Chandra* burst times. With the benefit of the simultaneous observations I obtained statistically significant measurements from 0.5–200 keV for each 1 ks interval (except 9–10 ks). To each dataset, I fit a model composed of Comptonized emission plus a broken power law. This preliminary model was only used to examine whether or not there were significant changes to the spectrum with time, and ultimately, a different model was determined to be more physically plausible (see below). Nevertheless, this exercise showed us that the best-fit parameters remain approximately constant after 1 ks, although with slightly elevated soft X-ray flux through 3 ks from the peak of the burst. In the following fits, I therefore define the persistent spectrum to be for $t > 3$ ks. In the integrated persistent emission analysis below, I found that the inclusion of data from 1–3 ks only minimally distorted most spectral parameters, however the inferred $N_{\rm H}$ was underestimated by $\sim 50\%$ due to the excess of soft photons.

I am fortunate to have *Chandra* data along with *RXTE* since observations of bursters with low-Earth orbit telescopes may miss some bursts if they occur during a gap in coverage when the source is occulted by the Earth or the telescope is passing through the South Atlantic Anomaly. Fig. 3.1*b* provides an illustration of the potential ambiguity involved with the selection of persistent emission datasets. For example, it is clear that any persistent emission analysis would be slightly distorted if the first 3 ks of the second PCA observation (corresponding to the decay of the first burst observed with *Chandra*) were included.

Integrated Spectrum

By summing all PHA datasets that fall within the 3–12 ks interval, we further constrain the statistics and explore standard models for LMXBs in addition to other models. LMXBs are typically modeled with a blackbody or disk blackbody to represent the NS surface or the inner accretion disk, plus Comptonized emission which can be modeled in XSPEC with `comptt` or a cut-off power law (`cutoffpl`). Although these models have similar profiles, they are not necessarily interchangeable. While Comptonized emission can be empirically described with a cut-off power law, the model of Titarchuk

(1994) is derived from analytical equations that are founded on the real analytical theory of Comptonization of soft photons, and the output parameters are physically explicit which allow direct interpretation. On the contrary, the index of a cut-off power law cannot be interpreted in physical terms, while in `comptt` it is related to the combination of the optical depth and plasma temperature. Albeit, the cut-off energy of `cutoffpl` is related to the plasma temperature as $E_{\rm cut} \sim 2kT_{\rm e}$. For these reasons I chose the Titarchuk (1994) model to represent Comptonized emission. With this description, the spectrum is governed entirely by the plasma temperature and the β parameter, which characterizes the distribution law of the number of scatterings (i.e., $P(n) \propto \exp(-\beta n)$ is the probability that a seed photon undergoes n scatterings before escaping the plasma). The optical depth of the plasma is calculated from the β parameter and depends on the input geometry: disk or spherical. Generally, for a given β parameter, a larger optical depth is inferred from a spherical geometry than a disk geometry. This is because the final spectral shape is determined by photons which undergo many more scatterings than the mean, and the longest dimension of a spherical plasma cloud is clearly shorter than that of a disk (Titarchuk 1994).

I initially tried to fit the data by employing a single `comptt` component, but the resulting fit was unacceptable due to excesses above 70 keV and below 1.5 keV. The addition of a blackbody component reduced the soft excess, and allowed the plasma temperature and thus the up-scattering efficiency to increase (since $\langle E_{\rm f} \rangle \sim \langle E_{\rm i} \rangle e^{y}$, where $y \equiv 4kT_{\rm e}\tau^2/m_{\rm e}c^2$ is the Comptonization parameter) to try to match the hard excess. Although the fit was better ($\chi^2_\nu = 1.30$), it was still unacceptable. This is contrary to the results of in 't Zand et al. (1999a), who successfully used this model, although the 3.8 keV best-fit blackbody temperature is probably non-physical. The best-fit blackbody temperature that we obtained with this model was ~ 0.5 keV, which seems more reasonable.

Table 3.3. Persistent Emission Spectral Parameters

Model:	1. Two Comptonized (disk + spherical)[a]	2. Comptonized plus Bkn. PL[b]	3. Blackbody plus CPL[c]
$N_{\rm H}$ ($\times 10^{21}$ cm^{-2})	$1.6^{+0.3}_{-0.6}$	1.50 ± 0.06	4.3 ± 0.2
$kT_{\rm d}/kT_{\rm s}$ $\vert_{\rm seed}$, kT$_{\rm bb}$[d](keV)	$0.42 \pm 0.04/0.82 \pm 0.04$	$0.68 \pm 0.01/0.86 \pm 0.04$	1.34 ± 0.04
$R_{\rm s}$, $R_{\rm bb}$[e](km)	4.0 ± 0.5	5.9 ± 0.4	2.4 ± 0.2
$kT_{\rm d}/kT_{\rm s}$ $\vert_{\rm electron}$ (keV)	$20.8^{+0.7}_{-1.1}/6.8 \pm 0.4$	$5.9 \pm 0.2/4.7 \pm 0.3$	...
$\tau_{\rm d}/\tau_{\rm s}$	$2.56 \pm 0.04/9.38 \pm 0.04$	$4.69 \pm 0.04/11.0 \pm 0.2$	...
$y_{\rm d}/y_{\rm s}$	$1.07 \pm 0.08/4.7 \pm 0.3$	$1.01 \pm 0.05/4.5 \pm 0.4$	...
Γ_1	...	1.19 ± 0.02	1.26 ± 0.02
Γ_2	...	2.43 ± 0.05	...
$E_{\rm break}$, $E_{\rm cut}$ (keV)	...	35.4 ± 0.5	41.6 ± 0.6
$E_{\rm line}$ (keV)	$6.44^{+0.03}_{-0.12}$	$6.45^{+0.02}_{-0.10}$	6.4 ± 0.1
EW$_{\rm line}$ (eV)	37^{+10}_{-8}	29^{+14}_{-12}	< 15
χ^2_ν (dof)	0.70 (521)	0.75 (522)	0.84 (527)

Note. — All errors are quoted at the 90% confidence level for a single parameter.

[a]XSPEC: `phabs*edge(comptt + comptt + gauss)`

[b]XSPEC: `phabs*edge(comptt + bknpower + gauss)`

[c]XSPEC: `phabs*edge(bbody + cutoffpl + gauss)`

[d]The parameters for spherical and disk geometries are listed as "disk/spherical", or "primary/secondary" for models 1 and 2. The two geometries are fit together in model 1, and separately in model 2.

[e]The spherical Wien emission radius (see text) and the blackbody radius.

After trying various models in conjunction with `comptt`, I found the fit to be most improved by an additional `comptt` component, resulting in a model that can be interpreted as the Comptonization of soft photons from two distinct emission regions. One of the emission regions contributes 62% of the total luminosity, so I label it as the "primary" emission region, and the other as the "secondary" emission region. The primary emission region is characterized by $kT_{\rm s} \sim 0.3$ keV, and $kT_{\rm e} \sim 19.7$–22.1 keV (depending on the chosen geometry), while the secondary emission region has $kT_{\rm s} \sim 0.8$ keV and $kT_{\rm e} \sim 6.1$–6.4 keV. The primary emission accounts for about 70% of the flux from 0.5–3 keV, and 80% of the flux from 20–200 keV, while each Comptonization component contributes nearly an equal amount of flux for 3–20 keV. Based on the inferred β parameter, which is not a direct input in XSPEC, the primary emission region has $\tau \sim 2.7$ if the region is disk-shaped, or $\tau \sim 6.3$ if it is spherical. The secondary emission region is characterized by $\tau \sim 4.7$ and $\tau \sim 9.9$ for disk and spherical geometries, respectively.

The physical interpretation of each Comptonizing region must be inferred from the best-fit parameters and the corresponding flux contributions. For one, I expect the Comptonizing region closer to the stellar surface to have hotter seed photons, which suggests that the secondary component is emitted nearer to the NS. The secondary component may therefore result from boundary layer or surface emission. Conversely, the primary emission possibly stems from the accretion disk or ADC, and a disk geometry implies $\tau \sim 2.7$. From the relative flux contributions, I see that this interpretation requires about 3/5 of the total flux to be emitted from the cooler disk region. Accretion theory predicts that half of the total gravitational binding energy per unit mass is released in the disk, and the other half in the boundary layer or on the stellar surface (Frank et al. 1985). This is not inconsistent since the accretion disk and the boundary layer are not physically distinct; rather, there may be a smooth transition from one to the other. Secondly, the optical depth of the secondary emission (independent of the true geometry) is large enough to naturally explain the lack of a visible blackbody component in the GS 1826–238 spectrum. According to Inogamov & Sunyaev (1999), the spreading of accretion flow from the equator to the poles leads to two bright rings of enhanced emission that are symmetric about the equator. The latitude of these rings increases with accretion rate,

and in the accretion regime of GS 1826–238, i.e. $\sim 10^{17}$ g s^{-1} (inferred from the total flux), these rings lie $\sim$ 0.5–1.5 km from the equator. Therefore, assuming the blackbody emission comes from these rings, the secondary Comptonized emission region only has to be large enough to cover the inner $\pm$1.5 km above and below the equator. Following in 't Zand et al. (1999b), an approximate effective radius for the spherical emission area of the Wien seed photons is given by $3 \times 10^4 d\sqrt{\frac{F_{\rm ctt}}{1+y}}/(kT_{\rm s})^2$ km, where d is in kpc, the flux is measured in erg s^{-1} cm^{-2}, and the seed photons are measured in keV. This approach yielded a soft photon emitting region with radius $R_{\rm s} \sim 4 d_{\rm 6kpc}$ km, which is only consistent with the seed photons being generated at the boundary layer if the region is confined to a half-thickness of $\sim$ 2.5 km, depending on the inclination of the system, and assuming that any emission from "below" the accretion disk is not observable. Finally, since the flux of photons passing through the boundary layer relative to the disk is larger per unit area, I expect Compton cooling to maintain a lower plasma temperature for the secondary Comptonized emission region. This is indeed what is observed (see Table 3.4).

In addition to a dual Comptonization model, I also modeled the spectrum with a single `comptt` plus a broken power law in order to give an estimate of its shape for possible non-thermal interpretation. If the secondary emission is indeed non-thermal, perhaps it stems from an ADC generated by magnetohydrodynamic turbulence, analogous to what is observed in the solar corona (Crosby et al. 1998). Alternatively, the emission may be synchrotron radiation from a relativistic jet escaping the system. Such jets have been found to be rather common among LMXBs and link these systems to active galactic nuclei (AGNs; e.g., Fender 2002). Clearly, these possibilities are highly speculative.

Iron Line Detection

After obtaining a fit with the two component models, the residuals revealed a line feature around 6.5 keV, which prompted the addition of a Gaussian to the models. The best-fit value for the line was measured to be approximately 6.45 keV, with a flux which corresponds to an equivalent width (EW) of $\sim$ 37.2 eV. I interpret this feature as a neutral Fe Kα line. An F-test showed that the probability for an improvement to the fit occurring by chance is 5.3×10^{-5} for the dual Comptonization model, and 6.8×10^{-4}

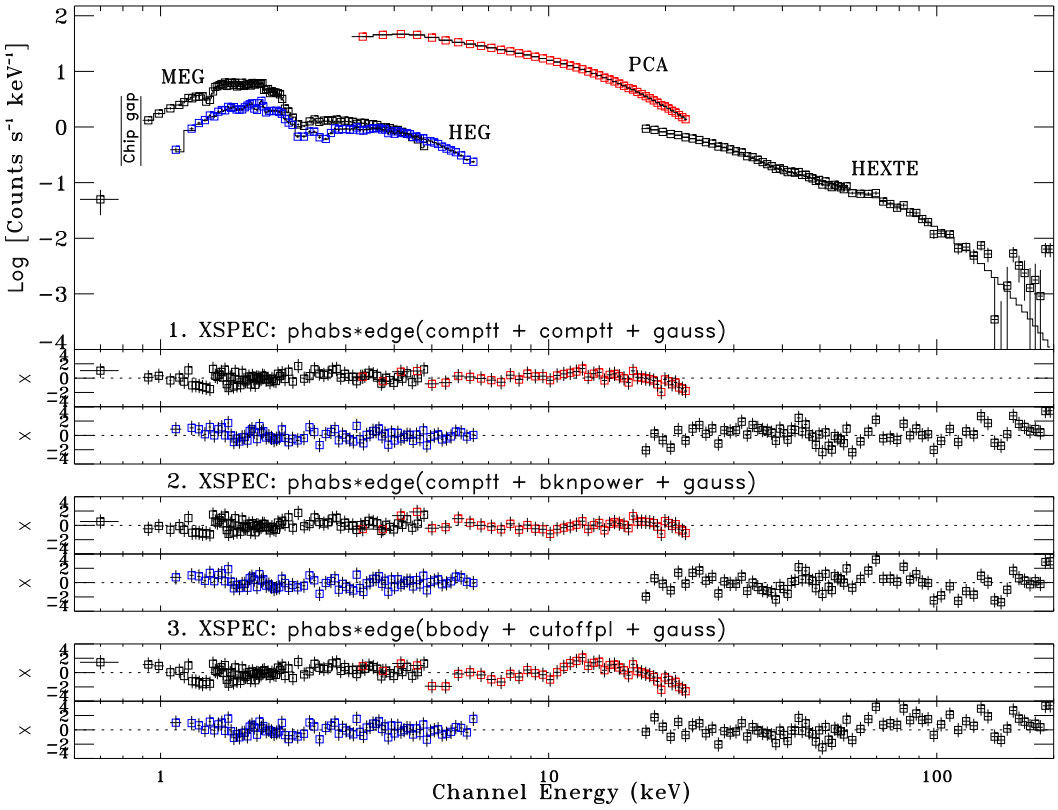

Figure 3.3: Persistent emission spectrum and residuals of the dual Comptonization model (1), and the residuals of models 2 and 3. For each model, the upper residuals are for the MEG and PCA, and the lower residuals are for the HEG and HEXTE. The range 0.8–0.9 keV is ignored since these MEG counts fall on a gap between ACIS CCDs. To provide clarity, I have only plotted every third (second) MEG (HEG) point.

for the Comptonization plus broken power law model. However, it should be noted that the use of an F-test to measure the significance of lines may not be valid (Protassov et al. 2002). I present the best-fit parameters for these models in Table 3.3. I also present the results of a blackbody plus cut-off power law model, which is described below. To account for the uncertainties in the relative instrumental flux calibrations, I introduced a multiplicative constant into the spectral models. For each model, the normalizations of the *Chandra* instruments relative to PCA were ~ 0.95, while for HEXTE the relative normalization was generally $\sim$ 0.85–0.9. Figure 3.3 shows the spectral fit for the dual Comptonization model, and the residuals for all three models.

Comparison to Previous Fits

To facilitate comparison to the results of previous work, I also fitted the spectrum of GS 1826–238 with a blackbody plus cut-off power law model (model 3), and a blackbody plus power law from 0.5–10 keV (not included in the table). These models have been used by others to provide acceptable fits to the GS 1826–238 persistent emission, but only the *BeppoSAX* observations had similar energy coverage. For example, the *ASCA* SIS instrument used in the Kong et al. (2000) analysis did not provide coverage above 10 keV, and the Barret et al. (1995) *ROSAT* observation was restricted to energies below 2.2 keV. In order to compare to the Kong et al. (2000) results, I used the same blackbody plus power law model and omitted all data above 10 keV. With this approach I obtained a fit with $kT_{\rm bb} \sim 0.8$ keV and $\Gamma \sim 1.0$, which are each within $\sim 15\%$ of their results. Extending the energy range to 200 keV, however, revealed a higher blackbody temperature, a steeper photon index, and the power law had to be changed to a cut-off power law (model 3). This shows that the use of *RXTE*'s extended energy range is crucial to minimize uncertainties in the soft component parameters due to less precise knowledge of the photon index or Comptonized component when measured with the lower *Chandra* energy range.

As mentioned above, in 't Zand et al. (1999a) fit the 0.1–200 keV persistent emission spectrum with a blackbody plus `comptt`, but they also modeled the spectrum with a blackbody plus a cut-off power law. The best-fit blackbody temperature was

$\sim$ 0.9 keV, $\Gamma \sim 1.4$, $E_{\rm cut} \sim 52$ keV, and $N_{\rm H} \sim 5.4 \times 10^{21}$ cm^{-2}, which slightly differs from $kT_{\rm bb} \sim 1.3$ keV, $\Gamma \sim 1.3$, $E_{\rm cut} \sim 42$ keV, and $N_{\rm H} \sim 4.3 \times 10^{21}$ cm^{-2} of model 3. If I set the model 3 parameters to those obtained by in 't Zand et al. (1999a), however, I obtain a similar $\chi^2_\nu \sim 1.4$.

By examining the residuals, the slope of the model 3 appears to be too steep from $\sim$ 2.5–5 keV and 12–20 keV, and too shallow for $\sim$ 5–12 keV. A slight excess also remains for energies above about 60 keV (see Fig. 3.3 *bottom*). The 2.4 km blackbody radius derived from this model is obviously smaller than expected for a NS, though the size of the radius may be explained if the blackbody emission is confined to the equatorial region. For a 10 km NS, a blackbody radius of 2.4 km would correspond to emission from a strip of half-height $\sim$ 0.6 km. I note that since $E_{\rm cut} \sim 2kT_{\rm e}$, the $\sim$ 42 keV cut-off energy is consistent with the $\sim$ 20 keV plasma temperature of the primary Comptonized component of model 1. However, unlike the dual Comptonization model and the Comptonized emission plus broken power law model, the addition of a line feature at $\sim$ 6.45 keV to model 3 did not significantly improve the fit, though I include it to preserve consistency. We place an upper limit on the equivalent width at 15.2 eV with 90% confidence.

Even though the blackbody plus cut-off power law fit that I obtained is acceptable, I am less confident with this model as compared to model 1 since the inferred $N_{\rm H}$ is inconsistent with the value obtained through the galactic hydrogen survey of Dickey & Lockman (1990), where the average column density in the direction of GS 1826–238 was found to be $\sim 1.9 \times 10^{21}$ cm^{-2}. By freezing $N_{\rm H}$ in model 3 to the lower value, the model fits the data poorly. I therefore conclude that the common LMXB model of a blackbody plus Comptonized emission described by `comptt` *or* `cutoffpl` is not appropriate for the persistent emission spectrum of GS 1826–238.

Interstellar Absorption Features

The persistent emission spectrum was searched for interstellar absorption features. This effort turned up a good candidate at about 17.15 Å. The feature is broad (0.102 ± 0.027 Å FWHM) with an optical depth at line center of 0.63 ± 0.09, when fitted

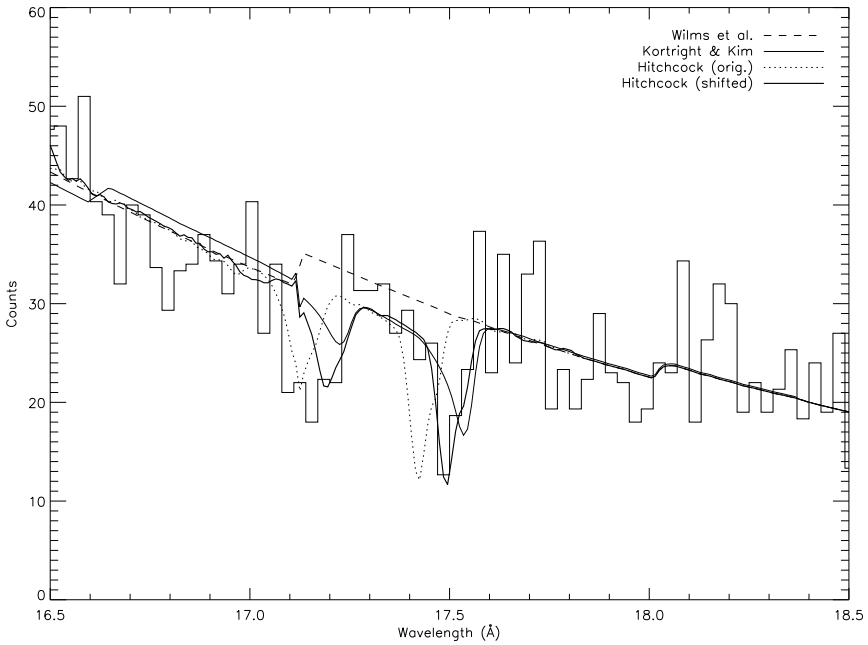

Figure 3.4: Spectrum of the persistent emission near 17.5 Å. A global model of the continuum is shown for several models of the Fe L edge complex due to the ISM. *Dashed curve:* The ISM opacity model provided in the `tbabs` model of XSPEC, using the prescription provided by Wilms et al. (2000). *Thin curve:* The Fe L edge opacity model based on measurements by Kortright & Kim (2000). *Dotted curve:* The Fe L edge structure is based on the transmission of butadiene iron tricarbonyl ($C_7FeH_6O_3$) from the Corex data base maintained by A. P. Hitchcock. *Thick curve:* The model based on the Hitchcock data but shifted by 3 eV to match the data better. The 17.15 Å line is somewhat broader than expected and may have an excess of absorption at the short wavelength side but these absorption features are generally consistent with a cosmic abundance of Fe.

with a Gaussian. The formal significance is about 3.8σ; based on about 800 bins searched at 0.03 Å binning, there is about a 6% chance that one would find such a feature due to random fluctuations. Including a narrower feature at about 17.5 Å with a significance of 2.9σ, I modeled both features with structure in the Fe L edge due to the interstellar medium (ISM). The wavelengths of these features are a good match to those of Fe L III at 17.51 Å and Fe L II at 17.19 Å. The match is not perfect. Figure 3.4 shows the near edge extended absorption fine structure (NEXAFS) of the Fe L edge as measured by Kortright and Kim (2000) and the edge structure of butadiene iron tricarbonyl ($C_7FeH_6O_3$) from the Corex data base maintained by A. P. Hitchcock[2]. Neither model matches the data without a slight energy shift to match the L III feature. Furthermore, the 17.15 Å line is somewhat broader than expected and may have an excess of absorption at the short wavelength side. Schulz et al. (2002) identified the Fe L features in the spectrum of Cyg X-1 and suspected that there is a mix of Fe molecules, citing, in particular, a feature near 17.15 A that might be due to a more pure form of Fe. Without the corresponding L III feature in our spectrum, however, I suspect that the extra broadening might result from statistical fluctuation. The models use a cosmic abundance of Fe (4×10^{-5} relative to H) and the observed ISM column density of 2.0×10^{21} cm^{-2}. Thus, these absorption features are consistent with Fe in the ISM.

3.1.5 Burst Spectrum & Evolution

I also studied the evolution of the spectrum throughout the burst and its decay by subdividing the first 1 ks from burst peak into 8 datasets with progressively larger integration times (Table 3.4). Those data above 40 keV were ignored as too few counts were obtained for significance. All of the datasets were fit with the XSPEC model `phabs*edge(comptt`$_{\rm d}$ `+ comptt`$_{\rm s}$ `+ bbody)` (d: disk, s: sphere), with the hydrogen column density frozen at the common value of 1.85×10^{21} cm^{-2}. I initially allowed the disk Comptonization parameters to vary, but the best-fit values for each dataset, including the normalizations, changed by $< 5\%$, so they were frozen at the persistent emission values. Since the blackbody emission during a burst provides a large influx of seed photons in the

[2]see http://unicorn.mcmaster.ca/corex

inner boundary layer, the spherical seed photon temperature was fixed to the blackbody temperature, which is justified since most Comptonized emission is emitted within ~ 20 km of the surface of the NS (Frank et al. 1985). Table 3.4 shows the evolution of the spectral parameters.

Table 3.4. Spectral Evolution During Burst Decay

Interval[a] (s)	$kT_{\rm bb}$ (keV)	Norm. ($\times 10^{-2}$)	$R_{\rm bb}$ (km)	$kT_{\rm e}$ (keV)	τ	F_X: 0.5–10.0 keV ($\times 10^{-9}$ erg s^{-1} cm^{-2})	0.5–40.0 keV
0–10	$1.76^{+0.06}_{-0.11}$	$12.0^{+0.6}_{-1.5}$	$11.6^{+0.8}_{-1.6}$	$3.1^{+0.6}_{-0.2}$	$9.9^{+22.1}_{-5.7}$	13.5	19.6
10–30	$1.72^{+0.04}_{-0.09}$	$10.8^{+0.5}_{-0.5}$	$11.5^{+0.6}_{-1.2}$	$3.8^{+0.6}_{-0.5}$	$7.8^{+31.7}_{-4.8}$	10.4	14.9
30–65	$1.50^{+0.09}_{-0.08}$	$5.1^{+0.2}_{-0.2}$	$10.4^{+1.3}_{-1.1}$	$4.3^{+0.4}_{-0.5}$	$8.0^{+15.6}_{-5.2}$	7.1	10.4
65–100	$1.24^{+0.11}_{-0.11}$	$3.1^{+1.3}_{-1.0}$	$11.9^{+3.3}_{-2.8}$	$4.5^{+0.9}_{-0.7}$	$10.2^{+5.6}_{-4.1}$	3.8	6.6
100–150	$1.01^{+0.19}_{-0.15}$	$0.6^{+0.7}_{-0.6}$	$7.9^{+5.5}_{-4.6}$	$5.0^{+1.4}_{-0.9}$	$11.8^{+6.2}_{-0.4}$	2.0	3.6
150–200	$0.86^{+0.08}_{-0.06}$	...	...	$7.1^{+0.9}_{-2.2}$	$11.2^{+5.5}_{-0.7}$	1.4	2.9
200–500	$0.83^{+0.05}_{-0.05}$	...	...	$6.8^{+1.4}_{-1.6}$	$8.7^{+1.1}_{-0.9}$	1.4	2.9
500–1000	$0.81^{+0.06}_{-0.03}$	...	...	$6.9^{+0.6}_{-0.4}$	$9.2^{+0.6}_{-0.3}$	1.3	2.8

Note. — All errors are quoted at the 90% confidence level for a single parameter. The XSPEC model used in this analysis was `phabs*edge(comptt`$_{\rm d}$ `+ comptt`$_{\rm s}$ `+ bbody)`. Only the last two components had free parameters. The column density was set to 1.85×10^{21} cm^{-2}, and the parameters describing disk Comptonization were fixed to the persistent emission best-fit values. The seed photon temperature of the spherical Comptonizing region was tied to the blackbody temperature. Good fits were obtained with χ^2_ν consistently ~ 0.9.

[a]The peak of the burst is defined to take place at $t = 0$.

Using the results from Table 3.4, I can place an upper limit to the source distance assuming the blackbody luminosity is Eddington-limited, which it is not since the bursts are significantly sub-Eddington. During the first 10 s following the peak of the burst, the average flux from 0.5–40.0 keV was measured to be 1.96×10^{-8} erg cm^{-2} s^{-1}. I corrected the peak flux by assuming an approximately constant spectrum for this interval (i.e. constant spectral parameters), and by measuring the burst decay scale time ($\sim$ 35 s over the energy band). The *peak* flux was found to be $\sim$ 12% larger than the 0–10 s mean, or 2.2×10^{-8} erg cm^{-2} s^{-1}. Moreover, I must account for radiation that is absorbed or scattered out of the line-of-sight on its way to the telescope. The hydrogen column density toward the source was assumed to be about 2×10^{21} cm^{-2}, which corresponds to a scattering optical depth of 0.02 (Predehl & Schmitt 1995). Thus scattering and absorption along the line of sight reduce the observed flux by $(1 - e^{-0.02}) \approx 0.02$. If I assume that the blackbody normalization is also $\sim$ 12% larger than the 0–10 s mean, and that the *unabsorbed* normalization is $\sim$ 2% larger still, I arrive at a maximum source distance of 9.2 kpc[3] for the bursts being at the Eddington limit. This upper limit on the distance is consistent with the 8 kpc upper limit derived by in 't Zand et al. (1999a).

The thermal nature of the burst spectrum with a blackbody temperature of $\sim$ 1.8 keV, accompanied by the cooling, is typical for a type I X-ray burst (Lewin et al. 1995). While the blackbody temperature deceases by a factor of about 2.2 during burst decay, the normalization decreases by more than a factor of 30. Nevertheless, the derived blackbody radius remains approximately constant as long as blackbody emission is observable. Figure 5 shows the derived blackbody radius and the fraction of blackbody flux ($F_{\rm bb}/F_{\rm total}$) from 2–10 keV during the first 150 s after burst ignition. Clearly these data are consistent with a blackbody radius of $\sim$ 10.3–11.7 km, assuming a source distance of 6 kpc and a ratio $T_{\rm bb}/T_{\rm eff}$ (spectral hardening factor) of 1.4. Such a correction must be applied since NSs do not radiate as perfect blackbodies during X-ray bursts because the thermalization of photons occurs at scattering optical depths greater than unity, where the temperature is higher than the effective temperature. Rather, the photons are thermalized at optical depths of $\sim$ 4–5 (e.g., Ebisuzaki et al. 1984, London et al.

[3]I do not include flux contributions from radiation that is thought to be emitted from outside the NS surface, since this radiation would not provide an impediment to accretion.

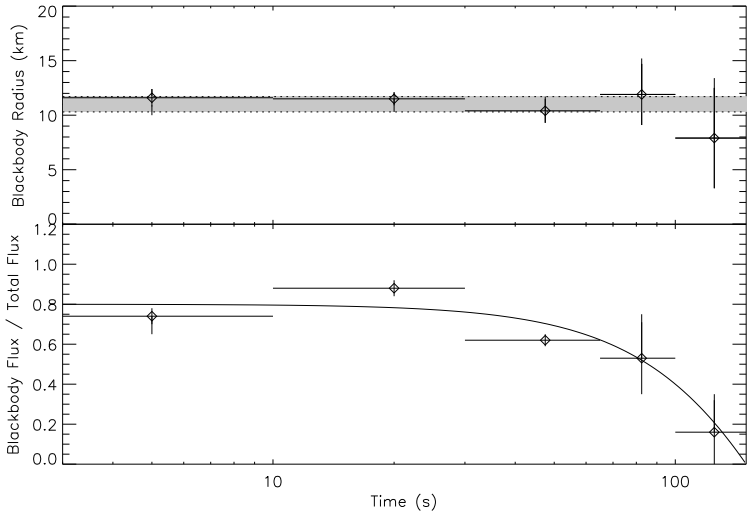

Figure 3.5: Blackbody radius and fraction of blackbody flux ($F_{\rm bb}/F_{\rm total}$) from 2–10 keV during the first 150 s after burst ignition. The bottom curve is fit "by eye" with a cosine. Beyond 150 s, the XSPEC blackbody normalization decays to zero. These data are consistent with a blackbody radius between 10.3 and 11.7 km for an assumed distance of 6 kpc.

1986, Madej et al. 2004). Assuming that the entire stellar surface is involved when blackbody emission is observable, i.e. the burning does not cease in one area sooner than another, the slight decrease in the inferred blackbody radius for the 100–150 s interval (see Fig. 3.5) could be explained by a $\sim 10\%$ increase in the spectral hardening factor. This is a possibility since at lower effective temperatures ($T_{\rm eff} < 1.5$ keV) the spectral hardening factor increases with decreasing temperature, as the relative contribution of electron scattering to the total opacity decreases (London et al. 1986). However, within the error limits, the blackbody radius for this interval is still consistent with the measured values during the first 100 s of the burst.

The derived blackbody radius cannot be interpreted as the physical size of the NS since LMXBs do not have isotropic radiation fields. Due to the presence of an optically thick accretion disk, any blackbody emission from the surface of the NS that is in the "shadow" of the accretion disk would not be directly observed but would possibly emerge as Comptonized emission. The only geometrical arrangements for which I can naively interpret the blackbody radius as the stellar radius is when the accretion disk is

perpendicular to the line of sight ($i = 0°$), or if the accretion disk does not extend to the surface of the neutron star. In all other cases the inferred blackbody radii underestimate the stellar radius, and so one must account for the covered region in order to extract a stellar radius from a measured blackbody temperature and flux.

The area of the covered region increases nonlinearly with increasing binary inclination, moving from 0% of the projected area when $i = 0°$ to 50% when $i = 90°$. Furthermore, since accretion disks are not infinitely thin there will also be some portion of the surface covered by the disk. The amount of covering by the disk can be parametrized by the disk half-height h. In spite of the nonlinear relation between the amount of covering and the inclination and disk half-height, the fraction of the stellar surface that is covered can be calculated using straightforward geometrical principles. With these issues in mind I interpreted $\pi R_{\rm bb}^2$ as the observable *projected* area of the star, and by calculating the fraction of surface covered I derived an effective stellar radius ($R_{\rm eff}$) as a function of inclination and disk half-height for source distances of 6 kpc and 5 kpc, which is presented in Fig. 3.6. Using optical observations of the counterpart of GS 1826–238, Mescheryakov et al. (2004) were able to derive an approximate inclination of $i \sim 40°$–$70°$, and so I only include this range in the figure.

From photometric measurements of the optical counterpart, Barret et al. (1995) derived an approximate lower limit to the distance to GS 1826–238 of 4 kpc. Assuming the range of possible binary inclinations used above is correct, it is apparent that a source distance near 5 kpc gives a NS radius within the commonly assumed range of $\sim$ 10–12 km (see the right axis of Fig. 3.6). On the contrary, a distance of 6 kpc does not give a NS radius within the common range. Even with an infinitely thin accretion disk and an inclination at the lower bound ($i = 40°$) of Mescheryakov et al. (2004), the smallest possible stellar radius at this distance within the error limits is $\sim$ 11 km.

From the results of the Table 3.4, it is clear that the burst photons immediately cool the Comptonizing plasma to $\sim$ 3.4 keV. Over the next 150 s, the plasma temperature recovers the persistent emission value of $\sim$ 6.8 keV. This type of plasma cooling during a burst may be an example of Compton cooling. The same inverse Compton scattering process that transfers energy to the persistent emission photons also transfers energy to

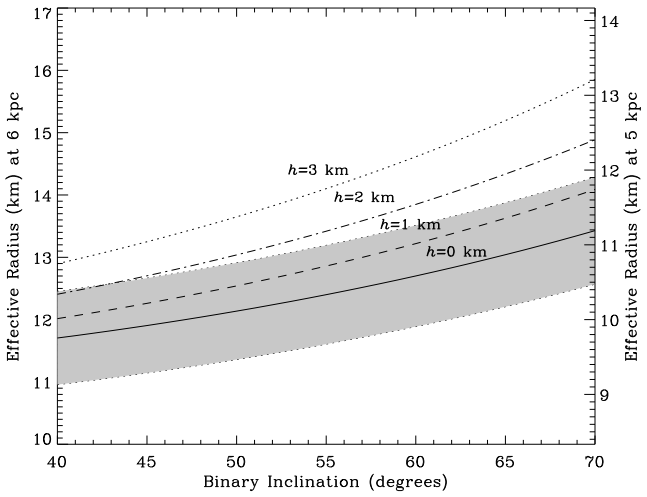

Figure 3.6: Effective stellar radius as a function of binary inclination and disk half-height (h) for source distances of 6 kpc (left axis) and 5 kpc (right axis). The shaded region represents the uncertainty and corresponds to the same range of blackbody radii as in Fig. 3.5. While the uncertainty is only plotted for $h = 0$, the magnitude of the uncertainties for the other values of h are approximately the same and have been omitted for clarity.

the photons emitted during a burst. The difference is that during the burst the flux of photons increases by more than an order of magnitude (for the 0–10 s interval), so that the balance between heating and radiative cooling is disturbed. It is also evident that the optical depth of the plasma is weakly constrained in the burst spectral analysis. Although the best-fit values for the first few intervals seem to indicate a larger optical depth, the range of uncertainty still includes the persistent emission value.

3.1.6 Emission Region Geometries

Since blackbody emission is observable during the bursts but not during the quiescent phase, I can speculate as to the geometries of the corresponding emission regions. To begin, GS 1826–238 has a weak magnetic field so infalling matter probably impacts the NS along the equator rather than at the poles. The release of gravitational binding energy through thermalization of the accreted material may result in a strip of blackbody emission along the equator (Church & Bałucińska-Church 2001), or the accumulation and spreading of accretion flow from the equator toward the poles may cause

two bright emission rings that are symmetric about the equator (Inogamov & Sunyaev 1999). The inability to see blackbody emission in the interval between bursts suggests that the equatorial strip or enhanced bright rings must be covered by an optically thick layer. This is explained naturally by the persistent emission dual Comptonization model. Note, however, that in § 3.2 I find that unusual deviations in the flux-recurrence time relationship which suggest that the accretion disk is truncated about one hundred kilometers from the stellar surface during this period. This provides an alternative explanation for the absence of blackbody emission between bursts.

At the onset of a burst, ignition likely starts near the equator and then rapidly spreads to cover the entire stellar surface in a couple seconds or less (Spitkovsky et al. 2002). Once the entire accumulated layer is burning, the subsequent blackbody emission indicates that there is an optical path for the radiation outside of the equatorial strip. It could be argued that the accretion flow is disrupted during a burst, or that a spherical corona surrounding the NS is temporarily blown away, and that this provides a path for the blackbody emission. However, the flux provided by the inner Comptonizing region also increases substantially during a burst, so the boundary layer plasma must still be present to up-scatter the seed photons. Moreover, our measurement of the Wien emission radius ($\sim$ 4 km) is too small for the corona to completely surround the star. Instead, I assume that this emission region is likely confined to the equatorial region. This explanation supports theories where the Comptonizing plasma or ADC is geometrically thin.

3.1.7 Summary

Our investigation of the LMXB GS 1826–238 using simultaneous *RXTE* and *Chandra* observations has led us to the following conclusions. From the observation of five uninterrupted burst intervals with *Chandra* in July 2002, I measured a burst recurrence time of 3.54 $\pm$ 0.03 hr, which is consistent with G04's measurement. G04's measured decrease in the burst recurrence time between 1997 and 2002 has been coupled with an even larger percentage increase in the mean persistent flux, possibly indicating that a greater fraction (as compared to 1997) of the stellar surface may be covered prior to ignition. I detected 611.2 Hz burst oscillations with a 0.033% chance that the signal

resulted from random fluctuations. The average rms amplitude of the peak is 4.8%. Effective stellar radius as a function of binary inclination and disk half-height (h) for source distances of 6 kpc (*left axis*) and 5 kpc (*right axis*) The *RXTE/Chandra* 0.5–200 keV integrated persistent emission spectrum is best fit with a dual Comptonization model, whereby two distinct Comptonizing regions exist and are characterized by a different set of parameters. The extended energy range of *RXTE* is essential to constraining the photon index or Comptonization parameter, and eliminates the need for a blackbody component. This result is contrary to most spectral models of LMXBs that include a visible blackbody component. The spectrum also requires a neutral Fe Kα emission line at 6.45 keV with EW $\sim$ 37.2 eV. In addition, I find strong evidence of interstellar Fe L absorption features at the about 17.15 Å and 17.5 Å, with significance 3.8σ and 2.9σ, respectively.

During a burst, blackbody emission accounts for the majority of the flux though it quickly disappears after $\sim$ 150 s. Throughout this period, the data are consistent with a blackbody radius between 10.3 km and 11.7 km for a distance of 6 kpc if one assumes the blackbody flux comes from the full $4\pi R^2$ of the neutron star surface. By accounting for the fraction of the surface that is obscured by the accretion disk, however, the source distance must be nearer to 5 kpc to be consistent with a neutron star radius of 10–12 km. I also see Compton cooling during the bursts, as the plasma temperature immediately decreases to $\sim$ 3 keV and then slowly returns to the persistent emission value of $\sim$ 6.8 keV after about 150 s. Since blackbody emission is not observed in the persistent spectrum yet dominates the burst spectrum, I conclude that the emission from those regions of the stellar surface along the equator are covered in the persistent phase. During the burst the entire surface is radiating as a blackbody, and so this emission can be seen outside of the covered region.

3.2 Deviations from the Flux-Recurrence Time Relationship

3.2.1 Introduction

Type I X-ray bursts result from unstable thermonuclear ignition of accreted material on the surfaces of weakly magnetic ($B < 10^{10}$ G) neutron stars (for a recent review, see Strohmayer & Bildsten (2006)). Freshly accreted hydrogen and helium on the neutron star surface is hydrostatically compressed by new material at a rate $\dot{m} \sim 10^4$ g cm^{-2} s^{-1}. In systems exhibiting bursts, the temperature and pressure at the base of the accreted layer slowly increase until the nuclear energy generation rate of the 3α-reaction becomes more sensitive to temperature perturbations than the radiative cooling. At this point the resulting thermonuclear instability leads to runaway burning of some or all of the matter that has been deposited since the previous burst. Typically, hours to days are required to accrete enough material to trigger the instability.

There are close to 100 type I bursters that are known in the Galaxy[4], and the vast majority are "atoll" type low-mass X-ray binaries (LMXBs) with luminosities above about 10^{36} erg s^{-1} (Hasinger & van der Klis 1989). Although the basic physics of type I X-ray bursts is understood, detailed comparisons between observations and theoretical models have had mixed success (e.g., Woosley et al. 2004). The most successful comparison has been with the "clocked burster" GS 1826–238 (also known as Ginga 1826–238), whose bursts are consistently quasi-periodic (Ubertini et al. 1989; Cocchi et al. 2001; Cornelisse et al. 2003). Studies of the bursts from GS 1826–238 began during the *BeppoSAX* mission, with the most detailed study of burst recurrence times and energetics coming from Galloway et al. (2004), who analyzed 24 bursts from the *Rossi X-Ray Timing Explorer* (*RXTE*) detected between 1997 November and 2002 July. They found that the recurrence time decreased from 5.74 ± 0.13 hr to 3.56 ± 0.03 hr while the persistent (between burst) flux level increased by 66%, so that the recurrence time decreased almost precisely as $1/F_x$. Assuming $F_x \propto \dot{M}$ implies that the accumulated mass required for the instability to occur is approximately the same even as the accretion rate changes. The

[4]For an updated list of Galactic type I X-ray bursters, see http://www.sron.nl/∼jeanz/bursterlist.html.

long burst durations (∼100 s) and the low value of α (≈40) – the ratio of the integrated bolometric persistent flux between bursts to the total bolometric burst fluence – both suggest that hydrogen constitutes a large portion of the fuel for these bursts (Bildsten 2000). between bursts, hydrogen burns stably via the hot CNO cycle at a rate that is only limited by the mass fraction $Z_{\rm CNO}$ (not the temperature), which modifies the composition of the fuel at the base of the accreted layer. Bursts from GS 1826–238 are clearly in the regime of mixed hydrogen and helium bursts triggered by unstable ignition of helium (Bildsten 2000). Further support for the H-rich fuel scenario comes from comparisons of the observed light curves with those predicted by time-dependent models, which also imply solar H and CNO composition in the material accreted by GS 1826–238 (Heger et al. 2008).

Additional *RXTE* observations have been made as part of a monitoring campaign from 2003 through 2007. These data reveal that the previously monotonic relation between burst recurrence time and persistent X-ray flux no longer fully describes the source behavior. Here I present an analysis of the full data set with the objective of more fully characterizing the complex burst behavior. I have also analyzed observations from the *Chandra X-ray Observatory* in 2002 July, and *XMM-Newton* in 2003 April, both of which occurred simultaneously with *RXTE*, in order to also study the low-energy spectrum. In addition, I used optical observations made with the UCT-CCD fast photometer at the South African Astronomical Observatory (SAAO) in 1998 June to determine the bursting behavior during gaps in the *RXTE* observations.

3.2.2 Observations & Analysis

RXTE

In this paper, I utilized all *RXTE* observations of GS 1826–238, which has been observed at least once per year since 1997, except during 2001. Overall, there are more than 600 ks of good exposure time. I analyzed data from the Proportional Counter Array (PCA; Jahoda et al. 2006) and the High Energy X-Ray Timing Experiment (HEXTE; Rothschild et al. 1998) instruments. The PCA has five identical co-aligned Proportional Counter Units (PCUs) sensitive to 2–60 keV photons. The HEXTE comprises two clus-

ters, each containing four scintillation detectors sensitive to 15–250 keV photons. Both instruments have large effective areas (∼6000 and 1400 cm^2, respectively) and microsecond timing resolution.

Recurrence Time Measurements

Measurements of the burst recurrence times were made using PCA event mode data with 1 s bins, including all photon energies. The times of the bursts were defined to be when the flux exceeds 25% of the peak flux of each of the bursts. Sometimes bursts took place when the satellite was not taking any data (e.g., during passages through the South Atlantic Anomaly), and recurrence times were inferred if bursts occurred near enough together to unambiguously know the number of intervening bursts. This method is acceptable because bursts from GS 1826–238 have *never* been observed to occur at irregular intervals. If the time between two observed bursts is Δt, the recurrence time is estimated as $\Delta t/(n+1)$, where n bursts are inferred in data gaps. Following Galloway et al. (2004), I adopted a fractional error of 2% on the individual recurrence time measurements. When n bursts are inferred in data gaps, the error is scaled by $1/(n+1)^{1/2}$ because I assume $n+1$ burst intervals in total. Although *RXTE* observations took place during 1999 and 2005, the duration and spacing of these measurements did not allow for an unambiguous recurrence time measurement. Table 3.5 shows the observation dates containing recurrence time measurements, the number of bursts that were observed, and the average burst recurrence time during each epoch. The observations taking place simultaneously (or nearly so) with *RXTE* are discussed below.

Energy Spectra Analysis

The evolving spectrum during the bursts was modeled using an absorbed blackbody, subtracting the pre-burst persistent emission as background. This approach is relatively standard for X-ray burst analysis, and I refer the reader to Galloway (2004) for further details. In addition to the burst spectra, I studied the persistent emission by extracting color-color diagrams and photon energy spectra. In each case I excluded data from 500 s before to 1500 s after a burst, the latter chosen to minimize the residual

Table 3.5. RXTE Observation Log of GS 1826–238

Date (U.T.)	Observatory[a]	Bursts[b]	Recurr. Time (hr)
1997 Nov 5–6	*RXTE*	2	5.88[c]
1998 Jun 7–12	*RXTE*	3	5.67 ± 0.04
1998 Jun 23–25	SAAO/*RXTE*	6/1	5.13 ± 0.19
2000 Jun 30–03[d]	*RXTE*	8	4.04 ± 0.06
2000 Sep 24–27	*RXTE*	7	4.11 ± 0.06
2002 Jul 29–30	*Chandra*/*RXTE*	6/4	3.54 ± 0.03
2003 Apr 6–9	*XMM-Newton*/*RXTE*	16/7	3.18 ± 0.14
2004 Jul 19–21	*RXTE*	7	3.47 ± 0.02
2006 Aug 9–12	*RXTE*	11	3.36 ± 0.07
2007 Mar 8–10	*RXTE*	9	3.53 ± 0.02

Note. — Observations allowing unambiguous recurrence time measurements. Additional *RXTE* observations are utilized in our study of the power spectra (see § 3.2.2).

[a]During three periods, simultaneous observations took place with *RXTE*.

[b]All bursts observed by *RXTE* were also observed with the other observatory.

[c]Only one burst interval was measured during this epoch.

[d]This observation ended in July.

blackbody flux seen during the decays of the bursts (Thompson et al. 2005). Colors were created by extracting light curves for each PCA channel and observation, reading in the channel energy boundaries from the observation's response matrix, and interpolating the counts spectrum to a standard grid. The soft and hard colors are defined as the counts ratio (3.5–6) keV/(2–3.5) keV and (9.7–16) keV/(6–9.7) keV, respectively, and were obtained by integrating over the interpolated grid. To correct for the long-term drift of the gain of each PCA channel, the colors were normalized to the colors of the Crab calculated with the closest observation available to each GS 1826–238 observation.

I extracted energy spectra from the persistent emission between X-ray bursts using the standard software for *RXTE* data reduction (FTOOLS v.6.2). For the PCA, I used the "Standard 2" data, ignoring the first three channels and photon energies greater than 30 keV. HEXTE data below 25 keV were ignored, as were data above 100 keV due to poor statistics. The HEXTE channels were rebinned so that there were a minimum of 1000 counts per bin. To each observation (minus the times surrounding the bursts), I fit an absorbed double Comptonization model using XSPEC v.11.3. This model was found by Thompson et al. (2005) to fit the broadband spectra of GS 1826–238 better than a single Comptonization model or empirical models like a cut-off power-law. For each measured *RXTE* burst recurrence time, the persistent flux was obtained from the best-fit model[5] during the time since the previous burst. Although the spectral model only applies to photons from 3–100 keV, I extrapolated the model from 0.1–3 keV and 100–200 keV to estimate the bolometric flux. were added to all channels.

Timing Analysis

To relate the burst behavior to the broadband (persistent) timing properties, I also analyzed the rapid variability in the X-ray emission by producing a series of power density spectra (PSDs). For each *RXTE* observation, including six observations that did not allow for a recurrence time measurement, I used 128 s segments of PCA event mode data with 2^{-12} s bins (corresponding to a Nyquist frequency of 2048 Hz), and normalized after Leahy et al. (1983). As with the energy spectra and colors, I excluded data 500 s

[5]Some of the fluxes had to be corrected for a 0.251° offset pointing in R.A., which decreased the efficiency of the PCA and HEXTE by a factor of $\sim$1.3.

before to 1500 s after each burst. Separate groups of power spectra close in time were merged if no systematic differences in PSDs were observed. In this manner we obtained 18 power spectra. On average, each PSD contained 36 ks of accumulated data (with the smallest being 8 ks and the largest being 83 ks). The contribution due to Poissonian statistics was estimated from the 1500–2048 Hz frequency band and removed (this also implicitly accounts for any decrease in power due to the PCA deadtime), and the spectra were converted to fractional rms squared.

Qualitatively, each PSD can be characterized as having roughly equal power per decade in frequency, which extends between a low and high frequency break. To quantitatively describe each power spectrum, we fit a combination of 4–6 Lorentzians following, e.g., Belloni et al. (2002), which overcomes the limitation of treating different power spectral components with intrinsically different models. Two to three of the Lorentzians are zero-centered and fit the broadband noise, giving a broad peak in the power times frequency (νP_ν) representation between ν_b at low frequencies and ν_l and ν_u at high frequencies (Belloni et al. 2002). There is also an additional component peaked at ν_h to cover the "hump" typically seen near 2–3 Hz (but much higher during 2003 April, as shown below) in GS 1826–238. Additional narrow Lorentzians that are interpreted as quasi-periodic oscillations (QPOs; where the coherence factor $Q \equiv \nu_0/2\Delta > 2$) were added if necessary to achieve acceptable fits. Due to limited statistics at high frequencies, only the lower frequency Lorentzian components (< 200 Hz) were useful for comparison. The frequencies are characterized using $\nu_{\rm max}$, the frequency at which the component contributes most of its variance per logarithmic frequency interval, which is equal to $\nu_{\rm max} = \sqrt{\nu_0^2 + \Delta^2}$, where ν_0 is the centroid frequency and Δ is the half-width at half-maximum of the Lorentzian. Errors on the fit parameters were determined using $\Delta\chi^2 = 2.71$ corresponding to the 90% confidence interval.

Chandra

The *RXTE* observations on 2002 July 29–30 occurred simultaneously with *Chandra* (also analyzed by Thompson et al. 2005), providing valuable low-energy coverage. A 68 ks observation was made with the Advanced CCD Imaging Spectrometer (ACIS;

Garmire et al. 2003), which is sensitive to photons from 0.3–10 keV. High-resolution spectra were obtained by having the High Energy Transmission Grating (HETG; Canizares et al. 2005) placed in the optical path. The HETG spectrometer is composed of the Medium-Energy Grating (MEG) and the High-Energy Grating (HEG). First-order MEG/HEG spectra were extracted with the *Chandra* Interactive Analysis of Observations (CIAO) v.3.4 software. Responses matrices were generated using calibration v.3.4.0. Spectra were rebinned with at least 1000 counts per spectral channel, giving statistically significant data for photon energies greater than 1 keV.

XMM-Newton

The *RXTE* observations during 2003 April 6–9 occurred simultaneously with an *XMM-Newton* (Aschenbach 2002) observation (also analyzed by Kong 2007), lasting for 200 ks. Timing mode data was acquired from both the European Photon Imaging Camera (EPIC) and the Reflection Grating Spectrometer (RGS), although I only made use of data from the EPIC pn detector. The Optical Monitor was turned off for this observation. Data analysis was performed with the *XMM-Newton* Science Analysis System (SAS) v.7.1.0. Photon energy spectra were extracted for energies between 0.5 and 6 keV, and were rebinned with at least 1000 counts per spectral channel. Rather than using the "canned" response matrices, I generated one specific to our observation.

Optical

During 1998 June, a set of three 7 ks *RXTE* observations were made at $\sim$1 day intervals, resulting in the detection of just one burst in X-rays. At the same time, however, observations of a small (50×33 arcsec^2) region surrounding the optical counterpart of GS 1826–238 were made using the UCT-CCD fast photometer (O'Donoghue 1995), at the Cassegrain focus of the 1.9 m telescope at SAAO. On June 23 and 24, the observations lasted for 8 hours in an uninterrupted series of 5 s exposures; on June 25, the observation was 9 hours long using 2 s exposures. In each case, the coverage included (unambiguous) consecutive optical bursts from GS 1826–238. I performed data reduction using the Image Reduction and Analysis Facility (IRAF), including photometry with the implementation

of DAOPHOT II (Stetson 1987). Point spread function (PSF) fitting was employed in order to obtain the best possible photometry, since there was moderate crowding of the counterpart and variable seeing. The details of this procedure are given by Homer et al. (1998).

Figure 3.7 shows the arrival times of the bursts seen in the optical and by *RXTE*. The bursts detected in the optical, coincident with (and immediately following) the burst detected by *RXTE* allowed an unambiguous measurement of the persistent flux and recurrence time during these observations. In addition, for the subsequent analysis, I associate the other two recurrence time measurements made possible by the pairs of bursts observed in the optical both before and after the burst detected by *RXTE*, with the X-ray flux measured during that observation.

3.2.3 Flux-Recurrence Time Relationship

Within any individual observation, GS 1826–238 exhibited quasi-periodic bursting behavior, with the average persistent flux in between bursts varying by at most a few percent. Figure 3.8 shows the variation of the burst recurrence time, burst fluence, and α as a function of the (absorbed) persistent X-ray flux using *RXTE* measurements. Except for the data from 2003 April, it is evident that the recurrence time of the bursts has a rough $1/F_{\rm X}$ dependence (Galloway et al. 2004), as has been observed previously, implying that typically, a similar amount of accreted fuel is required to trigger each burst. The typical scatter on the recurrence times within each epoch is just 1%. However, the 2003 April measurements are significant outliers, with recurrence times that are shorter than expected based on the persistent flux. During this epoch, the recurrence time was about 3.2 hr even though the persistent flux was $\sim$10% lower than in 2000 June/September, when the recurrence time was about 4.1 hr. Other measurements also deviate from the $1/F_{\rm X}$ trend, but to a lesser extent. For example, in 1998 June the recurrence time was typically near 5.65 hr, but about twelve days later optical burst intervals were 4.9 and 5.2 hr even though the persistent X-ray flux (from *RXTE* observations) had not substantially changed. Therefore, the occasional discrepancy between the burst recurrence time and the expected value (given the persistent flux level and their previously observed

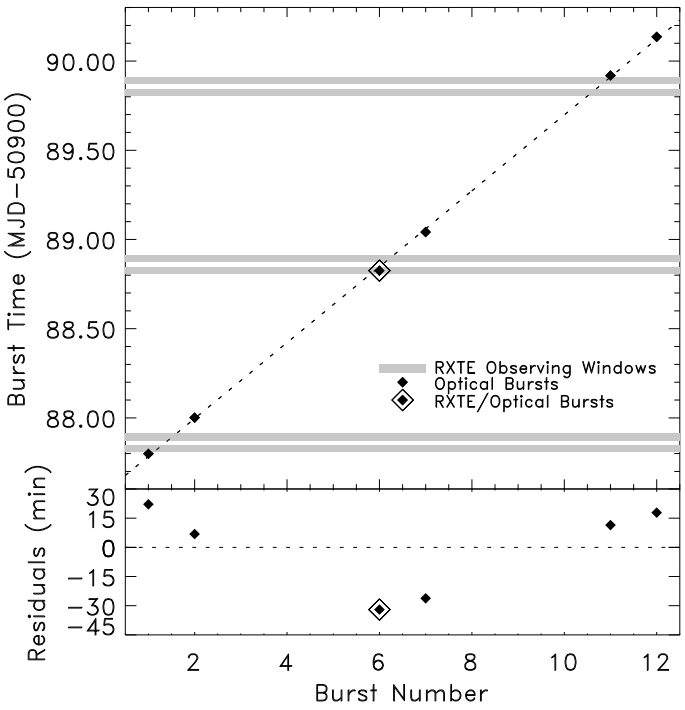

Figure 3.7: Burst arrival time plot during the optical observations in 1998 June. Intervening bursts (#3–5 & #8–10) were inferred to take place with consistent separations, although since the inferred times were during daylight at SAAO they could not be observed. The shaded bars show the observing windows for the nearly concurrent *RXTE* observations. The dashed line assumes a constant burst recurrence time of 5.10 hr, although the burst behavior is more accurately described by a recurrence time of 4.92 hr for the first three observed bursts (1, 2, & 6, assuming constant intervals between 2 & 6), and 5.24 hr for the last four observed bursts (6, 7, 11, & 12, assuming constant intervals between 7 & 11), using burst 6 for each measurement. The apparent V-shaped residual plot is due to this change in recurrence time. If I assume the recurrence time changed discontinuously at burst 6, the residuals are only $\sim$2 min.

relationship) seems to be a general property of GS 1826–238, and not something that (for example) only occurs near the highest persistent flux levels. More recent *RXTE* data from 2004, 2006, and 2007, have shown that the persistent flux versus recurrence time relationship has at other times obeyed the previously observed monotonic behavior.

Figure 3.9 shows the fractional difference between the estimated bolometric flux and the flux derived from the empirical relationship between flux and burst recurrence time (hereafter; referred to as the "recurrence time flux"), as a function of burst recurrence time. Note that this figure can be equivalently considered as the residuals of the x-axis in Fig. 3.8, *top* panel. Assuming the empirical curve describes the actual flux-recurrence time relationship, Fig. 3.9 suggests that the 2003 April X-ray flux measured by *RXTE* is underestimated by 30–40%.

The discrepant measurements suggest either that the proportionality between the persistent 0.1–200 keV flux (derived from extrapolating the model fit in the 3–100 keV range) and accretion rate was different than during other observations, or that the heating of the accreted layer (or some other factor) changes to alter the ignition depth at the same accretion rate. In order to discriminate between these two possibilities, I made a more detailed study of the burst characteristics, and of the persistent spectral and timing behavior of the source.

3.2.4 Energy Spectrum-Accretion Rate Relationship

It is conventionally assumed that the accretion rate in LMXBs is proportional to the X-ray flux, and since I measure the flux in an instrumentally-determined passband, there is always the possibility that spectral variations outside our passband will cause the proportionality to change between observation epochs. Here I explore this possibility in detail, both from the spectral shape (via the X-ray colors) within the *RXTE* passband (which is common to all the measurements), and in a broader band possible thanks to several occasions of contemporaneous *Chandra* and *XMM-Newton* observations.

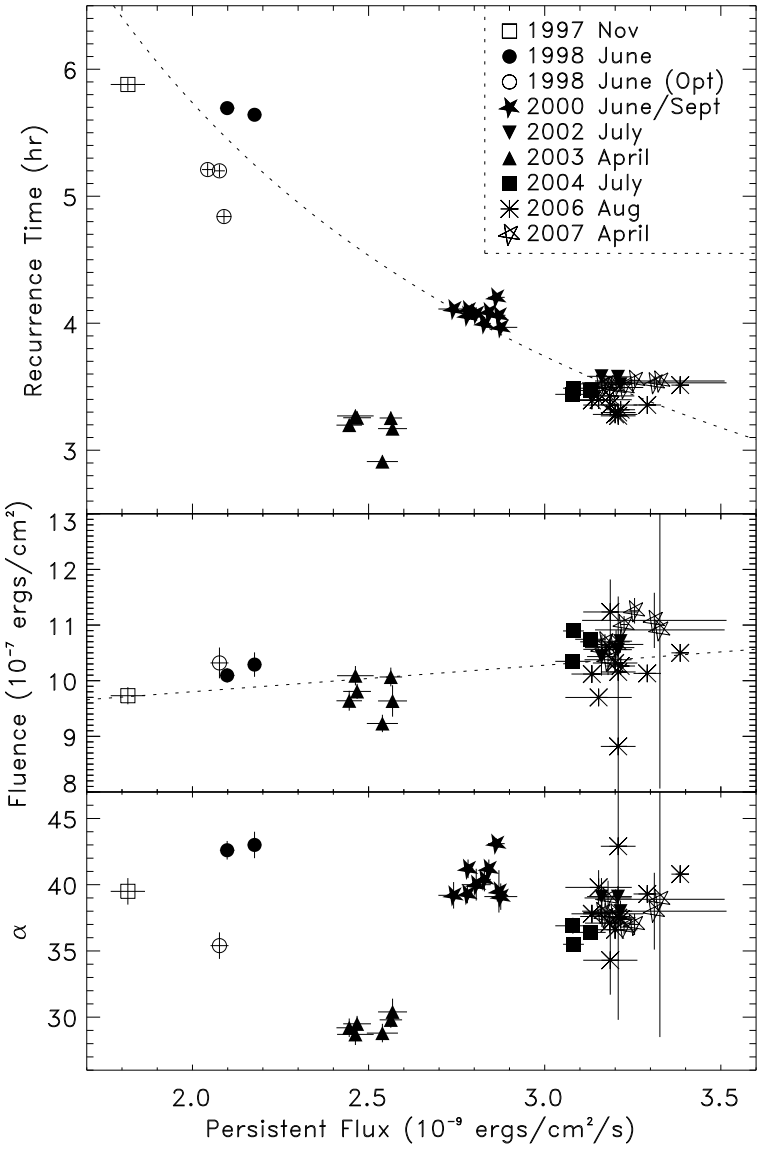

Figure 3.8: Variation of the burst recurrence time, burst fluence, and α ($\equiv \int_0^{\Delta t} F_{\rm p} dt / \int_0^{\Delta t} F_{\rm b} dt$) as a function of the absorbed persistent (between burst) flux in the range 0.1–200 keV (derived from extrapolating the model fit to *RXTE* data in the 3–100 keV range). Note that the unabsorbed fluxes are consistently ∼5% larger. The dotted curve in the top panel shows the empirical fit to the data (excluding 2003 April), using $\Delta t \propto F_x^{-1.05}$ (Galloway et al. 2004); the middle panel contains a linear fit. The 1998 June (opt) measurements in the top panel use optically-measured recurrence times and X-ray fluxes from the nearest *RXTE* observations (see Fig. 3.7). The lower panels only have one corresponding data point because *RXTE* measurements are only available for a single 1998 June (opt) burst.

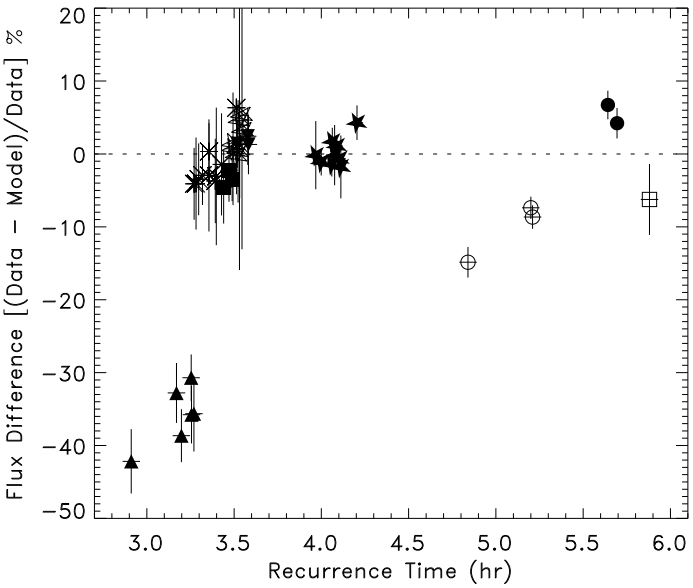

Figure 3.9: Fractional difference between the estimated bolometric flux and the "expected" flux derived from the empirical relationship between flux and burst recurrence time ("recurrence time flux") as a function of the recurrence time. The symbols correspond to the same time periods as in Fig. 3.8.

X-ray Colors

Figure 3.10 shows the average *RXTE*/PCA colors within 0.2 days of each burst. The individual 128 s colors (not shown here) show some scatter in the color-color diagram but all remain in the "island" state that typically characterizes bursting atoll LMXBs. Evidently, the colors from 1997, 2002, 2004, 2006, and 2007 are similar. The colors from 1998 and 2000 are comparable, although the soft color from 2000 and the hard color from 1998 are slightly smaller than the colors from the other periods. On the other hand, the colors from the 2003 April are both significantly smaller, with fractional changes in the soft and hard colors of about 4% and 3%, respectively.

Broadband Spectra

To test the extrapolation of our spectral models to energies below the PCA and HEXTE passband, I also fitted the simultaneous 2002 July *Chandra/RXTE* and 2003 April *XMM-Newton/RXTE* broadband spectra (§ 3.2.2 & § 3.2.2). In both cases, two

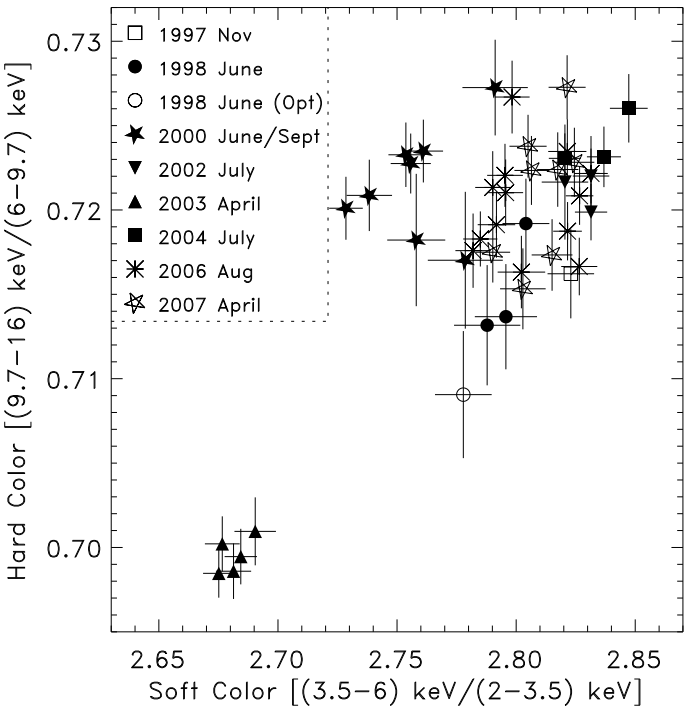

Figure 3.10: Average *RXTE*/PCA colors of GS 1826–238 within 0.2 days of the times of the bursts shown in Fig. 3.8.

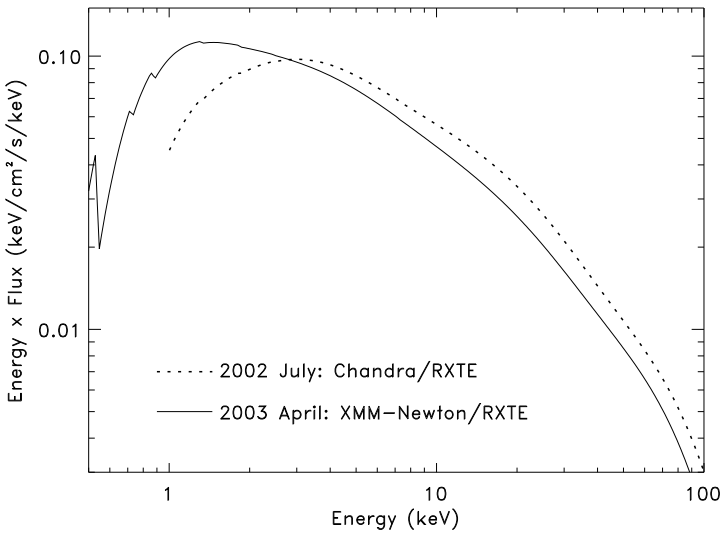

Figure 3.11: Model spectra for the simultaneous *Chandra/RXTE* observations in 2002 July (dotted curve), and the simultaneous *XMM-Newton/RXTE* observations in 2003 April (solid curve). The *Chandra/RXTE* spectrum is restricted to $E > 1$ keV to reflect the energy range utilized in the fits; *XMM-Newton* provided good data down to 0.5 keV.

Comptonization components (`comptt` in XSPEC; Titarchuk 1994) were found necessary in order to accurately model the data (Thompson et al. 2005). Each spectrum contains a component with ∼0.1–0.2 keV seed photons, and a component with ∼0.8–0.9 keV seed photons. One of these components is characterized by a ∼6 keV electron plasma, and the other by a hotter electron plasma (∼20 keV or greater), to fit the hard tail. I could not unambiguously associate the high or low seed photon temperatures with either the high or low plasma temperatures, however, due to the model degeneracy that is introduced by the use of two Comptonization components. Table 3.6 lists the best-fit parameter values for each spectrum and for the model coupling $kT_{\rm s,hot}$ to $kT_{\rm e,hot}$ and $kT_{\rm s,cold}$ to $kT_{\rm e,cold}$, plus fits to the 2003 April spectrum including an additional soft thermal component (see below).

The model spectra for both epochs are presented in Figure 3.11, which shows that the major model-independent differences are that the 2002 July spectrum peaks (in νF_ν) at 1.3 keV, while the 2003 April spectrum peaks at 3.1 keV. *RXTE* observations without simultaneous low-energy coverage are, for the most part, insensitive to such

changes in the soft flux, although the smaller soft colors (Fig. 3.10) during 2003 April are suggestive of this difference. The model fitting the broadband 2003 April spectrum implies a 6% increase in the flux relative to the fit with only *RXTE* data, illustrating how a wider passband can reveal additional flux not apparent in the model extrapolated from the 3–100 keV band. Still, the discrepancy between the persistent flux and the "recurrence time flux" is 30–40% (Fig. 3.9).

Relevant to the calculation of accurate bolometric fluxes for GS 1826–238 (see § 3.2.2) is the question of additional soft spectral components. To test for the presence of such components, I separately tried adding a multicolor disk blackbody (`diskbb` in XSPEC; Mitsuda et al. 1984) and a blackbody to our original spectral model, with the temperature of the soft component tied to the seed photon temperature of the cooler Comptonization spectral component. We interpret the model with a multicolor disk blackbody as an approximation to the accretion disk spectrum, or partial covering of the accretion disk due to the disappearance of the Comptonizing medium over a limited volume, and the model with a blackbody as partial covering of the neutron star surface, or an extended optically thick boundary layer. In this picture, the soft photons acting as seed photons therefore emerge without being Comptonized.

For the 2002 July spectrum, I found that the additional component in each case (disk blackbody or blackbody) did not improve the fit to the data, yet allowed for a 4–5% increase in the unabsorbed bolometric flux relative to the fit without the additional component. On the other hand, the fit to the 2003 April spectrum significantly improved in each case, with F-test probabilities of essentially zero that the improvement to the fit occurred by chance. The unfolded spectra and residuals for the double Comptonization plus multicolor disk blackbody model is shown in Figure 3.12 (top & bottom panels). The residuals for the double Comptonization model derived using *RXTE* data alone, and using both *XMM-Newton* and *RXTE* data are also shown (middle panels). I stress, however, that the spectral fits for the models including a soft component should be considered *illustrative*. Accurately fitting a soft spectral component together with Comptonization components is problematic for larger seed photon temperatures because the `comptt` model assumes a Wien input spectrum rather than a thermal spectrum. This approximation,

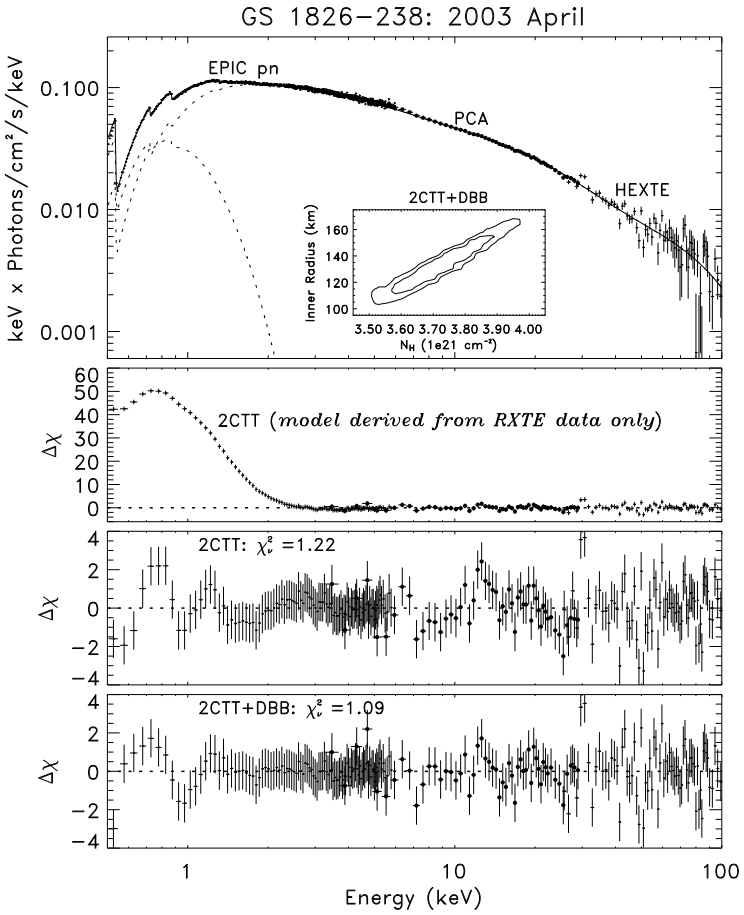

Figure 3.12: Unfolded 0.5–100 keV spectra and residuals for the 2003 April observations using the double Comptonization plus multicolor disk blackbody model (2CTT+DBB, top and bottom panels). The two middle panels show the fit residuals for the double Comptonization model derived using *RXTE* data alone (upper middle panel), and using both *XMM-Newton* and *RXTE* data (lower middle panel). The EPIC pn and HEXTE unfolded spectra are divided by 0.74 and 0.90, respectively, to account for the differences in the flux normalization between the instruments. The relatively large discrepancy between the PCA and EPIC normalizations has been noted previously; see e.g., Yaqoob et al. (2003). The residuals in the *XMM-Newton* data compared to the fit derived from *RXTE* data alone clearly indicate a substantial soft excess. By including *XMM-Newton* data, the double Comptonization model provides an acceptable fit, but the fits with an additional soft thermal component are superior. The 2CTT+BB residuals are not shown, although they are nearly indistinguishable from the 2CTT+DBB residuals. For clarity, only every tenth residual for the *XMM-Newton* data are shown. *Inset, top panel:* Confidence contours (68% and 90% levels) between the absorbing column density and the inner disk radius of the multicolor disk blackbody component (assuming a 6 kpc source distance and 60° inclination).

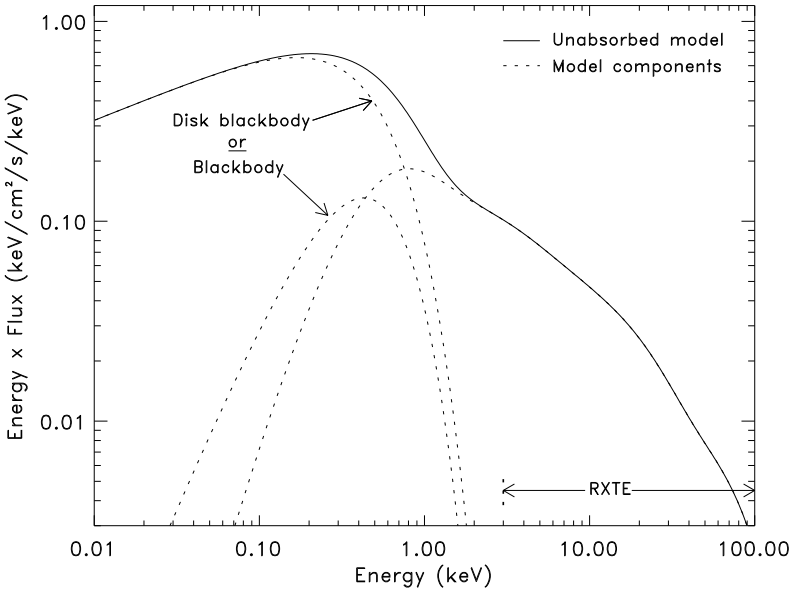

Figure 3.13: Unabsorbed 2003 April model spectrum containing an additional disk blackbody component or an additional blackbody component. The model is extrapolated to energies below the fitted range (0.5–100 keV). The dotted curves show the decomposition of the model components (the two Comptonized components are added together). The passband for *RXTE* is shown in the bottom of the figure, illustrating how a soft component could reside below *RXTE* coverage. Note how similar *absorbed* spectral shapes for $E > 0.5$ keV are achieved with a model containing a combination of either a blackbody and an absorbing column density of 3.2×10^{21} cm^{-2}, or a relatively brighter disk blackbody and a larger absorbing column density of 3.7×10^{21} cm^{-2}.

while leading to negligible changes to the spectrum at high energies, leads to an underestimation of the low-energy flux.[6] Compounding the issue is the interplay between the soft spectral component and the absorbing column density (see Fig. 3.12, inset); although the single-parameter uncertainty in the absorbing column density is very small ($\sim$0.2%), the two-parameter confidence contour between the absorbing column density and disk blackbody normalization ($\propto R_{\rm in}$) suggests a much larger uncertainty. Because reliable interpretation of the fits is not possible, I do not include the soft component normalization values in Table 3.6. Nevertheless, with the additional disk blackbody component the *unabsorbed* bolometric flux of the 2003 April spectrum is 3.7×10^{-9} erg cm^{-2} s^{-1}, which is $\sim$50% larger than the values obtained with only *RXTE*. With an additional blackbody,

[6]Nevertheless, the Comptonization model is more appropriate than empirical models such as a cutoff power law which, for $\Gamma > 1$, diverges at low energies.

the unabsorbed flux is 3.3 $\times 10^{-9}$ erg cm^{-2} s^{-1}, or $\sim$30% larger than the values obtained with *RXTE* alone. Although the flux-recurrence time relation (Fig. 3.8) used the *absorbed* fluxes, a direct comparison can be made by noting that the *unabsorbed* fluxes for the other observing epochs are consistently $\sim$5% larger (because a constant absorbing column density was used when extrapolating the 3–100 keV models to the wider 0.1–200 keV passband). The large fraction of soft flux contained in these components can clearly be seen in Figure 3.13. Therefore, despite the limited ability to acquire physical understanding of a soft thermal component in the 2003 April spectrum, it is a distinct possibility that the presence of one can account for the apparent disparity between measured persistent flux and the flux level that is expected given the burst recurrence time (Fig. 3.8).

3.2.5 Rapid Variability

Each of the 18 average power spectra show very similar characteristic frequencies and rms amplitudes for the Lorentzian components representing the band-limited noise. The one major exception is the power spectrum from 2003 April, in which the characteristic frequencies are significantly higher. The 1998 June optical/*RXTE* data show frequencies higher by a factor of $\sim$2. A single low frequency QPO is present in seven of the PSDs, and in all but two cases this QPO appears to be associated with ν_h. Five of the PSDs have two low frequency QPOs, and in each case the higher (lower) frequency QPO also appears to be associated with ν_h (ν_b). Similar low frequency QPOs have been observed in black holes and other neutron stars (e.g., Olive et al. 1998, Nowak 2000, Jonker et al. 2000), and even in previous observations of GS 1826–238 (Barret et al. 2000).

Three of the power spectra are displayed in Figure 3.14. The top panel shows the power spectrum from 1998 June (optical), the middle panel from 2003 April, and the bottom panel from 2006 August. The latter is more indicative of the timing characteristics seen during the other *RXTE* observation epochs. Figure 3.15 shows the correlation between the two Lorentzian components that are present and well-constrained in all of the power spectra: ν_b and ν_h. The dotted line shows the best-fit linear trend. Similar

Table 3.6. Broadband Spectral Fits during 2002 July and 2003 April

Parameter	2002 July 2CTT[a]	2003 April 2CTT[a]	2003 April 2CTT+DBB[b]	2003 April 2CTT+BB[c]
$N_{\rm H}$ (10^{21}/cm^2)	3.33 ± 0.01	2.4 ± 0.1	3.73 ± 0.01	3.19 ± 0.01
1. $kT_{\rm s}$ (keV)	0.21 ± 0.01	0.16 ± 0.01	[0.19 ± 0.01]	[0.15 ± 0.01]
1. $kT_{\rm e}$ (keV)	6.46 ± 0.03	5.9 ± 0.4	5.9 ± 0.3	6.0 ± 0.3
1. τ	4.72 ± 0.01	4.2 ± 0.1	4.4 ± 0.1	4.3 ± 0.1
2. $kT_{\rm s}$ (keV)	$0.85^{+4.65}_{-0.01}$	0.94 ± 0.02	0.75 ± 0.04	0.84 ± 0.05
2. $kT_{\rm e}$ (keV)	> 29.5	$17.4^{+2.2}_{-1.8}$	$19.5^{+2.4}_{-1.8}$	$19.3^{+2.5}_{-2.1}$
2. τ	$1.65^{+8.93}_{-0.01}$	$2.9^{+0.3}_{-2.9}$	2.9 ± 0.2	2.8 ± 0.2
χ^2_ν (d.o.f.)	0.89 (1498)	1.22 (1152)	1.09 (1151)	1.02 (1151)

Note. — Errors correspond to the 90% confidence interval for a single parameter. The 2002 July *Chandra/RXTE* spectrum had statistically significant data from 1–100 keV, and the 2003 April *XMM-Newton/RXTE* spectrum had statistically significant data from 0.5–100 keV. A multiplicative constant was included in the models to account for differences in the absolute flux normalizations between the instruments.

[a]XSPEC model: `tbabs*(comptt`$_1$ `+ comptt`$_2$`)`. Each `comptt` component assumes cylindrical geometry.

[b]XSPEC model: `tbabs*(comptt`$_1$ `+ comptt`$_2$ `+ diskbb)`. The temperature of the disk blackbody at the inner disk radius was tied to the cooler seed photon temperature (indicated by "[...]").

[c]XSPEC model: `tbabs*(comptt`$_1$ `+ comptt`$_2$ `+ bbody)`. The blackbody temperature was tied to the cooler seed photon temperature (indicated by "[...]").

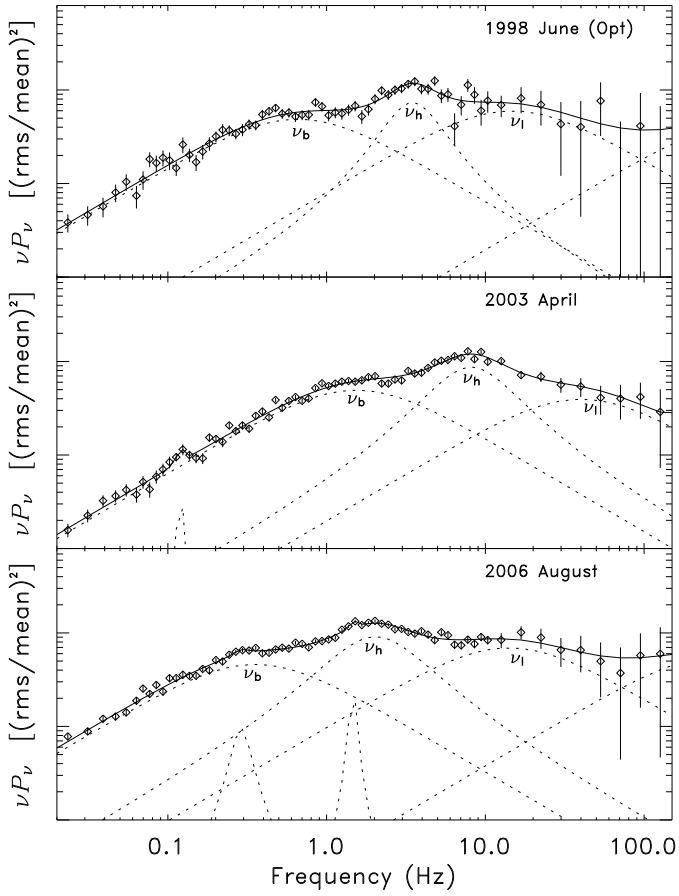

Figure 3.14: Example power spectra from 1998 June (during the time of the optical bursts), 2003 April, and 2006 August, with the individual Lorentzians superposed. The power spectra are presented in the νP_ν representation, which has the advantage of emphasizing higher frequency features and showing the maximum strength and frequency of the signal more directly. The components with characteristic frequencies of $\nu_{\rm b}$, $\nu_{\rm h}$, $\nu_{\rm l}$ are labeled (the high frequency feature centered on $\nu_{\rm u}$ is poorly constrained). The characteristic frequencies of the 2006 August PSD are more typical of the long-term average. The 2003 April PSD shows a dramatic increase in the characteristic frequencies, and the 1998 June PSD has moderately higher frequencies.

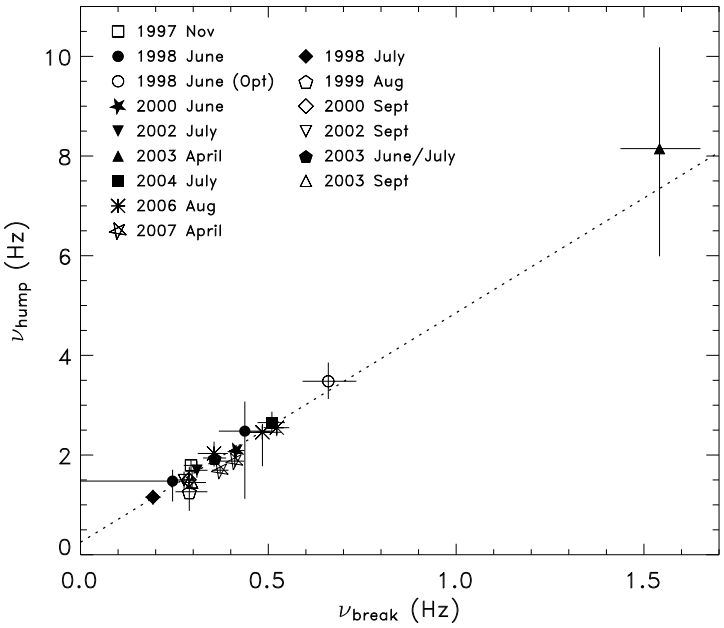

Figure 3.15: Characteristic frequencies of ν_b and ν_h for the 18 average *RXTE*/PCA PSDs. The dotted line illustrates the correlation among these parameters. The additional symbols on the right (compared to Figs. 3.8–3.10) are from observations lacking a recurrence time measurement.

correlations between the Lorentzian characteristic frequencies has been seen in many other sources (e.g., Psaltis et al. 1999; Wijnands & van der Kils 1999; Belloni et al. 2002; van Straaten et al. 2002), whether it be between the horizontal branch oscillation frequency and the lower frequency kHz QPO in Z-sources, or between the lower and upper frequency kHz QPOs in atolls, etc. Given that these correlated timing features are rather common in neutron stars and black holes, the present correlation does not come as a surprise.

3.2.6 Early Ignition

Although the X-ray spectral shape and timing characteristics are both atypical during 2003 April (and, to a lesser extent, 1998 June), it is also possible that some variation in the burst ignition properties contributes to the unexpectedly short burst recurrence times measured during those observations. Bildsten (2000) pointed out that because the instability leading to bursts is a local phenomenon, the time for instability to develop depends on the accretion rate per unit area rather than the global accretion

Table 3.7. Burst Profile Comparison

Parameter	2003 April	2000 June/Sept	>2002 July[a]
τ	39.7 ± 0.6	38.8 ± 1.2	40 ± 4
τ_1	18.0 ± 0.9	17 ± 2	19 ± 2
τ_2	47.3 ± 1.1	43.5 ± 0.8	45 ± 9
$F_{\rm peak}$	24.5 ± 0.6	26.5 ± 0.7	25.5 ± 1.2

Note. — The units of τ, τ_1, and τ_2 are seconds, and the units of $F_{\rm peak}$ are 10^{-9} erg cm^{-2} s^{-1}.

[a]Excluding 2003 April.

rate. A faster ignition time in 2003 April could thus be explained by accretion over a more limited area of the surface of the neutron star relative to the other observing epochs. Even if the instability begins sooner, I expect the burst will consume all of the fuel that has been accreted since the previous burst because, although the instability leading to the burst is a local phenomenon, the subsequent spreading burning front encompasses the entire stellar surface (Spitkovsky et al. 2002; Bhattacharya & Strohmayer 2007). In this case, I would expect the burst fluences to be reduced approximately to the ratio of the recurrence times, i.e., $\sim$3/4, assuming no change in the fuel composition at ignition, and a similar accretion rate in 2003 April as for the observations at similar persistent flux levels. Instead, the fluences for the 2003 April are roughly similar to the bursts at higher or lower accretion rates (Fig. 3.8, *middle* panel).

One way the burst fluences in 2003 April could still match the measured values for the other bursts despite $\sim$25% less fuel is a change in the composition of the fuel. The nuclear energy generation rate during bursts is $Q_{\rm nuc} = 1.6 + 4X$, where X is the mean hydrogen mass fraction in the layer, and I assume $\approx$35% energy loss due to neutrinos during the *rp*-process burning (e.g., Fujimoto et al. 1987). A H-fraction that is $\approx$35% greater at ignition for the 2003 April bursts could thus compensate for the smaller accreted mass. Naturally, the mean H-fraction will be higher for bursts with shorter recurrence times, since less time has passed for steady H-burning to reduce the accreted composition.

The time to burn all the accreted hydrogen is $t_{\rm burn} = 11(Z/0.02)^{-1}(X_0/0.7)$ hr (e.g., Cumming & Bildsten 2000), where Z is the CNO mass fraction, and X_0 the accreted composition. Assuming the accreted hydrogen begins burning immediately upon being accreted, the mean H-fraction in the fuel layer at ignition is then (for $\Delta t < t_{\rm burn}$): $X_0(1-0.5\Delta t/t_{\rm burn})$. For $X_0 = 0.7$ and $Z = 0.02$ this gives a H-fraction that is only $\approx$6% larger for the 2003 April bursts. Therefore, changes to the composition of the accreted material cannot explain how the fluences of the bursts in 2003 April are in agreement with the other observing epochs.

Significant changes to the *shape* of the burst light curves may indicate unusual or unexpected nuclear burning regimes. In order to characterize the burst profiles, I fitted a composite exponential curve to each burst, and I refer the reader to Galloway et al. (2006) for the details of the fitting procedure. I compared the 2003 April burst decay parameters to those from the period of the most similar persistent flux (2000 June/September), and to the periods with the most similar burst recurrence times (all observations after 2002 July, except 2003 April). This exercise revealed that the shapes of the burst profiles in 2003 April are qualitatively similar to the other epochs (Galloway et al. 2004; Heger et al. 2008). The parameter values are presented in Table 3.7. The only real indication of a significant difference between the light curves is in the second decay constant (τ_2), which is somewhat longer for 2003 April than in 2000 June/September. However, these parameters do systematically depend on the recurrence time due to the changing hydrogen fraction (see Fig. 4 from Heger et al. 2008). A more appropriate comparison might be with the bursts at the closest recurrence time, i.e., the bursts with a recurrence time of $\sim$3.5 hr (2002 July and later, excluding 2003 April). Although this is a more inhomogeneous sample compared to 2003 April and 2000 June/September, τ_2 for 2003 April is consistent with the others, though slightly higher (but not significantly) in the mean. There is a slightly longer second decay constant and lower peak flux for the 2003 April bursts compared to the bursts at the next nearest flux determined by *RXTE*, but, similar to the comparison of τ_2, it is consistent with the bursts at the nearest recurrence time.

3.2.7 Discussion

During 2003 April, the recurrence times of thermonuclear bursts from GS 1826–238 were unexpectedly short given the persistent flux measured by *RXTE* and the previously-determined monotonic relation between these two parameters. At the same time, the spectrum from a simultaneous *XMM-Newton* observation (§ 3.2.4) suggests that an additional soft thermal component may be present which could increase the unabsorbed bolometric flux by up to 50%. A significant piece of evidence supporting a redistribution of the accretion energy within the X-ray bands is the accompanying shift of the variability to faster timescales (Fig. 3.15), because correlations between higher power spectral frequencies and softer energy spectra are observed almost ubiquitously in black hole candidates and in many neutron stars. A direct relationship between QPO frequency and power-law index has been seen in many black hole candidates (e.g., Vignarca et al. 2003; Kalemci et al. 2004, 2005, 2006; Shaposhnikov & Titarchuk 2006), and in at least five neutron stars (e.g., Titarchuk & Shaposhnikov 2005). Moreover, episodes of rare soft thermal components (interpreted as the accretion disk) lasting for several months in the black hole candidate GRS 1758–258 seem to be triggered by a decrease in the hard emission (Pottschmidt et al. 2006). Perhaps the most relevant example is from Ford et al. (1997), however, who showed that there is a direct correlation between the flux of the blackbody component and the QPO frequency in the burster 4U 0614+091. Although high frequency QPOs are not observed in the GS 1826–238 power spectra, the correlations between the frequencies of QPOs and broadband noise components in other sources make it tempting to speculate that the higher PSD frequencies in 2003 April are indeed coupled with a soft spectral component, the presence of which is presumably related to changes in the accretion geometry.

The correlations between faster variability and soft spectral components can be understood in the context of truncated disk models for accretion in X-ray binaries, which explain the low/hard to high/soft spectral transitions seen in both black hole and neutron star systems (for a recent review, see Done et al. 2007). For neutron star binaries at low $L/L_{\rm Edd}$ ($\sim$0.04–0.08 in GS 1826–238, assuming $d = 6$ kpc), such models consist of a thin accretion disk that is truncated at some radius far from the surface, probably due to

evaporation of the accretion disk (Mayer et al. 2007; Meyer et al. 2000), and an optically thin[7] but geometrically thick hot inner flow that smoothly transitions to the boundary layer. Seed photons from the surface of the star and from the inner edge of the disk cool the inner flow. At higher accretion rates, the inner radius of the disk moves inwards, which reduces the volume of the region occupied by the hot inner flow. Assuming that most of the variability comes from this region, then a smaller volume would naturally account for the faster variability. In addition, the smaller disk radius will lead to a more prominent soft spectral component.

One could argue that the soft photon flux should be present all the time, and perhaps just not detectable in the other observations due to poorer low-energy coverage. According to truncated disk models, however, at low accretion rates the accretion disk is expected to be far from the surface of the neutron star (e.g., Esin et al. 1997). If I assume that the power spectral break frequency $\nu_{\rm b}$ is associated with the inner disk radius and the orbital frequencies are Keplerian ($\nu_{\rm Kep} \propto R^{-3/2}$), I expect the inner disk radius in 2002 July, for example, to be $\approx$3 times larger than in 2003 April, and the integrated disk flux to be $\approx$3 times smaller (Frank et al. 1992, p.73). This is roughly consistent with the ratio of the absorbed soft fluxes shown in Fig. 3.11.

Given that the 2003 April power spectral frequencies are the highest, and at the same time the burst recurrence time suggests the accretion rate is the highest, it is worth considering that an alternative indicator for the mass accretion rate may be the timing data rather than the X-ray flux. For example, it has been proposed that $\nu_{\rm b}$ is positively correlated with the mass accretion rate (e.g., van der Klis 1994). If this were the case, however, I would expect a monotonic relationship between $\nu_{\rm b}$ and burst recurrence time (which I also assume to trace mass accretion rate). Such a relationship does not exist. To see this, one must only consider the data from 1998 June (optical); the break frequency is the second highest value even though the inferred accretion rate is the third lowest (only 1997 November and 1998 June have longer burst recurrence times, Fig. 3.8). On the other hand, the two observing epochs showing the largest disparity between the recurrence time flux and the observed flux (Fig. 3.9), i.e., 1998 June (optical) and 2003 April, also exhibit

[7]Note that the spectral parameters in Table 3.6 do not support an optically thin interpretation. I defer a detailed analysis of the spectrum using more sophisticated models such as `eqpair` for a subsequent paper.

the highest break frequencies. Therefore, it may be the case that $\nu_{\rm b}$ is a better tracer of the soft thermal flux and not the bolometric flux, although the absence of low-energy spectral coverage in the majority of GS 1826–238 observing epochs precludes a detailed comparison.

An alternative explanation is that the bursts are igniting earlier, perhaps because the area over which the accretion occurs has decreased; however, any plausible mechanism to ignite the bursts earlier would also give rise to bursts that were significantly less energetic than others at comparable X-ray fluxes, whereas I find bursts in 2003 April with fluences comparable to those in other epochs. Thus, I conclude that the X-ray flux measured by *RXTE* in 2003 April underestimates the bolometric flux to a much greater degree than in other epochs, likely due to the presence of enhanced X-ray emission below $\sim$2 keV. This implies that although the X-ray flux measured by *RXTE* in 2003 April was similar to what was observed in 2000 June/September, the accretion rate (and "true" bolometric flux) in 2003 April must have been at its highest level because the recurrence time was the smallest. This idea is consistent with truncated disk models, which explain the emergence of the soft spectral component by a reduction of the inner disk radius at high accretion rates. In this scenario, the previous and subsequent *RXTE* observations of GS 1826–238 fortuitously maintained a fairly strict correspondence between X-ray flux in the *RXTE* passband and accretion rate due to a relatively constant spectral shape. Our results indicate that the spectral shape in GS 1826–238 starts to undergo a significant transformation when the bolometric flux is above about 3.5×10^{-9} erg cm^{-2} s^{-1}, or when the luminosity is above 1.5×10^{37} erg s^{-1} $(d/6\ {\rm kpc})^2$.

There are other factors that could play a role during the periods of discrepant bursting behavior. One possibility is that the photon emission from GS 1826–238 may be anisotropic. Such emission is expected any time the scattering optical depth is much lower over a limited range of solid angles than in other directions (King et al. 2001), and includes any source with an accretion disk. Recent work by Heger et al. (2008) suggests that emission anisotropy does indeed influence the observational characteristics of GS 1826–238. In order for the burst timing and energetics from *RXTE* observations between 1997 November to 2002 July to match theoretical ignition models, they found

that $\xi_p/\xi_b = 1.55$. Different anisotropy factors for the burst and persistent emission are expected because the radiation can be attributed to geometrically distinct regions (Fujimoto 1988). If we assume that the burst emission is isotropic, the results of Heger et al. (2008) indicate that the persistent luminosity may be underestimated by a factor of 1.55 in all observing epochs. To determine if anisotropic emission affected the 2003 April data to a higher degree than the other time periods, however, would require the results to be extended to include this epoch.

3.2.8 Summary of Results

Now that I have developed a reasonable picture to explain the deviations in the flux-recurrence time relationship in GS 1826−238, it is worthwhile to reflect on where these results fit into the larger study of accretion disk properties. In Figure 3.16, I present a flow chart that illustrates the connection of the various phenomena exhibited in GS 1826−238 to the underlying physics.

In most "atoll" LMXBs like GS 1826−238, it is thought that the accretion disk extends all the way to the boundary layer. However, if the accretion flow becomes tenuous enough, the protons are unable to transfer their gravitational binding energy to the electrons (the efficient radiators). I have found evidence that strongly suggests the accretion disk in the "clocked burster" is in fact truncated roughly a few hundred kilometers from the stellar surface. This conclusion is based on using the intervals between type I bursts as a measure of the accretion rate.

3.3 Acknowledgement

Chapter 3 is in part a reprint of material that appears in The Astrophysical Journal, Vol. 634, p. 1261, and Vol. 681, p. 506. The dissertation author was the primary investigator and author of these papers.

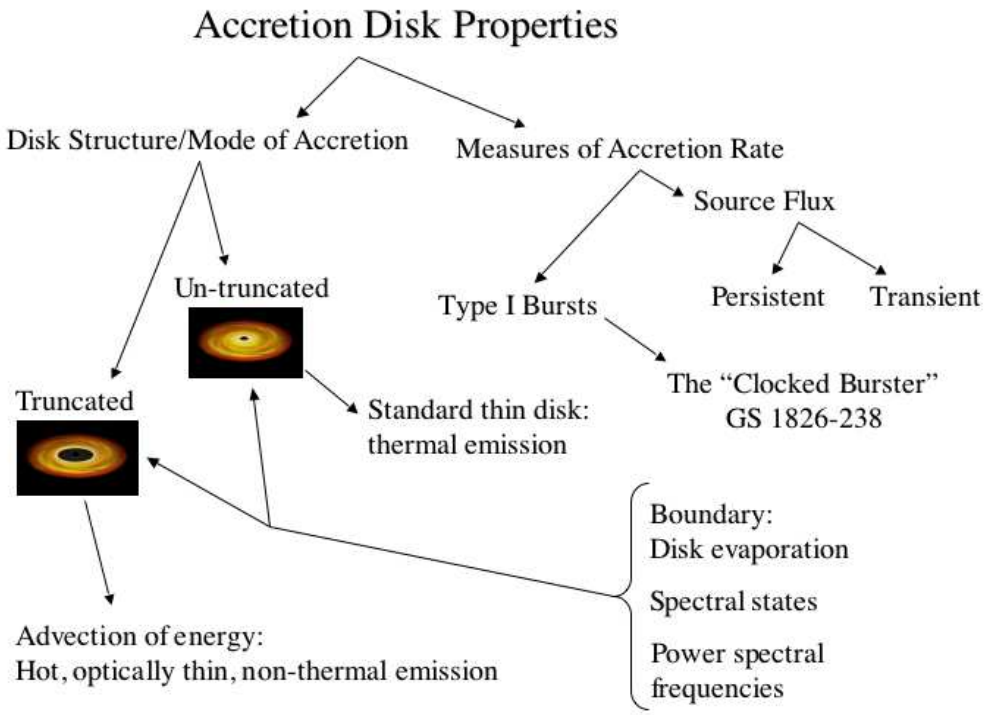

Figure 3.16: Flow chart connecting the areas of accretion disk properties that are studied throughout § 3.2.

4

X-ray Halos & Delayed Variability

4.1 X-ray Halos

X-ray halos, which appear as diffuse emission surrounding X-ray sources, are created by small-angle scattering of soft X-ray photons from dust grains in the interstellar medium (ISM). Their study can provide information on interstellar grain properties (density, morphology, composition) and on the spatial distribution along the line of sight. Given a dust distribution, variability in the X-ray halo can be used to geometrically measure the distances to X-ray sources based on the time delays of the photons scattered along the line of sight (Trümper & Schönfelder 1973). This method has been applied in a number of cases (e.g., Predehl et al. 2000; Thompson et al. 2006; Audley et al. 2006; Xiang et al. 2007).

Although initial studies of X-ray halos by *Einstein* and *ROSAT* significantly advanced our understanding of the scattering of X-rays and the composition of dust in the interstellar medium, the absence of a telescope with superb angular resolution had inhibited detailed investigations, and had also limited investigations of small spectral features. Due to the superb imaging capabilities, the *Chandra X-ray Observatory* has ushered in a new era of astrophysical studies of X-ray sources.

The theory of X-ray scattering and the production of X-ray halos has been described by a number of authors (e.g., Overbeck 1965; Mauche & Gorenstein 1986; Klose 1991; Mathis & Lee 1991; Smith & Dwek 1998; Draine 2003). Various interstellar grain

models have been proposed. Mathis et al. (1977) developed a model composed of silicate and graphite grains with a size distribution of $n(a) \propto a^{-3.5}$, which reproduces the observed extinction of starlight. Weingartner & Drain (2001, hereafter WD01) produced a grain model that additionally accounts for the diffuse infrared and microwave emission emission from the ISM by including sufficient small carbonaceous grains. Zubko et al. (2004) created a series of models by simultaneously fitting the extinction, infrared emission, and elemental abundance constraints, by including, for example, amorphous carbon particles, organic refractory material, water ice, and voids.

One of the many challenges in developing a viable model is that the characteristics of the dust may vary in different Galactic locations due to different local evolutionary histories and ISM phases. Given such difficulties, a preeminent interstellar grain model has not been established. For my purposes, I use the WD01 grain model, although I allow the energy dependence of the scattering cross section to be a free parameter.

The basic quantity that determines the characteristics X-ray halos is the differential scattering cross section $d\sigma/d\Omega$. This can be calculated using the exact Mie solution or the simpler Rayleigh-Gans approximation. For the WD01 grain model, the differential scattering cross section as a function of scattering angle ϕ can be approximated by the simple analytic form

$$\frac{d\sigma}{d\Omega} \approx \frac{\sigma_{\rm sca}}{\pi\phi_{\rm s,50}^2}\left[1+\left(\frac{\phi}{\phi_{\rm s,50}}\right)^2\right]^{-2} \tag{4.1}$$

where $\phi_{\rm s,50} \approx 360''({\rm keV}/E)$ is the median scattering angle as a function energy (Draine 2003). It is important to note that the following results are probably somewhat dependent on this chosen form of the differential scattering cross section.

4.1.1 Analytical Modeling of X-ray Halos

Following Draine & Tan (2003; hereafter DT03), for a steady source, the intensity of single-scattered photons arriving at halo angle θ is given by

$$I_1(\theta) = F_{\rm X}\tau_{\rm sca}\tilde{I}_1(\theta), \tag{4.2}$$

where

$$\tilde{I}_1(\theta) \approx \int_0^1 \frac{\tilde{\rho}(x)}{(1-x)^2}\frac{d\sigma}{d\Omega}dx, \tag{4.3}$$

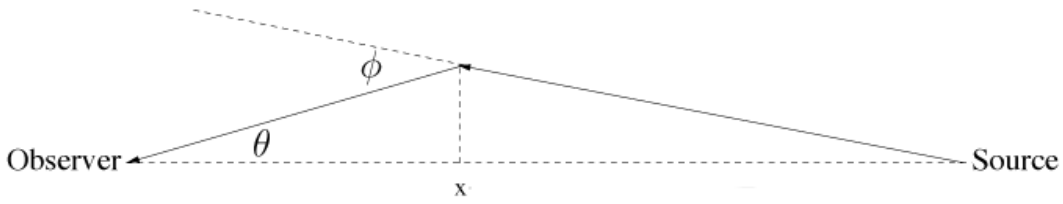

Figure 4.1: Dust scattering geometry for single-scattered photons.

$\tilde{\rho}(x)$ is the dimensionless dust density at fractional distance x to the source, the scattering angle and the halo angle are related through $\phi \approx \theta/(1-x)$, and the normalization is chosen such that $\int \tilde{I}_1(\theta) 2\pi\theta d\theta = 1$. The scattering geometry for photons scattered once is shown in Fig. 4.1. For a variable source, a photon appearing at halo angle θ after scattering from a dust grain at a fractional distance x to a source D kpc away will be delayed with respect to the central source by

$$\delta t = 1.21 \frac{D}{\mathrm{kpc}} \left(\frac{\theta}{\mathrm{arcsec}} \right)^2 \frac{x}{1-x} \text{ s.} \tag{4.4}$$

In this case, F_X must be moved inside the integral (eq. 4.2) because the halo flux at time t is proportional the flux of the central point source at the "retarded time" $t' = t - \delta t$, i.e., $I_1(t,\theta) \propto F_\mathrm{X}(t - \delta t(x,\theta))$.

It is clear that to accurately determine the proportionality between the source flux and the halo (which for a steady source is simply $F_\mathrm{X}\tau_\mathrm{sca}$), one must know the history of the source flux for a sufficiently long time period preceding the observation. In most cases this is not practical, so typically one assumes that any change in the source flux took place sufficiently long ago for the halo to have completely responded to it (as I do when determining the dust distribution to Cen X-3, § 4.4.3), or one models the history of the source flux using reasonable estimates (as I do when determining the distance to Cen X-3, § 4.4.4).

The intensity of the X-ray halo due to photons scattering two or more times (I_2, I_3, ...) is straightforward for a steady source given an assumed dust distribution. The main difference is that for each point along the line of sight x', the single-scattered halo must be calculated ($I_{\mathrm{n}-1}(x',\alpha)$) by integrating over the dust distribution between x' and 1. The double-scattered halo is then derived by integrating over the single-scattered halo that appears at each point between the source and observer (Fig. 4.2). DT03 presented

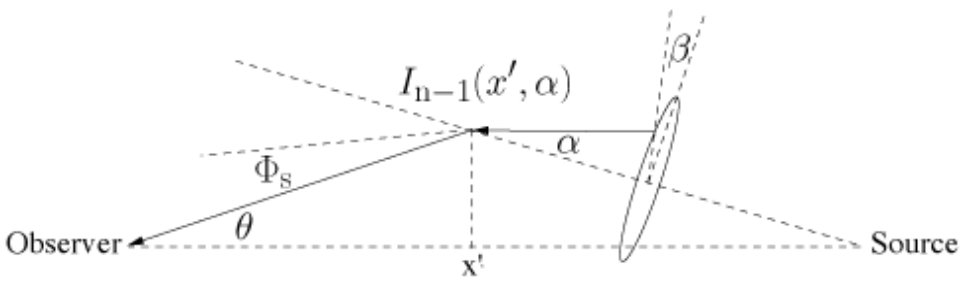

Figure 4.2: Dust scattering geometry for double-scattered photons.

the appropriate recursion formula:

$$I_2(\theta) = F_X \frac{\tau_{sca}^2}{2} \tilde{I}_2(\theta), \tag{4.5}$$

where

$$\tilde{I}_2(\theta) \approx \int_0^1 \tilde{\rho}(x')dx' \int_0^{\pi/2} \tilde{I}_1(x', \alpha)d\alpha \int_0^{2\pi} \frac{d\sigma}{d\Omega}(\Phi_s)\, d\beta, \tag{4.6}$$

where

$$\Phi_s(x', \theta, \alpha, \beta) = \arccos\left(\cos\alpha\cos\phi + \sin\alpha\cos\beta\sin\phi\right), \tag{4.7}$$

and $\tilde{I}_2(\theta)$ is normalized in the same fashion as $\tilde{I}_1(\theta)$.

Accounting for the time delays for multiply-scattered photons, however, is extremely cumbersome. Fortunately, the intensity of the halo due to photons scattered n-times, relative to the observed source flux, is $\tau_{sca}^n/n!$ (Mathis & Lee 1991), so the halo intensity for multiply-scattered photons decreases rapidly for reasonably small optical depths ($\tau_{sca} < 2$). Usually, the first- and second-order scatterings are sufficient to model the total halo.

Of course, the differential scattering cross section (eq. 4.1) is energy-dependent. Given the equations above, the spectrum of the X-ray halo (integrated over all halo angles) is a function of the source's spectrum prior to absorption and scattering along the line of sight $F_\star(E)$, the measured point source spectrum $F_X(E)$, and the optical depths through:

$$F_{halo}(E) = F_\star(E)e^{-\tau_{abs}(E)}\left[1 - e^{-\tau_{sca}(E)}\right] = F_X(E)\left[e^{\tau_{sca}(E)} - 1\right], \tag{4.8}$$

where $\tau_{abs(sca)}$ is the optical depth to absorption (scattering) and $F_\star e^{-\tau_{abs}} = F_X + F_{halo}$. The halo spectrum for singly-scattered photons is obtained by replacing the term

$[e^{\tau_{\rm sca}} - 1]$ on the right side of eq. (4.8) with $\tau_{\rm sca}$. Equation 4.8 can be directly related to the halo surface brightness distributions through

$$F_{\rm halo}(E) = \sum_{n=1}^{\infty} \int_0^{\pi/2} I_n(\theta, E) 2\pi\theta d\theta \tag{4.9}$$

As pointed out above, from a practical standpoint the first two or three terms in the summation are usually sufficient to accurately model the halo; likewise for the halo spectrum. Note that the upper limit of $\pi/2$ for integration over α and θ in eqs. (4.6) and (4.9), respectively, is rather arbitrary because $I_n \rightarrow 0$ rapidly with increasing θ.

4.1.2 An Alternative Method

An alternative method of calculating the characteristics of X-ray halos is to use the distribution function of delayed photons, plus an analytic equation from Draine (2003). Using the WD01 interstellar grain model, Draine (2003) determined that the fraction of the total single-scattered halo flux interior to halo angle θ is characterized by the normalized (dimensionless) dust density $\tilde{\rho}(x)$:

$$g(\theta) \approx \int_0^1 \tilde{\rho}(x) \left[1 + (1-x)^2 \left(\frac{\phi_{\rm s,50}}{\theta} \right)^2 \right]^{-1} dx, \tag{4.10}$$

where x is the fractional distance to the source. Using these relations, I define the fractional halo density (in units of arcsec^{-2}) as

$$g_\rho(E, \theta) \equiv \lim_{\delta\theta \rightarrow 0} \frac{g(E, \theta + \frac{\delta\theta}{2}) - g(E, \theta - \frac{\delta\theta}{2})}{2\pi\theta\delta\theta}. \tag{4.11}$$

With an appropriate normalization, the fractional halo density for a given energy will produce approximately the same halo profile as $I_{\rm sca}(\theta)$, the conventional formula for halo surface brightness distributions (e.g., Mathis & Lee 1991).

In conjunction with the fractional halo density, it is also possible to calculate the halo light curves by integrating over the distribution of time-delayed photons, which in the single scattering approximation is

$$H(\delta t, \theta, E) = \frac{\tilde{\rho}(x)}{\delta t + t_\theta} \frac{d\sigma(\phi, E)}{d\Omega}, \tag{4.12}$$

where I have defined $t_\theta \equiv D\theta^2/2c$. This distribution can be understood by noting that the delayed light curve in the halo is only a function of the time delay and viewing angle, although physically, the light curve is governed by the distribution of dust, and the differential scattering cross section of the dust; the latter are functions of x and ϕ, respectively. Therefore, $H(\delta t, \theta)$ is simply the product of $\tilde{\rho}(x)$, $d\sigma(\phi)/d\Omega$, and the Jacobian determinant relating the area elements $\left|\partial(x,\phi)/\partial(\delta t,\theta)\right|$ (Trümper & Schönfelder 1973; hereafter TS73). Although $d\sigma/d\Omega$ is a function of the scattering angle, it is implicitly a function of the time delay through $\phi \approx \theta/(1-x)$. An alternative derivation of $H(\delta t, \theta)$ is provided by Alcock & Hatchett (1978, see eq. [17]), who also derived formulae describing the propagation of a pulse of radiation in the large optical depth limit.

The distribution of single-scattered delayed photons has a form similar to a decaying exponential, falling off more slowly at larger halo angles and for larger source distances. Considering that more than half of the space along the line of sight is covered within about $600(D/5\text{ kpc})(\theta/10'')^2$ s ($dx/d\delta t \sim \delta t^{-2}$), this type of functional behavior is not surprising. The distribution of delayed photons also shows that the extent of smearing increases dramatically with halo angle, which can also be seen in eq. (4.4), where $\delta t \propto \theta^2$. While the delayed light curve of a δ-function burst at a given angle can be obtained directly from $H(\delta t, \theta)$, for an arbitrary light curve one must convolve the non-delayed light curve $I(t)$ and the distribution of time-delayed photons:

$$\tilde{B}(\delta t, E, \theta) = \frac{\int_{-\infty}^{\delta t} I(t) H(\delta t - t, E, \theta) dt}{\int_{-\infty}^{\delta t} H(\delta t - t, E, \theta) dt}. \tag{4.13}$$

4.2 Chandra Point Spread Function

In order to accurately study X-ray halos, it is extremely critical to develop a representation of the instrumental point spread function (PSF) to separate the dust-scattered halo from the "mirror-scattered" halo. In this work, I use the best instrument ever built to study X-ray halos, the *Chandra X-ray Observatory*. The excellent angular resolution of the HRMA and the good spectral resolution of the Advanced CCD Imaging Spectrometer (ACIS) provide the best opportunity to date for the study of X-ray halos.

However, careful subtraction of the PSF is still required to produced accurate results. The raw images of X-ray sources are the convolution of the X-ray halo surface brightness distribution and the PSF of the mirror assembly, modified by the instrumental response of the CCDs, the reduction of effective area at larger off-axis angles due to vignetting, and the dithering of the telescope throughout the observation. Exposure maps account for all of these effects, with the exception of the PSF. At small halo angles ($<5''$) MARX[1] simulations can be used to model the PSF, but at larger halo angles the results of MARX simulations appear to be unreliable (Gaetz 2004). Furthermore, with piled-up sources it becomes difficult to obtain the correct PSF normalization.

In order to address these issues, I developed a representation of the PSF by utilizing all *Chandra* High Energy Transmission Grating (HETG) observations of PKS 2155-304 and Her X-1. These two sources are both out of the plane of the Galaxy and have interstellar hydrogen column densities of $N_{\rm H} < 10^{20}$ cm^{-2} along the line of sight. Presumably, this also means that the amount of dust along the line of sight is nearly negligible, meaning the radial profiles of the zeroth-order images are almost purely due to the PSF, with only a very small contribution due to dust-scattering. I use the HETG observations of these sources for two reasons: (1) The grating allows for flux and spectral measurements, making it possible to accurately normalize the PSF as a function of energy; and (2) the use of the grating will provide consistent analysis when I apply the resulting PSF parameter values to our observations of Cen X-3 in Chapter 4 (in case the diffraction of photons from the HETG modifies the PSF). The drawback to this approach, however, is that grating reduces zeroth-order effective area and the statistical quality of the images. To try to overcome the problem of limited statistics, i co-added the zeroth-order images and first-order MEG/HEG spectra from five observations of Her X-1 (ObsIDs 2749, 3821, 3822, 6149, & 6150) and ten observations of PKS 2155-304 (ObsIDs 1014, 1705, 3167, 3706, 3708, 5173, 6926, 7291, 8380, & 8436), for a total exposure time of 373 ks.

For each observation, twenty different radial profiles were extracted in 200 eV energy bands from 1–5 keV using 40 logarithmically-spaced bins from $0.492''$ (1 pixel) to $110''$, with spatial filters applied to the readout transfer streak and the MEG and HEG

[1] http://space.mit.edu/ASC/MARX/

Table 4.1. Chandra/HETG PSF Parametrization

Energy Range (keV)	Normalization[a] (10^{-5} arcsec^{-2})	Γ	χ^2_ν
1.0–1.2	9.9 ± 0.3 (3.6%)	2.62 ± 0.04	1.40
1.2–1.4	9.1 ± 0.4 (4.8%)	2.51 ± 0.05	0.99
1.4–1.6	7.8 ± 0.5 (6.4%)	2.48 ± 0.07	1.24
1.6–1.8	7.9 ± 0.6 (8.4%)	2.30 ± 0.09	1.92
1.8–2.0	8.7 ± 0.5 (5.9%)	2.48 ± 0.07	1.21
2.0–2.2	10.4 ± 0.6 (6.0%)	2.52 ± 0.07	1.44
2.2–2.4	9.0 ± 0.5 (6.8%)	2.44 ± 0.07	1.20
2.4–2.6	7.7 ± 0.7 (10.4%)	2.36 ± 0.12	2.20
2.6–2.8	7.8 ± 0.6 (8.9%)	2.12 ± 0.09	1.60
2.8–3.0	8.7 ± 0.7 (8.8%)	2.20 ± 0.10	1.21
3.0–3.2	9.6 ± 0.8 (9.7%)	2.24 ± 0.10	0.95
3.2–3.4	9.6 ± 0.8 (8.9%)	2.37 ± 0.10	1.12
3.4–3.6	10.0 ± 0.8 (8.7%)	2.13 ± 0.09	1.48
3.6–3.8	9.6 ± 0.8 (9.3%)	2.03 ± 0.09	1.23
3.8–4.0	10.5 ± 0.7 (7.4%)	1.97 ± 0.07	0.73
4.0–4.2	10.8 ± 0.8 (7.8%)	2.09 ± 0.07	1.16
4.2–4.6	11.8 ± 0.8 (7.2%)	2.00 ± 0.07	0.97
4.4–4.8	11.7 ± 0.8 (7.7%)	2.04 ± 0.07	1.29
4.6–4.8	11.6 ± 0.8 (7.3%)	1.92 ± 0.06	1.07
4.8–5.0	12.1 ± 0.8 (7.4%)	1.98 ± 0.06	1.83

Note. — PSF approximated by co-adding HETG observations of Her X-1 (ObsIDs 2749, 3821, 3822, 6149, & 6150) and PKS 2155-304 (ObsIDs 1014, 1705, 3167, 3706, 3708, 5173, 6926, 7291, 8380, & 8436). The PSF can be approximated by the function $S_{\rm PSF}(E,\theta) = A_5(E)\,(\theta/5'')^{-\Gamma(E)}$, where $A_5(E)$ is the normalization $5''$ from the point source. Parameters apply from $3''$ to $100''$ from the central point source; an exponential cut-off is required for analysis of larger off-axis angles (Gaetz 2004).

[a] $A_5(E)$: Fraction of the point source flux comprising the PSF $5''$ from the central source in units of 10^{-5} arcsec^{-2}. The fit parameters $A_5(E)$ and Γ are correlated, so the uncertainty in $A_5(E)$ does not precisely correspond to the uncertainty in the integrated PSF flux ($\int 2\pi\theta S_{\rm PSF}(E,\theta)d\theta$). The percentage in parenthesis more accurately represents the fractional uncertainty in the integrated PSF flux.

diffraction pattern (offset by $-4.725°$ and $5.235°$ from a line perpendicular to the readout) using rectangular regions 10 pixels wide. The radial profiles from each observation were then summed together and scaled to the total exposure time, resulting in images with units of [counts/s/pixel].

To account for differences in the detection efficiencies between the individual observations, separate instrument maps were created for each observation and energy band. Traditional instrument maps account for varying effective area and photon detection efficiencies across the CCD chip, but for PSF analysis it is only appropriate to use the effective area at the source position (Gaetz 2004). The aspect histograms of each observation were then used to project the instrument maps onto the plane of the sky, resulting in effective area maps accounting for bad rows on the CCD and the dither of the telescope. The dithered instrument maps, which showed deviations in the effective area at the source position of a few percent from observation to observation, were averaged by weighting each individual map by the number of counts in each energy and angular bin from the corresponding observation, correcting for the area of the spatial filters that were applied to the images. Radial profiles of the exposures maps were then created for the same annular regions as the profiles of the zeroth-order images, resulting in maps with units of [$\mathrm{cm}^2 \times$ counts/photons]. The final exposure-corrected radial profiles were then created by dividing the summed counts images by the averaged exposure map in each energy band. Using the summed spectrum, fluxes in each energy band were measured in units of [photons/cm^2/s]. By dividing the exposure-corrected images by the fluxes in each energy band, I obtained normalized PSF profiles in 200 eV bands.

To each PSF profile (with background subtracted), I fit the function

$$S_{\mathrm{PSF}}(E,\theta) = A_5(E)\left(\frac{\theta}{5''}\right)^{-\Gamma(E)}, \tag{4.14}$$

where $A_5(E)$ is the normalization $5''$ from the central point source in units of flux fraction per square arcsecond. When modelling the PSF at larger off-axis angles (e.g., $\theta > 100''$) it is necessary to include an exponential cut-off in the fitting function to account for the diffuse PSF wings (Gaetz 2004), but at smaller angles ($\theta < 100''$) a simple power-law representation appears to be adequate. The final product that I obtained though this analysis is the energy- and angle-dependent fraction of the source flux comprising the

PSF, as shown in Table 4.1. These results can be safely applied to *Chandra*/HETG observations $3''$ to $100''$ from the central source.

The High Energy Transmission Grating may affect the shape of the PSF when it intercepts photons as the exit the mirror assembly and diffracts them. It is therefore necessary to also be able to model the PSF for observations that do not have the HETG inserted into the optical path. Following Gaetz (2004), the *Chandra* PSF flux for halo angles greater than $10''$ can be approximated by a power law with an exponential cutoff. Over a given energy range, the PSF can be approximated by

$$C_{\rm PSF}(\Delta E, \theta) \approx \int_{E_1}^{E_2} \frac{F_X(E)\left[1 - f_{\rm EEF,10}(E)\right]}{f_{10}\left(E, \frac{-\gamma(E)}{c(E)}\right)} \left[\frac{\theta}{10}\right]^{-\gamma(E)} e^{-c(E)\theta} dE, \tag{4.15}$$

where $f_{\rm EEF,10}(E)$ is the encircled energy fraction at $10''$ and is given in the CPOG for various energies, and the denominator is defined as

$$f_{10}(E, \theta) \equiv \int_{10}^{\theta} 2\pi\theta \left[\frac{\theta}{10}\right]^{-\gamma(E)} e^{-c(E)\theta} d\theta, \tag{4.16}$$

where the units of angle are arcsec. The denominator of eq. (4.15) is simply a normalization; $\frac{-\gamma(E)}{c(E)}$ is the inflection point of the power law times exponential function. The coefficients $\gamma(E)$ and $c(E)$ were measured in 1 keV bands by Gaetz (2004) using observations of Her X-1. Integration was performed by interpolating the values of $f_{\rm EEF,10}(E)$, $\gamma(E)$, and $c(E)$ to form a nearly continuous grid.

4.3 Geometric Distance Determination using Type I X-ray Bursts

4.3.1 Introduction

In principle, any type of variability can be used to determine the distance to a variable X-ray source. It is clear, however, that larger amplitude variability will provide a signal that is easier to detect. In this dissertation, two types of variability are examined in terms of their ability to constrain source distance. In this section, Monte Carlo simulations are used to estimate the potential distance accuracy using type I X-ray bursts as distance indicators. In § 4.4, the distance to the eclipsing HMXB Cen X-3 is determined.

Type I X-ray bursts potentially provide a delayed signature in the halo that can be used to measure the distance to variable X-ray sources with a method proposed by TS73, prior to the detection of the first X-ray halo around GX 339-4 by *Einstein* (Rolf 1983). The TS73 method is based on the phenomenon that grain-scattered photons from an X-ray source travel along slightly longer paths to the telescope than the direct, unscattered photons. Temporal variations in the intensity are therefore delayed and smeared when they appear in the X-ray halo. Using the single scattering approximation, it is possible to predict the delayed light curve as a function of halo angle, energy, and distance to an accuracy that is limited by knowledge of the distribution of dust along the line of sight and by the accuracy of the interstellar grain model. Hu et al. (2004) developed a similar method to measure distances with X-ray halo variability using the frequency domain.

The feasibility of the TS73 distance measurement method has been demonstrated by Predehl et al. (2000), who derived a distance of 9^{+4}_{-2} kpc to Cyg X-3 using the source's quasi-sinusoidal variability. In this section, I examine the applicability of the TS73 method to the abrupt increase in flux provided by type I X-ray bursts, which result from unstable thermonuclear ignition of accreted material on the surface of the neutron star. Sharp and temporary intensity changes, such as that produced by type I bursts or gamma-ray bursts (GRBs), produce a qualitatively different response in the X-ray halo than the response from smooth intensity variations like those of Cyg X-3. For example,

consider a smooth change in point source flux over an hour or so. Eventually the halo brightness will reach a new base level corresponding to the new point source intensity, and information on the source distance and dust distribution is contained in the rate of response and the resulting phase shift of the light curve. With X-ray bursts a new base level is not obtained; rather, the burst appears as a slight and temporary increase in halo flux after a time delay that depends on the scattering geometry. The intrinsically small signal-to-noise (S/N) ratio provided by bursts makes their potential application as distance indicators particularly difficult, requiring the physical parameters governing the delayed light curve in the X-ray halo be measured to a high degree of accuracy, and requiring careful treatment of the point spread function (PSF).

Gamma-ray bursts produce a similar halo light curve, although the problem is much simpler: With spectroscopic determination of the distances to host galaxies of GRBs, the degeneracy between the distribution of dust and the distance to the source is removed. This has been exploited by both the *Swift* and *XMM-Newton* observatories to determine the distances to Galactic interstellar dust clouds along various sightlines (Vaughan et al. 2004; Tiengo & Mereghetti 2006; Vaughan et al. 2006).

The physical parameters governing the delayed light curve in the halo are the peak and persistent flux, the spectral shape, the scattering optical depth, the scale time of the approximately exponential burst light curve, and the distribution and composition of interstellar dust along the line of sight.

4.3.2 Observations & Analysis

Here, I use a 29 ks *Chandra* observation of GX 13+1 (Obs. ID 2708). The observation uses the Advanced CCD Imaging Spectrometer (ACIS), with the source focused on the back-illuminated ACIS-S3 chip, and with the High Energy Transmission Grating (HETG) inserted in the optical path. GX 13+1 has a substantial halo (Smith et al. 2002), yet it is not a consistent type I burster (two bursts were observed in Sept. 1989; Matsuba et al. 1995). Nevertheless, this observation allows us to test the potential for using bursts as distance indicators. I accomplish this by measuring the GX 13+1 SBD, from which I predict the size of a delayed burst signal in the halo as a function of

delay time. Figure 4.3 shows the observed surface brightness distribution of GX 13+1 (diamonds with error bars) and the best-fit halo (see below). Statistical errors for the SBD are slightly less than 1% for $\theta > 10''$. Included in the figure is the contribution from the X-ray background (XRB) and the PSF, the treatment of which is in Chapter 2. Note the clear turnover in the observed SBD within the innermost $2''$–$3''$, resulting from the rejection of events due to pile-up. Pile-up is defined to be when more than one photon arrives in the same 3×3 pixel island in a single frame time. This can result in spectral hardening, "grade migration," or rejected events in the case of pulse saturation. According to the *Chandra* Proposers' Observatory Guide v8.0 (CPOG), a pile-up fraction[2] of 10% will very likely impact the observation. Smith et al. (2002) found the pile-up fraction reaches 10% when the count rate per pixel is 0.012 counts/frametime/pixel, which corresponds to halo angles less than about $3''$ in this observation. While pile-up in the GX 13+1 observation is most prevalent for halo angles $< 5''$, it likely affects the data to larger angles. Given the relatively large calibration uncertainties of the PSF (CPOG) and its increasing contribution nearer to the point source, I conservatively ignore halo angles less than $10''$ in our final analysis.

Spectral response matrices and auxiliary response files for GX 13+1 were created with the standard CIAO scripts.[3] The GX 13+1 source spectrum was fitted using XSPEC v11.3.2 with an absorbed blackbody plus a power law model, which allowed us to infer its hydrogen column density, measure the source flux, and predict X-ray halo spectra. The best-fit spectral parameters for this observation are $kT_{\rm bb} = 0.81 \pm 0.02$ keV, $\Gamma = 0.81^{+0.39}_{-0.52}$, and $N_{\rm H} = (2.46 \pm 0.04) \times 10^{22}$ cm^{-2}.

Figure 4.4a shows the measured point source spectrum, the inferred halo spectrum, and the single-scattered halo spectrum for GX 13+1. For an arbitrary energy range, the SBD as observed by *Chandra* (minus the PSF contribution) can be obtained from

$$C_{\rm halo}(\Delta E, \theta) = \int_{E_1}^{E_2} F_X(E) \left[e^{\tau_{\rm sca}(E)} - 1 \right] g_\rho(E, \theta) A_{\rm eff}(E, \theta) dE. \qquad (4.17)$$

[2]The ratio of the number of detected events that consist of more than one photon to the total number of detected events.

[3]see http://cxc.harvard.edu/ciao/

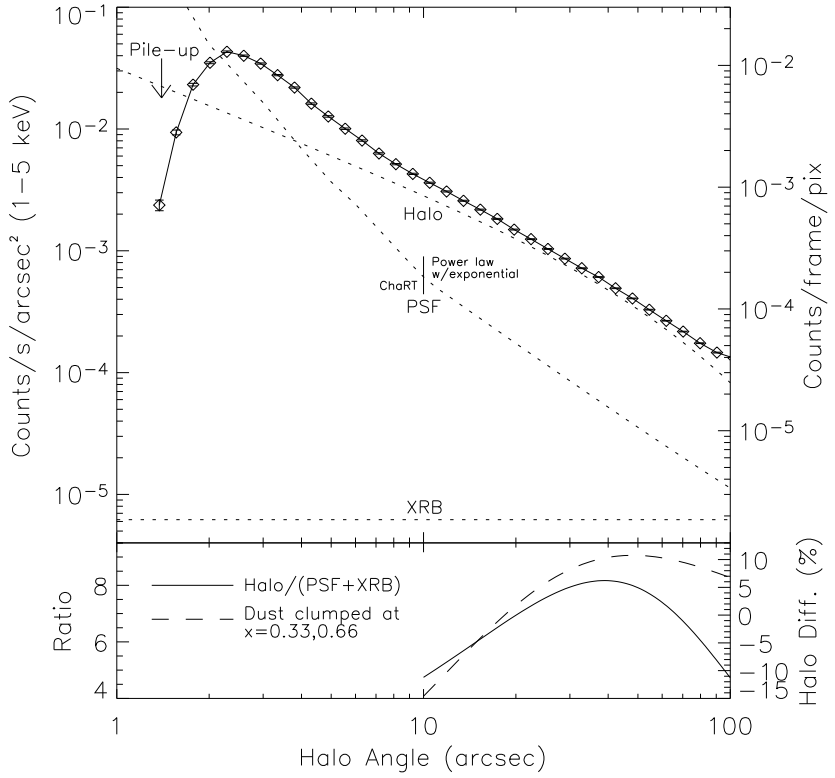

Figure 4.3: Surface brightness distribution of GX 13+1 (diamonds with error bars). The halo profile assumes uniformly distributed dust. The best-fit column density for $10''$–$100''$ is $N_{\rm H} = (2.75 \pm 0.06) \times 10^{22}$ cm^{-2}, corresponding to $\tau_{\rm sca}(1\ {\rm keV}) \approx 1.4$ using the WD01 grain model. For halo angles less than $10''$ the PSF is modeled using ChaRT, and for halo angles greater than $10''$ the PSF is modeled using a power law with an exponential term, using coefficients from Gaetz (2004). The pile-up fraction reaches 10% at about 0.012 counts/frametime/pix (Smith et al. 2002), corresponding to $\theta_{\rm h} < 3''$. The lower panel shows the ratio of the halo flux to the sum of the PSF and background fluxes (solid curve), and the fractional difference in the halo contribution to the SBD assuming half of the dust is uniformly distributed, and half is divided into two clumps at $x = 0.33$ and $x = 0.66$ (dashed curve).

By removing the fractional halo density from eq. (4.17), equivalent to integrating over all halo angles, the integrated counts spectrum is obtained (Fig. 4.4b and Fig. 4.4c).

The scattering optical depth to GX 13+1 was found by matching the observed SBD to that produced by the sum of eqs. (4.17) and (4.15) and the measured XRB (see Fig. 4.3). Note, however, that the use of eq. (4.17) assumes photons scattered two or more times produce the same halo SBD as singly-scattered photons, although multiply-scattered photons tend to produce somewhat broader halo profiles (Mathis & Lee 1991). The best-fit hydrogen column density leading to the observed halo is $(2.75 \pm 0.06) \times 10^{22}$ cm^{-2} (assuming a 20% [10%] uncertainty in the PSF [XRB] contribution), corresponding to $\tau_{\rm sca}(1\ {\rm keV}) \approx 1.4$ using the WD01 interstellar grain model, while the best-fit column density using the a blackbody plus power law model is $N_{\rm H} = (2.46 \pm 0.04) \times 10^{22}$ cm^{-2}. The 8–14% difference could be attributed to an incorrect assumption of uniformly distributed dust, to an inaccurate grain model, to the assumption that the SBDs for singly- and multiply-scattered photons are the same, or perhaps the gas-to-dust ratio along the sightline differs from the Galactic mean.

Finally, the measured halo SBD can also be used to constrain the distribution of dust along the line of sight by applying eq. (4.17) for various dust distributions. In the bottom panel of Fig. 4.3 I show the fractional difference in the halo contribution to the SBD assuming half of the dust is uniformly distributed, and half is divided into two clumps at $x = 0.33$ and $x = 0.66$ (approximated as Gaussians with $\sigma = 0.1$). The statistical errors in the SBD are much smaller than the fractional difference due to different distributions.

4.3.3 Delayed Burst Light Curves in the Halo

In order to be able to clearly observe the delayed pulse of radiation from type I X-ray bursts in the X-ray halo, the product of the source flux and scattering optical depth must be large enough to provide adequate statistics despite smearing of the delayed burst photons over many kiloseconds. A burst light curve is shown by Thompson et al. (2005, see Fig. 1) for Ginga (GS) 1826-238, and can be well-approximated by an exponential with e-folding time $t_{\rm b} \approx 60$ s. In general, burst decays are shorter at higher photon

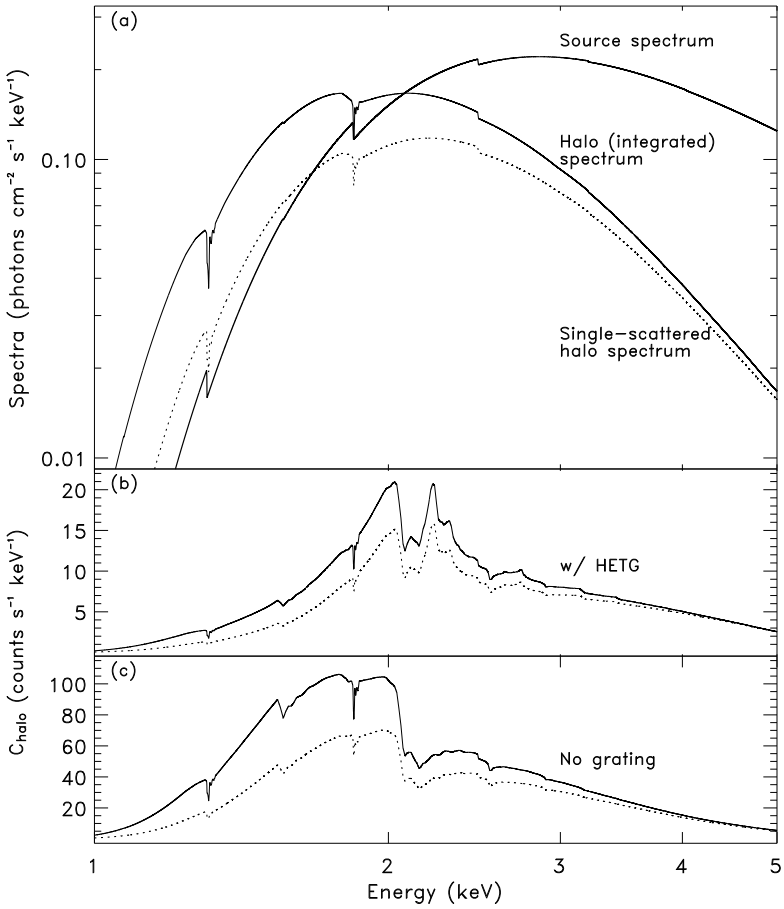

Figure 4.4: (*a*) Best-fit spectral model for GX 13+1 (bold solid curve), the halo spectrum integrated over all halo angles (solid curve), and the single-scattered halo spectrum (dotted curve), using the WD01 interstellar grain model. (*b*)-(*c*) The predicted counts spectra, obtained by multiplying the halo spectra by the *Chandra* zeroth-order effective areas for grating and non-grating observations. The decrease in effective area with off-axis angle has been ignored. For $\theta < 100''$ and $E < 5$ keV, the decrease in area is only $\sim$1%.

energies due to a softening of the burst spectrum during the decay, but I treat $t_{\rm b}$ as energy-independent for simplicity. The 60 s burst scale time for GS 1826-238 is relatively long; in fact, the majority of type I bursters have scale times less than 20 s (see Fig. 4, Cornelisse et al. 2003). Unfortunately, the amount of dust towards GS 1826-238 is too low to apply the TS73 method, with $N_{\rm H} \approx 1.9 \times 10^{21}$ cm^{-2} (Dickey & Lockman 1990) implying $\tau_{\rm sca} \sim 0.05$ at 1 keV (Predehl & Schmitt 1995).

The small size of the expected signal from a type I X-ray burst is immediately apparent considering that approximately $(F_{\rm peak} - F_{\rm persistent})\tau_{\rm sca} t_b$ singly-scattered photons cm^{-2} keV^{-1} are expected over all halo angles and delay times for an X-ray burst approximated by an exponential. At halo angles larger than $100''$, the burst photons are smeared to such a large extent that any signature of the delayed burst is hard to observe.

The delayed burst light curve (in units of counts/s) for singly-scattered photons for a given range of halo angles and energies, and for a given dust distribution and source distance is

$$B(t_{\rm d}, \Delta E, \Delta\theta) = \int_{E_1}^{E_2}\int_{\theta_1}^{\theta_2} \tilde{B}(t_{\rm d}, E, \theta)\langle F_{X,{\rm b}}(E)\rangle \tau_{\rm sca}(E) A_{\rm eff}(E,\theta) g_\rho(E,\theta) 2\pi\theta d\theta dE, \quad (4.18)$$

where $\langle F_{X,{\rm b}}(E)\rangle$ is the average burst spectrum (with the persistent spectrum subtracted out), and requiring eq. (4.13) to be normalized, which is obtained naturally if $I(t)$ is normalized, i.e. $I(t) = t_{\rm b}^{-1} \exp(-t/t_{\rm b})$, for a type I burst approximated by an exponential. Figure 4.5 shows the normalized delayed light curves for X-ray bursts with $t_{\rm b} = 60$ s and $E = 2$ keV for sources at three distances with uniformly distributed dust. The ratio of the peak to persistent flux was chosen to be 7, similar to that of GS 1826-238. This ratio is fairly typical of brighter bursters (low persistent emission sources have much higher ratios; Cornelisse et al 2002), although the typical range is rather wide. A cartoon of the corresponding annular regions is presented in Figure 4.6. To facilitate interpretation of Fig. 4.5, consider the case of a unit annulus centered on $5''$ and a 4 kpc source distance (top panel, dotted curve): About 12% of the total burst fluence would be expected in a 100 s bin centered at a time delay of 100 s. Small angles are shown, though the general trend of a smaller signal at larger angles due to greater smearing is clear.

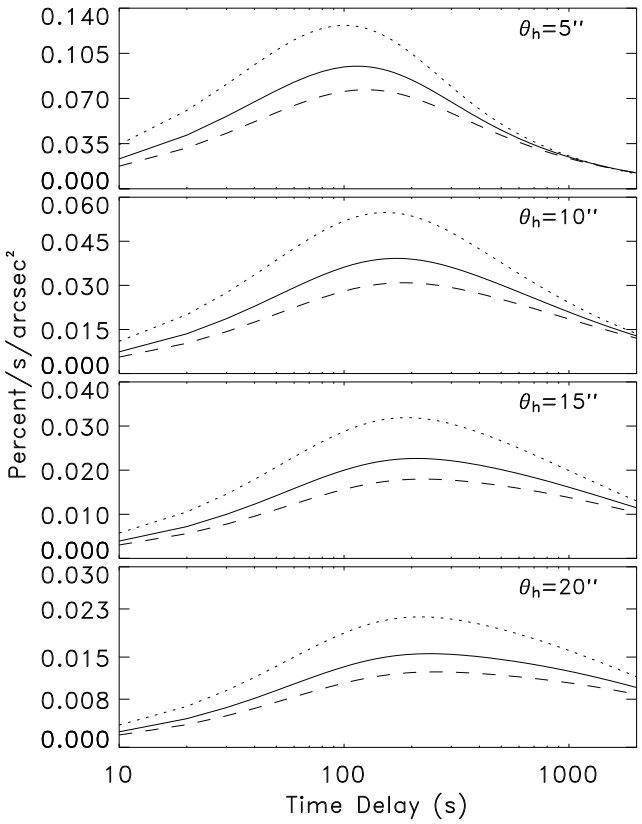

Figure 4.5: Predicted delayed burst light curves for small halo angles (top to bottom: $\theta \equiv \theta_{\rm h} = [5, 10, 15, 20]$ arcsec), and for three source distances (dotted: 4 kpc, solid: 6 kpc, dashed: 8 kpc) assuming uniformly distributed dust, 2 keV photons, and $t_{\rm b} = 60$ s. The y-axis units are the percent of total burst photons appearing per second per unit solid angle.

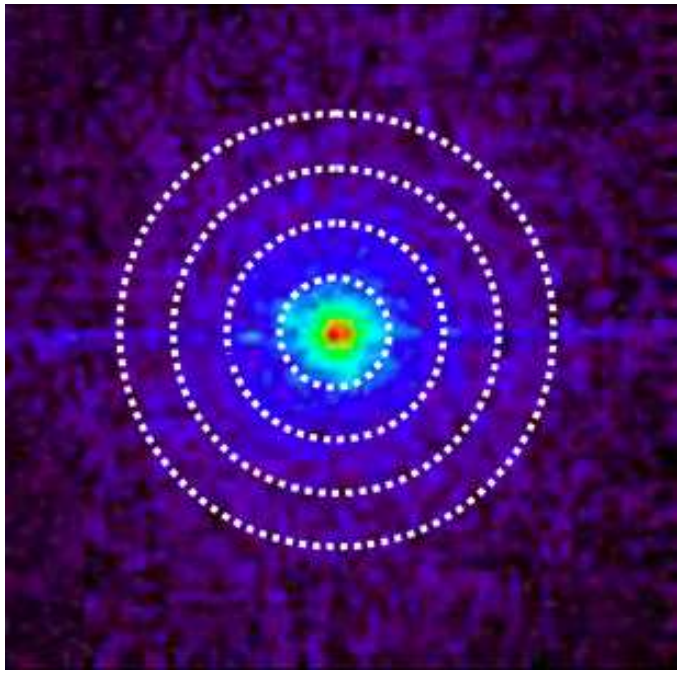

Figure 4.6: Cartoon of the annular regions corresponding to Fig. 4.5.

4.3.4 Simulating Light Curves

Maximizing the Signal-to-Noise Ratio

The feasibility of using type I bursts as distance indicators was tested by simulating burst light curves in the halo, including both statistical and systematic errors, and finding the deviation of the best-fit distances. Systematic errors include uncertainties in the calibration of the PSF, and in the measurements of the optical depth, the peak and persistent fluxes, and the scale time of the burst. Due to the small size of the expected delayed burst signal, it is essential to maximize the S/N ratio (where the signal refers to counts due to the burst and the noise refers to the total Poisson noise) by binning the data in a favorable configuration for the simulations. At higher energies, for example, the dust-scattered halo is rapidly decreasing while the PSF contribution is increasing. Not only does this binning depend on the spectrum and optical depth of the source, the observing telescope's effective area and PSF, and the distribution and composition of interstellar dust, but also on the time after the onset of the burst. Due to the energy dependence of the differential scattering cross section, harder photons appear at smaller

time delays and halo angles relative to softer photons. Our goal was therefore to find an effective binning of the data averaged throughout the dynamical time period of the delayed burst evolution, meaning the period when the delayed light curves for sources at different distances differ by more than a few percent. For uniformly distributed dust, the dynamical period is isolated to time delays less than ∼10 ks because the delayed burst light curves for sources at different distances converge at longer time delays (see Fig. 4.5). The time-averaged optimal binning was obtained by selecting an energy grid from 1-6 keV with 0.5 keV bins, and a radial grid from 10″–160″[4] with 10″ bins. Because the cross section for X-rays scattering off of interstellar grains is proportional to $\sim E^{-2}$, and because the smearing of the burst signal increases dramatically with angle ($\delta t \propto \theta^2$, see Fig. 4.5), the lower bounds of the trial binning were fixed to 1 keV and 10″. Using 200 s time bins, trial combinations of angle and energy were selected. The included photon energies were increased incrementally, and for each energy increment the included range of halo angles was also increased incrementally. For each trial binning, the time-averaged S/N ratio was calculated. I find that averaged throughout the dynamical portion of the delayed burst, the optimal annular region is about 10″–50″ and the optimal energy is from about 1–5 keV for a source with $\tau_{\rm sca}(1\ {\rm keV}) \approx 1.4$ and the spectrum of GX 13+1 observed with *Chandra*'s effective area and PSF. This range of halo angles is not surprising considering the ratio plot in the lower panel of Fig. 4.3, although the reader should note that I did not optimize the plotted ratio but rather the S/N ratio.

Potential Accuracy using Type I Bursts

The best-fit distance to the simulated light curves was measured using χ^2-minimization. A five-dimensional array composed of the predicted flux as a function of delay time for an arbitrary distance, halo angle, and energy was created. The energy and angle degrees of freedom were removed by integrating over the predicted single-scattered burst halo spectrum for GX 13+1, and the angles 10″–50″ assuming an azimuthally-symmetric halo profile. The persistent halo was treated as a constant. The value of χ^2 was then calculated by comparing predicted light curves for sources at distances in 0.01

[4]Halo angles larger than 160″ were not analyzed due to the presence of a diffuse "transfer swath" caused by the diffracted spectrum, analogous to the so-called "transfer streak" centered on the source.

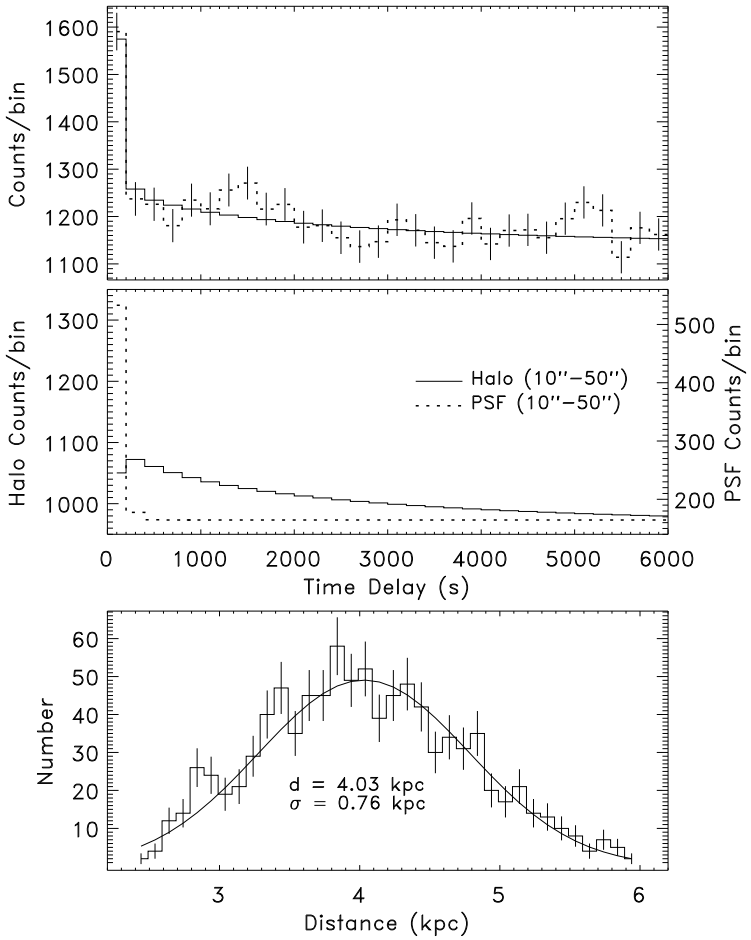

Figure 4.7: *Top:* Predicted 10″–50″ halo light curve and a sample simulated light curve after the onset of a type I X-ray burst for a source at 4 kpc, assuming only statistical errors. *Middle:* Relative contributions to the predicted light curve. *Bottom:* Histogram (0.1 kpc bins) of the best-fit distances for one thousand simulated light curves, and the Gaussian fit to the distribution.

kpc increments to each trial of simulated data; the best-fit distance for each simulated light curve had the smallest fit statistic. One thousand trial light curves were used in each simulation.

I first examined the potential accuracy of a distance measurement using a *Chandra* grating observation assuming the only uncertainties are due to Poisson noise. By simulating burst light curves for source distances from 3 kpc to 11 kpc in 0.5 kpc increments, I find that as the source distance becomes larger, the distribution of best-fit distances becomes increasingly distorted from a Gaussian due to a slight tail for larger source distances (forming a Gamma-like probability density function). This makes sense because the differences in the delayed light curves become smaller at larger distances. Therefore, a negative statistical error (fewer counts than the average) will overestimate the distance more than an equal positive statistical error will underestimate the distance. Figure 4.7 shows predicted and simulated $10''$–$50''$ halo light curves, the relative contributions of the halo and the PSF, and a histogram of the best-fit distances for a source distance of 4 kpc. I find the fractional error on the inferred distance to a source 4 kpc away is $^{+22}_{-17}\%$ for a single burst (68% confidence). At 6 kpc and 8 kpc, the errors are $^{+29}_{-19}\%$ and $^{+40}_{-21}\%$ respectively. The positive and negative errors increase approximately linearly with distance. For two bursts the uncertainty is about 15%, and for five bursts the uncertainty is 10%.

For a source with a smaller optical depth to scattering than GX 13+1, e.g. $\tau_{\rm sca}(1\ {\rm keV}) \approx 0.5$, roughly five aligned and summed bursts would be required to obtain similar accuracy. By including realistic systematic uncertainties of 10% for the scattering optical depth, 20% for the PSF contribution, and 5% on the flux and scale time of the burst, the potential accuracy decreases by only $\sim$10% for distances between 3 kpc and 11 kpc. Future large area observatories with adequate spatial resolution (e.g., *XEUS* and *Constellation-X*) will effectively minimize the Poisson noise, in which case the distance measurement accuracy is limited by systematics. By simulating data with systematic errors only (which is also equivalent to stacking many bursts), the uncertainty in the distance measurement is 7% at 3 kpc, increasing approximately linearly with distance to 12% at 11 kpc .

The simulations above assumed a constant persistent halo, but due to the nature of the accretion processes in LMXBs, there is likely to be source variability on all time scales. With reliable flux measurements (from a grating observation), handling the PSF is straightforward because its contribution is essentially a constant fraction of the point source flux (see eq. [4.15]), and there is no time delay associated with it. Likewise, halo variability can be handled by including additional terms in the light curve $I(t)$ in eq. (4.13), and appropriately changing the normalization. As a worst case scenario, however, assume that variability exists on 200 s scales, yet I still assume the persistent halo is constant in the calculation of the delayed light curve. To test the effect of this assumption, I calculated delayed light curves for halo angles of $10''$ to $50''$ in $10''$ increments for time-averaged constant source light curves (on a scale much longer than 200 s) but with stochastic variability on 200 s scales with rms amplitudes of 10%, 20%, 30%, and 40%. Because this variability is spread out over many kiloseconds due to scattering along the line of sight, the rms amplitude is smaller in the halo. Interestingly, the halo rms amplitudes seem to be only weakly dependent on the halo angle, with corresponding rms amplitudes are ∼2%, 4%, 5–7%, and 6–9% respectively. These percentages were added to the statistical and systematic errors for the persistent halo contribution in our simulations. For the worst case of 40% point source variability, I find the inferred distance errors increases by about 15% for a grating observation, e.g., for a 6 kpc source distance and a simulation including systematics, the error increases from about 30% to 35%. This can also account for dust distributions that are overall uniform, but patchy on scales $x \ll 1$.

A non-grating observation with *Chandra* increases the effective area and signal by about a factor of 4 (see Fig. 4.4), but the reduction in Poisson noise is offset by larger systematic uncertainties in the flux measurements and the burst scale time. Without the dispersed grating counts, one is required to extract spectral and flux characteristics from the source transfer streak (e.g., Smith et al. 2002, Clark 2004), generally a much coarser and poorly calibrated method. More importantly perhaps, a non-grating observation would significantly increase the extent of pile-up, forcing one to look at larger halo angles where the evolution of the delayed burst occurs on longer time scales.

4.3.5 Conclusions

I studied the applicability of the TS73 method to the delayed signature of type I X-ray bursts in the halo. The signal produced by an X-ray burst in the halo is invariably small. Regular type I bursts last ∼5–150 s, but the scattering geometry, which governs the distribution of time delays, assures that these photons will be spread out over time delays greater than ∼10 ks for uniformly distributed dust. Nevertheless, if the physical parameters governing the light curve of the burst in the halo are well-known, the statistics provided by *Chandra*'s effective area can yield a distance measurement to about 25% accuracy with a single burst. By stacking many bursts, systematic errors likely limit the potential accuracy to roughly 10%. Although non-grating observations have improved statistics due to larger effective area, pile-up precludes accurate flux measurements (although the transfer streak can be used) and require the use of larger halo angles, decreasing the S/N as the evolution of the delayed burst light curve occurs on longer time scales. Source variability on 200 s scales with 40% rms amplitude increase the distance uncertainty by ∼15%. The quoted errors assume very favorable source characteristics: (1) a bright source with a flux ∼0.6 photons/cm^2/s during persistent emission from 1–5 keV; (2) a large optical depth to scattering ($\tau_{\rm sca}$ ≈1.4 at 1 keV), both of which increase the S/N ratio of the delayed burst light curve in the halo; (3) a burst with large total fluence, characterized by $t_{\rm b} = 60$ s and $F_{\rm peak}/F_{\rm persistent} = 7$. In the general case, the uncertainty in the inferred distance will be somewhat larger. Finally, note that the interstellar grain model represents an additional source of systematic error.

In many cases the distance to Galactic X-ray sources has been estimated using other methods, e.g., using the requirement that the inferred peak luminosity is sub-Eddington, or using optical photometry of the (low-mass) binary companion, and the potential accuracy of the TS73 method applied to bursters may only provide additional distance constraints for a small fraction of all type I bursters. Moreover, if the distribution of dust differs significantly from the assumed or inferred distribution, the distance measurement can be unreliable. A future observatory with a larger effective area and arcsec resolution would provide superior statistics, however, making the TS73 method an attractive means of measuring the distance to a larger subset of the population of

absorbed X-ray bursters.

4.4 The X-ray Halo of Cen X-3

4.4.1 Introduction

Cen X-3 is one of the brightest accreting X-ray pulsars, and it is one of the six pulsars in which the observation of eclipses has permitted the determination of all orbital and stellar parameters. The rotation period of the pulsar is 4.8 s, and the binary orbital period is 2.1 days. The inclination of the orbital plane and the mass of the neutron star have been estimated to be $i \sim 70^\circ$ and $M = 1.21 \pm 0.21\ M_\odot$ (Ash et al. 1999). The optical counterpart of Cen X-3 has been identified as an early type star of radius $R \sim 12\ R_\odot$ and mass $M \sim 20\ M_\odot$ (Rappaport & Joss 1983). Accretion in the system probably occurs via an accretion disk (Bildsten 1997; Takeshima et al. 1992), although the mass transfer mechanism probably includes an X-ray excited wind (Day & Stevens 1993).

Although well-studied, the distance to Cen X-3 remains uncertain. Using a B0 II stellar classification model, an 8 kpc distance to Cen X-3 was obtained (Krzemiński 1974), however, subsequent work indicated that the supergiant primary was of type O6-8 III (Hutchings et al. 1979). Day & Tennant (1991) observed soft emission during two eclipses using *EXOSAT* and attributed it to the dust-scattered halo, from which they derived a distance of 5.4 ± 0.3 kpc. Discrepancies of $\sim$2.5 kpc in distance estimates to Cen X-3 lead to nearly a factor of two difference in the inferred optical and X-ray luminosities.

Cen X-3 ($l = 292.09^\circ, b = 0.34^\circ$) is particularly suited for X-ray halo studies. The source is usually very bright, and the interstellar hydrogen column density along the line of sight is 1.20×10^{22} cm^{-2} (Dickey & Lockman 1990), implying a large enough optical depth to result in an appreciable halo (Predehl & Schmitt 1995). Moreover, the eclipsing nature of the binary system is advantageous because it should produce the largest fraction of variability in the X-ray halo, which makes a geometric distance measurement more direct.

4.4.2 Observations & Data Reduction

In this section, I use two *Chandra*/HETG observations of Cen X-3 (ObsIDs 1943 & 7511). Although the use of the grating reduces the zeroth-order image count rate by about a factor of 3, the dispersed spectrum provides accurate measurements of the source flux and spectrum, which is necessary to accurately model the characteristics of the X-ray halo and the PSF. One of the observations (ObsID 1943) began at MJD 51908.01 and lasted for 45 ks, corresponding to $\Phi_{\rm orb} \approx 0.38 - 0.63$, where determination of the orbital phases was accomplished using the mid-eclipse ephemeris from Burderi et al. (2000), and the orbital period and evolution ($\dot{P}_{\rm orb}/P_{\rm orb} = -(1.738 \pm 0.004) \times 10^{-6}$ yr^{-1}) from Nagase et al. (1992). A dip in the flux was observed at about $\Phi_{\rm orb} \approx 0.57$, so I ignored data after this time to simplify analysis by removing any time dependence (eq. 4.4). X-ray halo measurements from this observation were used to determine the dust distribution along the line of sight. The other observation of Cen X-3 (ObsID 7511), which resulted from a successful observing proposal with the primary goal of geometrically measuring the distance to the system, took place during an egress from eclipse. The 40 ks observation began at MJD 54355.46 ($\Phi_{\rm orb} \approx 0.08 - 0.30$). The preceding mid-eclipse epoch was calculated to be MJD 54355.313 ± 0.007. Figure 4.8 (top-left panel, solid curve) shows the *Chandra*/HETG light curve during the eclipse egress observation. I also present an *RXTE*/PCA light curve for comparison. Clearly, the *Chandra* observation occurred during a relatively lower flux state, leading to a more gradual increase in flux coming out of eclipse as compared the PCA observation. Priedhorsky & Terrell (1983) discussed the aperiodic 120–165 day timescale between the different flux states, and Clark et al. (1988) studied how the stellar wind and the shape of the egress light curves are affected by the different states.

Data analysis was performed using the standard tools of the Chandra Interactive Analysis of Observations (CIAO) software version 4.0 and Calibration Database (CALDB) version 3.4.3. A single first-order Medium Energy Grating (MEG) and High Energy Grating (HEG) spectrum was extracted for the plateau phase observation (ObsID 1943). For the eclipse egress observation (ObsID 7511), ten 3968 s first-order MEG/HEG spectra were extracted to model the evolution of the point source spectrum. Spectral models were

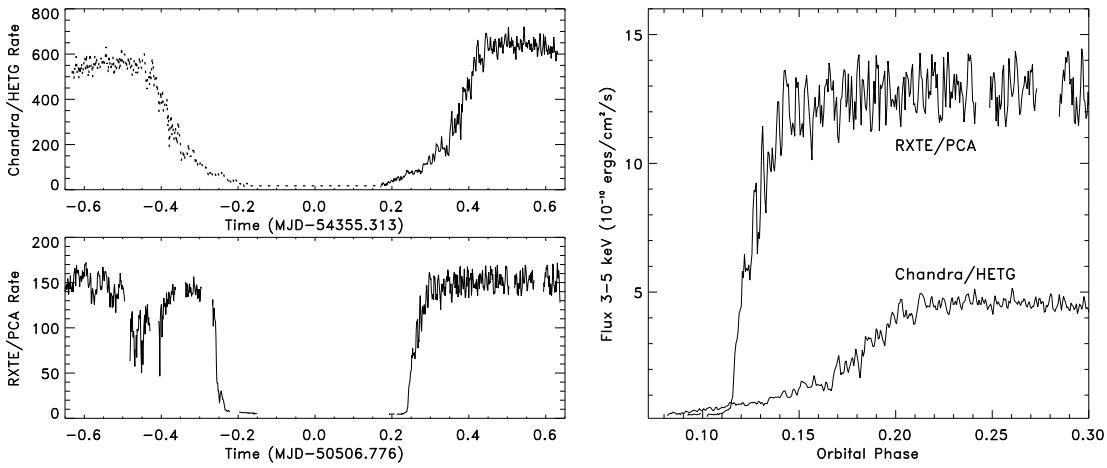

Figure 4.8: Comparison of the eclipses and flux states in count rates (left panels) and fluxes (right panel) from 3–5 keV between the *Chandra* eclipse egress observation (ObsID 7511) and an *RXTE*/PCA observation. No data was obtained for the *Chandra* eclipse ingress (dotted curve). The ingress is modelled as the mirror image of the egress (multiplied by 0.87, see § 4.4.4).

fit to each spectrum using XSPEC version 11.3, and fluxes (in units of [photons/cm^2/s]) were measured in 15 energy bands of 200 eV width from 2–5 keV. Finer time resolution on the flux evolution was obtained by comparing the average HETG count rates in each time range and energy band to the relative count rates in smaller 100 s time bins.

Separate X-ray halo images and exposure maps were extracted in 200 eV bands from 2–5 keV, from which I obtained exposure-corrected surface brightness distributions using 40 logarithmically-spaced annular regions surrounding the source. For the plateau phase observation, a single exposure map was created for each energy band. On the other hand, accurate measurements of the evolution of the halo flux in each energy band during the eclipse egress observation required the use of separate exposure maps (due to the dither of the telescope) using 500 s bins (1200 exposure maps in total). Due to issues with the diffracted HETG photons confusing the background analysis (HETG photons create a diffuse "transfer swath" analogous to the "transfer streak" in the zeroth-order image), I did not use halo angles greater than $110''$. The surface brightness distributions were divided by the flux measurements in each band to produce images in units of flux fraction per square arcsecond. Halo angles smaller than about $3''$ are affected by pile-up

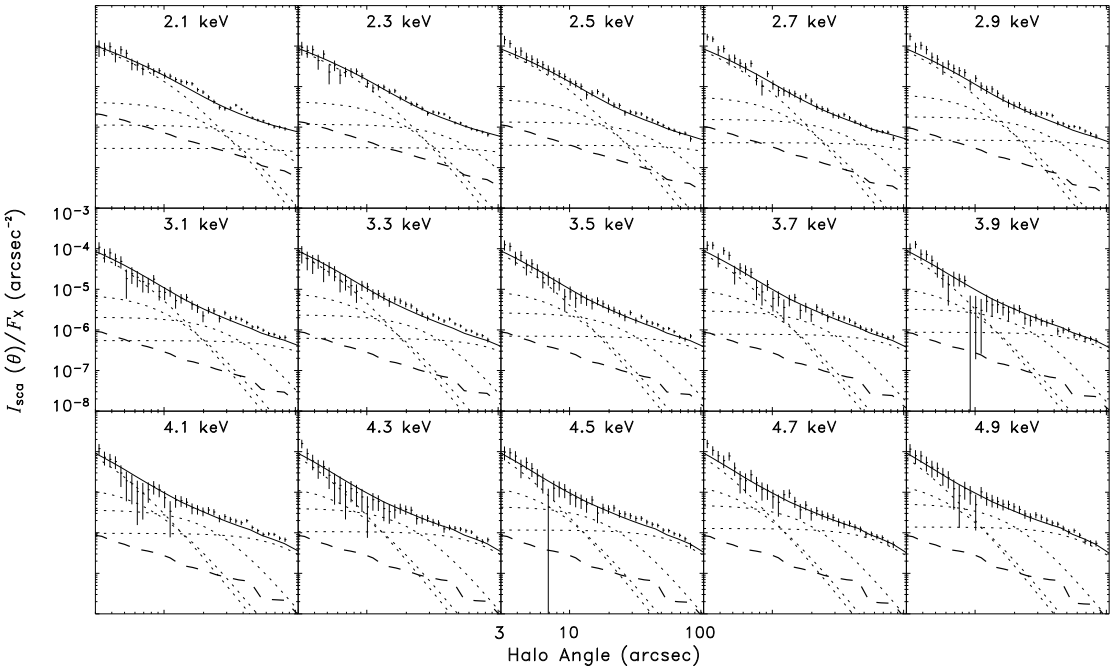

Figure 4.9: Cen X-3 halo measurements and best-fit model halos (§ 4.4.3) in fifteen 200 eV bands from 2–5 keV in units of source flux per square arcsecond. The dotted curves show the contribution to the halo from the individual single-scattered ($\Delta x = 0.05$) clouds (see Fig. 4.10 for the cloud locations), the dashed curves show the halo contribution from photons scattered twice, and the solid curves show the sum of the single- and double-scattered halos ($\chi^2_\nu = 1.05$, 502 d.o.f.). (Third- and higher-order scatterings are nearly negligible and are not included in the model.) The center of the energy band is labeled at the top of each panel.

and ignored. To minimize concerns due to multiply-scattered photons, I excluded energies below 2 keV in each observation.

In § 4.2, I parametrized the PSF as the fraction of the point source flux comprising the PSF as a function of halo angle. Although the observed surface brightness distributions represent the convolution of the PSF and the X-ray halo, in this analysis I treat it as the sum. This is acceptable because I restrict the investigation to angular scales that are much larger than the $\sim 0.5''$ resolution of the telescope mirrors. The PSF contribution in each energy band is simply subtracted from the observed surface brightness distribution. The resulting X-ray halos for each energy band are shown in Figure 4.9. The fitted halo components are discussed below.

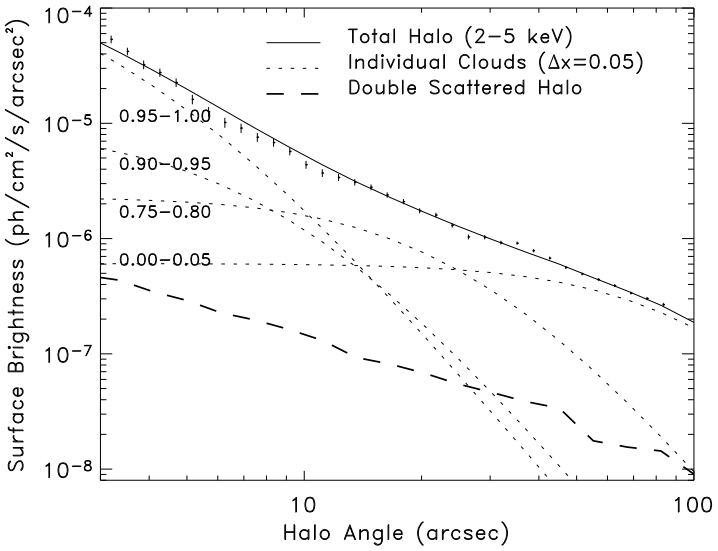

Figure 4.10: Surface brightness distribution (with PSF subtracted) from 2–5 keV. As in Fig. 4.9, the dotted curves show the contribution to the halo from the individual ($\Delta x = 0.05$) clouds and the dashed curves show the halo contribution from photons scattered twice. The location of the dust for each single-scattered halo component is labelled at left (also see Fig. 4.12).

4.4.3 Determining the Dust Distribution

In order to obtain the dust distribution to Cen X-3, I used the plateau phase *Chandra* observation. I *assumed* the halo had sufficient time to respond to the eclipse egress, which based on the orbital ephemeris occurred ∼30 ks earlier. Once I established a dust distribution, I checked whether or not the assumption was acceptable. First, I created separate single-scattered X-ray halo profiles for twenty step-function dust distributions of width $\Delta x = 0.05$ (hereafter referred to as "clouds"), spanning the entire line of sight, i.e., 0.00 to 0.05, 0.05 to 0.10, and so on, for each energy band. By summing the twenty profiles with equal weighting, one could obtain the single-scattered X-ray halo for dust distributed uniformly along the line of sight. The normalization of each cloud (a_x), which is proportional to the contribution to the total scattering optical depth (due to the normalization $\int \tilde{I}_1(\theta) 2\pi\theta d\theta = 1$), was allowed to vary freely. The initial fit function at

each energy is

$$\frac{I_{\rm sca}(\theta)}{F_{\rm X}} = \sum_{x=0}^{19} a_x \tilde{I}_1^x(\theta), \tag{4.19}$$

where

$$\tilde{I}_1^x(\theta) \approx \int_{0.05x}^{0.05(x+1)} \frac{1}{(1-x)^2} \frac{d\sigma}{d\Omega} dx. \tag{4.20}$$

Note that the superscript in $\tilde{I}_1^x$ is a label that indicates a position along the line of sight and is not an exponent. Using this method, the dimensionless dust density and scattering optical depth are simply

$$\tilde{\rho}(x) = \frac{a_x}{\sum a_x}, \ \sum a_x = \tau_{\rm sca}, \tag{4.21}$$

respectively. The halos for each energy band were fit simultaneously. For the initial fit, I used the energy scaling of the scattering optical depth from the WD01 interstellar grain model ($R_V = 3.1$); however, I found it to underpredict the halo flux at higher energies (or overpredict the flux at lower energies). I therefore allowed the energy scaling to also be a free parameter, although I required it to be a smooth function, i.e., $\tau_{\rm sca}(E) \propto (E - E_0)^{-\beta}$, where E_0 and β are fit parameters. Nevertheless, the angular dependence of the scattering at a particular energy still follows the functional form predicted by the WD01 model (see eq. [4.1]). The best-fit normalization of each cloud provided a preliminary dust distribution. Given the preliminary model, the X-ray halo for double-scattered photons was calculated ($I_2(\theta)$), included in the model as an additional term in eq. (4.19), and the normalization for each cloud was refit. This process was repeated in an iterative manner to coverage to the dust distribution whose single- and double-scattered X-ray halos accurately described the Cen X-3 halo. Third- and higher-order scatterings were ignored, but their contribution to the halo is negligible. The Cen X-3 X-ray halos in units of source flux for each energy and the best-fit halo models are presented in Figure 4.9, and the integrated (2–5 keV) surface brightness distribution is shown in Figure 4.10. Evidently, the 3″–100″ halo can be modeled using only four separate dust clouds (Fig. 4.10, dotted curves).

The energy dependence of the scattering optical depth is presented in Figure 4.11, showing the relatively brighter halo at higher energies as compared to the WD01 interstellar grain model predictions (see discussion). The Cyg X-1 and GX 13+1 points are

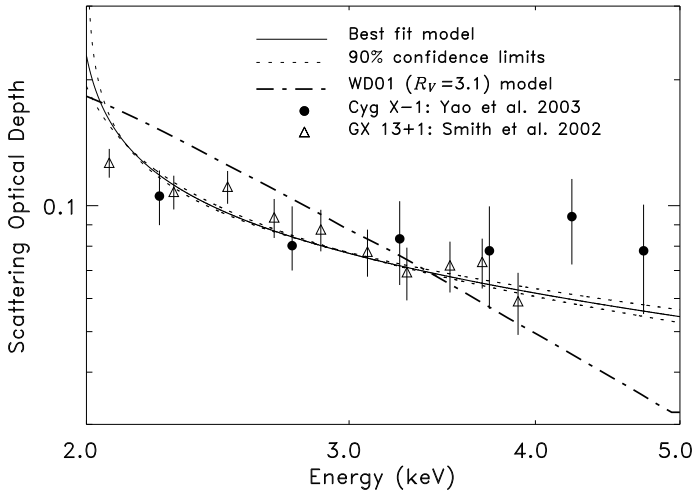

Figure 4.11: Best-fit scattering optical depth to Cen X-3 as a function of energy (solid curve). The empirical best-fit curve is described by $\tau_{\rm sca}(E) \propto (E - E_0)^{-\beta}$, where $E_0 \sim 1.96$ and $\beta \sim 0.32$. The optical depth predicted by the WD01 interstellar grain model ($R_V = 3.1$) is shown as a dash-dotted curve. The normalization for the WD01 model was chosen so that the areas under each curve are the same. Also included are Cyg X-1 data from Yao et al. (2003; filled circles) and GX 13+1 data from Smith et al. (2002; triangles) (see discussion). The normalizations for the Cyg X-1 and GX 13+1 data have been modified to more closely align the points with the empirical curve for Cen X-3. The data points from Yao et al. (2003) have been corrected assuming uniform dust, and the data points from Smith et al. (2002) have been corrected assuming the dust density is proportional to distance. See Draine (2003) for further details on the correction method.

the same data as presented in Fig. 11 of Draine (2003), who compared the optical depth calculated from the WD01 model to observations. Although Draine (2003) extended his comparison to other sources, only Cyg X-1 and GX 13+1 span the 2–5 keV energy range that I investigate for Cen X-3.

One of the primary goals of this work is to geometrically determine the distance to Cen X-3, therefore it is important to quantify the uncertainty in the dust distribution because this directly affects the size of the time delays of photons scattered along the line of sight. By fixing the double-scattered halo model to the one corresponding to the best-fit dust distribution, the single-parameter 90% confidence uncertainties in the contribution from each of the twenty clouds was calculated. In each case the lower limit on the cloud size was zero, i.e. no dust, simply because the clouds to either side of the

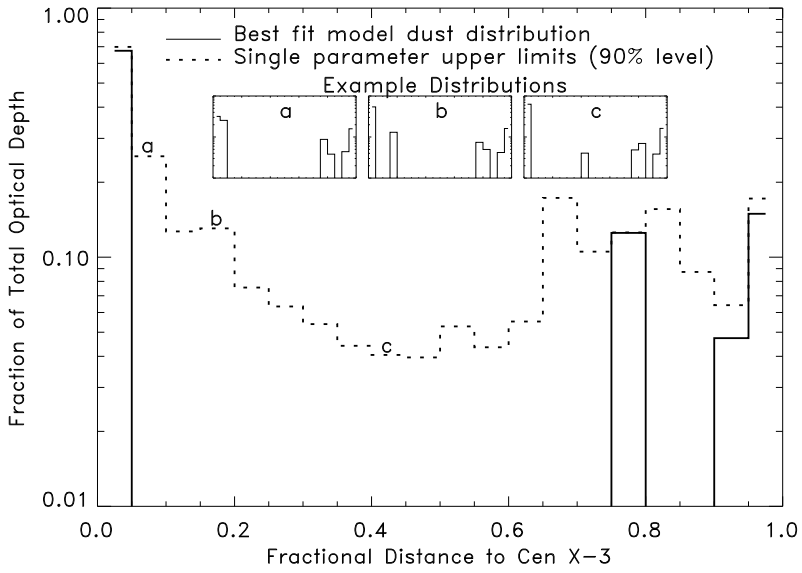

Figure 4.12: Best-fit model dust distribution to Cen X-3 (*solid histogram*). The majority of the dust is located near the Sun ($0.00 < x < 0.05$), and the other primary dust locations are at $x > 0.75$. Although the best-fit distribution accurately models the data ($\chi^2_\nu = 1.05$, 502 d.o.f.), the size of any individual dust cloud is not well-constrained (*dotted histogram*). The three small panels labeled a, b, and c (corresponding to the upper limits shown in the main panel) show examples of dust distributions that are also consistent with the data at the 90% confidence level.

cloud in question could produce a surface brightness distribution with a similar shape. On the other hand, the upper limits to the size of each cloud are constrained. Figure 4.12 shows the best-fit dust distribution towards Cen X-3 and the single-parameter upper limits for the size of each cloud. Three examples of different dust distributions that are also consistent with X-ray halo data are presented. The majority of the dust (≈70%) in each case is located at small fractional distances to Cen X-3. Note, however, that I do not have reliable data for halo angles less than about $3''$, so I am mostly insensitive to dust that produces centrally-peaked halos, i.e., dust very near the source ($x > 0.99$). Therefore, it is more accurate to consider the scattering optical depth in Fig. 4.11 as a lower limit.

It could be argued that lack of knowledge of the dust very near the source poses a problem for our distance determination. This is not the case: For an assumed distance of 8 kpc, the $\sim 0.5''$ angular resolution of the *Chandra* mirrors corresponds to approximately

4000 AU, which, based on the orbital parameters of the binary system, is more than 4 orders of magnitude larger than the semi-major axis of the orbit. Therefore, the point source flux already includes all of the effects due to scattering within the vicinity of binary system.

Considering the best-fit dust distribution, it is clear that the assumption that the halo during the plateau phase observation had responded to the preceding eclipse egress is not valid for all halo angles. As pointed out above, an estimate of the time Cen X-3 has been out of eclipse at the beginning of the observation is about 30 ks. The causally-connected regions of x vs. θ phase space for delay times less than 30 ks are shown in Figure 4.13 for three source distances, indicating that the assumption is invalid for large x and θ. Fortunately, the vast majority of the dust along the line of sight is located at $x < 0.05$ which presents no inconsistency, and the two clouds closest to the source ($0.90 < x$) dominate the halo at $\theta < 10''$ (see Fig. 4.10), where the halo angles are small enough to have responded to the previous eclipse egress. The only potential problem concerns the $x = [0.75, 0.80]$ dust cloud, which for $\theta > 30''$ have not had sufficient time to respond to source flux variability. However, the dust cloud at $x < 0.05$ also begins to dominate for sufficiently large halo angles, so I conclude that the assumption is reasonably valid.

4.4.4 Estimating the Source Distance

Because our goal is to use the Cen X-3 halo during the eclipse egress to measure the distance to the system, it is necessary to model the source flux history for a sufficiently long time period preceding the observation. I chose to model the flux history by first assuming the shape of the light curve during the eclipse ingress in each energy band is same as the shape during egress, but scaled to 87% of flux after egress (Fig. 4.8, top-left panel, dotted curve). It is widely known that the Cen X-3 flux decreases after $\Phi_{\rm orb} \sim 0.5$, and the scaling factor represents the average 2–10 keV flux change that was observed during two consecutive binary orbits by Suchy et al. (2008). So-called "pre-eclipse dips" are also commonly seen in Cen X-3 light curves (Fig. 4.8, lower-left panel), however, I did not include these features in our model. Second, for the 60 days prior to the observation

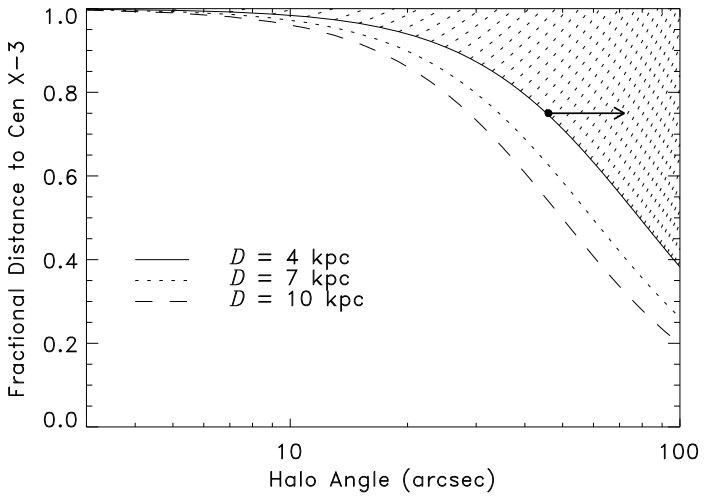

Figure 4.13: Phase space boundaries showing causally-connected regions for delay times less than 30 ks. The hatched regions of phase space have yet to respond to changes in the source flux 30 ks earlier (see eq. 4). For example, assuming a source distance of 4 kpc and dust at $x = 0.75$, for $\theta > 46''$ the halo has not yet responded to changes in the source flux 30 ks earlier (see point and arrow).

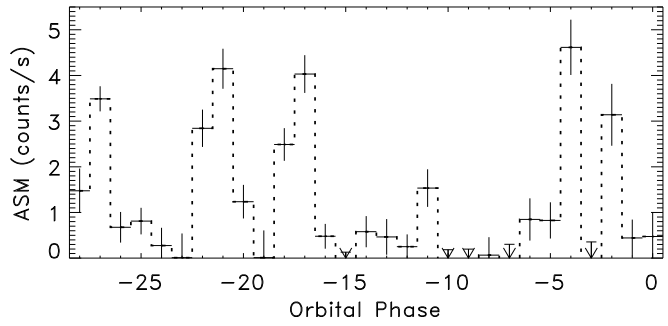

Figure 4.14: *RXTE*/ASM light curve of Cen X-3 for the 60 days (corresponding to $x = 0.98$ for $D = 8$ kpc and $\theta = 100''$ preceding the *Chandra* observation during eclipse egress. The long-term Cen X-3 light curve was modeled using the *Chandra* fluxes scaled by the ASM count rate. Orbital phase 0.0 corresponds to MJD 54355.31.

I modeled the flux history by multiplying the *Chandra* light curve (and modeled ingress) by the relative *RXTE*/ASM count rate at the time (linearly interpolating the ASM rates at intervening times). The ASM light curve for Cen X-3 is shown in Figure 4.14.

Admittedly, the modeled flux history is rather approximate. Not only have I ignored the pre-eclipse dips, but the assumption that the shape of the Cen X-3 light curve is independent of the absolute flux (the relative ASM count rates span $\sim$0.05$\times$ to 5$\times$ of the flux during *Chandra* observation; Fig. 4.14) is incorrect (see Fig. 4.8, right panel). Yet most of the flux at sufficiently large halo angles is due to dust located within 300 pc of the Sun. The corresponding delay times are small, and the precise history of the source light curve can be measured directly from the *Chandra* observation. Therefore, any inaccuracies in the modeled flux history will have a very limited effect, so a crude model is probably sufficient. On the other hand, at smaller angles the halo can be attributed to dust at larger x, making any inaccuracies in the flux history model more problematic. For this reason, I ultimately chose not to investigate halo angles smaller than $\sim 20''$. Separate 200 eV PSF-subtracted surface brightness distributions were extracted, using time bins of 1.5 ks. The energy bands were summed together, and halo light curves were created for four annular regions (units are arcseconds): $[22.8, 33.5]$, $[33.5, 49.2]$, $[49.2, 72.2]$, & $[72.2, 106.0]$.

Using the model flux history, I created model halo light curves for various energies, halo angles, and source distances, using the best-fit dust distribution as well as the three example dust distributions that are also consistent with the X-ray halo data. The final 2–5 keV single-scattered model light curves for the four annular regions is then derived by summing the energy bands and integrating over the annular regions, *viz.*

$$I_1(t, \Delta\theta) = \sum_{i=0}^{14} \frac{1}{\pi(\theta_2^2 - \theta_1^2)} \int_{\theta_1}^{\theta_2} 2\pi\theta I_1^i(t, \theta) d\theta, \tag{4.22}$$

where the superscript i is a label that indicates the center of the 200 eV energy band at $(2.1 + 0.2i)$ keV, and θ_1 and θ_2 are the boundaries of each annular region.

Although the single-scattered halo light curves can be easily modeled, I must also account for multiply-scattered photons, as well as our ignorance of the specific form of the dust distribution (Fig. 4.12). Calculating the time dependence of multiply-scattered

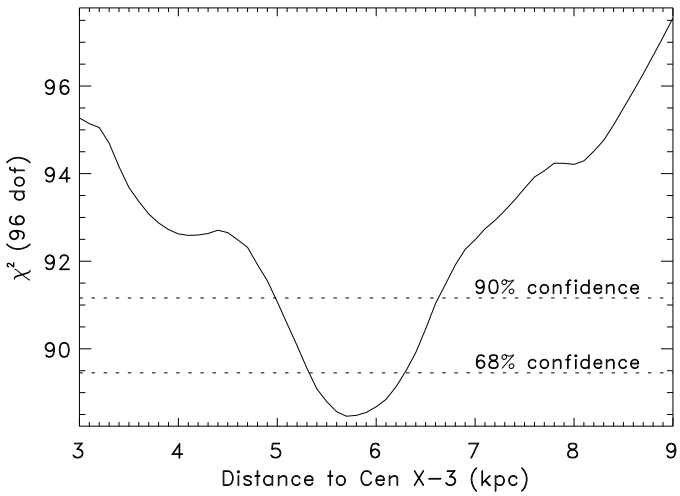

Figure 4.15: Fit statistic (χ^2) versus distance to Cen X-3. At the 68% (90%) confidence level, the distance is $5.7^{+0.5}_{-0.3}$ ($^{+0.9}_{-0.7}$) kpc. The quality of the fit at the best-fit distance is $\chi^2/\mathrm{dof} = 88.4/96 = 0.92$. A more appropriate method for error determination is discussed below.

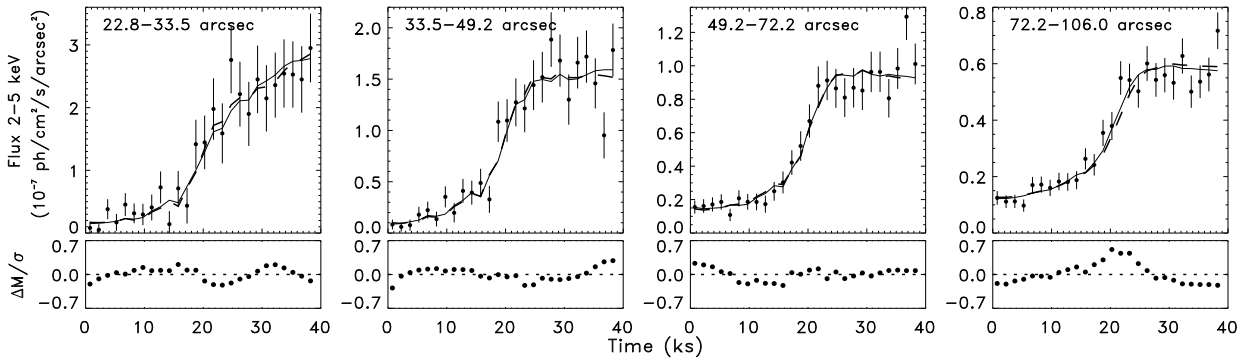

Figure 4.16: *Upper panels:* Eclipse egress light curves from 2–5 keV for four annular regions (labeled in each panel). The model light curves for $D = 5.7$ kpc and $D = 8$ kpc are shown as solid and dashed curves, respectively. *Lower panels:* Difference between model light curves (ΔM) for $D = 5.7$ kpc and $D = 8$ kpc in units of data uncertainty, showing that the differences between the models is usually much smaller than the error bars.

photons is computationally cumbersome (DT03). Fortunately, these photons comprise ∼10% of the total halo flux over the angles of interest (Fig. 4.10), so a rather simple treatment should be sufficient. Moreover, because the dust is concentrated at small x, the response of the halo to multiply-scattered photons should occur almost as rapidly as the response to single-scattered photons. Thus, to roughly account for multiply-scattered photons, I added 10% (the approximate value of I_2/I_1 over the angles of interest in the plateau phase observation) to the normalization of the single-scattered model light curves. I also allowed the normalization to vary by 10% when obtaining the fits.

To address the uncertainties in the dust distribution, I calculated model light curves for the best-fit distribution and for the three example distributions shown in Fig. 4.12. Although the general characteristics of the light curves (shape and normalization) for the different dust distributions were similar, subtle differences were present. The size of the differences in the light curves were about 7% ± 3% (relative to the model light curve for the best-fit distribution) at the beginning of the observation (and for the most part, independent of distance and angle), and 4% ± 1% at the end. Clearly, these measured differences only apply to the selected set of four potential dust distributions. In each case, however, the majority of the dust is located close to the Sun, so the differences in the light curves from this set should provide a decent measure of the uncertainty in $I_1(t, \Delta\theta)$ due to the uncertainty in $\tilde{\rho}(x)$. I chose to account for the uncertainty in the dust distribution by adding ∼4%–7% (depending on differences in the model light curves as a function of time) to the intrinsic uncertainty of the halo light curves.

Finally, the distance to Cen X-3 was obtained by fitting the model halo light curves for the four annular regions and for source distances between 3 kpc and 12 kpc in steps of 0.1 kpc to the observed light curves. For each distance, the χ^2 statistic was used to determine the quality of the fit. Our results indicate that the distance to Cen X-3 is $5.7^{+0.5}_{-0.3}$ ($^{+0.9}_{-0.7}$) kpc with 68% (90%) confidence (Figure 4.15). Note that I derive a more reasonable estimate of the distance uncertainty below.

The comparison of the measured halo light curves to the model fits for a source distance of 5.7 kpc (solid curves) and 8 kpc (dashed curves) is shown in Figure 4.16. Evidently, it is difficult to distinguish the differences between the models for the two

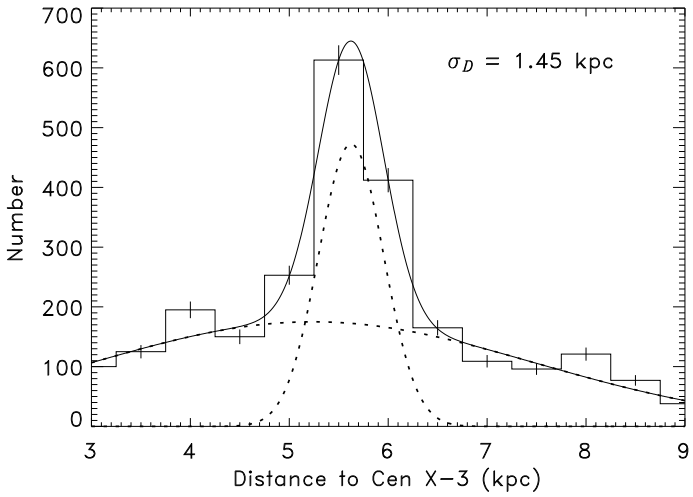

Figure 4.17: Histogram of the best-fit distances to Cen X-3 from 2500 synthetic data sets. The distribution is fitted with the sum of two Gaussians. The standard deviation of the distribution is 1.45 kpc, and the 90% confidence level lower and upper limits, which are determined from the model of the distribution, are 2.1 kpc and 8.3 kpc, respectively.

source distances, which are smaller than the uncertainty in the data (lower panels).

Because the model light curves are not strictly linear in distance, $\Delta\chi^2$ may not be a legitimate estimator of the distance uncertainty (Fig. 4.15). A more reasonable estimate of the uncertainty can be obtained using Monte Carlo simulations. We accomplished this by simulating 2500 synthetic data sets, assuming the light curve models for $D = 5.7$ kpc accurately describe physical reality, and assuming the measurement uncertainties are normally distributed. For each realization the best-fit distance is determined from the χ^2 minimum. The resulting probability distribution of best-fit distances is presented in Figure 4.17, indicating that the uncertainty in distance based on $\Delta\chi^2$ is indeed too small, and that a more reasonable distance estimate to Cen X-3 is 5.7 ± 1.5 $(^{+2.6}_{-3.6})$ kpc with 68% (90%) confidence. The 68% error limits were determined simply from the standard deviation of the distribution, and the 90% limits were determined by integrating over the model of the distribution, which is composed of the sum of two Gaussians.

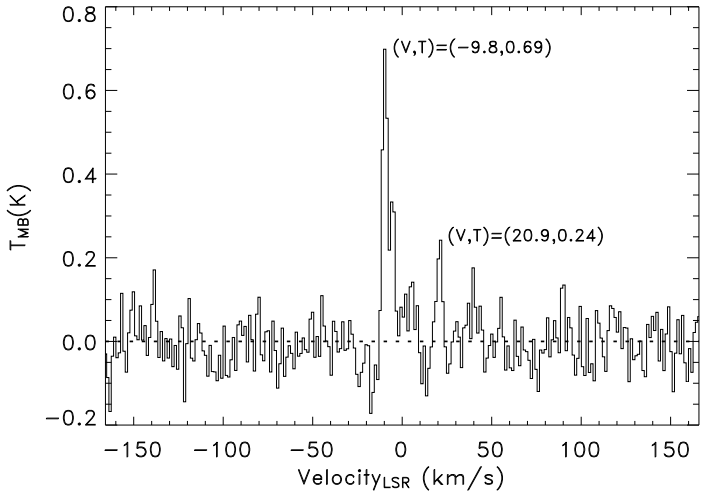

Figure 4.18: CO emission observed in the direction of Cen X-3 (Dame et al. 2001), with the two most prominent emission features labelled.

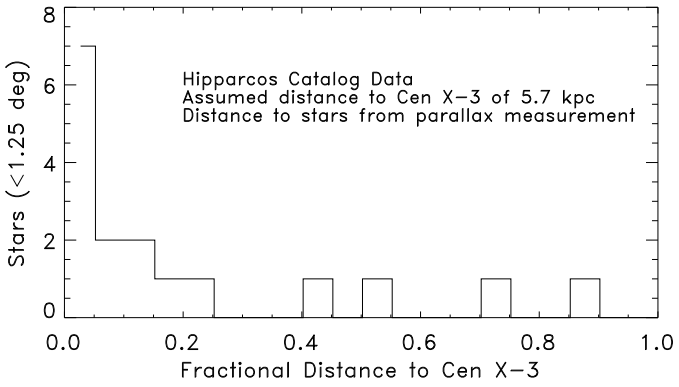

Figure 4.19: Histogram of the number of stars within 1.25° of the line of sight to Cen X-3. Data are based on the *Hipparcos Catalog*. The fractional distance assumes a source distance of 5.7 kpc.

4.4.5 Comparison to CO Emission and Star Counts

The dust distribution to Cen X-3 can be checked for consistency in a number of ways. Here I apply two methods. First, using the results of Dame et al. (2001), I can map the CO emission in the direction of Cen X-3, which presumably also traces the dust. The most prominent peak in the emission has a velocity of -9.8 km/s (Fig. 4.18), indicating a local origin (T. M. Dame, priv. comm.). Second, parallax measurements provide the spatial density of stars along the line of sight to Cen X-3. Using data from the *Hipparcos Catalog*, we created a histogram of the number of stars within 1.25° of the line of sight (Figure 4.19). Of course, the parallax data are subject to certain selection effects. For one, stars at larger distances are less likely to be above the flux limit of the survey. On the other hand, a given solid angle corresponds to a larger volume of space at larger distances. Nevertheless, assuming star-forming regions are cospatial with regions of higher dust density, the histogram of star counts supports that conclusion that most of the dust is located at relatively small distances from the Sun.

4.4.6 Discussion

I have discovered that most of the dust along the line of sight to Cen X-3 is located relatively nearby the Sun, and that the distance to the binary system appears to be closer than the commonly assumed distance of 8 kpc. However, the best-fit distance and 8 kpc are only marginally inconsistent at the 68% confidence level, and our results are consistent with an 8 kpc distance at the 90% level. Nevertheless, it is worth considering the implications of a distance of 5.7 kpc. For one, the measured fluxes of the X-ray source and the optical counterpart would imply almost a factor of two decrease in their luminosities. The optical luminosity is relevant to determining the mass-loss rate from a stellar wind, and the X-ray luminosity can yield a determination of the absolute mass accretion rate. Such uncertainty in the distance therefore has important consequences for modeling many characteristics of the binary system, such as the interaction between the magnetosphere of the pulsar and the accretion disk.

Secondly, a $\sim$5.7 kpc distance suggests the system may *not* located in the Carina spiral arm, where there is a higher *a priori* probability for the system to be located, but

$\sim$500 pc towards the Galactic center from the center of the arm. A distance of 5.7 kpc would place Cen X-3 at about an equal distance from the Galactic center as the Sun (8 kpc), versus about 9 kpc if Cen X-3 is in the Carina arm. Spiral arms are simply quasi-stationary density waves propagating through the Galaxy (Lin & Shu 1964). Stars do not stay in the same relative location in the arm as it moves; rather, the arms pass through the stars as the stars travel in their orbits about the Galaxy. The typical velocity of a star in its orbit about 8–9 kpc from the Galactic center is 220 km s^{-1}, and the pattern speed of the spiral arms is about 15 km s^{-1} kpc^{-1} (e.g., Shaviv 2003), corresponding to 120–135 km s^{-1}. Thus, in the inertial frame rotating with the stars, the relative velocity of the spiral arms is $\sim$100 km s^{-1}. The faster rotation speed of the stars relative to the spiral arm makes it unlikely that the progenitor stars of the Cen X-3 system formed when the Carina arm passed through the location of the system at some point the past, since at this time the system would have been trailing even further behind the arm. In addition, it is also unlikely that the system formed in the Scutum-Crux arm and then traveled through its orbit to its present location (e.g., Fig. 5 of Russeil 2003). Based on the 06–8 III stellar classification of the companion to the Cen X-3 pulsar, the age of the system is probably less than about 15 Myr. For a relative velocity of 100 km s^{-1}, at its birth the system would only be $<$1.5 kpc closer to the Scutum-Crux arm, whereas it is presently $\sim$10 kpc away (along a circle about the Galactic center) according to the four-arm model of Russeil (2003). It is thought that star formation occurs in the spiral arms because the gas clouds are compressed in the arms, subsequently forming stars. Due to the young ages of high-mass systems, OB stars generally do not live far from spiral arms. For Cen X-3 to reside 5.7 kpc from the Sun, either the system did not form in a spiral arm, or the system formed in the Carina arm and has a systemic velocity of $>$25 km s^{-1} toward the Galactic center.

Despite the uncertainty in the distance to Cen X-3, by all indications the dust along the line of sight to the system is heavily concentrated within about 300 pc of the Sun. Presumably, this dust is from the local Orion spur where the Sun resides. Not only do the X-ray halo measurements, the CO emission measurements, and the density of stars along the line of sight support this idea, but the halo light curves during egress clearly

show a rapid response to changes in the point source flux (Fig. 4.16). In fact, model light curves for a uniform dust distribution (not shown) grossly misrepresent the data.

It is also worth examining the difference between the energy dependence of the scattering optical depth predicted by the WD01 interstellar grain model, and the empirical curve describing Cen X-3 as well as data from Cyg X-1 and GX 13+1 (Fig. 4.11). Clearly, the shape of the WD01 curve and the Cen X-3 empirical curve differ substantially. One possible explanation for the discrepancy is our choice of $R_V = 3.1$. After all, higher values of R_V are observed in dense clouds, and I have found that most of the dust along the line of sight is located in a relatively small region of interstellar space. Yet this is not a viable explanation because the difference in the scattering optical depth for different values of R_V (over 2–5 keV) is more in the normalization and not the *shape* of the curve. For a given optical depth at 2 keV, the increase in optical depth at 5 keV for $R_V = 4.0$ ($R_V = 5.5$) is 6–7% (14–15%), whereas a ∼60–80% difference is required to explain the energy dependence of $\tau_{\rm sca}$ in Cen X-3. Furthermore, the energy scaling of the scattering optical depth in Cyg X-1 and GX 13+1 more closely resembles the empirical curve for Cen X-3 than the WD01 model curve. In his comparison, Draine (2003) focused on the apparent differences between the predicted and measured values of $\tau_{\rm sca}/A_V$ for various X-ray sources, and not on the shape of the energy dependence. Our results, and those of Smith et al. (2002) and Yao et al. (2003), suggest that the WD01 model fails to accurately reflect the energy dependence of the scattering optical depth. Relative to the WD01 model, there appears to be less scattering at low energies, or alternatively, more scattering at high energies (due to uncertainties in the absolute normalization of the scattering optical depth) in Cyg X-1, GX 13+1, and Cen X-3.

4.4.7 Conclusions

1. The vast majority of the dust along the line of sight to Cen X-3 is located within 300 pc ($0.00 < x < 0.05$) of the Sun. The most likely location of the dust is the local Orion spur. However, I am not sensitive to dust located in the vicinity of Cen X-3 because data within ∼3″ of the central source are affected by pile-up.

2. The geometric distance to Cen X-3 of 5.7 ± 1.5 (68% confidence level) suggests

the system may *not* be located in the Carina spiral arm, but ∼500 pc towards the Galactic center from the center of the spiral arm.

3. The energy scaling of the scattering optical depth predicted by the WD01 interstellar grain model does not accurately represent the results determined by X-ray halo studies of Cen X-3. Relative to the WD01 model, there appears to be less scattering at low energies or more scattering at high energies in Cyg X-1, GX 13+1, and Cen X-3.

4.5 Acknowledgement

Chapter 4 is in part a reprint of material that appears in The Astrophysical Journal, Vol. 650, p. 1063, and also includes work submitted to the journal that is not yet published (see astro-ph/0806.2859). The dissertation author was the primary investigator and author of these papers.

5

Orbital Determination of X-ray Pulsars

5.1 Introduction

Pulsars are neutron stars with very large magnetic fields. The companion stars of pulsars are typically very massive and produce a strong stellar wind that absorbs much of the soft X-ray radiation that is being emitted. Due to this heavy obscuration, many pulsars in high-mass systems are missed when observing the sky with low passband observatories.

The hard X-ray imaging of the Galactic plane by the *INTEGRAL (INTErnational Gamma-RAy Laboratory)* satellite is uncovering a large number of new high energy sources. Since *INTEGRAL*'s launch in 2002 October, ∼170 "IGR" sources have been discovered (or, in some cases, re-discovered), including 19 new confirmed HMXBs, with the IBIS (Imager on Board the *INTEGRAL* Satellite) hard X-ray and gamma-ray coded aperture mask instrument (Ubertini et al. 2003; Lebrun et al. 2003; Bird et al. 2006). The new sources have mostly been found in the ∼20–50 keV energy range using images with $12'$ angular resolution.

Until recently, only 10 supergiant X-ray binaries were known to exist in the Galaxy (e.g., Liu et al. 2000), although many new members of this class are being uncovered by the *INTEGRAL* Galactic plane scans. Thus, there is a bias against detecting

supergiant X-ray binaries in the soft X-ray band. Removal of this bias by *INTEGRAL* along with confirmation of the nature of the companions through IR observations and determination of the orbital solutions could significantly alter estimates for the number of supergiant systems in the Galaxy as well as impact our understanding of HMXB evolution.

Although the IGR sources do not represent a uniform population, with some of them being Active Galactic Nuclei while others are Cataclysmic Variables or X-Ray Binaries, a subset of the IGR sources appear to be persistent, but variable, highly-absorbed X-ray sources close to the Galactic plane. For these sources, the high levels of absorption, with $N_{\rm H}$ in the range from 10^{23} cm^{-2} up to 2×10^{24} cm^{-2}, explain why they have largely gone undetected by previous soft X-ray surveys. Follow-up observations of these sources with *XMM-Newton* or *Chandra*, which provide accurate position measurements, indicate that some of them are coincident with bright infrared (IR) sources (Filliatre & Chaty 2004; Walter et al. 2003, 2006; Patel et al. 2004; Bodaghee et al. 2006; Zurita Heras et al. 2006), suggesting that much of the absorbing material is local to the source. In addition, variable column densities have been seen for some of the sources (Patel et al. 2004; Thompson et al. 2007).

Significant progress has been made on understanding the nature of these "obscured" sources. For the source with the most extreme column density, IGR J16318–4848, IR spectroscopy has been performed, indicating a spectrum consistent with an unusual supergiant B[e] spectral type (Filliatre & Chaty 2004; Chaty & Filliatre 2005). It is most likely that this is a binary system consisting of a supergiant and a neutron star or a black hole. Another major step forward in understanding these systems has been the detection of X-ray pulsations from several sources and the association of some of the IGR sources with previously known *BeppoSAX*, *EXOSAT*, and *ASCA* pulsars (Lutovinov et al. 2005; Patel et al. 2004; Augello et al. 2003; Bodaghee et al. 2006; Zurita Heras et al. 2006) Recently, Patel et al. (2006) reported that the pulse period changes ($\dot{P} = 1.6 \times 10^{-4}$ s s^{-1}) observed in IGR J16358–4726 can be explained by a magnetic field of strength $\sim 10^{13}$–10^{15} G, possibly supporting a magnetar nature for the source. If more potential magnetars are uncovered, it has the potential to modify our understanding of the formation of neutron stars, and of soft gamma repeaters and anomalous X-ray pulsars.

In addition, studies of accreting pulsars are important because it is often possible to measure the fundamental neutron star parameters for these systems. Neutron star mass measurements are important for constraining their equation of state (EOS), and finding that even a single neutron star has a mass considerably more than 1.4 $M_{\odot}$ provides a direct EOS constraint. The supergiant wind accretor Vela X-1 provides one of the most convincing cases for an over-massive neutron star (van Kerkwijk et al. 1995; Charles & Coe 2006).

While the detection of pulsations indicates that an accreting neutron star is present for these systems, and it is very likely that these are HMXBs, knowledge of the complete orbital solutions, including the projected semi-major axis ($a_{\rm X} \sin i$) and the eccentricity, facilitates understanding the nature of the companion donor star, and could possibly reveal a large pulse period derivative that is indicative of magnetars. In this chapter two pulsars are investigated, with the goals of determining the orbital solutions, and, assuming an orbital solution can be unambiguously obtained, of measuring the orbital phase evolution of the spectral parameters to further facilitate understanding of these systems. The two pulsars are IGR 16393–4643 and EXO 1722–363 (=IGR 17252–3616).

5.2 Pulsar Timing for Orbital Determination

5.2.1 Measuring Pulse Arrival Times

Pulse arrival times for both IGR J16393–4643 and EXO 1722–363 were measured in a multi-step iterative process. First, data that clearly affected by flares are removed to avoid biasing the inferred pulse arrival times. More specific criteria for removing data are discussed below. Then each individual observation was divided into ∼1.5 ks "light segments" (∼3–4 pulse cycles), and each segment was folded modulo the most recent measurement of the pulse period to improve statistics. Then the light segments were cross correlated with each other. The cross correlation lag times were measured to the nearest second. The resultant pulse arrival times were then used to create a more refined pulse template, and this process was repeated until the pulse arrival times and the pulse

template no longer changed. The specifics of the analysis of each individual source is discussed in the corresponding section.

5.2.2 Error Analysis

Statistical Errors

Statistical errors on the pulse arrival times were calculated using Monte Carlo simulations. The PCA background errors were estimated from the unmodeled background variations shown in Fig. 29 of Jahoda et al. (2006), ranging from about 3% to 8% over 3–24 keV with 16 s binning. The background and errors were interpolated to 1 s resolution. For each light segment, one hundred trial light curves were created. Each point on the light curve was chosen randomly from a Gaussian distribution centered on the measured number of counts, and with the standard deviation determined by Poisson counting statistics from source and background errors added in quadrature. Each trial light curve was cross correlated with the template, yielding slightly different pulse arrival times. The quoted statistical uncertainty is the standard deviation of the difference in pulse arrival time relative to what was measured from each light segment. Statistical errors usually ranged from 3 to 10 s for IGR J16393–4643 and $\sim$5 s for EXO 1722–363.

Systematic Errors

In addition to statistical errors, systematic uncertainties in the pulse arrival times can be caused by distortions in the average pulse profile. These distortions can be caused by varying flux, contamination from nearby sources (e.g., 4U 1630-47 in the case of EXO 1722–363), and the energy dependence of the pulse shape can be affected by varying levels of local absorption. To estimate these errors, we aligned each folded light segment with the pulse template using the measured pulse arrival times, and each aligned and folded light segment was then used as a trial pulse template for all of the other folded light segments. The resultant arrival times from each trial generally created a Gaussian distribution centered on the measured arrival time, though occasionally there were outliers. The width of the resultant distributions was used as an indicator of the systematic error in the pulse arrival times due to changes in the pulse shape.

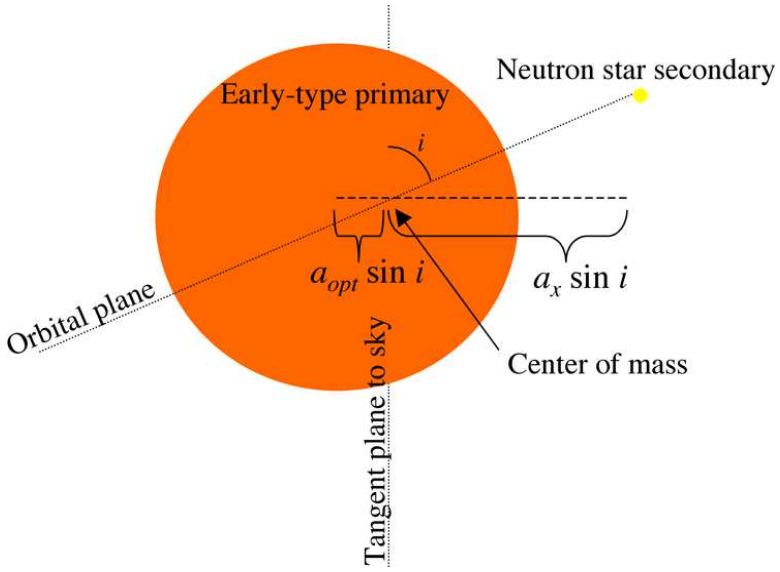

Figure 5.1: Geometry of the orbit for a HMXB system.

5.2.3 Fitting the Orbit

The pulse arrival times were fitted with a seven parameter model of the orbit and pulse period evolution. The arrival time of the nth pulse is given by

$$t_n = t_0 + nP_0 + \frac{n^2}{2}P_0\dot{P} + a_x \sin i \cos\left[\frac{2\pi\,(t_n - \mathrm{T90})}{P_{\mathrm{orb}}}\right], \tag{5.1}$$

where P_0 is the pulse period at time t_0, $\dot{P}$ is the pulse period derivative and is assumed to be constant, $a_x \sin i$ is the projected semi-major axis of the orbit, P_{orb} is the orbital period of the system, and T90 is a reference time corresponding to mid-eclipse for a circular orbit. The pulse number n is given by the nearest integer to

$$n = \frac{t_n - t_0}{\langle P \rangle} = \frac{t_n - t_0}{P_0 + 0.5\dot{P}(t_n - t_0)}. \tag{5.2}$$

A picture of the geometry of the orbit of a pulsar in a HMXB system is presented in Figure 5.1. Understanding eq. (5.1) is straightforward: The second term determines the pulse arrival time if the pulsar were stationary in space, the third term accounts for the fact that the pulse period is probably changing in time (assuming a constant pulse period derivative), and the last term, which is referred to as the "delay time" in subsequent plots of the pulsar orbits, accounts for the binary motion of the system. If the orbit was not

consistent with circular, I tried adding eccentricity to the orbital model by including the term

$$-\frac{e}{2}\frac{a_x}{c}\sin i \sin\left[\frac{4\pi(t_n - \mathrm{T90})}{P_{\mathrm{orb}}} - \omega_{\mathrm{p}}\right] \tag{5.3}$$

in eq. (5.1), where e is the eccentricity and ω_{p} is the longitude of periastron. The additional term represents the first-order term in a Taylor series expansion in the eccentricity and is reasonably accurate for a mildly eccentric orbit (Levine et al. 2004). These analysis techniques and equations are applied to each of the following sources.

5.3 Orbital Parameters for IGR J16393–4643

IGR J16393–4643 was initially discovered by Sugizaki et al. (2001) and is listed as AX J16390.4-4642 in the *ASCA* Faint Source Catalog. It was later detected by *INTEGRAL* during the first Galactic Plane Scan (GPS) of the Norma spiral arm (Bodaghee et al. 2006). The *INTEGRAL* GPSs have revealed many highly-absorbed sources that were not easily detectable with the soft bandpasses (< 10 keV) of most previous observatories. The brightest sources detected during the first year of the GPSs are listed in Bird et al. (2004). Among the sources, a few tens of them have never been detected prior to *INTEGRAL*'s observation. The second year catalog has doubled the number of sources that are either new or without a firm classification (Bird et al. 2006). Most of the new objects from the first catalog share common characteristics such as their location in the Norma region and high intrinsic absorption (Lutovinov et al. 2005). They are believed to be HMXBs (see Kuulkers 2005), and IGR J16393–4643 ($l = 338.0°, b = 0.1°$) is probably a member of this class. That this system may be a HMXB has also been suggested by Sugizaki et al. (2001) and Combi et al. (2004) due to the huge hydrogen column density towards the source, the hard spectral index (0.7–10 keV band), and its flux variability.

Bodaghee et al. (2006) studied IGR J16393–4643 with *INTEGRAL* and *XMM-Newton* observations. *XMM-Newton EPIC* clearly detected pulsations at 2–10 keV with a $38 \pm 5\%$ pulse fraction and allowed for a refined position measurement; a potential counterpart, 2MASS J16390535-4642137, is about $2''$ away from the position. Using 15–40 keV *INTEGRAL ISGRI* data spanning about 54 days, the pulse period was measured

to be 912.0 ± 0.1 s with a pulse fraction of 54 ± 24%. By fitting a Comptonized emission model (`comptt` in XSPEC) to the non-simultaneous *ISGRI* and *EPIC* data, the column density was measured to be $N_{\rm H} = (25 \pm 2) \times 10^{22}$ cm^{-2}. The spectrum also required an Fe Kα line, and marginally, an Fe Kβ line. The absorbed integrated flux was 4.4×10^{-11} erg cm^{-2} s^{-1} in the 2–10 keV band and 5.1×10^{-11} erg cm^{-2} s^{-1} in the 20–60 keV band. By creating pulse phase-resolved spectra, Bodaghee et al. (2006) found that the pulsations affect the normalizations but do not modify the spectral shape significantly.

Table 5.1. RXTE Observation Log of IGR J16393-4643

Obs. ID	Epoch	Date (U.T.)	Time Span (ks)	Exp. Time (ks)	Rate[a] (cts/s/PCU)
90069-03-02	1	2004 Jul. 29.67–30.00	28.52	15.54	41.49[b]
90069-03-01	1	2004 Jul. 30.00–31.99	171.94	50.22	40.77[b]
91080-01-01	2	2005 Oct. 11.98–12.22	20.88	12.32	10.89
91080-01-02	2	2005 Oct. 15.91–16.17	22.08	12.50	11.50
91080-01-03	2	2005 Oct. 20.05–20.28	20.40	11.63	11.04
91080-01-04	2	2005 Oct. 24.56–24.75	16.86	11.73	11.47
91080-01-05	2	2005 Oct. 28.44–28.66	18.96	12.19	10.48
91080-01-06	2	2005 Nov. 01.36–01.68	27.48	12.45	10.20
91080-01-07	2	2005 Nov. 05.30–05.65	30.36	11.50	8.81
91080-01-08	2	2005 Nov. 09.16–09.41	21.30	12.38	14.70
91080-01-09	2	2005 Nov. 13.03–13.28	21.18	12.35	12.68
91080-01-10	2	2005 Nov. 17.03–17.27	21.12	12.70	10.25
91080-01-11	3	2006 Feb. 13.80–13.90	8.48	4.69	13.60
91080-01-12	3	2006 Feb. 14.86–14.96	8.63	4.53	10.41
91080-01-13	3	2006 Feb. 16.83–16.95	9.86	5.09	7.26
91080-01-14	3	2006 Feb. 17.80–17.91	9.26	5.28	11.68

[a]For 3–24 keV photons.

[b]Note the contamination during epoch 1 due to 4U 1630-47.

5.3.1 Observations

Ten *RXTE* observations of IGR J16393–4643 were obtained (Obs. ID 91080) at four day intervals during 2005 October–November (hereafter; epoch 2), with each observation roughly 12 ks in duration (three to four *RXTE* orbits). Four additional 5 ks observations (two *RXTE* orbits) were obtained at 1 and 2 day intervals in 2006 February (epoch 3). In addition, I use an archival observation (Obs. ID 90069) spanning about 2.2 days from 1.2 years earlier (epoch 1). The epoch 1 data was contaminated by the recurring black hole transient 4U 1630-47, which is about 1° from IGR J16393–4643 on the sky. The pointing position for epochs 2 and 3 was offset by 0.2°, excluding 4U 1630-47 from the field-of-view. A summary of these observations is shown in Table 5.1. Overall, these data extend over 1.56 yr and probe a range of timescales.

Source and background light curves were created with data from the Proportional Counter Array (PCA; Jahoda et al. 1996) using standard FTOOLS. The PCA instrument consists of five identical multianode proportional counter units (PCUs), operating in the 2–60 keV range, with an effective area of approximately 6500 cm^2 and a 1° field-of-view at FWHM. PCUs 0 and 2 were always operating, but any additional PCUs were also used if their good-time-intervals spanned entire *RXTE* orbits. Photon energies were restricted to 3–24 keV, and the light curves were binned by 16 s, which balanced the desires for fine time resolution while maximizing the signal-to-noise. The SkyVLE[1] background model was used for the epoch 1 data, and the Faint background model was used for epochs 2 and 3. The arrival times of individual events were reduced to the solar system barycenter using the Jet Propulsion Laboratory DE-200 ephemeris (Standish et al. 1992) and *faxbary*. The averaged PCU 0 and 2 light curves are shown in Figure 5.2. Characteristic error bars for each epoch of data are shown in the top-right corner of the corresponding panel.

The pulse phase averaged flux varied by ∼15% on hour time scales during epoch 1 (see Fig. 5.2*b*). Due to the contamination from 4U 1630-47, however, the variability cannot unambiguously be attributed to IGR J16393–4643. During epoch 2, the phase averaged flux was constant at the 10% level for most of the observations, but varied by

[1]see http.heasarc.nasa.gov/docs/xte/pca_news.html

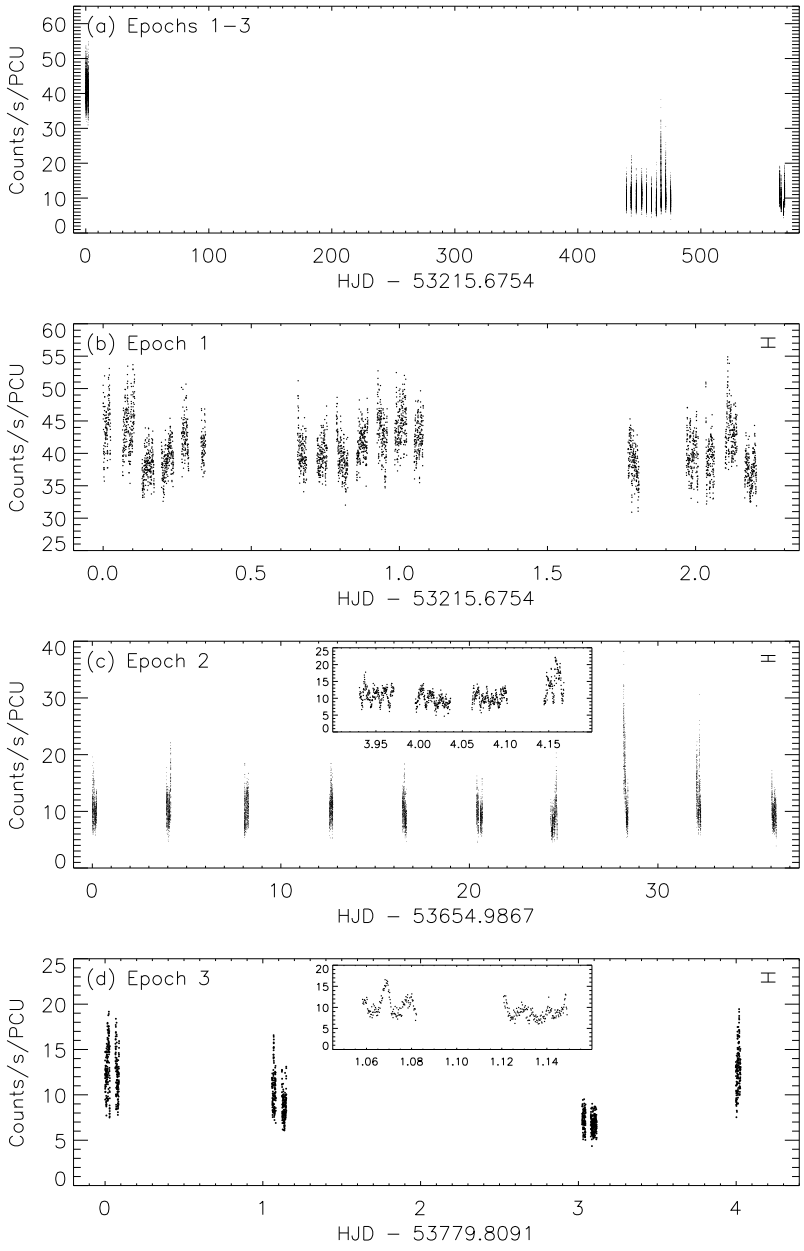

Figure 5.2: Barycenter-corrected and background-subtracted 3–24 keV light curves. From top to bottom the plots are (*a*) a merged light curve of all observations, (*b*) epoch 1 data, (*c*) epoch 2 data, and (*d*) epoch 3 data. A characteristic error bar for each epoch is shown in the top-right corner of the panel. The sub-panels for epochs 2 and 3 show variability on shorter time scales. Note the range of time scales present and the higher flux level for the epoch 1 observation due to contamination from 4U 1630-47.

more than a factor of two over 3 hrs at one point. This outburst was in progress at the beginning of observation 91080-01-08 at HJD 53683.17. The epoch 3 phase averaged flux was also constant within about 10% for the individual observations (two *RXTE* orbits), but varied by ∼80% over the scale of days. For roughly half of the observations, the pulses are clearly defined, while at other times the light curves are noisy or are highly variable (flares) on ∼100 s time scales. Figure 5.3 shows six examples of uninterrupted light curves, each spanning one orbit (hereafter called a "light segment").

Using the analysis techniques that are described in § 5.1.1, a pulse template was created, statistical and systematic errors were estimated, and arrival times were measured. For IGR J16393–4643, I began by removing data within 500 s of a flare, which is defined to be when the flux is more than 75% above the mean level for the light segment. A preliminary pulse template was then created by manually aligning a selected set of epoch 2 light segments with clearly defined pulses. The alignment was accomplished by fitting a combination of sine functions to the selected light segments, and adjusting the phases accordingly. Manual alignment of the pulses is preferable to folding the entire light curve because it corrects for variations in the arrival times due to the source's position in the orbit. All light segments were folded modulo 912.0 s (Bodaghee et al. 2006), and then the epoch 2 and 3 light segments were cross correlated with the preliminary pulse template. The cross correlation lag times were measured to the nearest second. The resultant pulse arrival times were then used to create a more refined pulse template including all epoch 2 and 3 data (minus the flares). I repeated this process until the pulse arrival times and the pulse template no longer changed. The final pulse template was then used to determine the pulse arrival times for the epoch 1 data separately. In total, sixty pulse arrival times were obtained.[2] They are presented with their associated errors in Table 5.2. The final pulse template, with a pulse fraction of 21 ± 1%, is shown in Fig. 5.4. I note that the pulse template obtained from the PCA is fairly similar to the *XMM-Newton* folded light curve (Fig. 7, Bodaghee et al. 2006) with the main and secondary minima occurring at phases 0 and ∼0.3.

Figure 5.5 shows a histogram of the difference in the measured pulse minima

[2]I do not include two additional pulse arrival times from Bodaghee et al. (2006) due to ambiguity in the location of the pulse minima.

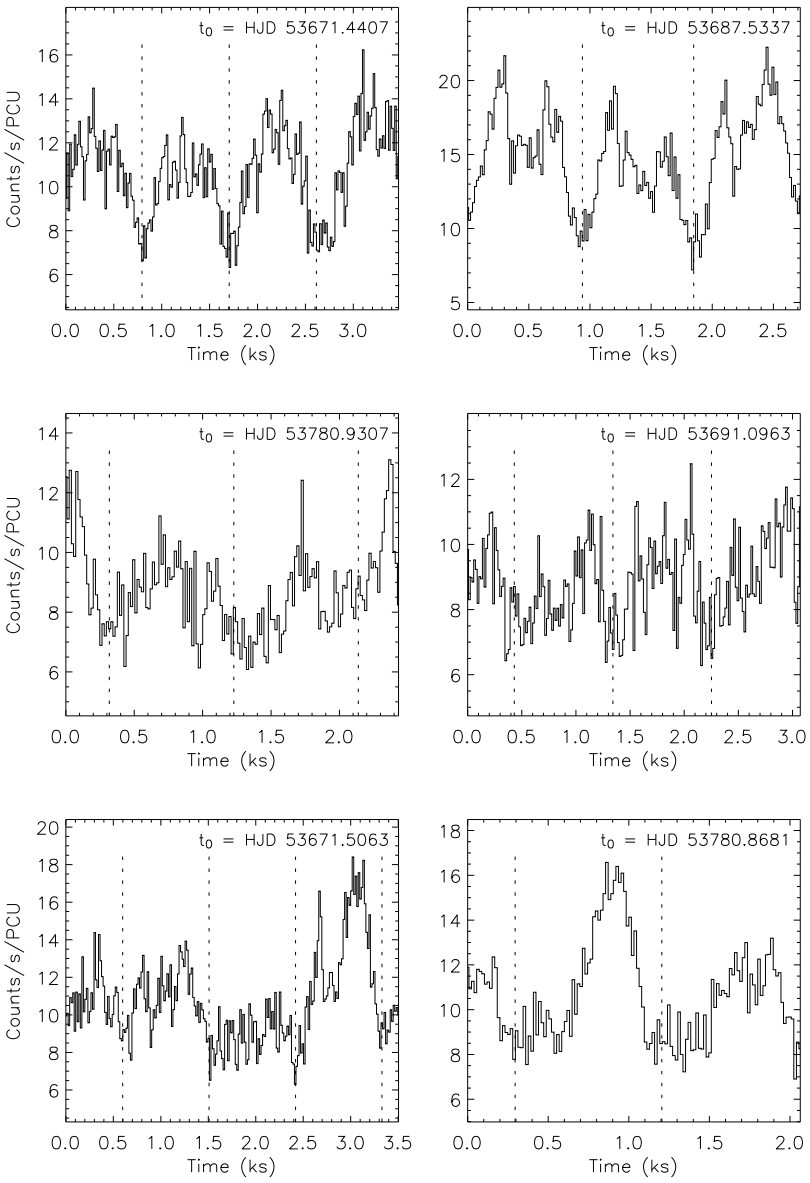

Figure 5.3: Examples of IGR J16393–4643 pulsations using 16 s bins. The top two panels show what are considered to be clean pulsations, the middle two panels show rather noisy or irregular light curve segments, and the lower panels show examples of flares. The pulse arrival times for the six examples are superimposed as vertical dotted lines. Note how the maxima of the flares tend to occur near the maxima of the pulse profile.

Table 5.2. IGR J16393-4643 Pulse Arrival Times

Arrival Time[a] (s)	Statistical/Total Uncertainty[b] (s)	Arrival Time[a] (s)	Statistical/Total Uncertainty[b] (s)
0	4.4/7.2	39054559	2.8/6.4
5448	8.2/10.0	39377752	3.1/6.5
6372	3.0/6.5	39383220	3.1/6.6
11845	72.0/72.3	39395054	4.9/7.6
22749	3.3/6.7	39717343	3.5/6.7
56428	7.6/9.6	39734649	3.8/6.9
61892	20.2/21.0	39740112	3.2/6.6
79182	5.0/7.6	40068776	5.9/8.2
84670	3.9/6.9	40074244	5.5/7.9
90134	3.6/6.8	40079709	3.6/6.8
95582	2.4/6.2	40081529	7.2/9.2
101964	2.8/6.4	40391059	1.4/5.9
153000	4.5/7.3	40396526	2.2/6.2
169432	14.2/15.3	40401980	4.3/7.2
175807	3.3/6.6	40408369	3.7/6.8
182183	3.5/6.7	40725128	2.8/6.4
186610	79.1/79.3	40730603	2.8/6.4
192203	15.2/16.2	40736993	2.3/6.2
37956572	4.4/7.3	40742452	3.9/7.0
37962023	2.6/6.3	41070181	3.5/6.7
37973850	3.5/6.8	41075629	5.0/7.7
38296118	3.0/6.5	41081075	2.5/6.3
38302510	5.2/7.7	41087460	4.5/7.3
38307969	3.6/6.8	48740706	2.2/6.2
38314333	1.8/6.0	48746156	4.0/7.0
38658474	3.0/6.5	48832691	27.5/28.1
38664855	3.3/6.7	48838122	355.1/355.2
38670316	2.5/6.3	49002025	25.9/26.5
39043641	3.5/6.7	49006544	23.8/24.4
39049098	1.8/6.0	49086621	4.3/7.2

[a]Arrival times begin at HJD 53215.688912.

[b]A systematic uncertainty of 5.76 s was added to each arrival time.

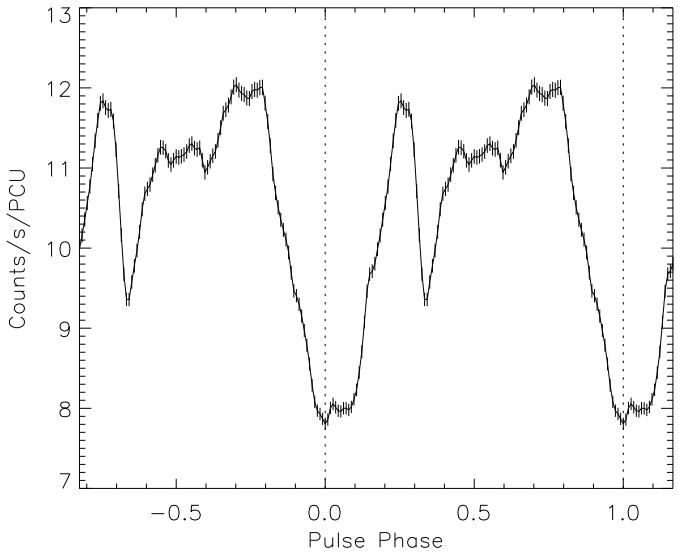

Figure 5.4: Final pulse template (3–24 keV) used to find the pulse arrival times via cross-correlation. The pulse fraction is 21 ± 1%. The dotted lines represent the phase corresponding to the pulse arrival times (Table 5.2). The error bars are 1σ statistical uncertainties.

versus the final template for IGR J16393–4643, created by using all light segments as trial templates for all other light segments, for a total of 1770 total elements. A Gaussian was fitted to the histogram to find a systematic standard deviation of 5.76 s, and this error was added in quadrature to each statistical error. Although the statistical and systematic errors may be correlated, whereby addition in quadrature would overestimate the total errors, the histogram has statistically significant deviations from the normal distribution at a pulse minima difference of 20–30 s, suggesting that the errors associated with some of the pulse arrival times are underestimated in this scenario. Moreover, if the pulse period is different from 912.0 s, folding each light segment on this period will result in slight smearing of the pulsations and will lead to additional systematic errors of order a few seconds.

5.3.2 Spectral Analysis

Motivated by the possibility of orbital modulation of spectral parameters, I extracted one spectrum from each epoch 2 and 3 observation. The epoch 1 spectra were

not analyzed due to contamination from 4U 1630–47. The IGR J16393–4643 spectrum consists of emission from the pulsar, plus diffuse emission from the Galactic ridge due to the 1° field-of-view of the PCA. The pulsar emission was modeled with an absorbed power-law with a high energy cut-off plus a Gaussian to model iron line emission. The Galactic ridge emission was modeled using the Valinia & Marshall (1998) parameterization, consisting of an absorbed Raymond-Smith plasma component of temperature ∼2–3 keV and a power-law component of photon index ∼1.8. The Galactic ridge components were fixed at the Valinia & Marshall (1998) best-fit values, but I included a variable overall multiplicative constant to adjust the normalization. The fourteen spectra were fitted simultaneously using XSPEC v11.3.2. Unfortunately, I found it difficult to constrain the spectral parameters, and especially the hydrogen column density, due to the Galactic ridge emission. From 3–5 (3–8) keV, the ridge emission accounts for about 75% (60%) of the total flux measured by the PCA. This explains the 21 ± 1% pulse fraction measured by the PCA, versus the 38 ± 5% measured by *XMM-Newton* from 2–10 keV, and 54 ± 24% by *INTEGRAL* from 15–40 keV: The ridge emission effectively washes out the signal. Any uncertainty in the ridge emission normalization leads to even larger uncertainties in the inferred column densities. More importantly, since pulsar spectra are typically complex functions of both phase and energy (White et al. 1983), changes in the IGR J16393–4643 spectrum with pulse phase confuse the analysis.

A final source of confusion in the spectral analysis results from brief flaring episodes, which last for ∼100–500 s. Interestingly, the strongest flares usually occurred at the pulse phase corresponding to the maximum of the pulse profile ($\phi \sim 0.7 - 0.8$, see Fig. 5.4). To illustrate spectral distortion during the flares, I created a spectrum of the central 150 s of the flare seen in the lower-right panel of Fig. 5.3 (Obs. ID 91080-01-12-00), and compared it to the spectrum from the remaining portions of that *RXTE* orbit. The spectra were fitted simultaneously, with the hydrogen column density and Galactic ridge emission normalization tied to common values. For this particular observation, a high energy cut-off was unnecessary, and $N_{\rm H} = 15^{+2}_{-3} \times 10^{22}$ cm^{-2} (90% confidence interval). The spectrum during the flare was best fit with a photon index $\Gamma = 0.86 \pm 0.14$, while $\Gamma = 1.46^{+0.16}_{-0.12}$ for the rest of the observation. This type of spectral hardening is not

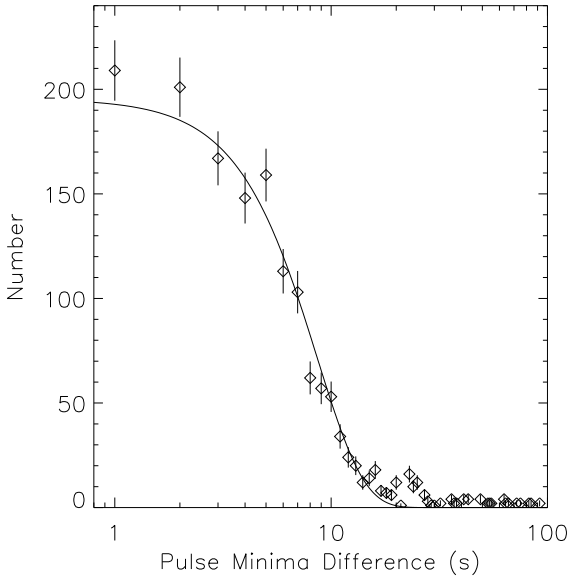

Figure 5.5: Histogram of the difference in pulse minima versus the final template created by using all light segments pulse templates for all other folded light curves. The fitted Gaussian distribution has $\sigma = 5.76$ s, though note the many outliers.

unexpected, yet it precludes constraining the hydrogen column density and power-law components simultaneously due to correlations between these parameters.

5.3.3 Results

I made sure the pulse period had not substantially changed from 912.0 s by creating Lomb-Scargle periodograms for the epoch 1 and epoch 2/3 data separately, which are presented in Figure 5.6. Determination of the orbital elements is complicated by the need to decouple the effects of the orbital Doppler delays and the intrinsic changes in the neutron star rotation rate. To minimize these concerns, I first searched for circular orbital solutions using the epoch 2 data only. The pulse arrival times were fitted to eq. (5.1), using a fine grid of initial values for the pulse period, projected semi-major axis, orbital period, and phase. An extensive search led to five potential fits that can be seen as the minima in Fig. 5.7, which shows the lowest χ^2_ν for circular orbits fits to the epoch 2 data as a function of pulse period. Given these fits, we then utilized all data by phase connecting the epoch 2 data to the data from epochs 1 and 3. To connect the three epochs

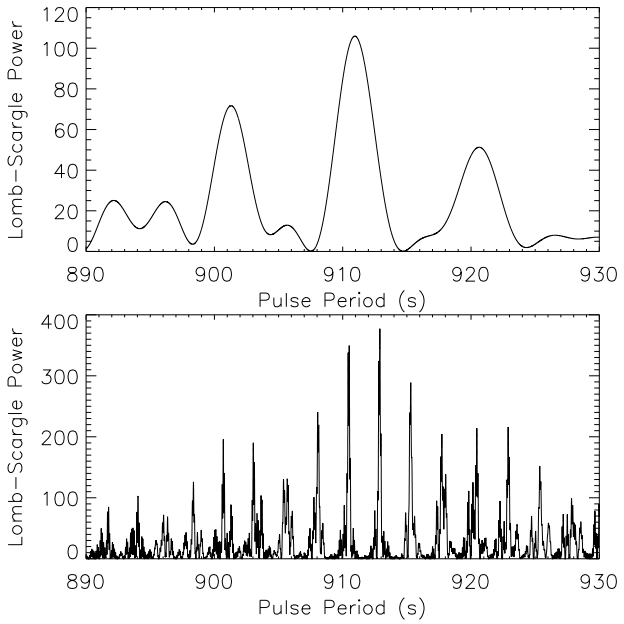

Figure 5.6: Lomb-Scargle periodograms for the epoch 1 data (top) and for the data from epochs 2 and 3 (bottom). Note the aliasing of the peaks in the lower panel due to the ∼4 day separation of the epoch 2 observations.

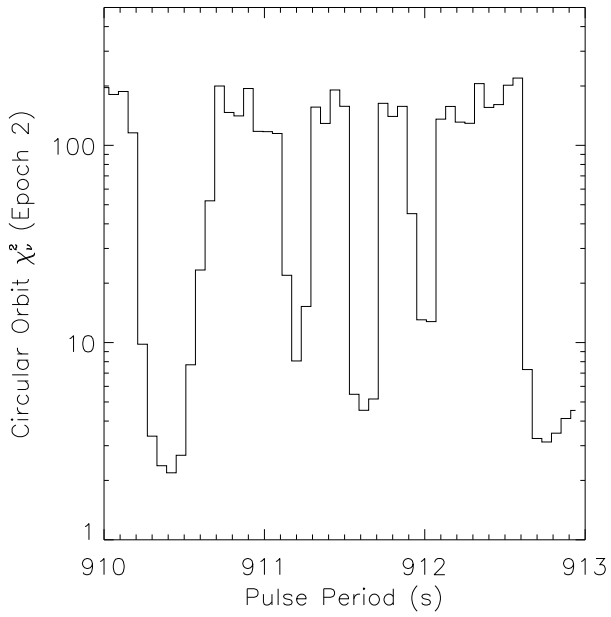

Figure 5.7: Lowest χ^2_ν for all circular orbits to the epoch 2 data as a function of the pulse period (0.06 s bins). The pulse period was allowed to vary by 0.03 s in either direction, and its derivative was allowed to span the range $\dot{P} = [-3, 3] \times 10^{-8}$ s s^{-1}.

of data, I used the best-fit circular orbit parameters for the epoch 2 data as initial values and cycled through a grid of pulse period derivatives $[-3, 3] \times 10^{-8}$ s s^{-1} with a step-size of 5×10^{-10} s s^{-1}. One of the initial fits was rejected due to an inability to connect the data sets, and one was rejected due to a substantially larger value of χ^2_ν, leaving three potential solutions. The results of the fits are presented in Table 5.3, and the orbital pulse arrival delays are plotted in Figures 5.8–5.10. The error bars in the figures represent the 68% confidence level, and the secular change in the pulse periods has been removed from the top and bottom panels so that the modulation is purely due to orbital motion.

Table 5.3. Circular Orbital Solutions to IGR J16393-4643

Solution:		1	2	3
$P_{\rm pulse}$[a]	(s)	910.4178 ± 0.0006	910.4028 ± 0.0007	911.6167 ± 0.0005
$\dot{P}$	(10^{-9} s s^{-1})	-10.81 ± 0.03	-9.34 ± 0.04	2.7 ± 0.3
$a_x \sin i$	(lt-s)	43 ± 2	60 ± 3	238 ± 2
$P_{\rm orb}$	(d)	3.6875 ± 0.0006	50.2 ± 0.5	8.1033 ± 0.0009
$f_x(M)$	($M_\odot$)	6.5 ± 1.1	0.092 ± 0.014	221 ± 6
χ^2_ν		2.55	5.29	7.72
χ^2_ν, rnm[b]		1.00	2.07	3.02

Note. — All errors are quoted at the 90% confidence level for a single parameter. The fits to eq. (5.1) each have 54 degrees of freedom.

[a]Pulse periods at t_0 = HJD 53654.98692.

[b]The renormalized χ^2_ν was obtained by multiplying each total error by 1.6.

Of the three potential orbital solutions presented in Table 5.3, only orbital solution 1 appears convincing. This solution has a projected semi-major axis of 43 ± 2 lt-s and an orbital period of 3.6875 ± 0.0006 days. The X-ray mass function is

$$f_x(M) = \frac{(M_c \sin i)^3}{(M_x + M_c)^2} = \frac{4\pi^2 (a_x \sin i)^3}{G P_{\rm orb}^2} = 6.5 \pm 1.1 \ M_\odot, \tag{5.4}$$

which is consistent with the HMXB interpretation proposed by Sugizaki et al. (2001), Combi et al. (2004), and Bodaghee et al. (2006). Finally, a pulse period of 910.4 s with a derivative of -1.08×10^{-8} s s^{-1} implies a pulse period of about 911.3 ± 0.1 s at the time of the 912.0 ± 0.1 s pulse period determination of Bodaghee et al. (2006). The 5σ difference potentially indicates that the pulse period derivative was not constant. This most likely was due to the average accretion rate increasing between 2003 February–March and 2004 July.

Orbital solution 2 is statistically acceptable, but it is not convincing for four reasons: (1) The value of χ^2_ν (see Table 5.3) is twice as large as that of orbital solution 1. (2) The residuals to the phase connection to the epoch 1 data systematically deviate from the orbital model. (3) There is a clear spread in the three to four pulse minima from each day of epoch 2 data, implying the pulse period and orbital period are not compatible. (4) Finally, with a mass function of 0.09 $M_\odot$, the system would have to be viewed nearly face-on ($i < 13^\circ$) for the companion to be a high mass star (assuming a 1.4 $M_\odot$ pulsar and a companion mass of 10 $M_\odot$). I also note that about 30% of the orbital phase is not sampled with these data.

Orbital solution 3 is immediately suspect because its mass function is greater than 200 $M_\odot$, and a star of this mass is hard (if not impossible) to rectify with theoretical predictions for the largest possible stellar mass (e.g., Krumholz 2005). If confirmed, solution 3 would represent an extremely important discovery because the orbital companion would more likely be an intermediate mass black hole (IMBH) rather than a normal star. Since the pulsar is observable in X-rays there is obviously a mass-donating companion, and therefore the system would necessarily be a triple system, which begs the question of how such a system could be dynamically formed. Moreover, there may be problems fitting the orbit of the pulsar and mass-donating companion outside of the Roche lobe of the IMBH. Unusually large companion mass aside, orbital solution 3 can be phase-connected

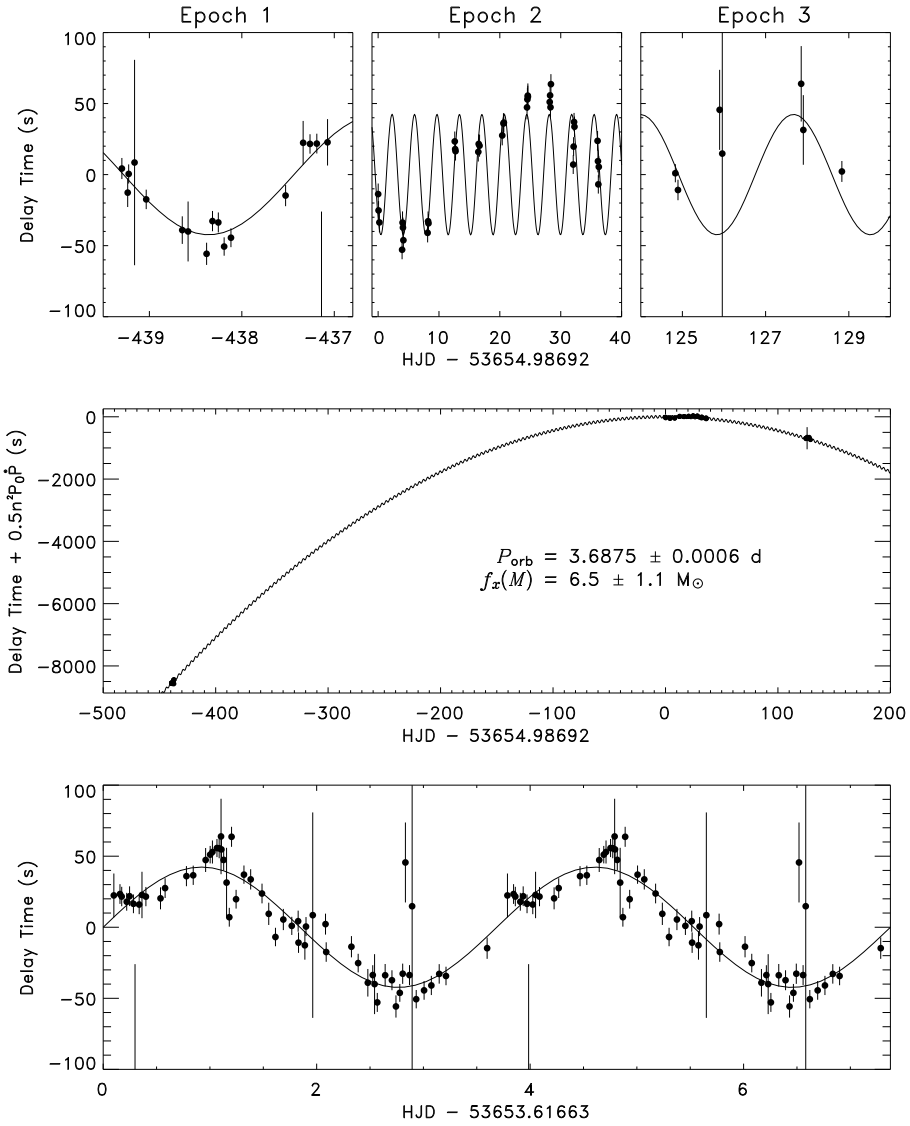

Figure 5.8: Orbital model fit to solution 1. *Top panels:* Zoomed in plots of the fits to each epoch. *Middle panel:* Fit to all epochs, explicitly showing the change in the pulse period over ∼1.5 yr. *Bottom panel:* All epochs plotted modulo the orbital period for two cycles.

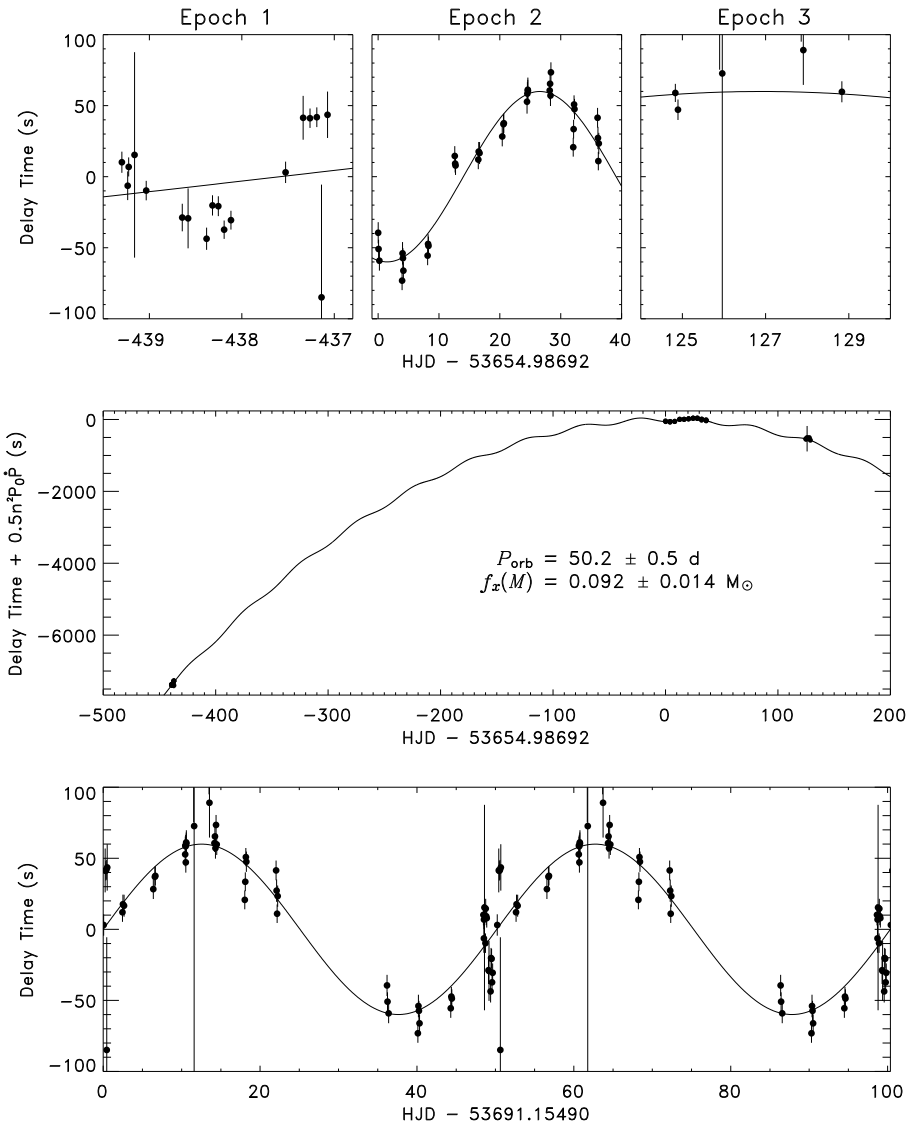

Figure 5.9: Same as Fig. 5.8, but for orbital solution 2.

over all three epochs, and a second orbit added to eq. (5.1) could possibly bring χ^2_ν to a level comparable to the other solutions. On the other hand, the secular pulse period derivative is positive, which is clearly inconsistent with the 912.0 $\pm$ 0.1 s pulse period measurement. Similar to orbital solution 2, nearly half of the orbital phase is not sampled with these data.

Orbital solution 1 stands out as the most likely one, yet with $\chi^2_\nu = 2.55$, the errors associated with the pulse arrival times would necessarily be underestimated by an average of about 60% to yield $\chi^2_\nu = 1.00$. This is not unreasonable considering the quality of the data (see Fig. 5.3), and the fact that there are statistically significant deviations from the Gaussian fit to the histogram used to estimate the systematic errors. As a final attempt to improve the fit, I added eccentricity to the orbital model, and an F-test showed that the addition of eccentricity to orbital models 2 and 3 was not significant, with chance probabilities of 0.16 and 0.09. Orbital solution 1, on the other hand, improved with a 3.4% probability of the improvement occuring by chance ($\chi^2/\nu \mid_{\rm circ\rightarrow ecc}= 137.7/54 \rightarrow 120.9/52$). With the improved fit to orbital solution 1, the best-fit parameters remained approximately constant with the exception of the projected semi-major axis which increased from 43 ± 2 to 55 ± 2 lt-s, yielding a new mass function of 13.1 ± 1.0 $M_\odot$. The best-fit eccentricity was 0.15 ± 0.05.

5.3.4 Discussion of IGR J16393–4643

By all indications, IGR J16393–4643 is a HMXB system. It is heavily absorbed, with roughly an order of magnitude more absorption than can be attributed to the Galactic interstellar medium (Dickey & Lockman 1990), indicating intrinsic absorption within the binary system. Such strong absorption is probably due to the stellar wind of a young companion star. Low-mass X-ray binaries, on the other hand, are generally not heavily extincted like IGR J16393–4643. In addition, sources like IGR J16393–4643 that undergo occasional flaring are typically found in wind-fed systems. Still, the nature of the companion star for this source is not certain. The most likely orbital solution has an X-ray mass function of about 6.5 $M_\odot$, although the reader should bear in mind that including mild eccentricity to the orbit increases the mass function to 13.1 ± 1.0 $M_\odot$. Nevertheless, it's

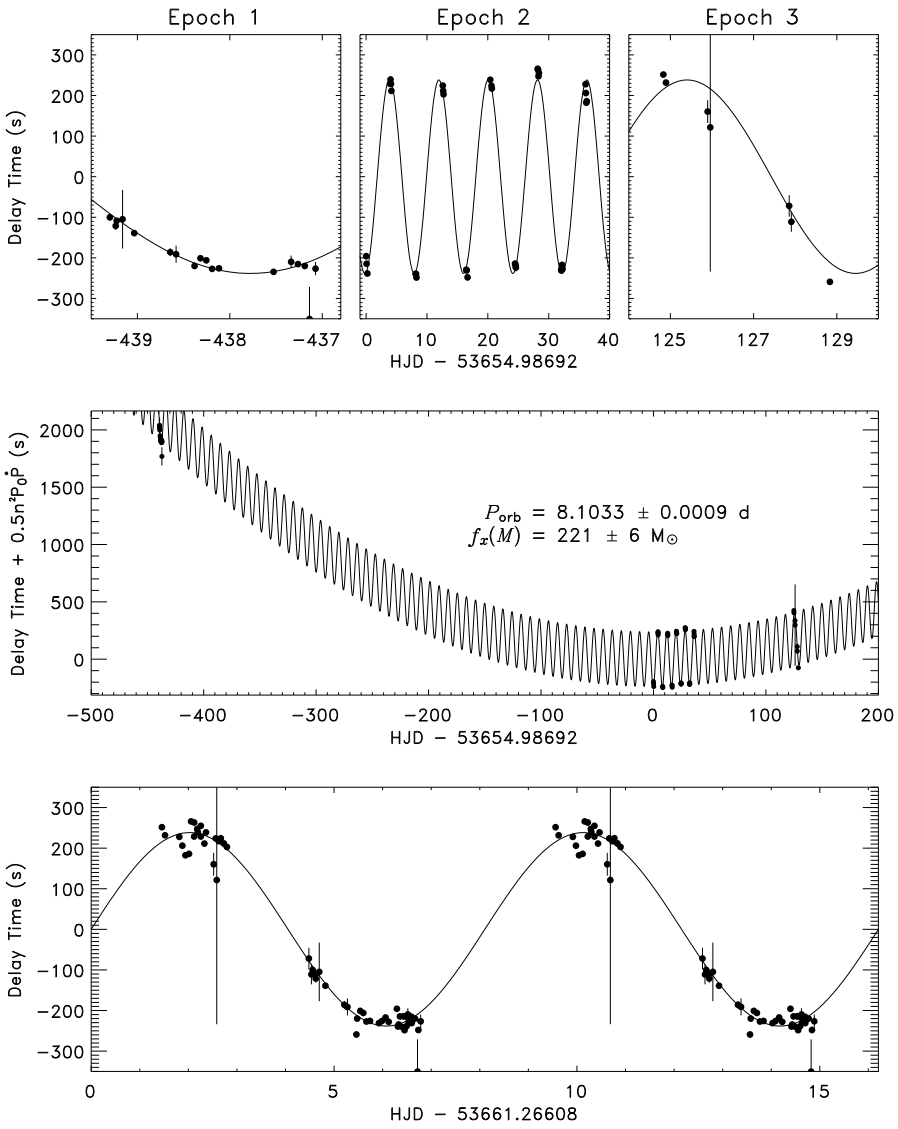

Figure 5.10: Same as Fig. 5.8, but for orbital solution 3.

position on the plot of pulse period versus orbital period—the so-called Corbet diagram (Corbet 1984)—implies that the companion is a supergiant with an underfilled Roche lobe rather than a Be star. The absence of transient behavior and the probable circular orbit further suggest that this is a supergiant system and not a Be X-ray binary. Until recently, only 10 supergiant X-ray binaries were known to exist in the Galaxy (e.g., Liu et al. 2000), although many new members of this class are being uncovered by the *INTEGRAL* GPSs (Walter et al. 2006). Eclipses are often observed in pulsars with supergiant binary companions if the inclination of the system is high enough. By folding the PCA light curves modulo the orbital period of the three solutions, I do not find any evidence for eclipses, which allows the constraint $R_c \tan i < 18.5\ R_\odot$ if I assume the companion mass is much larger than that of the pulsar. Assuming a companion radius of 10 $R_\odot$, the inclination must be less than about 60°. Nevertheless, further observations are required to obtain an unambiguous orbital solution for IGR J16393–4643. When combined with an optical mass function and a constraint on the inclination, the X-ray mass function would determine the masses of the two stars, which is important for constraining neutron star equations of state, and for understanding the evolution of binary systems.

5.4 The Orbit of the Eclipsing Pulsar EXO 1722–363

EXO 1722-363 (IGR J17252-3616) was first discovered by *EXOSAT* scan observations in 1984 along with 7 other sources in the Galactic ridge and 14 sources outside the Galactic ridge (Warwick et al. 1988). A pointed *Ginga* observation in 1987 October for a total of 80 ks discovered pulsations with a 413.9 ± 0.2 s period (Tawara et al. 1989). The source exhibited significant variability, with the 6–21 keV flux decreasing from about 2 mCrab to 0.2–0.3 mCrab over 8 hrs. Using an absorbed power-law model, they found $N_{\rm H} = 1.26^{+0.74}_{-0.47} \times 10^{24}$ cm^{-2}, suggesting a dense envelope of circumstellar matter surrounding the pulsar. Additional *Ginga* observations were performed in 1988 March–April by Takeuchi et al. (1990). Using pulse timing analysis, lower limits on the orbital period and mass of the companion were set to 9 days and 15 $M_\odot$, assuming a canonical neutron star mass of 1.4 $M_\odot$. Takeuchi et al. (1990) also measured the spectrum but included a high energy cut-off, and found a lower column density $N_{\rm H} = 1.26^{+0.33}_{-0.26} \times 10^{23}$ cm^{-2}. The orbital period constraints, along with the ∼414 s pulse period, places this system in the part of the Corbet diagram populated by supergiant wind accretors (Corbet 1984).

Using *RXTE* Proportional Counter Array (PCA) scans of the Galactic center region from 1999 February to 2003 October, Corbet et al. (2005; hereafter CMS05) measured a 9.741 ± 0.004 day orbital period through periodic changes in the source flux. By folding the scan observations on this orbital period, eclipses were detected lasting 1.7 ± 0.1 days (eclipse half-angle $\theta_e = 31.8° \pm 1.8°$). Using five pointed PCA observations lasting about 10 ks each at roughly 4–5 day intervals in 1998 October–November, CMS05 used the orbital modulation of the pulse arrival times to find illustrative orbital parameters, although the accuracy was limited by the assumption of no spin period changes during their observations, and by limited phase coverage. CMS05 also used these observations to measure the spectrum, finding that it varies but not dramatically.

EXO 1722-363 has also been observed by *INTEGRAL* during surveys of the Galactic plane. Zurita Heras et al. (2006) found that the source is persistent in the 20–60 keV band but is not detected above 60 keV. On a time scale of ∼3 days, the 20–60 keV source flux varied by a factor of about 4. Flaring activity was also observed, with the source flux increasing by a factor of 5 and returning to its base level in about a day.

Using *INTEGRAL*, the pulse period was measured to be 413.7 ± 0.3 s in 2003 August. Thus, aside from slight (∼1 s) changes, the neutron star pulse period has been stable for over a decade. Phase-resolved spectroscopy did not show any variation of the continuum emission with pulse phase. Using a follow-up *XMM-Newton* observation from 2004 March, a 414.8 ± 0.5 s pulse period was measured. More importantly, however, *XMM-Newton* measured the source position to 4″ accuracy, and an IR counterpart 2MASS J17251139-3616575 is located 1″ away from the best position. The possible IR counterpart is not detected in the 2MASS survey in the *J*-band but appears in the *H*-band and K_s-band with 11.8 mag and 10.7 mag respectively.

5.4.1 Observations

To find the orbital solution to EXO 1722–363, I obtained twenty new *RXTE* observations (ObsID 91080-02) at carefully chosen intervals during 2006 January to March (hereafter referred to as epoch 3[3]), with each observation roughly 3–5 ks in duration. In addition, I used two archival observations: One archival dataset (ObsID 30142-01) contains five observations from 1998 October to November at ∼4 day intervals (epoch 1) and are the same pointed observations used by CMS05, while the other (ObsID 80424-01) contains two observations from 2003 August of 1 and 2 ks, respectively (epoch 2). A summary of these observations is shown in Table 5.4.

[3]Not to be confused with PCA calibration epochs. See Jahoda et al. (2006) for a paper on PCA calibration.

Table 5.4. RXTE Observation Log of EXO 1722–363

ObsID[a]	Epoch	Date (U.T.)	Exposure (ks)	Rate[b] (Cts/s)	Pulse Minima[c]	Orbital Phase[d]	Spectrum Number[e]
30142-01-02-01	1	1998 Oct 23.08–23.25	14.80	24.77	10	0.67	
30142-01-02-00	1	1998 Oct 27.14–27.31	15.14	6.30	4	0.09	
30142-01-03-00	1	1998 Oct 31.93–01.10[f]	14.22	13.13	7	0.58	
30142-01-04-00	1	1998 Nov 05.00–05.17	14.16	4.18	0	0.00	
30142-01-05-00	1	1998 Nov 09.07–09.25	15.84	7.89	4	0.42	
80424-01-01-00	2	2003 Aug 22.21–22.22	0.96	9.40	1	0.78	
80424-01-02-00	2	2003 Aug 29.58–29.61	2.10	14.30	1	0.54	
91080-02-04-00	3	2006 Jan 16.92–17.00	4.92	4.49	0	0.00 (1)	1
91080-02-06-00	3	2006 Jan 17.90–17.99	5.04	5.21	0	0.10 (1)	3
91080-02-14-00	3	2006 Jan 21.84–21.92	4.86	13.73	4	0.50 (1)	11
91080-02-08-00	3	2006 Jan 28.63–28.71	4.98	7.43	1	0.20 (2)	5
91080-02-01-00	3	2006 Feb 04.05–04.13	4.74	7.94	2	0.86 (2)	18
91080-02-02-00	3	2006 Feb 04.52–04.55	2.82	5.22	0	0.91 (2)	19a
91080-02-01-01	3	2006 Feb 04.57–04.60	2.10	5.28	0	0.91 (2)	19b
91080-02-10-**	3	2006 Feb 08.38–08.46	4.86	25.32	4	0.30 (3)	7
91080-02-16-00	3	2006 Feb 11.26–11.30	3.54	13.50	3	0.60 (3)	13
91080-02-12-00	3	2006 Feb 19.18–19.22	3.36	20.90	3	0.41 (4)	9
91080-02-15-**	3	2006 Feb 20.56–20.65	3.18	13.51	3	0.55 (4)	12
91080-02-18-00	3	2006 Feb 22.00–22.04	3.42	13.29	3	0.70 (4)	15

Table 5.4—Continued

ObsID[a]	Epoch	Date (U.T.)	Exposure (ks)	Rate[b] (Cts/s)	Pulse Minima[c]	Orbital Phase[d]	Spectrum Number[e]
91080-02-20-00	3	2006 Feb 23.05–23.09	3.18	9.82	3	0.81 (4)	17
91080-02-17-**	3	2006 Mar 03.26–03.40	3.18	8.76	1	0.65 (5)	14
91080-02-19-**	3	2006 Mar 04.24–04.39	3.24	6.90	1	0.76 (5)	16
91080-02-03-**	3	2006 Mar 06.20–06.29	2.88	4.18	0	0.95 (5)	20
91080-02-05-**	3	2006 Mar 07.12–07.20	3.30	4.12	0	0.05 (6)	2
91080-02-07-**	3	2006 Mar 08.10–08.19	3.42	6.05	0	0.15 (6)	4
91080-02-09-**	3	2006 Mar 09.08–09.17	3.48	8.27	1	0.25 (6)	6
91080-02-11-**	3	2006 Mar 10.13–10.22	3.42	8.68	2	0.36 (6)	8
91080-02-13-**	3	2006 Mar 11.04–11.13	4.02	13.05	3	0.45 (6)	10

[a]Observation IDs ending with asterisks (**) represent two or more merged observations.

[b]For 3–24 keV photons per PCU after background subtraction.

[c]The number of pulse minima obtained after excluding light segments that are consistent with a constant flux (see text).

[d]The orbital phase at the middle of the observation, inferred from the fit presented in § 5.4.3. The phases typically extend about ±0.01 in either direction. The numbers in parenthesis next to the epoch 3 phases are the orbit number.

[e]Epoch 3 spectra number labels for Tables 5.7 & 5.8, ordered by orbital phase. Observations 91080-02-02-00 and 91080-02-01-01 were summed for spectral analysis.

[f]This observation ended in November.

Source and background light curves were created with data from the PCA (Jahoda et al. 2006) using standard FTOOLS. Due to the faintness of the source and short observations, HEXTE data were not included in the analysis. The PCA instrument consists of five identical multianode proportional counter units (PCUs), operating in the 2–60 keV range, with an effective area of approximately 6500 cm^2 and a 1° FWHM field of view. Photon energies for pulse timing analysis were restricted to 3–24 keV, and the light curves were binned by 1 s. Data accumulated in the Good Xenon data mode was used when available. The Faint[4] background model was used for the all epochs. The times of individual events were reduced to the solar system barycenter using the Jet Propulsion Laboratory DE-200 ephemeris and the FTOOL `faxbary`. I use the heliocentric modified Julian day (HJD) to refer to barycenter-corrected times throughout this paper. Figure 5.11 shows representative epoch 3 light curves at three different points in the orbit.

For EXO 1722–363, first, each individual observation was divided into ∼1.5 ks "light segments" (∼3–4 pulse cycles), and each segment was folded modulo 414.0 s to improve statistics. Although the true pulse period may differ slightly from this value, I expect smearing of the pulsation to be minimal, leading to systematic errors in the measured pulse arrival times of < 1 s. EXO 1722–363 is known to be an eclipsing system (CMS05). Zurita Heras et al. (2006) found that the *INTEGRAL* ISGRI flux drops to zero during the eclipse. The PCA flux, on the other hand, does not drop to zero during eclipse, probably because of Galactic ridge emission or possible weak contaminating sources within the 1° field of view. To limit the potential for including spurious pulse minima when the pulsar is obscured by the high-mass companion, each observation was fit with a constant flux and χ^2 was calculated. Based on the null hypothesis that the light segments are consistent with a constant flux, pulse minima were only measured if the null hypothesis was rejected at the 1% level of significance. While this may exclude data when the pulsar is out of eclipse, I prefer to be conservative and potentially exclude usable segments rather than include segments in eclipse. With the orbital solution obtained below, I find that all excluded light curves are within $|\Phi_{\rm orb}| < 0.15$, where mid-eclipse is defined to be orbital phase 0.0. The eclipse duration implies that pulsations should be observable at

[4]See http://heasarc.nasa.gov/docs/xte/pca_news.html.

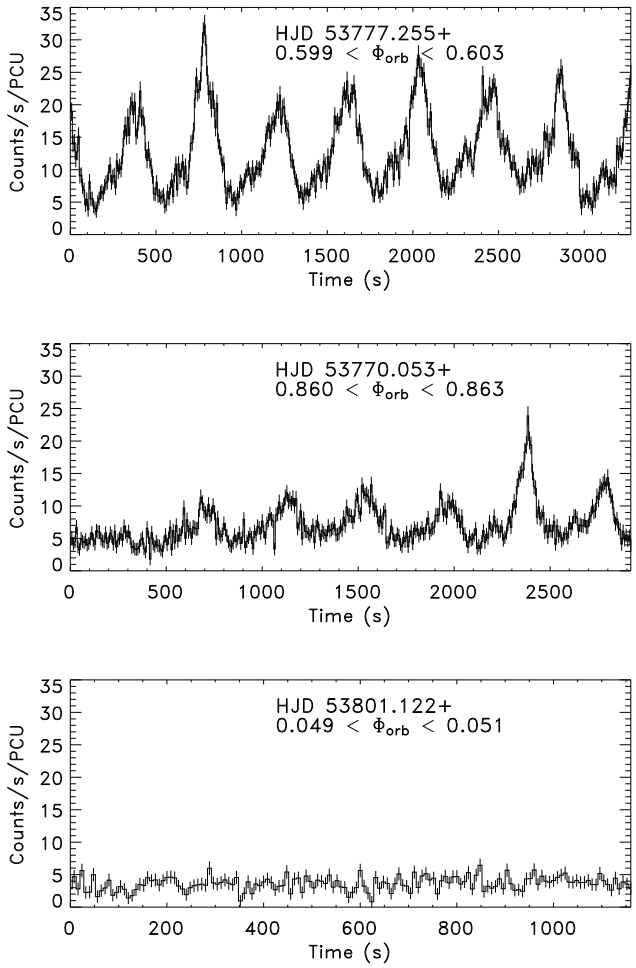

Figure 5.11: Representative light curves at three points in the pulsar's orbit for 3–24 keV photons using 8 s bins. The orbital phases are inferred from the orbital solution in § 5.4.2.

phase 0.1. Therefore, although all of the excluded observations occurred near the eclipse, they did not necessarily take place during the eclipse. The light segments that were not consistent with a constant were then manually aligned to create a preliminary pulse template. Each light segment was cross correlated with the preliminary pulse template, and the cross correlation lag times were then used to create a more refined pulse template. This process was repeated until the pulse arrival times and the pulse template no longer changed, and was performed on the epoch 1 and epoch 3 data separately. The epoch 3 pulse template was used to find the epoch 2 pulse minima. In total, 61 pulse arrival times were obtained. They are presented with their associated errors in Table 5.5. The final pulse templates for epochs 1 and 3 are shown in Figure 5.12. It is interesting to note that the epoch 1 pulse profile is more peaked at $\phi \approx 0.5$–0.6 than the epoch 3 pulse profile.

For EXO 1722–363, Figure 5.13 shows the resulting histograms of the magnitude of the difference in the measured pulse minima versus the final templates for epochs 1 and 3. I find a systematic standard deviation of 4.5 s for the epoch 1 data, and 5.9 s for the epoch 3 data. Epoch 2 consists of only two observations, so no systematic deviation can be obtained. I therefore chose to apply a value of 5 s to these data. The systematic errors were added to the statistical errors in quadrature, which may slightly overestimate the total errors because the statistical and systematic errors are likely correlated.

5.4.2 Pulse Timing Analysis

Because the epoch 3 data has the greatest phase coverage, I first fit these pulse minima alone, yielding an orbital solution with $a_x \sin i = 101 \pm 4$ lt-s and $P_{\rm orb} = 9.78 \pm 0.04$ days (90% confidence). The constraint on the orbital phase from this fit and the observation of an apparent egress from eclipse on 1998 October 27 (see CMS05, their Fig. 5), coupled with the higher accuracy orbital period from CMS05, remove any ambiguity in the number of orbital cycles that took place between the epoch 1 and 3 observations. This allowed us to constrain the orbital period further by performing a combined fit to the epoch 1 and 3 data. The pulse periods and derivatives for both epochs were allowed to vary independently. With this fit, the precision of the projected semi-major axis increased slightly to $a_x \sin i = 101 \pm 3$ lt-s, and the orbital period was refined to 9.7403 ± 0.0004

Table 5.5. EXO 1722–363 Pulse Arrival Times

Arrival Time[a] (s)	Statistical/Total Uncertainty[b] (s)	Arrival Time[a] (s)	Statistical/Total Uncertainty[b] (s)
0	2.3/5.0	229359623	3.1/6.7
823	1.6/4.8	229910149	2.6/6.5
1650	1.8/4.8	229910977	1.6/6.1
5798	1.5/4.7	230282137	0.5/5.9
6627	1.5/4.7	230283372	0.5/5.9
7455	1.7/4.8	230284614	0.5/5.9
8287	2.1/4.9	230287911	1.3/6.1
11604	0.9/4.6	230531238	2.8/6.5
12439	2.0/4.9	230532480	0.3/5.9
13674	1.0/4.6	230533308	1.1/6.0
351102	27.6/30.0	231216181	0.5/5.9
353169	11.3/12.2	231217016	1.0/9.2
356875	3.0/5.4	231218242	0.5/5.9
363493	3.0/5.4	231334948	2.5/6.2
765590	1.4/4.7	231340752	0.9/7.2
771385	1.7/4.8	231341580	0.7/6.8
772214	2.8/5.2	231459595	1.5/6.4
773458	2.7/5.2	231460421	1.4/6.4
777171	1.5/4.7	231461665	1.4/6.1
778004	2.8/5.3	231550305	3.1/6.7
778837	1.0/4.6	231551114	1.7/6.2
1468308	3.1/5.5	231552374	1.0/6.0
1470385	2.3/5.0	232259983	6.0/8.4
1474508	2.2/5.0	232344878	2.6/6.5
1475756	2.6/5.2	232762873	1.9/6.2
152421254	5.2/7.2	232853859	2.7/6.5
153058868	3.6/6.2	232859646	3.6/6.9
228766823	0.8/6.0	232932443	1.6/6.1
228770532	2.1/6.3	232933281	4.4/7.4
228771378	1.2/6.0	232938665	0.8/6.0
228772626	0.3/5.9	...	...

[a]Arrival times begin at HJD 51109.07143.

[b]A systematic uncertainty of 4.5 (5.9) s was added to each epoch 1 (3) arrival time. The epoch 2 data consist of only two minima, so no systematic standard deviation could be obtained. I chose to apply a value of 5 s.

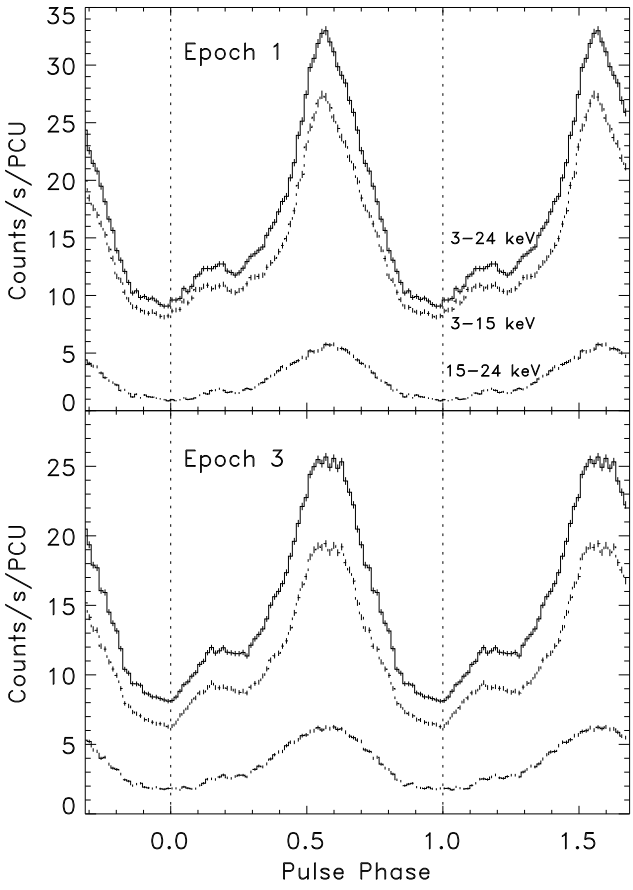

Figure 5.12: Final pulse templates for epochs 1 and 3 that were used to find the pulse arrival times via cross-correlation, for 3–24 keV photons (solid line), 3–15 keV photons (dotted line), and 15–24 keV photons (dashed line). The vertical dotted lines represent the phase corresponding to the pulse arrival times (Table 5.5). The error bars are 1σ statistical uncertainties.

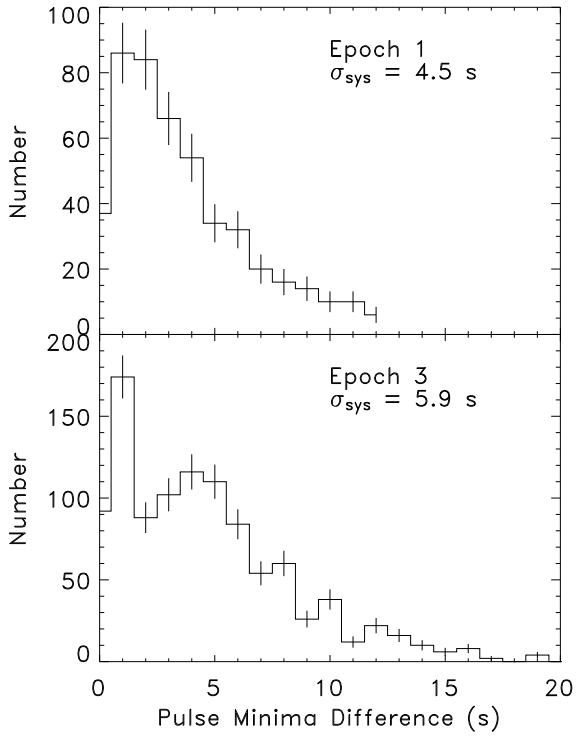

Figure 5.13: Histograms of the absolute difference in pulse arrival time per light segment after employing a pulse profile template from any other light segment instead of the final template. Only epoch 1 and 3 light segments are included.

Table 5.6. Circular Orbital Solution to EXO 1722–363

Parameter	(units)	Epoch 3	Epochs 1 & 3[a]	
$P_{\rm pulse}$[b]	(s)	413.894 ± 0.002	413.851 ± 0.004	413.894 ± 0.002
$\dot{P}_{\rm pulse}$	(10^{-9} s s^{-1})	-10.66 ± 0.99	0 ± 6	-10.66 ± 0.99
$a_x \sin i$	(lt-s)	101 ± 4	101 ± 3	
$P_{\rm orb}$	(d)	9.78 ± 0.04	9.7403 ± 0.0004	
$f_x(M)$	($M_\odot$)	11.2 ± 1.3	11.7 ± 1.2	
T90[c]	(HJD)	53761.60 ± 0.09	53761.68 ± 0.04	
χ^2_ν (dof)		1.45 (28)	1.45 (50)	

Note. — All errors are quoted at the 90% confidence level for a single parameter.

[a]For this fit, $P_{\rm pulse}$ and $\dot{P}_{\rm pulse}$ were varied independently for epoch 1 (*left*) and epoch 3 (*right*).

[b]Pulse periods at t_0 = HJD 51112.18662 for the fits to epochs 1, and t_0 = HJD 53761.73126 for the fits to epochs 2 & 3.

[c]T90 is defined to the epoch of mid-eclipse at $\Phi_{\rm orb} = 0$.

days. In addition, the mass function was found to be $f_x(M) = 11.7 \pm 1.2\ M_\odot$, and we define an epoch of mid-eclipse at HJD 53761.68 ± 0.04. The results of the fits are presented in Table 5.6. By including the first-order term in a Taylor series expansion in the eccentricity to equation (5.1) for the combined epoch 1 and 3 fit, the eccentricity is $0.08^{+0.11}_{-0.08}$, the projected semi-major axis is 96 ± 7 lt-s, the orbital period is $9.7400^{+0.0006}_{-0.0007}$ days, and T90 is HJD 53761.58 ± 0.04. However, the fit does not improve significantly, and with additional model parameters the value of χ^2_ν increases slightly from 1.45 to 1.48. The EXO 1722–363 orbit is therefore consistent with circular, and $e < 0.19$ with 90% confidence.

With the refined orbital period from the combined epoch fit, the orbital time delays for the two epoch 2 pulse minima are known. If we assume that the pulse period derivative is constant between epochs 1 and 2 or between epochs 2 and 3, it is possible to obtain fits to all three epochs of pulse minima. For example, a connection between epochs 2 and 3 can be made using pulse period derivatives of $-0.3147 \pm 0.0019n$ s yr^{-1},

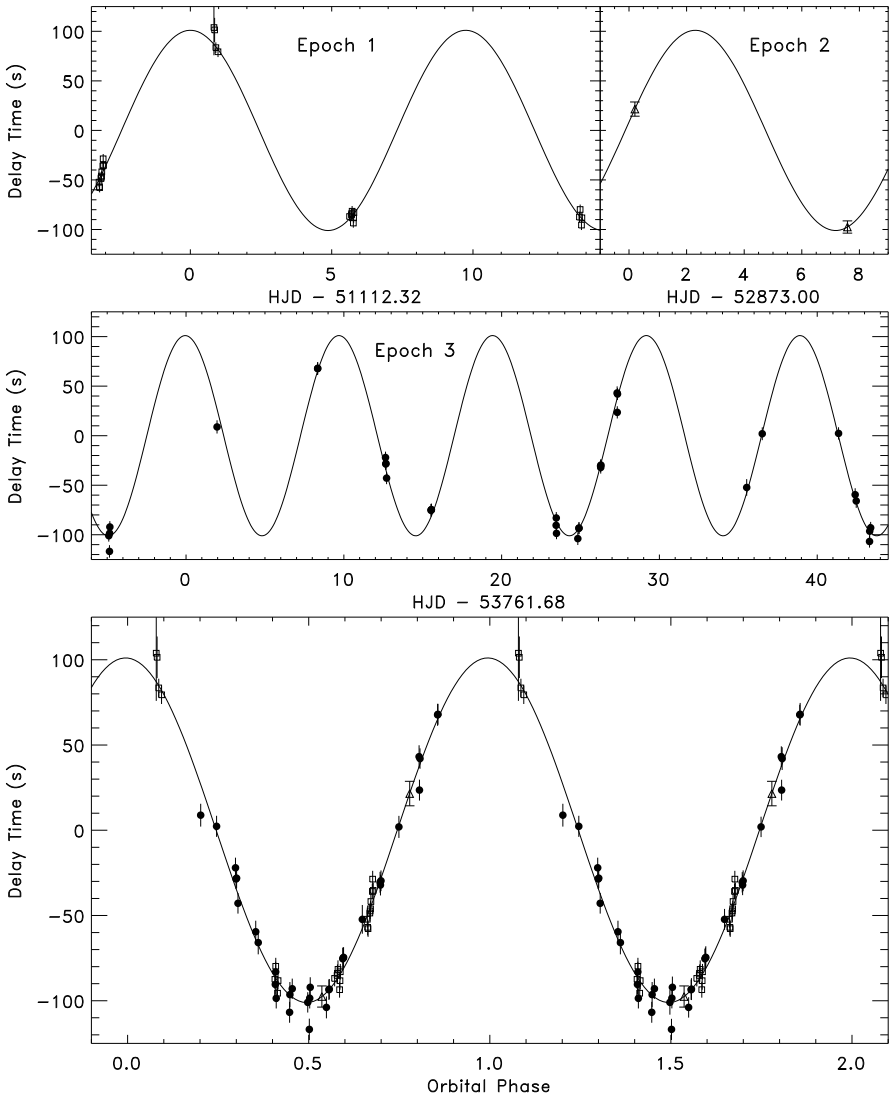

Figure 5.14: Orbital solution to EXO 1722-363. *Top* and *middle* panels: Plots of the fits to each epoch. The epoch 1 (3) data is plotted with open squares (filled circles). The epoch 2 data is plotted with open triangles and have hats on the error bars, and I have used $\dot{P} = -0.3147$ s yr^{-1} between epochs 2 and 3 for this fit (see text). *Bottom* panel: All epochs plotted modulo the orbital period for two cycles.

where n is 1 or 2. Thus, five connections can be made between epochs 2 and 3 within the 90% confidence interval, and the different integer values of n represent solutions where the number of pulse cycles between epochs 2 and 3 changes by an integer. Many more connections can be made for the alternative case assuming a constant $\dot{P}$ between epochs 1 and 2. This is because the large uncertainty in the epoch 1 pulse period derivative ($\dot{P}$ = -0.01 $\pm$ 0.19 s yr^{-1}) allows solutions where the number of pulse cycles between epochs 1 and 2 changes by an integer (as above), plus solutions where the number of pulse cycles *within* epoch 2 changes by an integer. Although multiple connections can be made between epochs 1 and 2 or epochs 2 and 3 assuming a constant pulse period derivative, the orbital solution still shows that a torque reversal happened at some time between 1998 November and 2006 February, simply because $\dot{P}$ is negative during epoch 3, and the epoch 1 pulse period is smaller than the epoch 3 pulse period. The pulse arrival delays are plotted in Figure 5.14, and for this case I have used $\dot{P} = -0.3147$ s yr^{-1} between epochs 2 and 3. The error bars in the figures represent the 68% confidence level, and the secular change in the pulse periods has been removed so that the modulation is purely due to orbital motion.

5.4.3 Orbital Modulation of Flux, Pulse Fraction, & Pulse Profile

Using the orbital solution, I searched for orbital modulation of the mean flux, the hardness ratio, and the pulse fraction using 20 orbital phase bins, shown in Figure 5.15. This figure clearly shows the orbital modulation of the flux, and the general shape is consistent with the *RXTE* ASM light curve presented by CMS05 (their Fig. 10) and the *INTEGRAL* ISGRI light curve of Zurita Heras et al. (2006, their Fig. 9), showing asymmetrical modulation of the orbital flux with a slightly higher average flux at orbital phases when the pulsar is moving towards the solar system barycenter than when the pulsar is moving away. The hardness ratio and pulse fraction are corrected for the Galactic ridge emission, which was measured from three observations occurring during eclipse (see below). The hardness ratio (using the PCA count rates in the 10–24 keV and 3–10 keV bands) is fairly constant except for the observations occurring near the eclipse, and at orbital phase 0.5. The pulse fraction for $0.15 < \Phi_{\rm orb} < 0.85$ varies between 40% and 65%

in both energy bands, but decreases outside this range and is consistent with zero during eclipse. I speculate that the decrease in pulse fraction near eclipse ingress and egress may be due to smearing of the pulsations from Thomson scattering along the line of sight. Figure 5.16 shows modulation of the average pulse profile as a function of the position of the pulsar in the orbit, created by folding all data in each phase bin, and accounting for slight changes in the pulse period and for the pulsar's orbital position. Because the average pulse profile may vary from orbit to orbit as well as within a single orbit, I have labeled the orbit number (where orbit 1 is the first orbit during epoch 3, see Table 5.4) in the top-right corner of each panel of the figure.

5.4.4 Spectral Analysis

The epoch 3 PCA observations have excellent orbital phase coverage, allowing us to observe changes in the source spectrum as the pulsar travels through its orbit. For spectral analysis, all datasets occurring within a single 4 hr period were summed (see labels in Table 5.4). Although PCUs 0 and 2 were on throughout the observations, the loss of the propane layer in PCU 0 has resulted in a higher background level. Since EXO 1722–363 is a relatively weak source, I only used data from PCU 2 to minimize concerns with background subtraction. Because of the 1° field of view of the PCA and EXO 1722-363's position in the Galactic plane ($b = -0.35°$), the spectrum consists of emission from the pulsar plus diffuse emission from the Galactic ridge. The Galactic ridge emission was modeled following Valinia & Marshall (1998), using an absorbed Raymond-Smith plasma with temperature ∼2–3 keV plus a power-law component with a photon index of ∼1.8. Fortunately, due to the presence of eclipses in EXO 1722-363, the Galactic ridge emission can be modeled by simultaneously fitting all observations occurring during eclipse. As pointed out by CMS05, the epoch 1 *RXTE* observation 30142-01-02-00 shows an apparent egress from eclipse (see their Fig. 5). Applying our circular orbital solution and assuming a symmetric eclipse, I obtained a 1.68 ± 0.08 day eclipse duration, consistent with 1.7 ± 0.1 days by CMS05, but inconsistent with the ∼1.3 day measurement by Zurita Heras et al. (2006). Note that our uncertainty is partly due to a lack of ability to precisely define when pulsations become apparent. Also note that the orbital solution including

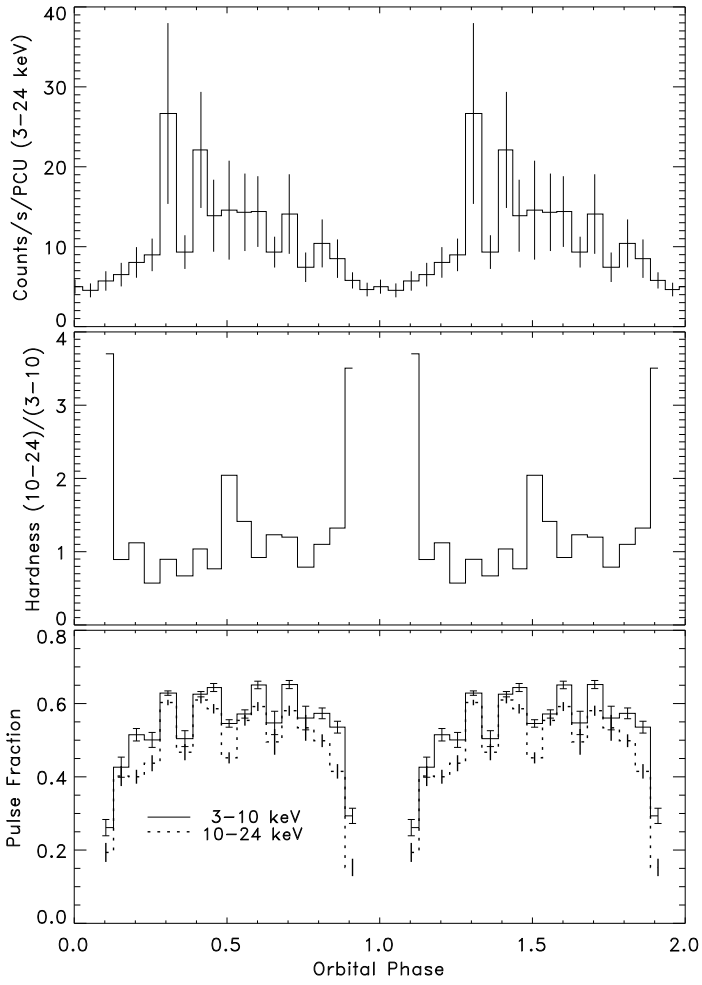

Figure 5.15: Orbital modulation of the mean flux (top panel), the hardness ratio (middle panel), and the pulse fraction (bottom panel) during epoch 3. The error bars for the top panel represent 1σ standard deviations (the uncertainty in the averages are less than 1%), and those of the bottom panel represent 1σ statistical uncertainties. The hardness ratio and pulse fraction are corrected for the Galactic ridge emission. The pulse fraction is shown in two energy bands; the 3–10 keV data (solid line) have hats on the error bars, and the 10–24 keV data (dotted line) do not have hats on the error bars.

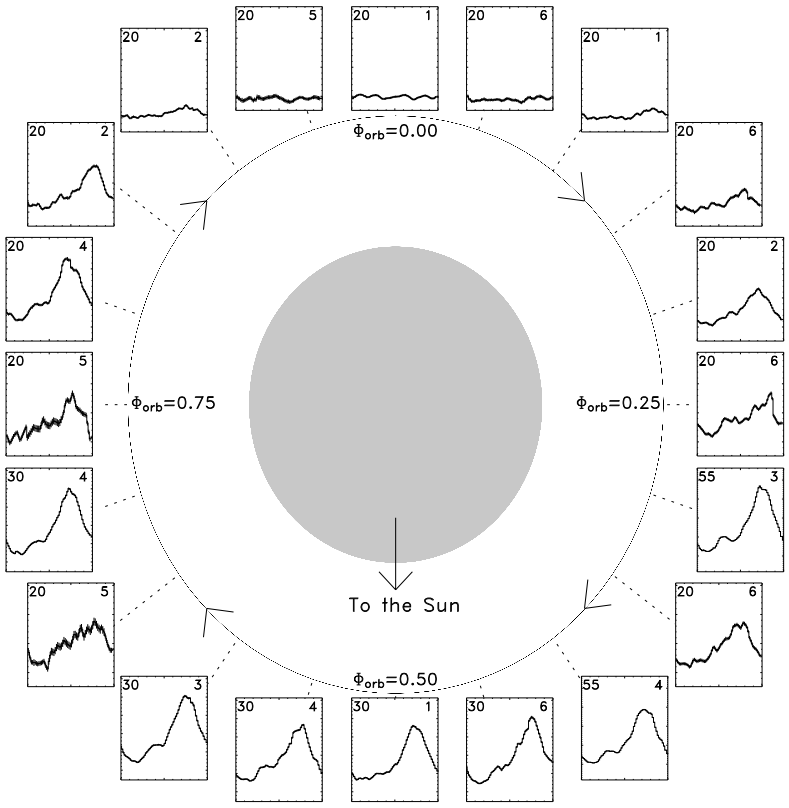

Figure 5.16: Orbital modulation of the epoch 3 average pulse profile from 3–24 keV. The labels for the axes are omitted for clarity: For each panel, the x-axis is pulse phase from 0.0 to 1.0 and the y-axis is counts s^{-1} PCU^{-1} from 3 to the number in the upper left corner of each panel. The orbit from which the pulse profile came is listed in the upper right corner of each panel. Pulsations cannot be seen during eclipse, and can only be seen weakly at phases 0.1 and 0.9. The system is viewed from below, and the circle represents the orbit of the pulsar moving clockwise. The size of the projected stellar radius relative to the size of the projected orbit is based on the CMS05 eclipse time measurement.

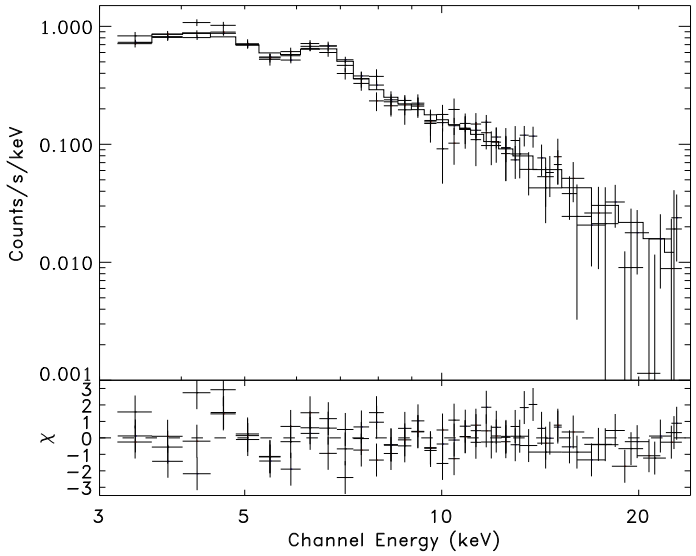

Figure 5.17: EXO 1722–363 spectrum and residuals for the three observations (spectra 1, 2, & 20) that occurred during eclipse. Emission is assumed to be dominated by emission from the Galactic ridge. The best-fit model was fixed for the fits to spectra numbers 3–19.

eccentricity implies a longer eclipse duration. For this reason, I chose to use the CMS05 result, which is based on folding light curves from scans of the Galactic center region over about 4.5 years, when inferring the radius of the companion star. Taking the lower limit of the eclipse duration at 1.6 days translates into $0.92 < \Phi_{\rm orb} < 0.08$. From this I find that three of the epoch 3 observations took place during eclipse (spectra numbers 1, 2, & 20). The Galactic ridge emission parameter values were then obtained by simultaneously fitting the spectra using XSPEC v11.3.2, the results of which are presented in Table 5.7. The model fit and residuals are shown in Figure 5.17. This model also accounts for any X-ray emission from the supergiant primary, possible contaminating sources in the field of view, and scattered emission from the pulsar.

With the Galactic ridge emission model parameters fixed at the best-fit values, the 17 remaining spectra were fit with an absorbed power law with a high energy cut-off plus a narrow Gaussian fixed at 6.4 keV to model iron line emission. Zurita Heras et al. (2006) found that phase-resolved spectroscopy did not show any variation of the continuum spectral shape with pulse phase, so pulse phase-resolved spectral analysis is

Table 5.7. Eclipse Spectrum for EXO 1722–363

Parameter	Value
$N_{\rm H}$ ($\times 10^{22}$ cm^{-2})	$7.1^{+2.2}_{-2.3}$
Raymond-Smith kT (keV)	$2.2^{+0.5}_{-0.3}$
Normalization ($\times 10^{-2}$)	$9.0^{+4.2}_{-3.5}$
Power law (PL) Index	$1.8^{+0.1}_{-0.3}$
Normalization ($\times 10^{-3}$)	$6.2^{+5.6}_{-3.1}$

Note. — All errors are quoted at the 90% confidence level for a single parameter. Spectra numbers 1, 2, & 20 were fit simultaneously from 3–24 keV; $\chi^2/\nu = 118.2/136 = 0.87$. The abundances of the Raymond-Smith plasma model were fixed at solar values. Model normalizations follow the definitions used in XSPEC (Arnaud 1996).

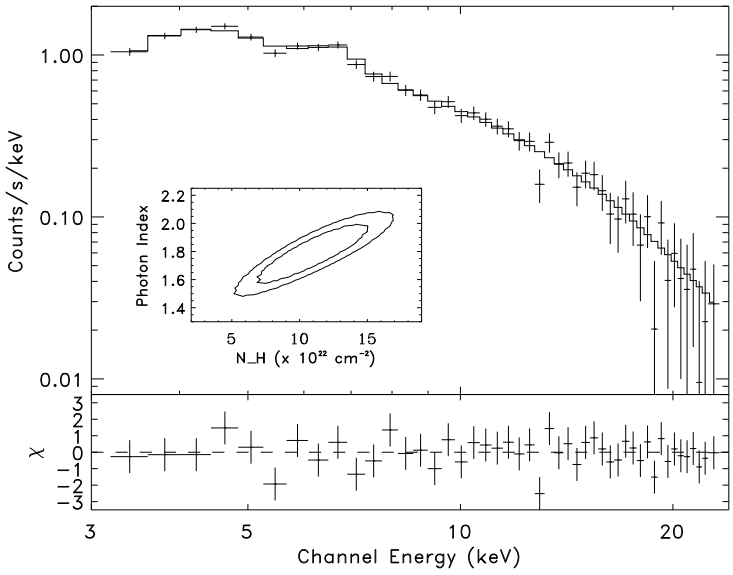

Figure 5.18: EXO 1722–363 spectrum number 8 and residuals. *Inset:* Contour plot of $N_{\rm H}$ versus photon index, showing the 68% and 90% confidence intervals ($\Delta\chi^2 = 2.3$ and $\Delta\chi^2 = 4.6$, respectively).

unnecessary. Limited statistics made a high energy cut-off unnecessary for 11 of the 17 spectra; however, we believe that the cut-off is probably still present because it is a common characteristic of pulsar spectra (Mihara 1995). I therefore chose to include a high energy cut-off in all spectra, but allowed the cut-off and folding energies to vary only if an F-test showed that there is less than a 5% probability that the improvement to the fit due to the cut-off occurred by chance. With this criterion, spectra numbers 7, 9, 11–13, & 16 had free values of $E_{\rm cut}$ and $E_{\rm fold}$. In all other cases, the cut-off and folding energies were fixed to the best-fit value found by fitting all spectra simultaneously with a single cut-off and folding energy. The best-fit cut-off energy was $16.2^{+0.8}_{-1.2}$ keV and the best-fit folding energy was $22.0^{+5.8}_{-4.7}$ keV. The spectral analysis results are shown in Table 5.8. As an example, I show the fit and residuals to spectrum number 8 (near $\Phi_{\rm orb} = 0.36$) in Figure 5.18. Also shown (see inset) are the 68% and 90% confidence intervals ($\Delta\chi^2 = 2.3$ and $\Delta\chi^2 = 4.6$, respectively) for $N_{\rm H}$ versus photon index. Note that the two parameter confidence interval implies uncertainties in $N_{\rm H}$ (photon index) that are about 20% (5%) larger than those quoted in Table 5.8. After subtracting the flux from the Galactic ridge, I find the unabsorbed X-ray flux to be in the range 0.7–4.8 $\times 10^{-10}$ ergs cm^{-2} s^{-1} from 2–24 keV.

Table 5.8. Epoch 3 Spectral Fits to EXO 1722–363

Number	Orb. Phase[a]	$N_{\rm H}$ ($\times 10^{22}$ cm^{-2})	Photon Index	PL Norm. ($\times 10^{-3}$)	Cut-off Energy[b] (keV)	Folding Energy[b] (keV)	EW[c] (eV)	χ^2_ν (dof)
3	0.10	86^{+87}_{-61}	$0.8^{+1.8}_{-1.3}$	$0.6^{+34.2}_{-0.5}$	16.2	22.0	< 4840	0.70 (43)
4	0.15	20^{+16}_{-12}	$2.0^{+0.7}_{-0.3}$	$12.2^{+58.1}_{-6.8}$	16.2	22.0	< 335	0.65 (43)
5	0.20	36^{+11}_{-12}	$1.7^{+0.4}_{-0.3}$	$14.3^{+22.1}_{-9.3}$	16.2	22.0	< 170	0.67 (43)
6	0.25	8^{+5}_{-4}	$1.8^{+0.3}_{-0.2}$	$13.0^{+12.2}_{-6.0}$	16.2	22.0	< 200	1.14 (43)
7	0.30	11 ± 2	1.2 ± 0.1	$18.6^{+3.8}_{-3.3}$	$16.6^{+1.2}_{-1.7}$	$19.0^{+10.0}_{-5.9}$	174^{+92}_{-54}	0.68 (41)
8	0.36	11 ± 5	1.8 ± 0.2	$15.3^{+11.6}_{-6.9}$	16.2	22.0	< 133	0.71 (43)
9	0.41	10 ± 2	0.9 ± 0.1	$8.2^{+2.6}_{-2.1}$	$16.5^{+1.9}_{-1.7}$	$17.3^{+10.4}_{-7.1}$	352^{+212}_{-144}	0.61 (41)
10	0.45	10 ± 3	1.4 ± 0.1	$12.9^{+2.3}_{-3.9}$	16.2	22.0	158^{+75}_{-116}	0.93 (43)
11	0.50	31 ± 14	0.1 ± 0.3	$1.0^{+2.3}_{-0.5}$	$12.8^{+0.9}_{-0.8}$	$14.2^{+3.2}_{-4.4}$	896^{+218}_{-157}	0.62 (41)
12	0.55	12 ± 6	$0.5^{+0.2}_{-0.3}$	$1.8^{+1.6}_{-0.9}$	$15.2^{+2.3}_{-2.0}$	$21.3^{+8.8}_{-10.2}$	675^{+138}_{-124}	1.04 (41)
13	0.60	14^{+4}_{-3}	1.3 ± 0.1	$10.9^{+3.5}_{-3.6}$	$20.5^{+2.7}_{-8.2}$	$5.0^{+63.0}_{-4.9}$	196^{+82}_{-98}	0.91 (41)
14	0.65	22^{+23}_{-13}	$1.1^{+0.7}_{-0.5}$	$4.5^{+26.1}_{-3.3}$	16.2	22.0	< 638	0.58 (43)

Table 5.8—Continued

Number	Orb. Phase[a]	$N_{\rm H}$ ($\times 10^{22}$ cm^{-2})	Photon Index	PL Norm. ($\times 10^{-3}$)	Cut-off Energy[b] (keV)	Folding Energy[b] (keV)	EW[c] (eV)	χ^2_ν (dof)
15	0.70	30^{+6}_{-5}	1.3 ± 0.2	$15.8^{+4.0}_{-5.9}$	16.2	22.0	< 202	1.10 (43)
16	0.76	16^{+14}_{-13}	1.5 ± 0.3	$6.9^{+2.3}_{-0.5}$	17.6 ± 1.4	$17.0^{+13.2}_{-14.4}$	< 380	0.61 (41)
17	0.81	25^{+8}_{-6}	1.3 ± 0.2	$9.1^{+9.0}_{-5.5}$	16.2	22.0	< 181	0.82 (43)
18	0.86	46^{+20}_{-12}	$1.7^{+0.5}_{-0.2}$	20^{+70}_{-13}	16.2	22.0	< 232	0.85 (43)
19	0.91	126^{+84}_{-60}	$1.3^{+0.7}_{-0.6}$	$3.8^{+175.4}_{-2.2}$	16.2	22.0	< 6490	0.94 (43)

Note. — XSPEC model: `phabs*(raymond + power) + phabs*highecut*(power + gauss)`. All errors are quoted at the 90% confidence level for a single parameter. The Galactic ridge emission parameters were fixed at the best-fit values of the simultaneous fit to spectra numbers 1, 2, & 20, which occurred during eclipse (see Table 5.7). Model normalizations follow the definitions used in XSPEC (Arnaud 1996).

[a]The orbital phase at the middle of the observation, inferred from the fit presented in § 5.4.2

[b]The high energy cut-off and folding energies were allowed to vary only if an F-test showed that there is less than a 5% probability that the improvement to the fit due to the cut-off occurred by chance. In all other cases, the cut-off and folding energies were fixed to the best-fit value found by fitting all spectra simultaneously with a single cut-off and folding energy (see text).

[c]Equivalent width of narrow Fe line at 6.4 keV.

5.4.5 Discussion of EXO 1722–363

5.4.6 Properties of the Mass-Donating Companion

Figure 5.19 shows the inferred companion radius and mass, as well as the Roche lobe radius (Eggleton 1983), as a function of the binary inclination. The curves were derived using our circular orbital solution, the CMS05 eclipse half-angle measurement, and a neutron star mass of 1.4 $M_{\odot}$. As shown in the figure, the radius of the companion (R_c) is greater than about 22 $R_{\odot}$, and at the limit of a zero mass neutron star $R_c > 21$ $R_{\odot}$. The figure also allows us to constrain the inclination assuming the primary underfills its Roche lobe. Since the uncertainties in the Roche lobe and primary radii are correlated through their interdependence on $a_x \sin i$, simulations were used to find that $i > 61^{\circ}$ at the 99% confidence level. With this firm constraint on the inclination, the radius of the primary must be less than about 37 $R_{\odot}$ and its mass must be less than about 22 $M_{\odot}$.

The radius and mass constraints are consistent with a supergiant star with a spectral type between B0 and B5 (Cox 2000). By combining photometric measurements by the Two Micron All-Sky Survey (2MASS) and the Deep Near-Infrared Survey of the Southern Sky (DENIS) in the J- and K-bands, comparing the colors that are obtained with empirical $(J-K)_0$ values for B0I–B5I stars, and applying extinction relationships (A_λ/A_V) from Cardelli et al. (1989), I find that the visual extinction is $A_V = 20.1 \pm 0.6$. The absolute visual magnitude for B0–B5 supergiants is $M_V \approx -6.5$ to -6.2 (Cox 2000), and the inferred spectral type is only consistent with the J and K apparent magnitudes if the distance to the system is between 5.3 kpc and 8.7 kpc.

5.4.7 Spectral Variability

The orbital modulation of the EXO 1722-363 spectrum, and especially the hydrogen column density, is intriguing. Figure 5.20 shows $N_{\rm H}$ plotted against orbital phase for two cycles; a vertical shaded bar shows when the pulsar is eclipsed by the primary. The two observations with the highest column densities occur just prior to ingress and just after egress, at a point where the pulsar is viewed through the base of the stellar wind at the very edge of the primary. CMS05 observed similarly large hydrogen column densi-

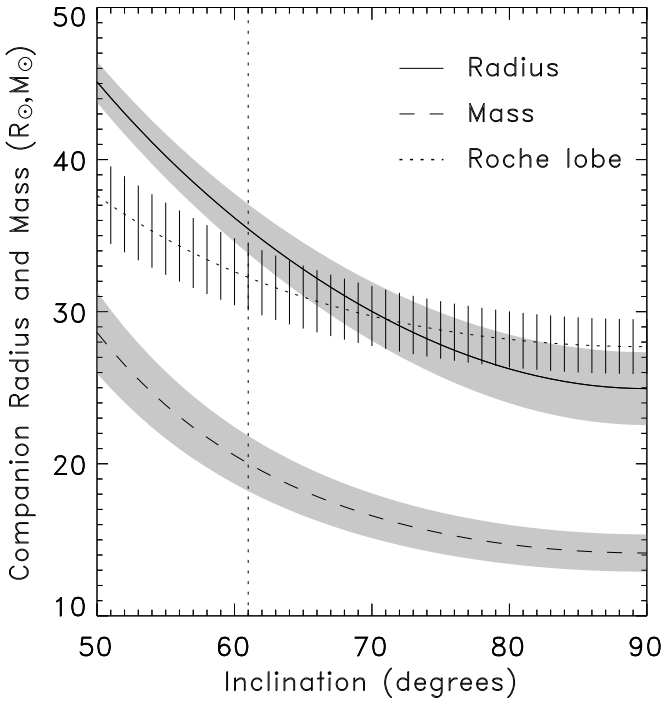

Figure 5.19: Binary inclination versus companion radius and mass, plus the size of the Roche lobe, using the best-fit orbital parameters, the CMS05 eclipse half-angle measurement, and assuming a neutron star mass of 1.4 $M_{\odot}$. The y-axis scale applies to both radius and mass although the units differ. The radius and mass curves have shaded error contours, and the Roche lobe curve has error bars. The vertical dotted line at $i = 61^{\circ}$ represents the lower limit to the inclination at the 99% confidence level.

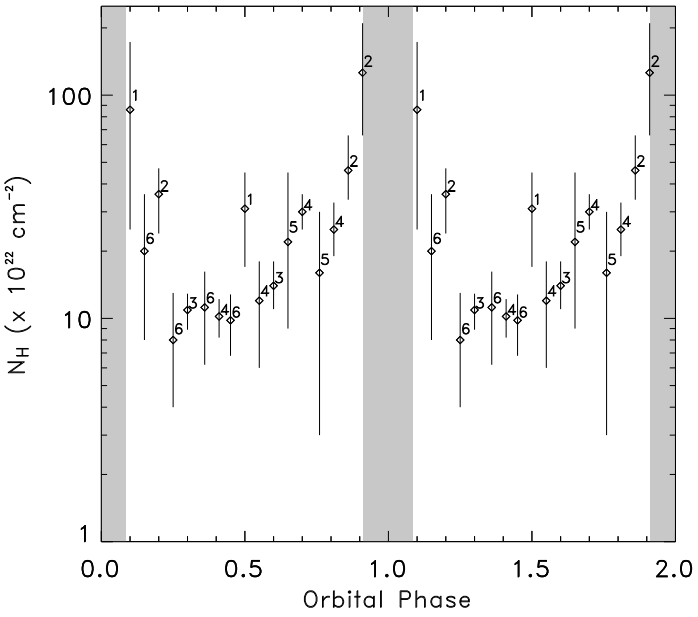

Figure 5.20: Best-fit hydrogen column density (Table 5.8) as a function of orbital phase. The orbit from which the $N_{\rm H}$ measurement was taken is labeled to the right of each point. The shaded bar indicates times when the pulsar is eclipsed by the primary.

ties shortly after eclipse egress. However, in our analysis I do not find a soft component necessary in any of the epoch 3 spectral fits, in contrast to what was observed by CMS05. Increased absorption for these observations is also supported by the abrupt increase in the hardness ratio near eclipse (see Fig. 5.15). Between phases 0.25 and 0.45, $N_{\rm H}$ is consistent at about 10^{23} cm^{-2}, but apparently increases for the second half of the orbit. It could argued that the observed increase at later phases is due to variability between orbits rather than within a single orbit, so in the figure we have labeled the orbit where each measurement was made next to its corresponding data point (see Table 5.4). Note that the four data points from orbit 4 seem to confirm the trend of increasing column densities at later phases without invoking orbit-to-orbit variation.

Phase-dependent modulation of the hydrogen column density has been investigated by several authors by studying the influence of a compact object on the stellar wind of the primary through observations and hydrodynamic simulations (e.g., Haberl et al. 1989; Blondin et al. 1990; Blondin et al. 1991; Blondin 1994). Stellar wind flowing past a compact object is affected by a number of competing forces (gravitational, rotational, and radiation pressure), and photoionization of the stellar wind can create an accretion wake (Fransson & Fabian 1980). In addition, if the orbital separation is small enough, tidal distortion of the surface of the primary can lead to enhanced mass loss through the inner Lagrangian point L_1 along the line of centers even if the primary does not fill its Roche lobe (Friend & Castor 1982). The presence of a tidal stream depends sensitively on the separation of the primary and the compact object, and only becomes apparent when the radius of the primary is greater than 95% of the radius of its Roche lobe (see Fig. 5.21; Blondin et al. 1991). Even if a tidal stream is not present, the simulations by Blondin et al. (1990) are described by the formation of nonsteady accretion wakes that produce dense filaments in the downstream wake. If the filaments are along the line-of-sight to the pulsar, which is likely to occur at orbital phases 0.5–1.0, the observed hydrogen column density will increase by a factor of a few to 10, qualitatively consistent with the phase-dependent photoelectric absorption seen in EXO 1722–363.

Observations of phase variability of the column density in Vela X-1 and 4U 1700-37 qualitatively agree with that seen in EXO 1722-363, with significantly higher

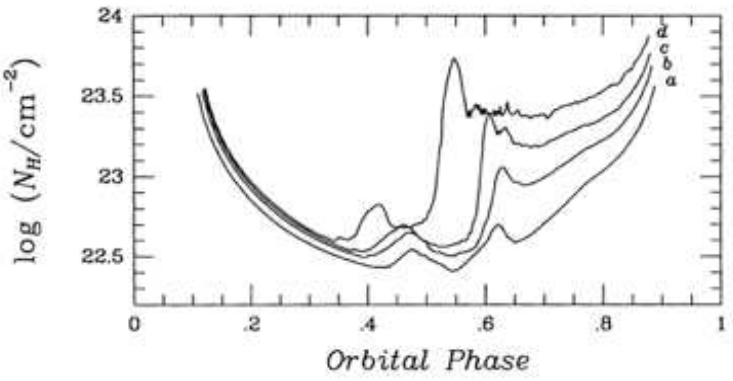

Figure 5.21: Orbital phase dependence of the absorbing column density for various binary separations, from Blondin et al. (1991). Compare the phase dependence to the EXO 1722-373 results from Fig. 5.20

absorption after $\Phi_{\rm orb} = 0.5$ (e.g., Haberl 1989; Haberl et al. 1989; Charles et al. 1978). A base level column density is seen to be reproducible over many orbits, along with a highly variable component causing $N_{\rm H}$ to increase by an order of magnitude over the base level, usually appearing at later phases. This variable component is suggested by Blondin et al. (1991) to result from separate clumps of material formed by dynamical instabilities in the accretion bow shock. Interestingly, one of the narrow peaks in Vela X-1 consistently appears at phase 0.5, and I see similar behavior, at least for one particular orbit, in EXO 1722-363.

The picture that emerged above is one of the pulsar moving through the stellar wind of its B-type companion, affecting the distribution of matter through a number of competing processes, and possibly leading to a wake of dense material trailing the pulsar in its orbit. This material will also reprocess the radiation incident upon it, leading to fluorescent iron line emission. The interpretation of the variability of the Fe Kα line is complicated because the equivalent width of the line depends on many factors, such as the spectrum of the continuum emission, and the distribution and density of the fluorescing material. The results of Table 5.8 show that the photon index varies over a wide range throughout the orbit (the photon index Γ is consistent with values between -0.5 and 2.7 at the 90% confidence level), as does the hydrogen column density. The distribution of the surrounding matter is also expected to vary over the orbit, given the nature of stellar

winds from massive stars and the effect of the pulsar on these winds.

Using Monte Carlo simulations, Leahy & Creighton (1993) found that an input spectrum with $\Gamma = 1$ emerging from a uniform and spherically symmetric distribution of matter will lead to an iron line equivalent width of about 100 eV for a column density of 10^{23} cm^{-2}. These authors also found that equivalent width increases approximately linearly below a column density of 10^{25} cm^{-2}. An input spectrum with $\Gamma = 2$, on the other hand, results in equivalent widths about one-third as large, simply because a spectrum described by a steeper power law has relatively fewer photons above the iron K-edge. Figure 5.22 shows the column density versus the equivalent width of the iron line (left panel), and the 7.1–24 keV continuum intensity versus the iron line flux (right panel). Unfortunately, upper limits on the iron line intensity were obtained for more than half of the spectra (closed circles in the figure). Also, the data points from spectra 3 and 19 were not included in the figure because the flux for these observations is only $\sim$10% above the Galactic ridge emission, and poor statistics lead to very weakly constrained equivalent widths. If I only consider the data points that are not consistent with zero (open diamonds in the figure), one can see a rough correlation between the Fe Kα equivalent width and the $N_{\rm H}$ column density, but the magnitude of the equivalent width is systematically larger than that predicted by the Leahy & Creighton (1993) simulations. Perhaps this reflects an iron abundance greater than the solar value. The dependence of the equivalent width on the iron abundance is linear when the optical depth is much less than one, but becomes less than linear when the effects of opacity become important (Matt et al. 1997). Nevertheless, by including data points that are upper limits, this rough trend no longer exists. One factor that may contribute to the lack of a clear correlation is the significant variability of the photon index. The three largest values for the equivalent width (disregarding upper limits) are from the three spectra with the flattest power laws (best-fit photon indexes of $\Gamma = 0.1$, 0.5, & 0.9, respectively), as I would expect. The right panel of Fig. 5.22 shows that the correlation between the iron line flux and the continuum intensity above the iron K-edge is better, though still not excellent. If the correlation were linear and the spectrum constant (minus changes in absorption), it would indicate that the origin of the iron line is from the same material

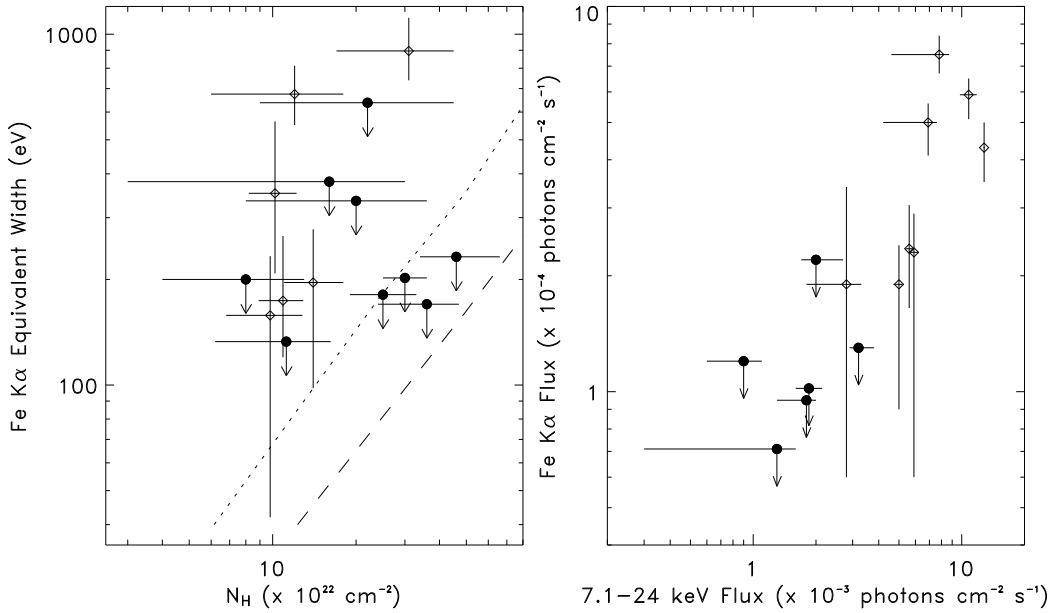

Figure 5.22: Column density versus the equivalent width of the iron line (left panel), and the 7.1–24 keV continuum intensity versus the iron line flux (right panel). Data points representing upper limits are indicated with filled circles, and the non-upper limit data points are indicated with open diamonds. The error bars in the left panel represent the 90% confidence level, while the error bars in the right panel represent the 68% confidence level. The data points from spectra 3 and 19, which have extremely large upper limits to the equivalent width, are not shown in either panel. The dotted line in the left panel shows the predicted relation between $N_{\rm H}$ and the Fe Kα equivalent width for power-law radiation with $\Gamma = 1$ emerging from a uniform sphere surrounding the source, and is the result of simulations by Leahy & Creighton (1993). The dashed line is the same but for $\Gamma = 2$.

as is responsible for the absorption of the continuum. Spectral variability makes such a comparison impossible, but I speculate that the pulsar may be illuminating matter that is not along its line of sight. That the equivalent width increases near $\Phi_{\rm orb} = 0.5$ possibly indicates that a component of the fluorescing material is the surface of the primary.

5.5 Summary & Conclusions

I have significantly improved the accuracy of the orbital parameters for the eclipsing HMXB EXO 1722–363 by applying pulse timing analysis to twenty recent *RXTE* observations (nearly evenly spaced in orbital phase) and two sets of observations occurring

2.4 years and 7.3 years earlier. With the orbital solution, I constrained the nature of the mass-donating companion star, and I investigated the evolution of the spectrum through the pulsar's orbit. Our primary results are summarized as follows:

1. The circular orbital solution is characterized by $a_x \sin i = 101 \pm 3$ lt-s, $P_{\rm orb} = 9.7403 \pm 0.0004$ days, and an epoch of mid-eclipse at HJD 53761.68 $\pm$ 0.06. The eccentricity is less than 0.19 at the 90% confidence level. Our orbital solution also implies that a reversal of the torque on the neutron star occurred between 1998 November and 2006 February.

2. Using the orbital solution and the eclipse half-angle measurement of $\theta_e = 31.8^\circ \pm 1.8^\circ$ from CMS05, I constrained the companion star's mass and radius as a function of inclination. Assuming a neutron star mass of 1.4 $M_\odot$ and that the primary underfills its Roche lobe and, the system must have an inclination greater than 61° with 99% confidence. With the lower limit on the inclination, the primary's mass is between about 11 $M_\odot$ and 22 $M_\odot$, and its radius is between 21 $R_\odot$ and 37 $R_\odot$. The range of acceptable masses and radii are consistent with a supergiant star with a spectral type between B0 and B5.

3. There is only one 2MASS IR counterpart in the 4″ *XMM-Newton* error circle. Assuming this source is the primary, I found that the photometric measurements from 2MASS and DENIS are consistent with the inferred spectral type if $A_V = 20.1 \pm 0.6$ and the distance to the system is between 5.3 kpc and 8.7 kpc.

4. The spectrum of EXO 1722–363 shows variable flux, absorbing column density, power-law photon index, and iron line equivalent width through the course of the orbit. Between orbital phases 0.25–0.45, $N_{\rm H}$ is consistent at about 10^{23} cm^{-2}, but apparently increases for the second half of the orbit. In the 2–24 keV band, the unabsorbed X-ray flux is 0.7–4.8 $\times 10^{-10}$ ergs cm^{-2} s^{-1}.

5.6 Acknowledgement

Chapter 5 is in part a reprint of material that appears in The Astrophysical Journal, Vol. 649, p. 373, and Vol. 661, p. 447. The dissertation author was the primary investigator and author of these papers.

Bibliography

Alcock, C., & Hatchett, S. 1978, ApJ, 222, 456

Arnaud, K. A. 1996, in ASP Conf. Ser. 101, Astronomical Data Analysis Software and Systems, ed. G. Jacoby & J. Barnes (San Francisco: ASP), 17

Aschenbach, B. 2002, Proc. SPIE, 4496, 8

Ash, T. D. C., Reynolds, A. P., Roche, P., Norton, A. J., Still, M. D., & Morales-Rueda, L. 1999, MNRAS, 307, 357

Audley, M. D., Nagase, F., Mitsuda, K., Angelini, L., Kelley, R. L. 2006, MNRAS, 367, 1147

Augello, G., Iaria, R., Robba, N. R., Di Salvo, T., Burderi, L., Lavagetto, G., & Stella, L., 2003, ApJ, 596, L63

Balbus, S. A., & Hawley, J. F. 1991, ApJ, 376, 214

Bałucińska-Church, M., Barnard, R., Church, M. J., & Smale, A. P. 2001, A&A, 378, 847

Barret, D., Motch, C., & Pietsch, W. 1995, A&A, 303, 526

Barret, D., Olive, J. F., Boirin, L., Done, C., Skinner, G. K., & Grindlay, J. E, 2000, ApJ, 533, 329

Barziv, O., Kaper, L., Van Kerkwijk, M. H., Telting, J. H., Van Paradijs, J. 2001, A&A, 377, 925

Belloni, T., Psaltis, D., & van der Klis, M. 2002, ApJ, 572, 392

Bevington, P., & Robinson, D. K. 2002, Data Reduction and Error Analysis for the Physical Sciences, 3rd ed. (New York: McGraw-Hill), 186

Bhattacharya, S., & Strohmayer, T. E. 2007, ApJ, 666, L85

Bhattacharya, D., & van den Heuvel, E. P. J. 1991, PhR, 242, 128

Bildsten, L., et al. 1997, ApJS, 113, 367

Bildsten, L., 2000, in AIP Conf. Proc. 522, Cosmic Explosions, ed. S. S. Holt & W. W. Zhang (Melville: AIP), 35 :

Bird, A. J., Barlow, E. J., Bassani, L., et al. 2004, ApJ, 607, L33

Bird, A. J., Barlow, E. J., Bassani, L., et al. 2006, ApJ, 636, 765

Blandford, R. D., & Begelman, M. C. 1999, MNRAS, 303, L1

Blondin, J. M., Kallman, T. R., Fryxell, B. A., & Taam, R. E. 1990, ApJ, 356, 591

Blondin, J. M., Stevens, I. R., & Kallman, T. R. 1991, ApJ, 371, 684

Blondin, J. M. 1994, ApJ, 435, 756

Bodaghee, A., et al., 2006, A&A, 447, 1027

Boirin, L., Méndez, M., Díaz Trigo, M., Parmar, A. N., & Kaastra, J. S. 2005, A&A, 436, 195

Brissenden, R. J. 2001, in ASP Conf. Ser., Vol. 238, Astronomical Data Analysis Software and Systems X, eds. F. R. Harnden, Jr., F. A. Primini, & H. E. Payne (San Francisco: ASP), 22

Burderi, L., Di Salvo, T., Robba, N. R., La Barbera, A., & Guainazzi, M. 2000, ApJ, 530, 429

Canizares, C. R., 1976, ApJ, 207, L101

Canizares, C. R., et al. 1992, AIAA Conf. Proc.: Space Programs and Technologies, 11

Canizares, C. R., et al. 2005, PASP, 117, 1144

Canuto, V., & Ventura, J. 1977, Fundamentals of Cosmic Physics, 2, 203

Cardelli, J. A., Clayton, G. C., & Mathis, J. S. 1989, ApJ, 345, 245

Chakrabarty, D., et al. 2003, Bulletin of the AAS, 35, 657

Chandra X-Ray Center. 2007, Chandra Proposers' Observatory Guide (ver. 10.0; Cambridge: *Chandra* X-Ray Cent.), http://cxc.harvard.edu/proposer/POG/html

Charles, P. A., Mason, K. O., White, N. E., Culhane, J. L., Sanford, P. W., & Moffatt, A. F. J. 1978, MNRAS, 183, 813

Charles, P. A., & Coe, M. J., 2006, in Compact Stellar X-Ray Sources, ed. W. H. G. Lewin & M. van der Klis (Cambridge: Cambridge Univ. Press), 215

Chaty, S., & Filliatre, P., 2005, Ap&SS, 297, 235

Church, M. J. 2001, Adv. Space Res., 28, 323

Church, M. J., Dotani, T., & Bałucińska-Church, M. 1997, ApJ, 491, 388

Church, M. J., Parmar, A. N., Bałucińska-Church, M., et al. 1998, A&A, 338, 556

Church, M. J., & Bałucińska-Church, M. 2001, A&A, 369, 915

Clark, G. W., Minato, J. R., & Mi, G. 1988, ApJ, 324, 974

Clark, G. W. 2004, ApJ, 610, 956

Cocchi, M., et al. 2000, AIP Conf. Proc., 510, 203

Cocchi, M., et al., 2001, Adv. Space Res., 28, 275 (Elsevier)

Combi, J. A., Ribo, M., Mirabel, I. F., & Sugizaki, M. 2004, A&A, 422, 1031

Conti, P. S. 1978, A&A, 63, 225

Corbet, R. H. D. 1984, A&A, 141, 91

Corbet, R. H. D., Markwardt, C. B., & Swank, J. H. 2005, ApJ, 633, 377 (CMS05)

Cornelisse, R., et al. 2002, A&A, 392, 885

Cornelisse, R., et al. 2003, A&A, 405, 1033

Cox, A. N., ed. 2000, Allen's Astrophysical Quantities (4th ed.; New York: AIP), 390

Crosby, N., Vilmer, N., Lund, N., & Sunyaev, R. 1998, A&A, 334, 299

Cumming, A., & Bildsten, L. 2000, ApJ, 544, 453

Dame, T. M., Hartmann, D., & Thaddeus, P. 1988, ApJ, 324, 248

Davidson, K., & Ostriker, J. P. 1973, ApJ, 179, 585

Day, C. S. R., & Tennant, A. F. 1991, MNRAS, 251, 76

Day, C. S. R., & Stevens, I. R. 1993, ApJ, 403, 322

Del Sordo, S., et al. 1999, AP Letters, 38, 125

Dickey, J. M., & Lockman, F. J. 1990, ARAA, 28, 215

Draine, B. T. 2003, ApJ, 598, 1026

Draine, B. T., & Tan, J. C. 2003, ApJ, 594, 347 (DT03)

Done, C., Gierliński, M., & Kubota, A. 2007, A&A Rev., 15, 1

Ebisuzaki, T., Hanawa, T., & Sugimoto, D. 1984, PASJ, 36, 551

Eggleton, P. P. 1983, ApJ, 268, 368

Esin, A. A., McClintock, J. E., & Narayan, R. 1997, ApJ, 489, 865

Faucher-Giguére, C.-A., & Kaspi, V. M. 2006, ApJ, 643, 322

Fender, R. P. 2002, Relativistic Flows in Astrophysics:, eds. A. W. Guthmann, M. Georganopoulos, Macrowith, A., & Manolakou, K. (Heidelberg: Springer)

Filliatre, P., & Chaty, S. 2004, ApJ, 616, 469

Fontaine, G., Brassard, P., & Bergeron, P. 2001, PASJ, 782, 409

Ford, E. C., et al. 1997, ApJ, 486, L47

Frank, J., King, A., & Raine, D. 1992, Accretion Power in Astrophysics (2d ed; New York: Cambridge Univ. Press), 73

Fransson, C., & Fabian, A. C. 1980, A&A, 87, 102

Friend, D. B., & Castor, J. I. 1982, ApJ, 261, 293

Fujimoto, M. Y, Hanawa, T., Iben, I., & Richardson, M. B. 1987, ApJ, 315, 198

Fujimoto, M. Y. 1988, ApJ, 324, 995

Gaetz, T. 2004, "Analysis of the Chandra On-Orbit PSF Wings", http://cxc.harvard.edu/cal/Hrma/psf/

Galloway, D. K., Cumming, A., Kuulkers, E., Bildsten, L., Chakrabarty, D., & Rothschild, R. E. 2004, ApJ, 601, 466 (G04)

Galloway, D. K., Muno, M. P., Hartman, J. A., Savov, P, Psaltis, D., & Chakrabarty, D. 2006, ApJS, submitted

Garmire, G. P., Bautz, M. W., Ford, P. G., Nousek, J. A., & Ricker, G. R., Jr. 2003, Proc. SPIE, 4851, 28

Ghosh, P., & Lamb, F. K. 1979, ApJ, 234, 296

Haberl, F. 1989, in Two Topics in X-ray Astronomy, ed. N. White (ESA SP-296), 31

Haberl, F., White, N. E., & Kallman, T. R. 1989, ApJ, 343, 409

Hansen, C. J., Kawaler S. D., & Trimble V. 2004, Stellar Interiors: Physical Principles, Structure, and Evolution (New York: Springer), 57

Hasinger, G., & van der Klis, M. 1989, A&A, 225, 79

Heger, A., Cumming, A., Galloway, D. K., & Woosley, S. E. 2008, ApJL, accepted

Homer, L., Charles, P. A., O'Donoghue, D. 1998, MNRAS, 298, 497

Hu, J., Zhang, S. N., & Li, T. P. 2004, ApJ, 614, L45

Hulse, R. A., & Taylor, J. H. 1975, ApJL, 195, L51

Hutchings, J. B., Cowley, A. P., Crampton, D., van Paradijs, J., & White, N. E. 1979, ApJ, 229, 1079

Iben, I. 1991, ApJS, 76, 55

Ibragimov, A., Poutanen, J., Gilfanov, M., Zdziarski, A. A., & Shrader, C. R. 2005, MNRAS, 362, 1435

Inogamov, N. A., & Sunyaev, R. A. 1999, Astron. Lett., 25, 269

in 't Zand, J. J. M., Heise, J. Kuulkers, E., Bazzao, A., Cocchi, M. & Ubertini, P. 1999(a), A&A, 347, 891

in 't Zand, J. J. M., et al. 1999(b), A&A, 345, 100

Jahoda, K., et al. 1996, Proc. SPIE, 2808, 59

Jahoda, K., et al. 2006, ApJS, 163, 401

Janka, H.-T., Marek, A., Müller, B., & Scheck, L. 2008, in AIP Conf. Proc. 983, 40 Year so Pulsars: Millisecond Pulsars, Magnetars and More, ed. Bassa, C., Wang, Z., Cumming, A., Kaspi, V. M. (Montreal: AIP), 369

Jonker, P. G., et al. 2000, ApJ, 531, 453

Kalemci, E., Tomsick, J. A., Rothschild, R. E., Pottschmidt, K., & Kaaret, P. 2004, ApJ, 603, 231

Kalemci, E., et al. 2005, ApJ, 622, 508

Kalemci, E., Tomsick, J. A., Rothschild, R. E., Pottschmidt, K., Corbel, S., & Kaaret, P. 2006, ApJ, 639, 340

King, A. R., Davies, M. B., Ward, M. J., Fabbiano, G., & Elvis, M. 2001, ApJ, 552, L109

Klose, S. 1991, A&A, 248, 624

Kong, A. K. H., Homer, L., Kuulkers, E., Charles, P. A., & Smale, A. P. 2000, MNRAS, 311, 405

Kong, A. H. K., et al. 2007, ApJ, 670, L17

Kortright, J. B., & Kim, S.-K. 2000, Phys. Rev. B, 62, 12216

Kreykenbohm, I., et al. 2004, A&A, 427, 975

Krumholz, M. R. 2005, in ASP Conf. Ser., Frank N. Bash Symposium 2005: New Horizons in Astronomy, eds. Kannappan, S., Redfield, S., Drory, N., Kessler-Silacci, J., & Landriau, M. (San Francisco: ASP), in press

Krzemiński, W. 1974, ApJ, 192, L135

Kuulkers, E. 2005, in Interacting Binaries: Accretion, Evolution and Outcomes, eds. L.A. Antonelli, et al. (AIP: New York), 402

Lampton, M., Margon, B., & Bowyer, S. 1976, ApJ, 208, 177

Leahy, D. A., et al. 1983, ApJ, 266, 160

Leahy, D. A., & Creighton, J. 1993, MNRAS, 263, 314

Lebrun, F., et al., 2003, A&A, 411, L141

Levine, A. M., et al. 1996, ApJ, 469, L33

Levine, A. M., Rappaport, S., Remillard, R., & Savcheva, A. 2004, ApJ, 617, 1284

Lewin, W. H. G., van Paradijs, J., & Taam, R. E. 1995, X-Ray Binaries, eds: W. H. G. Lewin, J. van Paradijs, & E. P. J. van den Heuvel, (Cambridge: Cambridge Univ. Press), 175

Lin, C. C., & Shu, F. H. 1964, ApJ, 140, 646

Liu, Q. Z., van Paradijs, J., & van den Heuvel, E. P. J. 2000, A&AS, 147, 25

Liu, Q. Z.; van Paradijs, J., & van den Heuvel, E. P. J. 2006, A&A, 455, 1165

London, R. A., Taam, R. E., & Howard, W. M. 1986, ApJ, 306, 170

Lutovinov, A., Rodriguez, J., Revnivtsev, M., & Shtykovskiy, P., 2005, A&A, 433, L41

Madej, J., Joss, P. C., & Różańska, A. 2004, ApJ, 602, 904

Makino, R., et al., 1988, IAU Circ., 4653

Marsden, D., Lingenfelter, R. E., Rothschild, R. E., & Higdon, J. C. 2001, ApJ, 550, 397

Mathis, J. S., Rumpl, W., & Nordsieck, K. H. 1977, ApJ, 217, 425 (MRN)

Mathis, J. S., & Lee, C.-W. 1991, ApJ, 376, 490

Matsuba, E., et al. 1995, PASJ, 47, 575

Mauche, C. W., & Gorenstein, P. 1986, ApJ, 302, 371

Matt, G., Fabian A. C., & Reynolds C. S. 1997, MNRAS, 289, 175

Mayer, M., & Pringle, J. E. 2007, MNRAS, 376, 435

Mescheryakov, A. V., et al. 2004, Astron. Lett., 30, 751

Meyer, F., & Meyer-Hoffmeister, E. 1994, A&A, 288, 175

Meyer, F., Liu, B. F., & Meyer-Hofmeister, E. 2000, A&A, 361, 175

Mihara, T. 1995, Ph.D. Thesis (University of Tokyo)

Miller, J. M., et al. 2002, ApJ, 578, 348

Mitsuda, K., et al. 1984, PASJ, 36, 741

Mitsuda, K., Inoue, H., Nakamura, N., & Tanaka, Y. 1989, PASJ, 41, 97

Miyamoto, S., & Kitamoto, S. 1989, Nature, 342, 773

Muno, M. P. 2004, AIP Conf. Proc. 714: X-ray Timing 2003: Rossi and Beyond, 239

Nagase, F., et al. 1992, ApJ, 396, 147

Narayan, R., & Popham, R. 1993, Nature, 362, 820

Narayan, R., & Yi, I. 1995, ApJ, 452, 710

Nowak, M. .A. 2000, MNRAS, 318, 361

O'Donoghue, D. 1995, BaltA, 4, 519

Olive, J. F., Barret, D., Boirin, L., Grindlay, J. E., Swank, J. H., & Smale, A. P. 1998, A&A, 333,942

Overbeck, J. 1965, ApJ, 141, 864

Paczyński, B. 1976, in Structure and Evolution of Close Binary Systems, IAU Symp. 73, ed. Eggleton, P., Mitton, S., & Whelan, J. (Reidel: Bordrecht), 75

Patel, S. K., et al., 2004, ApJ, 602, L45

Patel, S. K., et al., 2007, ApJ, 657, 994

Peterson, L. E. 1975, ARA&A, 13, 423

Pottschmidt, K., Chernyakova, M., Zdziarski, A. A., Lubiński, P., Smith, D. M., & Bezayiff, N. 2006, A&A, 452, 285

Predehl, P., & Schmitt, J. H. M. M. 1995, A&A, 293, 889

Predehl, P., Burwitz, V., Paerels, F., & Trümper, J. 2000, A&A, 357, L25

Priedhorsky, W. C., & Terrell, J. 1983, ApJ, 273, 709

Pringle, J. 1976, MNRAS, 177, 65

Pringle, J. 1981, A&A, 19, 137

Protassov, R., van Dyk, D. A., Connors, A., Kashyap, V. L., & Siemiginowska, A. 2002, ApJ, 571, 545

Psaltis, D., Belloni, T., & van der Klis, M. 1999, ApJ, 520, 262

Psaltis, D., & Norman, C. 2000, ApJ, submitted, preprint: astro-ph/001391

Rappaport, S. A., & Joss, P. C. 1983, Accretion Driven Stellar X-ray Sources, eds. W. H. G. Lewin and E. P. J. van den Heuvel, Cambridge University Press, 1

Rolf, D. P. 1983, Nature, 302, 46

Rothschild, R. E., et al. 1998, ApJ, 496, 538

Różańska, A., & Czerny, B. 2000, A&A, 360, 1170

Russeil, D. 2003, A&A, 397, 133

Rybicki, G. B., & Lightman, A. P. 1979, Radiative Processes in Astrophysics (New York: Wiley-Interscience), 198

Scargle, J. D. 1982, ApJ, 263, 835

Schreier, E., Levinson, R., Gursky, H., Kellogg, E., Tananbaum, H., & Giacconi, R. 1972, ApJL, 172, L79

Schulz, N. S., et al. 2002, ApJ, 565, 1141

Shapiro, S. L., Lightman, A. P., & Eardley, D. M. 1976, ApJ, 204, 187

Shaposhnikov, N., & Titarchuk, L. 2006, ApJ, 643, 109

Schulze, H.-J., Polls, A., Ramos, A., & Vidaña, I. 2006, PhRevC, 73, 5

Shakura, N. I., & Sunyaev, R. A. 1973, A&A, 24, 337

Shaviv, N. J. 2003, New Astron., 8, 39

Smale, A. P., Church, M. J., & Bałucińska-Church, M. 2001, ApJ, 550, 962

Smith, R. K., & Dwek, E. 1998, ApJ, 503, 831 (erratum 541, 512 [2000])

Smith, R. K., Edgar, R. J., & Shafer, R. A. 2002, ApJ, 581, 562

Spitkovsky, A., Levin, Y., & Ushomirsky, G. 2002, ApJ, 566, 1018

Standish, E. M., Newhall, X. X., Williams, J. G., & Yeomans, D. K. 1992, in Explanatory Supplement to the Astronomical Almanac, ed. P. K. Seidelmann (Mill Valley: University Science), 279

Stetson, P. B. 1987, PASP, 99, 191

Strickman, M., Skibo, J., Purcell, W., Barret, D., & Motch, C. 1996, AAPS, 120, 217

Strohmayer, T. E., & Bildsten, L. 2006, in Compact Stellar X-ray Sources , ed. W. H. G. Lewin, & M. van der Klis (Cambridge: Cambridge University Press), 113

Suchy, S., et al. 2008, ApJ, 675, 1487

Sugizaki, M., Mitsuda, K., & Kaneda H., et al. 2001, ApJS, 134, 77

Sunyaev, R. A., & Titarchuk, L. G. 1980, A&A, 86, 121

Takeshima, T., Dotani, T., Mitsuda, K., & Nagase, F. 1991, PASJ, 43, L43

Takeuchi, Y., Koyama, K., & Warwick, R. S. 1990, PASJ, 42, 287

Tanaka, Y. 1989, in Proc. 23rd ESLAB Symp., Two Topics in X-Ray Astronomy, ed. J. Hunt & B. Battrick (SP-296; Noordwijk: ESA), 3

Tananbaum, H., Gursky, H., Kellogg, E., Levinson, R., Schreier, E., & Giacconi, R. 1972, ApJL, 174, L143

Tawara, Y., Yamauchi, S., Awaki, H., Kii, T., Koyama, K., & Nagase, F. 1989, PASJ, 41, 473

Thompson, T. W. J., Rothschild, R. E., Tomsick, J. A., & Marshall, H. L. 2005, ApJ, 634, 1261

Thompson, T. W. J., Tomsick, J. A., Rothschild, R. E., in 't Zand, J. J. M, & Walter, R. 2006, ApJ, 649, 37

Thompson, T. W. J., Rothschild, R. E., & Tomsick, J. A. 2006, ApJ, 650, 1063

Thompson, T. W. J., Tomsick, J. A, in 't Zand, J. J. M., Rothschild, R. E., & Walter, R. 2007, ApJ, 661, 447

Tiengo, A., & Mereghetti, S. 2006, A&A, 449, 203

Titarchuk, L. 1994, ApJ, 434, 570

Titarchuk, L., & Shaposhnikov, N. 2005, ApJ, 626, 298

Trümper, J., & Schönfelder, V. 1973, A&A, 25, 445 (TS73)

Ubertini, P., et al. 1997, IAU Circ., 6611

Ubertini, P., et al., 1999, ApJ, 514, L27

Ubertini, P., et al., 2003, A&A, 411, L131

Valinia, A., & Marshall, F. E. 1998, ApJ, 505, 134

van der Klis, M. 1989, in Timing Neutron Stars, eds. Ogelman, H., & van den Huevel, 27

van der Klis, M. 1994, ApJS, 92, 511

van Kerkwijk, M. H., van Paradijs, J., & Zuiderwijk, E. J., 1995, A&A, 303, 497

van Straaten, S., van der Klis, M., Di Salvo, T., & Belloni, T. 2002, ApJ, 568, 912

Vaughan, S., et al. 2004, ApJ, 603, L5

Vaughan, S., et al. 2006, ApJ, 639, 323

Vignarca, F., Migliari, S., Belloni, T., Psaltis, D., & van der Klis, M. 2003, A&A, 39 729

Wallace & Woosley, 1981, ApJS, 45, 389

Walter, R., et al., 2003, A&A, 411, L427

Walter, R., et al., 2006, A&A, 453, 133

Warwick, R. S., Norton, A. J., Turner, M. J. L., Watson, M. G., & Willingale, R. 1988, MNRAS, 232, 551

Weingartner, J. C., & Draine, B. T. 2001, ApJ, 548, 296 (WD01)

White, N. E., & Holt, S. S. 1982, ApJ, 257, 318

White, N. E., Swank, J. H., & Holt, S. S. 1983, ApJ, 270, 711

Wilms, J. 1998, *Ph.D. Thesis*, University of Tuebingen, Tuebingen

Wilms, J., Allen, A., & McCray, R. 2000, ApJ, 542, 914

Wijnands, R., & van der Klis, M. 1998, Nature, 394, 344

Wijnands, R., & van der Klis, M. 1999, ApJ, 514, 939

Woosley, S. E., et al. 2004, ApJ, 151, 75

Yaqoob, T., George, I. M., Kallman, T., Padmanabhan, U., Weaver, K., & Turner, T. J. 2003, ApJ, 596, 85

Yoshida, K., Mitsuda, K., Ebisawa, K., Ueda Y., Fujimoto, R., & Yaqoob, T. 1993, PASJ, 45, 605

Xiang, J., Lee, J. C.; Nowak, M. A. 2007, ApJ, 660, 1309

Yao, Y., Zhang, S. N., Zhang, X. L., & Feng, Y. X. 2003, ApJ, 594, L43

Zubko, V., Dwek, E., & Arendt, R. 2004, ApJS, 152, 21

Zurita Heras, J. A., et al., 2006, A&A, 448, 261